An Investigation into the Dynamic Response of Cardboard Honeycombs

Jonathan J. Reay

A thesis presented for the degree of

Doctor of Philosophy

Department of Civil and Structural Engineering

University of Sheffield

January 2014

Abstract

Cardboard honeycombs are used extensively in the packaging industry to protect objects from abnormally high loading conditions. They provide a substantial amount of energy dissipation while being lightweight, structurally efficient, cost-effective and easily disposed of (or recycled) once used. These beneficial properties have also led to the widespread use of cardboard honeycombs as a method to protect air-dropped cargo from the shock loading encountered during parachute deployment and impact with the ground.

When cardboard honeycombs are crushed at the strain-rates typical of a low-velocity impact event, such as an air drop, the air pressures, which develop within the honeycomb as a result of a compaction of the entrapped air, are comparable in magnitude to the stiffness of the cell wall deformation response. Thus, the dynamic energy dissipation properties of cardboard honeycombs are dependent on the mechanics of a coupled air-structure deformation mechanism.

This thesis studies the mechanics of the air-structure deformation mechanism and investigates how it is affected by variations in the material and geometrical properties of the cardboard honeycomb cell walls.

During a series of experimental impact tests on cardboard honeycomb samples of various known geometries, both macroscopic behaviour and the development of air pressures at four internal locations are measured (Chapter 3). An explicit Lagrangian/ALE numerical model of the cardboard honeycomb and entrapped air is then developed, using the commercial hydrocode LS-Dyna (Chapter 4). The numerical model is used to study the effects of variations in the cell wall material properties (Chapter 5), and their meso and macroscale geometrical arrangement (Chapter 6) on the cardboard honeycomb's energy dissipating characteristics. A summary of the experimental and numerical findings is then given (Chapter 7), with consideration of implications for an end user.

Acknowledgements

I would like to express my gratitude to my supervisor Dr T. Bennett for the opportunity to carry out this research and for the support and guidance throughout. I am also grateful to my second supervisor Dr A. Tyas for the ever valuable input and thought provoking discussions.

I would like to thank Blastech Ltd for providing the invaluable facilities and resources, without which the experimental work would not have been a reality. I am also extremely grateful to Dr J. Warren, S. Fay and all the fantastic technical staff at Blastech Ltd.

I acknowledge with gratitude the financial support from DSTL and EPSRC who provided the funding for this project.

Finally, I would like to thank G. K. Hajduk for the endless patience and support.

Contents

List of Tables

List of Figures

List of Symbols

α	internal angle, $\alpha = \theta - 90°$
$\bar{\Delta}_{x,y}$	average rigid body lateral displacement of cell walls due to outwards drift
$\bar{\Delta}_x$	average rigid body lateral displacement of cell walls, in x
$\bar{\Delta}_y$	average rigid body lateral displacement of cell walls, in y
$\bar{L}$	average cell wall length
$\bar{L}_{1t}$	average single-ply cell wall length
$\bar{L}_{2t}$	average double-ply cell wall length
δA	change of internal cross sectional area
$\delta A_{\bar{\Delta}_{x,y}}$	total increase of internal plan area due to cell wall lateral drift
$\delta A_{\bar{\Delta}_x}$	increase of internal plan area due to cell wall lateral drift in x
$\delta A_{\bar{\Delta}_y}$	increase of internal plan area due to cell wall lateral drift in y
ΔH_{Yield}	vertical displacement equivalent to ε_{Yield}
Δt_{crit}	critical time step
Δt_{global}	global time step
δ_{ELh}	element size (horizontal)
δ_{ELv}	element size (vertical)

δ_{EL}	element size (avg)
Δ_x	rigid body lateral displacement of cell wall, in x
δ_X	width of macroscopic footprint, in x
Δ_y	rigid body lateral displacement of cell wall, in y
δ_Y	width of macroscopic footprint, in y
$\dot{\varepsilon}_{avg}$	average strain rate
$\dot{\varepsilon}_i$	initial strain rate
γ	adiabatic index
κ	penalty stiffness coefficient
κ_y	global permeability in direction of blow out
λ	wavelength of one progressive fold
ω/ω_c	normalised angular frequency
ν	poissons ratio of cell wall material
ω	angular frequency
ϕ_{Card}	proportion of cross section composed of cardboard
ϕ_{Conf}	current degree of lateral confinement provided by structure
ϕ_{Cost}	ratio of required real time and a given analysis time
ρ	density of cell wall material
ρ_0	initial density (air)
$\rho_{An,Fin}$	final density as predicted by mathematical model
ρ_{Fin}	final density (air)

ρ_m macroscopic density

ΣL total length of cell wall

ΣL_{1t} total length of single-ply cell wall

ΣL_{2t} total length of double-ply cell wall

σ stress

$\sigma'_{PeakNum}$ peak stress transmitted by numerical model (secondary)

σ_0 flow stress

$\sigma_{Air,1D}$ air pressure as predicted by a 1-D adiabatic compaction

$\sigma_{Air,\delta V}$ internal pressure change due to change of internal volume

$\sigma_{Air,max}$ maximum internal air pressure

$\sigma_{Air,Vent}$ internal pressure change due to loss of air via venting

σ_{Air} gaseous component of macroscopic transmitted stress

σ_{Card} solid component of macroscopic transmitted stress

σ_{Glue} glue strength

$\sigma_{PeakCru}$ peak stress due to crushing of cell walls

$\sigma_{PeakEul}$ peak stress due to Euler buckling

$\sigma_{PeakNum}$ peak stress transmitted by numerical model

σ_{Peak} peak transmitted stress

σ_{PlatAn} plateau stress as predicted by mathematical model

$\sigma_{Plateau}$ plateau transmitted stress

$\sigma_{PlatNum}$ plateau stress transmitted by numerical model

σ_{Total}	total macroscopic transmitted stress
$\sigma_{Y,t1}$	yield stress of single-ply cell wall
$\sigma_{Y,t2}$	yield stress of double-ply cell wall
σ_{Yield}	yield stress of cell wall material
τ	temperature
θ	internal expansion angle
ε	axial strain
ε_p	plastic strain
ε_{Comp}	compaction strain
ε_{Yield}	yield strain
ξ	(t/L) value for which crushing and Euler buckling modes are equally dominant)
A_1	initial cross sectional area
A_2	final cross sectional area
A_i	tributory area of one corner element
A_{Air}	total cross sectional area of entrapped air
A_{Card}	total cross sectional area of cardboard cell wall material
A_c	total cross sectional area of cardboard cell wall material
A_{Hex}	internal area of one hexagonal cell
A_{Loss}	loss of internal area due to structural deformations
A_{Net}	net change of internal area

A_{Trib}	total tributory area of load bearing components
c_p	heat capacity at constant pressure
c_v	heat capacity at constant volume
E	elastic modulus of cell wall material
E_t	post-yield tangent hardening modulus of cell wall material
H_1	initial height
H_2	final height
K	adiabatic expansion constant
L_{1t}	single-ply cell wall length
L_{2t}	double-ply cell wall length
n_f	number of progressive folds
$P_{An,Fin}$	final pressure as predicted by mathematical model
P_{Crit}	critical buckling load
$P_i(\varepsilon)$	load transmitted by one corner element
P_{Plat}	load transmitted during plateau region
$R_{Specific}$	specific gas constant
T_{Num}	required analysis time
T_{Real}	real time required to complete numerical analysis
T_{Wave}	time for stress wave to travel distance H
T_{Yield}	time to reach ε_{Yield}
U	total energy dissipated per unit volume

$U_{\varepsilon_{Comp}}$	total energy dissipated per unit volume, by compaction
U_{Air}	energy dissipated per unit volume, during compaction of the entrapped air
U_{Card}	energy dissipated per unit volume, during plastic strain of the cell walls
v_i	initial impact velocity
$v_{i,cru}$	minimum impact velocity required to ensure the crushing buckling mode
A	area
a	acceleration
c	longitudinal wave speed
D	flexural rigidity
F	frequency
F_c	filter cut-off frequency
G	gain
H	height (thickness) of the honeycomb
K	end fixity coefficient
k	ratio of double-ply to single-ply cell wall yield stress
L	cell wall length
n	order
ncell	number of complete, closed, cells
ncol	number of complete adjacent columns of cells
nrow	number of complete adjacent rows of cells
P	pressure

P_1	initial pressure
P_2	final pressure
Q	hourglass stiffness coefficient
t	cell wall thickness
V	volume
V_1	initial volume
V_2	final volume
v_f	final impact velocity

Chapter 1

Introduction

Air drops allow the rapid delivery of supplies to areas which are difficult or impossible to access by land. They are heavily relied upon in difficult times such as war or natural disaster, where masses of people can suddenly be placed in life threatening situations in need of humanitarian aid. Recent conflicts in Iraq and Afghanistan have seen the amount of air-dropped supplies increase year on year. The US army dropped £9 million worth of aid in 2008, a record that was broken in 2009 with £10 million being dropped by the end of August [1].

Humanitarian aid air-drops consist of a compartmentalised delivery system (CDS) connected to a parachute. The configuration of the CDS is shown in Figure 1.1. The base is formed using a 1 inch thick plywood panel, known as the skid board. On top of the skid board there are alternate layers of a cardboard honeycomb energy dissipating material and the cargo. The layers are wrapped with cellophane and a parachute is connected to the skid board and placed on top. Depending on the volume and type of cargo the CDS weight can vary from around 200 to 1000 kg [1, 2].

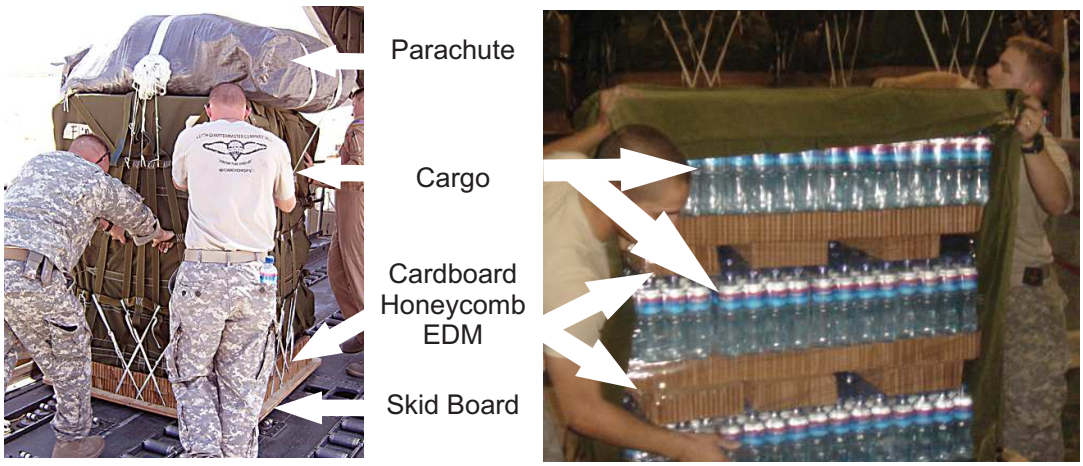

Figure 1.1 The cardboard honeycomb in use as an energy dissipating material to protect air-dropped cargo [1].

During both parachute deployment and contact with the ground the air-drop is subject to an impulse causing a sudden change in velocity. The impulse is applied to the skid board and then transmitted to the layers of cargo and cardboard honeycomb [2–4]. If the force applied to the cargo is too large, it will be damaged. The cardboard honeycomb protects the cargo by acting as a non-linear spring, reducing the transmitted peak force by distributing the impulse over a longer time and reducing the total impulse by absorbing kinetic energy through plastic deformation of its cell walls.

Cardboard honeycombs provide a substantial amount of energy dissipation while being lightweight, structurally efficient, cost-effective and easily disposed of (or recycled) once used. These properties make them ideally suited to their use as a sacrificial, non-recoverable energy dissipating material during air-drops; however, cardboard honeycombs are also used extensively in the packaging industry [5], construction industry [6], and as a method of energy absorption in lightweight cycle helmets [7].

The energy dissipation characteristics of a honeycomb are dependent on its mesoscopic response. When cardboard honeycombs are subject to dynamic axial crushing, the internal air pressures generated by compaction of the entrapped air develop to magnitudes comparable with the load transmitted through the cell wall material

[8]. The result is a complex coupled air-structure deformation mode, the mechanics of which are as yet to be understood.

As the relationship between a given cardboard honeycomb's constitutive structure and its dynamic macroscopic response is unknown, cardboard honeycombs have historically been designed via ad-hoc experimental impact tests [9, 10]. Due to unforeseen deviations between tightly controlled laboratory conditions and those which occur during non-perfect in-theatre use, this method generally necessitates inefficient over-design. Furthermore, due to a large number of material and geometrical parameters (each of which are variable), without a fundamental understanding of the mechanisms which drive the macroscopic response, any collected experimental data is valid solely for the combination of material and geometrical parameters specific to the tested samples.

1.1 The cardboard honeycomb EDM

Figure 1.2 shows a sample of the cardboard honeycomb EDM situated in its pre-test position, prior to being rapidly crushed by a hydraulic ram.

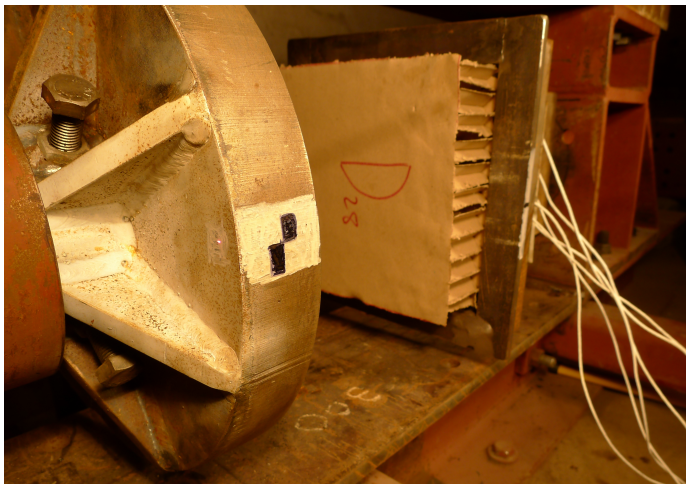

Figure 1.2 A square 250 x 250 mm by 70 mm thick square cardboard honeycomb sample located in the gas gun test rig, which was used to perform impact tests on cardboard honeycombs of varied geometry, and measure their response (Chapter 3).

A cardboard honeycomb consists of three parts: a cellular honeycomb core and two liners (Figure 1.3). Both the core and the liners are composed of sheets of some type of cardboard material. The top and bottom liners are bonded to the top and bottom edges of the cellular core.

In Figure 1.3 several macroscopic geometrical parameters are defined along with a convention for labelling the three Cartesian axes. Height H refers to the thickness of a cardboard honeycomb sample in the z plane, δ_x and δ_y refer to the footprint widths in x and y dimensions, and A_{Trib} refers to the total footprint area of the cell walls. Note that: A_{Trib} also corresponds to the area of the top and bottom liner sheets; and the z axis refers to the direction of loading and collapse.

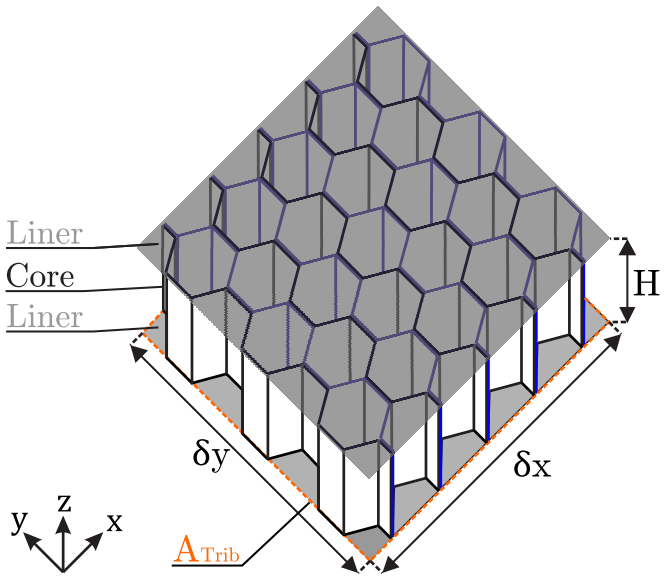

Figure 1.3 Definition of the basic macroscopic geometrical parameters of a cardboard honeycomb.

To create the cellular honeycomb core, rectangular strips of glue are applied to sheets of cardboard material. These sheets are then overlaid and offset, ensuring an alternating glue bond pattern and pulled apart (in the direction of the x axis) to form the cellular structure shown in Figure 1.4. The glue bond thickness is negligible, thus each hexagonal cell possesses four cell walls of single thickness t and two cell walls of double thickness 2t. The length of a cell wall on plan is referred to as L.

The cross sectional area of structural cell wall material within the footprint area of A_{Trib} is defined as A_c (also referred to as A_{Card}). A_c can be computed by multiplying the total length of cell wall by its thickness.

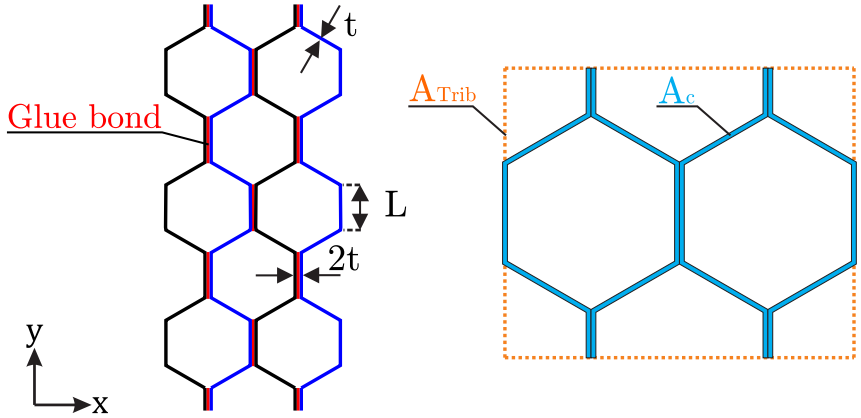

Figure 1.4 Detail of a cardboard honeycomb cellular configuration, and definition of the basic mesoscopic geometrical parameters.

It is worth nothing at this time, that any reference to *pressure* or *internal air pressure*, unless otherwise stated, will herein refer to *overpressure* rather than *absolute pressure*.

1.2 Scope and Outline of the thesis

This thesis presents an investigation into the mesoscopic mechanics which govern the cardboard honeycomb's dynamic, macroscopic, response. Consideration is given to the spatial and temporal development of internal air pressures and their mechanisms of interaction with the cellular structure. By studying the effects of isolated variations of the cell wall material and geometrical properties on the mesoscopic mechanisms, a fundamental understanding of the complex air-structure buckling mode is developed. Additionally, by analysing variations of the cardboard honeycombs energy dissipating characteristics (caused by variations of the material and geometrical parameters), conclusions are drawn which will guide more efficient design and deployment of the cardboard honeycomb energy dissipating material.

Chapter 2 reviews the current state of knowledge regarding the dynamic axial crushing response of cardboard honeycombs. Research regarding the response of other, similar, energy dissipating materials is also discussed and consideration is given to the cell wall material properties which have been observed to be responsible for the cardboard honeycombs quasi-static response.

Chapter 3 details a series of experimental impact tests performed on cardboard honeycomb samples of fixed macroscopic, but varied mesoscopic geometries. In addition to measurements of macroscopic axial strain and the corresponding total transmitted stress, simultaneous measurements of air pressures at four internal locations are made. Exact cellular geometries of all tested samples are recorded, allowing each recorded experimental response to be attributed to a known cellular arrangement.

Chapter 4 describes the development of a numerical model capable of capturing the physics of the dynamically crushed cardboard honeycomb and the entrapped air. The deformable cell wall structure is modelled using Lagrangian finite shell elements, the air is represented using a fixed Eulerian background domain and the coupling between the structure and the air is achieved via penalty contact algorithms. Individual modelling techniques are verified, while addressing stability and computational efficiency concerns, before being combined to create a full-scale numerical model which is then compared with recorded experimental data.

The numerical techniques developed during Chapter 4 are refined, to a create a computationally efficient model of an ideal honeycomb structure. During Chapter 5 and Chapter 6 the idealised numerical model is used as a platform to perform a thorough investigation into the effects of variations of the cell wall material and geometrical parameters, on the cardboard honeycombs dynamic response. Tables 5.6 and 6.4 display the scope of parameter variations covered by the material and geometrical parameter studies respectively.

The thesis concludes in Chapter 7 by summarising the main findings from the experimental and numerical investigations, highlighting implications from the perspective of an end user, and identifying key areas of future work.

Chapter 2

Literature review

This chapter highlights existing research relevant to the impact behaviour of cardboard honeycomb energy-dissipating materials. The concept of energy dissipating materials (EDMs) is introduced (Section 2.1), and then literature regarding the behaviour of other energy dissipating materials, of similar structural configuration to the cardboard honeycomb, is reviewed (Section 2.2). An overview of the research which has advanced the understanding, of the structural mechanics, of axially crushed honeycombs is given (Section 2.3).

Research which has investigated the response of cardboard honeycombs is outlined (Section 2.4), and the small body of existing literature which directly considers the *axial impact response of cardboard honeycombs* is identified (Section 2.4.1). An overview of the understanding of paper/cardboard material properties and the parameters which have so far been identified to affect the quasi-static cardboard honeycomb response, is given (Section 2.5). Finally, the void in knowledge, which this thesis attempts to fill, is identified (Section 2.6).

2.1 Energy dissipating materials (EDMs)

Energy dissipating materials (EDMs) provide protection to objects from higher than normal loading conditions. They work by dissipating potentially damaging kinetic energy and by limiting the magnitude of load transmitted to an object. EDMs act

as viscous non-linear springs, dissipating energy through internal work, and limiting the load by extending the timebase over which it is applied. The internal work is often provided by plastic strain of the constitutive material during macroscopic compaction of the EDM, and at any point during the compaction the transmitted load is limited by the EDM's current stiffness, which is a function of the material properties and their current geometrical arrangement. If the mechanics of the EDM's response are known in advance, the magnitude of dissipated energy and transmitted load, can be tailored to protect against an expected loading event.

It is desirable to maximise the efficiency of an energy dissipating material, i.e. the amount of energy absorption provided per unit volume, weight or cost. Efficiency can be increased by maximising the magnitude of plastic strain experienced by the constitutive material. This can be achieved by arranging the material in such a way as to encourage a deformation mode which subjects the cell wall to a substantial amount of plastic work as it propagates. Figure 2.1 shows the pattern of loading, typically experienced by an object protected by an EDM of this kind, where the load transmitted to the object (Stress, σ) varies as the EDM is compacted by an increasing strain ε, and the area under the graph is the energy dissipated (per unit volume) $U(\varepsilon)$ by a given strain.

Three features are of note: the peak stress σ_{Peak}, which occurs as a result of the structure existing in its initial unbuckled, most geometrically stiff configuration; the plateau stress $\sigma_{Plateau}$, which is a function of stiffness of the propagating deformation mode; and compaction, which occurs once the unbuckled cell wall is completely exhausted, adjacent folds begin to touch and bear on each other, allowing the transfer of additional load through the honeycomb. The compaction strain marks the end of the useful EDM response and occurs when the plateau stress begins to exceed the initial peak.

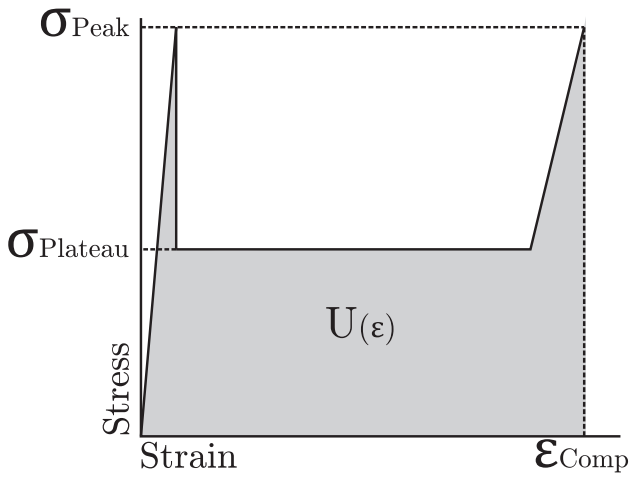

Figure 2.1 A typical EDM stress vs strain response.

2.2 Overview of axially loaded EDMs

A substantial body of research has been performed into the understanding of the deformation mechanics for a wide range of structural configurations [11]. Configurations which are of most relevance to this thesis are those, where the material is arranged with a constant 2 dimensional thin-walled cross section, extruded along a third axis by a distance much greater than the thickness of the walls. These structures have extremely high strength to weight ratios due to their efficient geometrical arrangement and when loaded axially (in the direction of extrusion) they tend to buckle via a progressive folding mechanism, which subjects a large proportion of the walls to plastic strain.

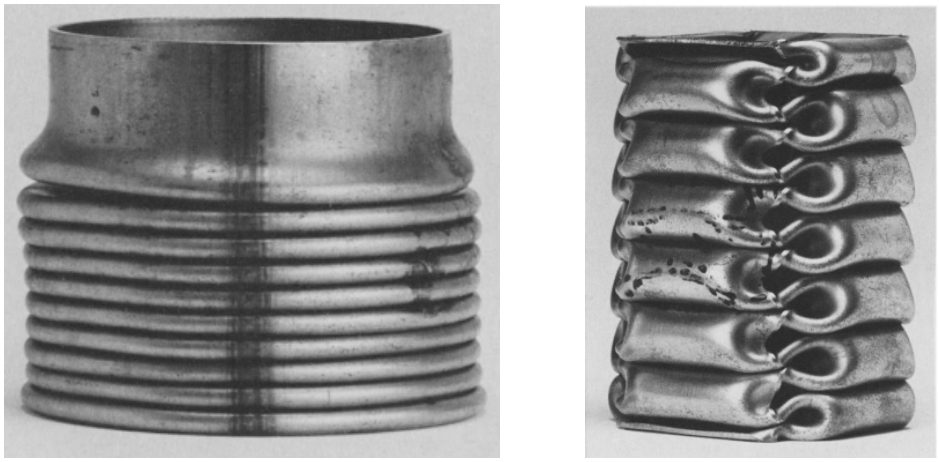

(a) H = 178 mm, ϕ = 56 mm (b) H = 289 mm, L = 39 mm

Figure 2.2 An illustration of an progressive folding mechanism observed in an axially crushed circular [12], and square [13] hollow tube. Initial height H, diameter ϕ and wall length L are given for scale. Figures taken from publications [12] and [13].

By analysing the mechanics of experimentally observed progressive buckling modes, in axially loaded square and circular steel tubes (Figure 2.2), Abramowicz and Jones [12–15] developed mathematical models to predict the load transmitted during their dynamic axial crushing response. They found that the deformation mode was heavily dependent on the tube geometry, particularly the cell wall thickness to tube diameter ratio. Experimental comparison between statically and dynamically crushed aluminium alloy 6060, square tubes, was given by Langseth and Hopperstad [16]. A strain rate effect was observed, with an increased strain rate causing higher loads to be transmitted by the tubes during their axial crushing response.

Zhao and Abdennadher [17] showed that the strain rate stiffening effect is also present in the axial crushing response of tubes constructed from non-strain-rate-sensitive material (brass), and that the strain rate effect was caused by a micro-inertia effect from the rapid acceleration of the tube wall material. This micro-inertia effect refers to the lateral restraint provided by the additional force required

to rapidly shift the initially-axially-aligned cell walls into their out of plane buckled state. Due to the high strength to weight nature of the cell wall material used in cardboard honeycombs, micro-inertial stiffening is not expected to be a driving mechanism in their dynamic response.

White, Jones and Abramowicz [18, 19] studied the quasi-static axial crushing response of top-hat and double-hat welded thin-walled sections (tubes constructed from two welded channels). By considering the mechanics of a progressive folding element, they were able to make predictions of the rigid-plastic mean crushing loads exerted by hat sections, of various geometries, during their quasi-static axial crushing response.

Figure 2.3 shows the geometry of a double top hat section (a), crushed states at the cusp of Euler buckling (b), and crushing load vs axial displacement of four double top hat sections, of varied flange length, were quasi-statically crushed [18]. Note the similarities between the measured responses and the classical EDM behaviour; there is a well defined peak, a post-peak softening limb and then a plateau.

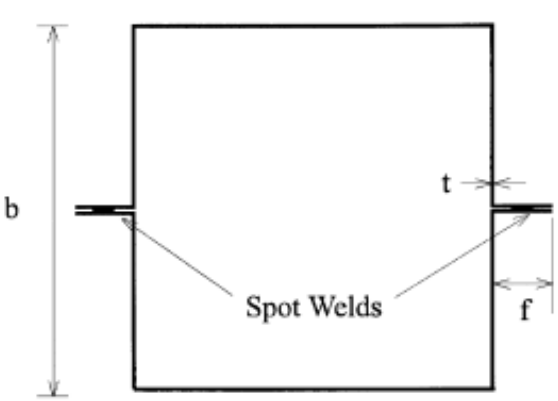

(a) Double tophat geometry

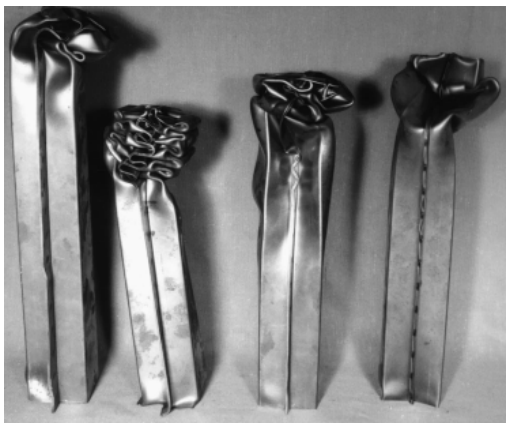

(b) H = 500 mm; f = 10, 15, 20, 25 mm

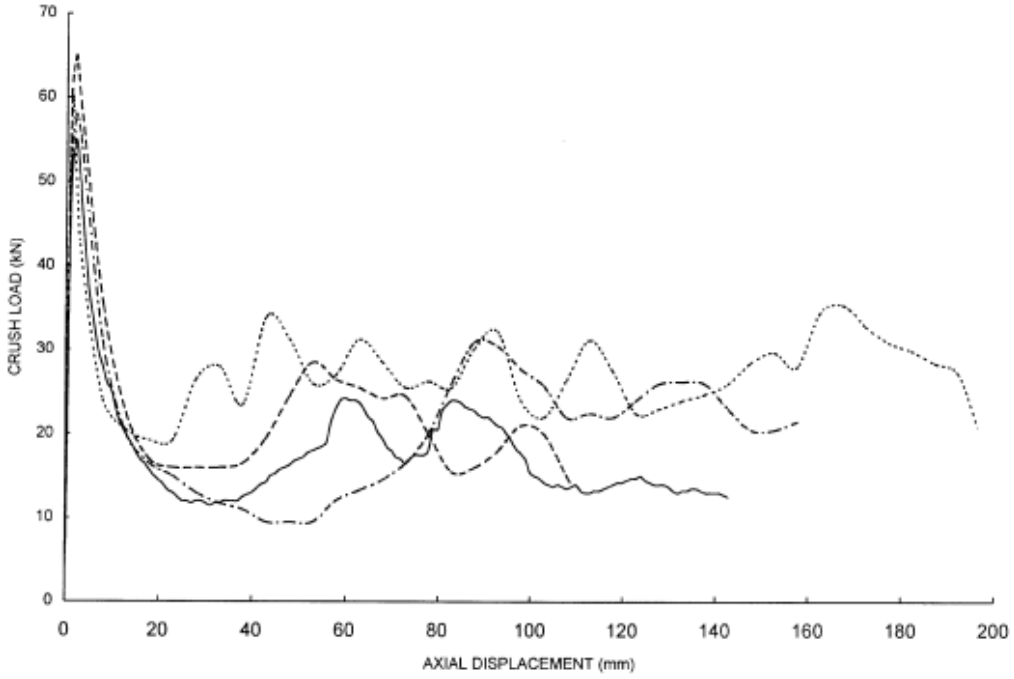

(c) Crushing load vs axial displacement

Figure 2.3 The geometry of a double tophat section is shown in (a); (b) shows the final crushed states of four double top hat sections of varied flange length 10 - 25 mm (left to right); and (c) shows the crushing load vs axial displacement as the top hat sections shown in (b) were crushed (—) f = 10 mm, (- - -) f = 15 mm, (·····) f = 20 mm, (– –) f = 25 mm. Figures taken from publication [18].

Slender tubes are prone to global Euler buckling. This can be a problem when using tubes as EDMs, because global buckling, limits, and discourages the efficient

progressive buckling mode. Reid, Reddy, and Gray [20] found that filling tubes with polyurethane foam dramatically improved their stability, reducing their susceptibility to Euler buckling, and encouraged a more symmetrical, efficient, collapse mode.

The inclusion of polyurethane foam was also observed to provide a significant enhancement to the quasi-static mean crushing load of tubes. Abramowicz and Wierzbicki [21] developed an analytical model of axially-loaded progressively-folding foam-filled tubes, and identified that the added restraint against Euler buckling is caused by an enhancement of the tube bending resistance. Figure 2.4 shows how the mean crushing load (P_{-}) transmitted through the honeycomb varied with the foam density (ρ). Due to the obvious strong correlation between the foam density and the strength enhancement of the honeycomb, it is likely that the strength enhancement was due to the stress-strain response of the polyurethane material rather than the trapped air within its pores.

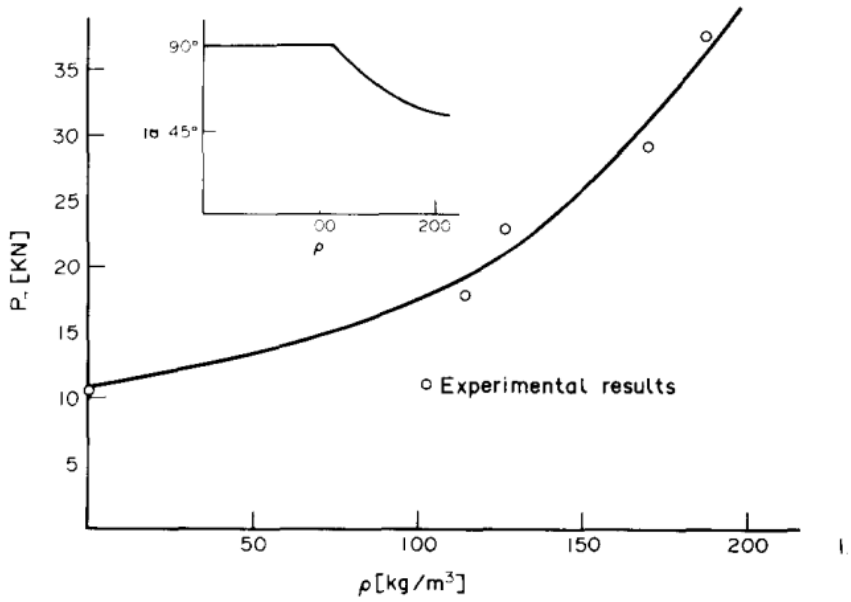

Figure 2.4 Variation in the quasi-static mean crushing load (P_{-}) as a result of variation in the internal foam density (ρ), for axially crushed foam filled tubes. Figure taken from publication [21].

Cellular structures, such as honeycombs, are effectively an array of multiple small tubes arranged in a tightly packed configuration. The EDM response of honeycombs has been studied extensively, especially metallic honeycombs, which are used extensively in the aerospace and automotive industries. Like tubes, honeycombs also undergo a progressive folding mechanism when subject to axial compaction. Wierzbicki [22] considered the mechanics of this buckling mode and derived a mathematical model to predict the mean stress transmitted through a hexagonal metallic honeycomb, when subject to an axial compaction.

Wu and Jiang [23] investigated the quasi-static and axial impact responses of aluminium 5052 and 5056 honeycombs of various geometries up to impact velocities of 26 m/s (using a gas gun fired projectile); Wierzbicki's [22] model was observed to underestimate the experimentally recorded honeycomb crushing strengths. Wu and Jiang [23] also noted a strain rate stiffening behaviour for honeycombs, and that aluminium honeycombs which are thinner in the axial-loading direction, have a smaller cell size and are constructed from a stronger cell wall material provide greater energy dissipation.

Zhao and Gary [24] performed a series of high strain rate tests on aluminium honeycombs. In contrast to previous impact tests, during which loading was applied directly via a drop-hammer or pneumatically driven projectile, samples were crushed within a Split Hopkinson Pressure Bar, which provided impact velocities of between 2 and 28 m/s (which was equivalent to a strain rate of between 55 and 777 s^{-1}) for the 36 mm thick samples. Over these loading rates, the mean crushing strength was observed to increase by as much as 40 %.

Using the same loading mechanism, Zhao, Elnasri, and Abdennadher [25] performed a series of quasi-static and high strain rate (10 m/s) axial crushing tests on aluminium 5052 and 5056 honeycombs of varied geometries. A stiffening of between 12 and 25 % was observed, between the quasi-static and impact responses. Zhao, Elnasri, and Abdennadher [25] attempted to identify the source of the high strain rate stiffening, and after discounting the effect of internal air pressures, concluded that the stiffening was provided partly by the strain rate sensitivity of the aluminium

cell wall material, but mostly by the effect of micro-inertia (as also observed in the response of tubes [17]).

Yamashita and Gotoh [26] compared the axial crushing response of A5052 aluminium honeycomb samples at quasi-static and dynamic (10 m/s = 66.7 s^{-1}) loading rates. They observed that while the plateau stress during quasi-static crushing is flat, at dynamic loading rates the plateau stress increases with strain. They determined that this strain stiffening of the plateau must have been due to the internal air pressures, as other previously discussed effects cause a stiffening which is constant with strain. The air pressure strain-stiffening was significant in comparison to the aluminium honeycomb's structural response, resulting in an increase of the plateau stress of roughly 50%, from 800 to 1200 kPa, by the time the honeycomb compacted.

Xu et al. [27] published work aimed specifically at studying the stiffening effect of the entrapped air on the aluminium honeycomb's axial crushing response. Samples consisting of 9 x 9 cells, constructed from A5050 aluminium, were crushed at velocities ranging from quasi-static to 5 m/s (giving a range of strain rates on the 50 mm thick samples from 10^{-3} to 10^{2} s^{-1}). Samples were sealed at both ends and a varied number of perforations were made, allowing the air to escape from a controlled number of cells.

Comparison between the response of samples with 0 and 100 % of the cells sealed (Figures 2.5 (a) and (b)) confirmed the observations of Yamashita and Gotoh [26]: the internal air pressures do indeed cause a strength enhancement (which increases with magnitude) during the dynamic axial crushing response of A5050 aluminium honeycombs. The magnitude of the strength enhancement due to the internal air pressures was observed to a) increase with loading rate (being non-existent for quasi-static tests, while being substantial at 10^{2} s^{-1}), and b) increase with the number of sealed cells.

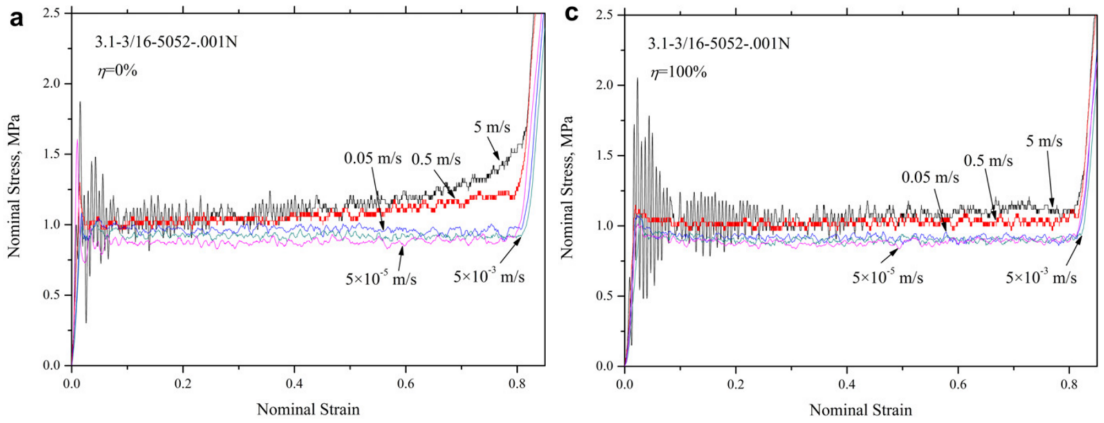

(a) 0 % perforated cells

(b) 100 % perforated cells

(c) 51 % perforated cells

Figure 2.5 Stress vs strain responses of A5052 aluminium honeycomb samples at varied strain rates, with (a) 0 % and (b) 100 % of the cells perforated to study the effect of entrapped air. The samples used to generate the responses in (a) and (b) had a cell size of 3/16 inch (4.8 mm), and cell walls which were 0.001 inch (0.025 mm) thick: (c) shows one of these samples but with 51 % of the cells perforated. Figures taken from publication [26].

2.3 Mechanics of an axially crushed honeycomb

In an attempt to quantify the post-peak axial crushing behaviour of honeycombs, for use as an energy dissipating materials, and identify the parameters which con-

trol their response, McFarland [28] proposed an analytical model to predict the magnitude of the mean post-peak crushing stress. McFarland observed that during buckling, the cell walls undergo a progressive folding mechanism; he assumed that the folding mechanism propagated primarily via in-plane shear and bending of the cell walls and he was able to demonstrate some correlation between his model and existing experimental data on the crushing response of aluminium honeycombs. The model was semi-empirical, relying on an experimental observation of the buckling wave length to predict the magnitude of load which would be transmitted by the honeycomb during progressive buckling. The deformed shapes predicted by the in-plane shear mechanism did not agree with those observed experimentally, although this initial mathematical model was still able to make reasonably good predictions of the mean crushing load [22].

McFarland's model was superseded in a paper published by Wierzbicki [22], who proposed a purely analytical model of the progressive folding mechanism, assuming that the primary energy absorption was provided by rolling of the cell wall over a moving toroidal surface. Wierzbicki demonstrated good agreement between his model experimentally recorded responses of axially crushed aluminium honeycombs (including McFarland's original experimental data); Wierzbicki's model correctly predicted both the transmitted load and final deformed shapes. Findings included, that the wavelength of each progressive fold is purely a function of the cell wall thickness and length, and that the plateau stress is a function of the cell walls thickness, length and yield stress.

While the models published by Wierzbicki and McFarland were concerned with the post-peak plastic progressive folding behaviour of honeycombs (the main determining factor of their energy absorption capacity), their models disregarded the initial pre-peak elastic behaviour. Zhang and Ashby [29] published work which looked at the mechanics of honeycombs in this early pre-peak region, and by considering the mechanics of the possible buckling mechanisms they were able to develop an analytical model, which gave predictions of the peak stress transmitted by a given

honeycomb of known geometry and material properties. Their model was in good agreement with a series of quasi-static uniaxial crushing tests performed on Nomex (a meta-aramid) honeycombs.

Zhang and Ashby [29] observed two dominant buckling modes for the Nomex honeycombs subject to uniaxial loading: elastic buckling (Euler buckling) and fracture (crushing of the cell wall material due to exceedance of the yield stress). The governing mechanism was dependent on the honeycomb relative density ($\rho_{Macroscopic}/\rho_{Cellwall}$ i.e. the quotient between the density of the honeycomb unit and the density of the cell wall material, if there was no air void the relative density would be 1 and the honeycomb unit would be a solid block of cardboard material).

For honeycombs with a low relative density the quasi-static peak stress was observed to be dependent on elastic buckling of the cell walls; and, for honeycombs with a high relative density, the quasi-static peak stress was observed to be dependent on yielding of the cell walls.

2.4 EDM response of cardboard honeycombs

Cardboard honeycombs are used extensively by the armed forces to protect air-dropped cargo from shock-loading [2, 30]. Considering their extensive use (dating back to 1957 [9]), the literature pertaining to the cardboard honeycomb EDM response is surprisingly sparse.

2.4.1 Cardboard honeycomb response to impact axial loading

Smithson [9] performed an early series of impact tests (commissioned by the U. S. Army) on various EDMs, with the aim of assessing their capability for use in air drops. Particular attention was given to the behaviour of cardboard honeycombs, as they were identified as an attractive solution providing substantial energy absorption capacity for their cost and weight.

Circular samples, 610 mm in diameter, of cardboard honeycomb from two manufacturers, of varied height and conditioned to a range of various relative humidities, were subject to impact velocities ranging between roughly 4.5 to 15 m/s. The cardboard honeycomb samples were found to have energy absorption capacities in the range of 240 to 410 kJ/m^3 with the magnitude reducing with increased relative humidity and macroscopic height, increasing with an increase of impact velocity and macroscopic density. Furthermore, the macroscopic density, and therefore associated energy absorption capacity, was observed to be highly variable between samples.

Wide variations in the cardboard honeycomb response prompted further investigation into the mechanisms which controlled its EDM properties. Using a purpose built machine, Ripperger and Briggs [8] developed a fabrication technique whereby perfectly hexagonal honeycomb samples could be constructed. These "precision" samples (12 x 12 inch square plan by 3 inch thick, i.e. 305 x 305 x 76 mm) were subjected to impact tests from a 220 lb (100 kg) mass travelling at 20.3 ft/s (6.2 m/s). Over the course of a year, inadvertent and unintentional changes were introduced to the adhesive type, glue strip widths, and paper weight; no correlation was observed between these "subtle" variations and the EDM response. Furthermore, the precision samples were observed to be as variable in their response as the standard non-perfect commercial samples. This led Ripperger and Briggs to conclude that manufacturing imperfections were not the main source of the cardboard honeycomb's inherent variability.

Ripperger and Briggs [8] hypothesised that the inherent variability was caused by the development of internal air pressures and their influence on the structural response; they suggested that the internal air pressures caused the cell walls to buckle in a non-uniform, and therefore more variable, way. Ripperger and Briggs proceeded to measure the development of internal air pressure within the honeycomb during its impact response. Samples were subject to impact velocities of 22 ft/s (6.7 m/s), were 12 x 12 inch (305 x 305 mm) on plan (x and y) and 3 inch (76 mm) thick (z), were constructed from 80 lb weight paper (118 g/m^2) with 1/2 inch cells (12.7 mm), and of the standard commercial type.

During each test, the pressure was recorded at one of three internal locations (on plan): in the central cell, in a cell mid-way to the honeycomb perimeter (edge) and in a cell located at the edge. The exact geometrical locations of the mid-way and edge cell pressure measurements are not given, nor are visible in the figures present in the scanned report. It is also not stated which edge is referred too, while the anisotropic geometry of the honeycomb core (Figure 1.3 and 1.4) would suggest that this is relevant as not all edges are equal relative to the cellular configuration.

Substantial pressures were measured at the central and mid-way location, the pressure development in the edge cell was almost non-existent. The example pressure traces given in the scanned copy of the report made available to the public are unreadable. However, a table of average air pressures is given, values at the centre and mid-way locations were similar (ranging between 8 and 26 psi, i.e. 55 and 178 kPa), while the average pressure recorded at the edge location was much lower (between 4.7 and 7.9 psi, i.e. 32 and 54 kPa) and did not develop until much later. It was also observed that the pressures in the centre and mid-way cell increased at a similar rate until 50 % strain, after which the pressure in the mid-way cell plateaued, while the central cell continued to increase. It was postulated that this plateauing was a result of blow out or some modification of the cell wall structural deformation mode during crushing, but no additional evidence was available to confirm this.

Ripperger and Briggs identified that, as the honeycomb is crushed, the proportion of load transmitted by the air pressures increases. In one particular test, it was noted that the total transmitted load at a point late in the response was 5450 lb/ft^2 (261 kPa), and that if the recorded pressure in the central cell was present in every cell at that point, the air pressures would be transmitting 4600 lb/ft^2 (220 kPa), a substantial proportion of the total load. Obviously, this was not the case as the pressure at the edge of the honeycomb was much lower. The exact pressure distribution and its evolution during the response were not known, and so the total load transmitted by the internal air pressures remained unknown.

Ripperger and Briggs hypothesised that, at low strains, the cardboard honeycomb crushing strength is mainly determined by the structural characteristics and

that at higher strains the crushing strength was mainly determined by the air; they highlighted the need for further investigation.

Ripperger and Briggs [31, 32] extended their research into the effect of the internal air pressures on the crushing strength of cardboard honeycomb by:

1. testing samples with and without the top and bottom liner sheets (both preventing and allowing the air to escape)

2. testing rectangular (long and narrow) samples with the glue bonds orientated parallel and perpendicular to the long side

3. testing samples with edges normal to the plane of the glue bonds covered and sealed within plastic bags

4. performing burst tests by inflation of specially created single cells with nitrogen.

The corresponding findings to each of these studies were:

1. samples with trapped air were approximately 15 % stiffer, their final crushed shapes were more random and evidence of de-bonding between the double-ply cell walls was observed

2. there was little effect during the early response, but during the late response samples with glue bonds orientated parallel to the long side were significantly stiffer

3. samples with additional restraint to blow out absorbed on average 10 % more energy and were much less variable than those without any blow out restrains

4. cells burst at roughly 5 psi (34.4 kPa), failure occurred in the glue joint (not the cell walls) and there was no apparent variation in burst strength between the two types of tested glue.

The above findings lead Ripperger and Briggs to conclude that the internal air pressures can provide additional energy absorption capacity if properly utilised (the

magnitude of which is dependent on the plan area), but may cause a reduction in the energy absorption if blow out is able to occur easily. Realising the potential of utilising the internal air pressures, Briggs and Ripperger filed for, and were granted, a patent for the "paper honeycomb cushioning pad" [33]. This invention consisted of a standard cardboard honeycomb core, but with additional paper end caps, to provide resistance to blow out and maximise the retention of the entrapped air.

In the work published by Ripperger and Hannon [34], an investigation of the effect of variations in moisture content on the cardboard impact response was performed. They concluded that moisture content has no significant effect when below 14 % (exposure of cardboard honeycomb samples to 65 % relative humidity at 80° F for 14 days produced moisture contents of 11 % [35]), above 14 % a reduction in the average crushing stress was observed; the moisture history (historic storage conditions) had no significant effect, only the moisture content at the time of testing.

Additional findings of note from the work published by Ripperger and Briggs [8, 31, 32, 34] were:

- a significant increase in crushing strength with an increase in plan area
- an increase in the crushing strength when honeycombs were crushed dynamically over when they were crushed quasi-statically,
- when the area of loading was small in comparison to the sample size there was an enhancement in the crushing strength
- loading at an oblique angle causes a reduction in the crushing strength, but not when the angle is less than 10°. At an angle of 20° the crushing strength was reduced by roughly 20 %
- when the glue bonds are orientated parallel to the direction of the horizontal component of the oblique loading vector, samples were 5 % stronger.

Guo and Zhang [36] performed a series of drop tests on cardboard honeycombs of various thickness, from which they developed a set of cushioning curves (one of

which is displayed in Figure 2.6). A cushioning curve is the relationship between the maximum deceleration experienced by an object (an indication of damage) and the static stress it exerts (the weight of the protected object over the contact area) on a given packaging material [37]. Cushioning curves (x axis static stress, y axis maximum deceleration) are concave and upwards facing. The point of minimum acceleration on the cushioning curve represents the point at which they are most efficient (provide the most protection). The cardboard honeycomb cushioning curves flattened out and reduced in magnitude as the honeycomb thickness was increased, suggesting that a thicker honeycomb provides more energy absorption over a larger range of static stresses.

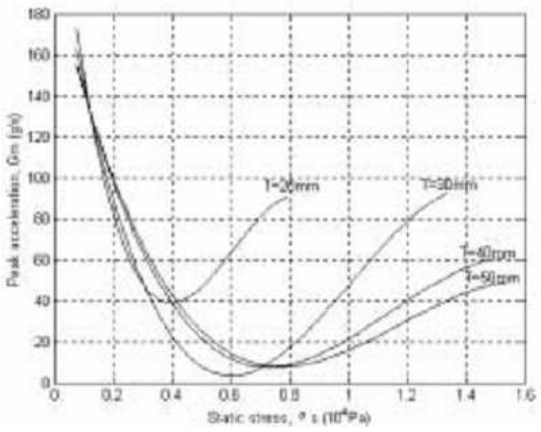

Figure 2.6 A cushioning curve generated by Guo and Zhang [36]. X and Y axes are labelled "Static stress, σ_s (10^4 Pa)" and "Peak acceleration, G_m (g's)" respectively. Each line represents the response of samples of one honeycomb thickness T (H in Figure 1.3) ranging from T=20 (left most curve) mm to T=50 mm (right most curve). Figure taken from publication [36].

Wang [38] investigated the effect of variations in the cell size (wall length), wall thickness and sample thickness on the impact response. This was the first publication which attempted to quantify the effects of specific variations in the cellular geometry on the cardboard honeycomb impact response. Findings included: a reduction in the energy absorbed per unit volume with an increase in the cell size (increased wall length and as the plan area was fixed, a reduced relative density),

and a relationship which was fluctuant, but generally positive between the sample height and energy absorbed per unit volume.

Wang also produced a series of cushioning curves for the tested variables, two of which are shown in Figures 2.7 (a) and (b). An increase in the sample thickness caused a flattening and lowering of the cushioning curve, an increase of the cell wall thickness shifted the curve to the right (increasing the static stress required for the honeycomb to provide maximum protection), and an increase in the cell size narrowed and shifted the cushioning curve to the left (reducing the magnitude and range of static stress over which the honeycomb will provide the minimum deceleration). These findings by Wang, were in agreement with the initial work published by Guo and Zhang [36] .

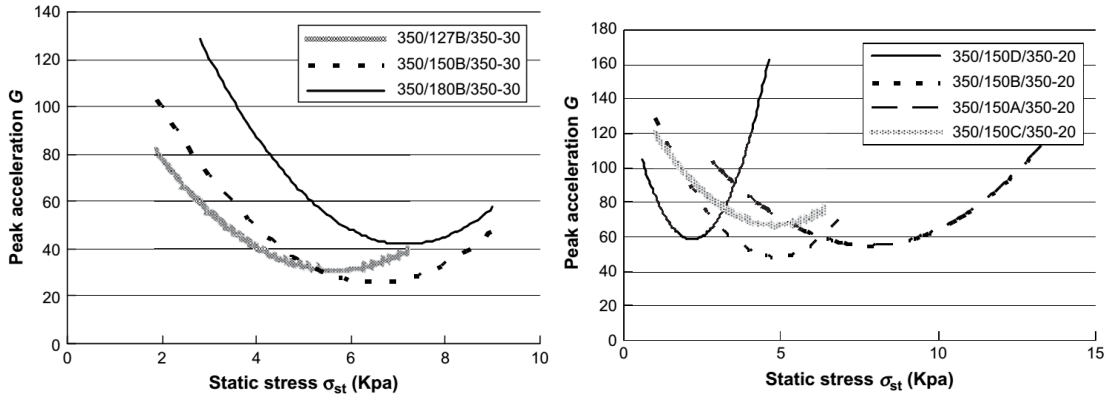

(a) (b)

Figure 2.7 Two cushioning curves published by Wang [38] showing the relationship between Peak acceleration and Static stress for variations in paper weight (cell wall thickness) from 127 to 150 g/m^2 and (b) honeycomb mesh type A to D (cell size, see Figure 3.1. Figures taken from publication [38].

No consideration to the effect of internal air pressures was given in the work published by Wang [38]. It is thought that this omission (when air pressures were previously shown to play such an important role in the cardboard honeycomb impact response [31, 33, 34]) may have contributed to the variable unexplained trends.

2.4.2 Cardboard honeycomb response to quasi-static axial loading

Majority of the recent literature regarding the energy-dissipating characteristics of cardboard honeycombs has been concerned with its response to loading rates in the quasi-static region. At these much slower loading rates the pressurised internal gasses have substantially more time to escape by venting through the inherently permeable structure. As a consequence, any internal air pressures which do develop are insignificant in comparison to the structural response, and so the quasi-static energy-dissipating characteristics are solely a function of the cardboard structure.

It is worth noting that Aminanda et al. [39] observed that the quasi-static axial crushing mechanism of paper honeycombs is similar to that of honeycombs consisting of aluminium and Nomex.

Lu, Sun, and Wang [40] developed a mathematical model to predict the critical (peak) axial buckling load of cardboard honeycombs by considering the mechanics of two possible mechanisms: peeling of the double cell walls and crushing of the material. Comparison between their model and crush tests (performed at 10 mm/minute) showed a closer correlation than was predicted by the existing theory for generic honeycombs. There were no specific material or geometrical parameters given for the tested honeycomb samples; results were presented as a graph of critical buckling load vs stretching ratio (degree of expansion).

The main findings from the work published by Lu, Sun, and Wang [40], were that the quasi-static critical buckling load reduced with an increase in the stretching ratio, and for low stretching ratios its magnitude was controlled by the peeling mechanism, while for high stretching ratios its magnitude was controlled by the crushing mechanism.

Wang and Wang [5] studied the effect of variations in a selection of honeycomb geometrical parameters on the quasi-static crushing response (2 mm/min). Variables studied were macroscopic height (10 to 50 mm), weight/thickness of cell wall material (112 to 180 g/m^2 i.e. 0.2 to 0.29 mm) and cell size (5.8 to 14.4 mm, i.e. mesh types

A to D). Wang and Wang [5] also studied the effect of top and bottom liners and the effect of stacking multiple thinner honeycombs, rather than using one thicker honeycomb. All samples were 200 x 200 mm plan area, tested at a constant temp and humidity of 23° C and 50 % relative humidity.

Main observations were that using liners significantly stiffens the full honeycomb crushing response (in the published figures there is a significant rise of the plateau stress over the response), and that the energy absorption capacity increased almost linearly with the relative density of the honeycomb (the quotient between the macroscopic density ρm and the density of the cell wall material ρ):

$$\frac{\rho_m}{\rho} = \left(\frac{t}{L_{t1}}\right) \frac{1 + {}^{L_{t2}}/_{L_{t1}}}{({}^{L_{t2}}/_{L_{t1}} + \sin\theta)\cos\theta} \tag{2.1}$$

where t is the cell wall thickness, L_{t1} is the length of the single cell walls, L_{t2} is the length of the double cell walls and θ is the internal expansion angle. Variations in the cell wall thickness, length and cell size (mesh type) were lumped together as variations in the relative density. An average cardboard density was calculated by taking an average density of the material constituting the liners and the cell walls; comparisons between this average cardboard density and the energy absorption capacity were made, unsurprisingly there was no obvious trend.

There was attention given to the effect of sample height and the effect of double stacking on the energy absorbed per unit volume, the response appeared to be affected, but the exact relationship was unclear. While samples with different cell wall thicknesses were tested, there were no direct comparisons made between the response of these samples, although Wang and Wang [5] did identify an increase in stiffness with increased cell wall thickness.

Energy absorption diagrams are one method used to characterise EDM materials, they plot the energy absorbed per unit volume (y-axis) against the transmitted stress (x-axis) for each response [41]. Wang, Wang, and Liao [42] produced a set of energy absorption diagrams for the quasi-static axial crushing response of cardboard honeycombs with varied cell wall thickness-to-length ratios ($^t/_L$).

A mathematical model of the cardboard honeycomb energy absorption was de-

veloped by integrating an analytical expression of its macroscopic response. The mathematical model was used to produce an energy absorption diagram, which was found to be in good agreement with a similar diagram composed from a set of experimental results. Finally, the energy absorption diagrams were used to identify the relationship between the total absorbed energy per unit volume (before compaction) and the honeycomb's cell wall thickness-to-length ratio. Wang, Wang, and Liao [42] observed that the energy per unit volume at compaction increases with an increased cell wall thickness-to-length ratio.

E and Wang [43] studied the effect of relative humidity (RH) on the quasi-static energy absorption properties of cardboard honeycomb. A series of experimental crush tests was performed on samples with different cell size (mesh type), a constant cell wall thickness of 0.19 mm (105 g/m^2 recycled cardboard) and plan area of 100 x 100 mm. Samples were conditioned at RHs ranging from 40 % to 95 % and crushed at the rate of 12 +/- 3 mm/min. It was observed that RHs below 75 % had no significant effect on the quasi-static plateau stress or energy absorption capacity of the cardboard honeycomb; for values of RH above 75 % there was a sharp drop off in both the plateau stress and energy absorption capacity, this drop off was proportionally more significant for higher cell wall thickness-to-length ratios.

A second publication by E and Wang [44] also studied the effect of relative humidity (RH) and cell wall thickness-to-length ratio, on the quasi-static cardboard honeycomb crushing response, this paper was more focused towards the development of an analytical model to incorporate the experimentally observed effects. They derived a piecewise expression for the stress transmitted by the honeycomb structure during each stage of its EDM response. Integration of the piecewise expression, gave a theoretical prediction of the energy absorption provided by a cardboard honeycomb with cell walls of known thickness-to-length ratio, yield strength and elastic modulus which has been stored at a certain RH. This model was used to produce energy absorption curves, which were in good agreement with those produced from experimentally recorded data.

2.5 Cardboard/paper material properties

The material of interest, consisting of pressed wood pulp, is commonly referred to by names such as paper, paper-board and cardboard, the definition of each varies. The general consensus seems to be that paper refers to pressed wood pulp in a thin and lightweight form (writing/newspaper), while cardboard has some structural significance (shoe boxes/egg cartons). The cardboard/paper honeycomb base material lies within a region where many would class it as one or the other; considering the common use of the honeycomb as a packaging material, the term cardboard seems to be most appropriate; and so, "cardboard" will be used as a blanket term to include all types of "papers" herein.

Cardboard is an inherently variable material, its mechanical properties depend on the pulp from which it is created, and recycled cardboard might by made from a range of different pulp. Furthermore, pulp is a natural material and hence its properties are dependent on many factors which may have influenced the growing conditions of the tree it was created from. As one would expect, with such a variable and commonly used raw material, much research has been performed into identifying various types of papers' mechanical properties.

The Poisson's ratio, elastic moduli, and in-plane shear moduli, of a high strength Kraft paper were determined by studying its acoustic response (wave speed) in each orthogonal direction [45, 46]. These methods are limited to measurements of the paper's elastic characteristics and therefore only relevant for small strains.

As part of the manufacturing process, cardboard is rolled; the act of rolling tends to orientate the fibres in the rolling direction i.e. machine direction (MD), the direction orthogonal to this is known as the cross direction (CD). This orientation of fibres causes cardboard to be stiffer and stronger in the MD than the CD. It's full constitutive relationship is orthotropic elastic-plastic. Cardboard also exhibits parabolic strain hardening, meaning that the curve flattens out with increased strain (to a constant gradient, less than the elastic modulus) [47, 48].

Mäkelä and Östlund [49] developed an analytical orthotropic elastic-plastic con-

stitutive model of paper, requiring only simple tensile tests in three directions for its calibration, capable of predicting the static anisotropic stress-strain response, at any angle of inclination, between the maximum MD and minimum CD directions. In the publication by Castro and Ostoja-Starzewski [47], it was shown that it is often possible to approximate the stress-strain material response of paper, with an almost linear curve.

Allaoui, Aboura, and Benzeggagh [50] showed that, when subject to cyclic loading, paper undergoes damage, inducing permanent strain. It was also shown that paper is strain rate dependent, a stiffening effect was visible when the strain rate was increased from 6×10^{-5} s^{-1} to 12×10^{-3} s^{-1}.

Recent published work regarding the mechanical behaviour of cardboard honeycombs have shown that the peak and plateau stresses, transmitted by cardboard honeycombs during quasi-static crushing, can be expressed with four material parameters: elastic modulus E, yield stress σ_{Yield}, ratio of double to single-ply cell wall yield stress k and Poisson's ratio ν [42–44, 51]. No consideration has been given to a) orthotropy, b) plastic strain hardening, and (since all mathematical predictions have considered only the quasi-static response) c) strain-rate hardening. Table 2.1 gives a summary of some experimentally determined values for each material parameter.

Table 2.1 Summary of experimentally measured cardboard material properties published in existing literature, showing elastic modulus E, yield stress σ_{Yield}, ratio of double to single-ply cell wall yield stress k, Poisson's ratio ν and weight per metre square. Values from publications [42–44, 51] were determined from quasi-static tensile tests on material from a cardboard honeycomb cell wall.

Publication	E (GPa)	σ_{Yield} (MPa)	k	ν	Weight (g/m^2)
[42]	0.89	4.25	-	-	127 - 180
[44]	2.44	7.21	-	-	105
[43]	2.44	-	-	-	105
[51]	-	5.14 - 7.25	1.30 - 1.57	-	105
[52]	-	-	-	0.16 - 0.33	65
[53]	-	-	-	0.25 - 0.38	130 - 220

2.6 Summary

Research regarding the high strain rate axial crushing response of cardboard honeycombs is sparse. Early work by Ripperger and Briggs identified that during high strain rate compaction, the air pressures which develop within a cardboard honeycomb are comparable in significance to the structural response, and therefore the mechanics which govern its energy-dissipating characteristics are dependent upon the complex interaction between the entrapped air and the cell walls [8, 31–33].

Other work has mostly focused on the quasi-static response of cardboard honeycombs [5, 40, 42–44, 51]; with the exception of two publications, which investigated how the cushioning properties of cardboard honeycombs were affected by variations in several geometrical parameters. These publications were limited in scope due to oversimplification and complete omission of the effect of internal air pressures. Furthermore, research into the high strain rate axial crushing of aluminium honeycombs (much stiffer in comparison to cardboard), has shown that the internal air pressures cause a significant stiffening effect, in comparison to the structural response, which

is not present during quasi-static loading [26, 27].

Ripperger and Briggs demonstrated that the internal air pressures are capable of carrying a significant proportion of load, and that their magnitude is non uniform throughout the honeycomb structure. No research has yet identified the exact spatial distribution of internal air pressures which develop within the cardboard honeycomb; thus, the actual contribution of the internal air pressures, to the macroscopic response, is as yet, unknown. It follows that there has also been no research into the mechanisms which drive the development of internal air pressures, and how the internal air pressures interact with the lightweight, deformable, structure they are contained within.

There has been no research aimed at quantifying the dynamic response of cardboard honeycombs, by consideration of the mechanics which evolve on the mesoscopic scale. There is no research capable of predicting the EDM characteristics of a dynamically loaded cardboard honeycomb, for a known set of material and geometrical parameters. Furthermore, as the mesoscopic mechanics of the air-structure coupled response are currently unknown, there is no fundamental understanding of how variations in the material and geometrical parameters, of the cellular structure, will effect a cardboard honeycombs dynamic EDM properties.

Chapter 3

Experimental impact testing

This chapter details three phases of testing, which were performed to investigate how variations in the cardboard honeycomb's cellular geometry affect its macroscopic impact response. Phase 1 (Section 3.1) was performed as a precursor to this thesis and is therefore not the author's own work; a summary of findings have been included to give chronological context to the development of knowledge. Phases 2 and 3 (Sections 3.2 and 3.3) were performed by the author. An initial series of impact tests (Phase 2) was performed, after which the experimental methodology was refined, before performing a secondary series of impact tests, with greater scope (Phase 3).

Ripperger and Briggs [8] measured the magnitude of internal air pressure, at three locations within cardboard honeycomb samples during a series of impact tests. On plan these locations corresponded to a cell in the centre, a cell mid-way towards a perimeter edge and a cell located at a perimeter edge. They showed that the magnitude of internal air pressure was a function of the distance from the sample edge. They also concluded that the internal air pressures must play a significant role during the cardboard honeycomb impact response and carry a significant proportion of the load.

The experimental work carried out during phases 2 and 3 was performed to identify the spatial distribution, and temporal development of internal air pressures within a honeycomb of known geometry, and to identify how the magnitude and significance of the internal air pressures is affected by variations of the cellular

geometry.

During Phase 2 and 3 reference is made to three "mesh types". These mesh types are labels used by cardboard honeycomb manufacturers to identify the density (cell size) of each cardboard honeycomb mesh. Figure 3.1 shows an approximate 0.5 m square section of the exposed honeycomb core for the F, D and B mesh types. The (measured) average cell wall length $\bar{L}$ for each mesh type is also given.

(a) "F mesh", $\bar{L} = 24.4$ mm. (b) "D mesh", $\bar{L} = 14.3$ mm. (c) "B mesh", $\bar{L} = 8.0$ mm.

Figure 3.1 Images of the exposed cardboard honeycomb core taken during the Phase 3 sample preparation. All three images show an approximate 0.5 x 0.5 m square plan area of bare core. The average recorded cell wall length $\bar{L}$, for each mesh type, is also given.

3.1 Phase 1 - Drop hammer

Regular occurrences of damage to air-dropped cargo prompted a series of impact tests on the cardboard honeycomb material. This initial series of tests was carried out prior to the commencement of this project by Tyas [10] at Blastech Ltd, a summary of which has been included in this thesis for background. This phase of testing highlighted the need for further investigation into the dynamic response of the cardboard honeycomb EDM and was therefore a precursor to this project.

3.1.1 Overview

Honeycombs with a 1/2 inch and 3/4 inch cell size, two plan areas 150 x 150 mm and 250 x 250 mm square, and samples with single and double stacks were subject to impact velocities of 5 ms^{-1} and 6.5 ms^{-1} using a drop hammer. It is unclear if the two if the 1/2 and 3/4 inch samples belonged to one of the mesh types shown in Figure 3.1 and so their original labels have been maintained. Findings from the drop hammer tests included:

- Samples with the finer, 1/2 inch cell size, behaved stiffer than the 3/4 inch samples in both the peak and plateau regions.
- Increasing the plan area increased the peak and plateau stresses.
- Some strain rate sensitivity was apparent from an increase on the initial peak.
- Double stacks gave either a sequential or simultaneous crush response, depending on the relative strength of the layers.

This initial run of tests was designed to provide a rule of thumb guideline for use in the field, and therefore had its limitations. The load cell recorded overlying oscillations on the genuine honeycomb response, disguising the exact behaviour of the honeycomb EDM. These oscillations had a frequency in the region of 400-900 Hz and could not be removed without removing a proportion of the genuine trace. Lack of repetition of identical tests limited the study of inherent variations of the cardboard honeycomb. The actual mesoscale geometry was not recorded, only a benchmark cell size was known. The significance of internal air pressures was not investigated.

3.2 Phase 2 - Gas gun

On commencement of this project it was decided that it was necessary to perform an additional series of experimental impact tests to investigate how the mechanisms driven by the cardboard honeycomb microstructure affect the macroscopic

behaviour. In an attempt to eliminate the spurious oscillations recorded by the load cell in Phase 1 and to increase the maximum impact velocity, a move was made to the gas gun rig shown in Figure 3.2.

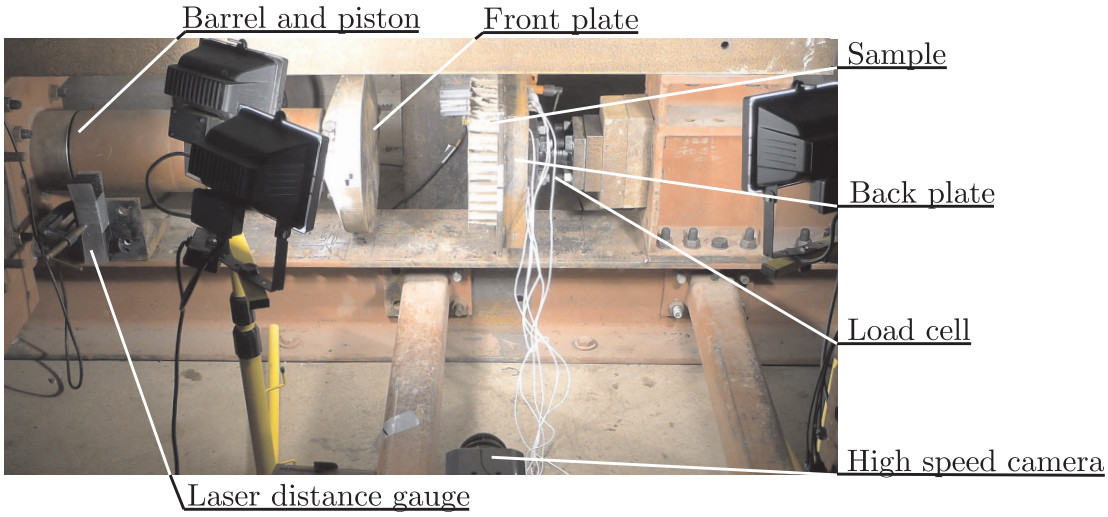

Figure 3.2 General arrangement of the gas gun apparatus used during Phase 2 and 3.

3.2.1 Scope of Phase 2

All samples were 70 mm in height and 250 mm x 250 mm plan area. Two mesh sizes, B and D, were tested (see Figure 3.1). Effort was made to control the impact velocity, however difficulties using thin diaphragms, as described in Section 3.2.5, meant that the impact velocity varied between 5.5 and 6.5 ms^{-1} when using the thinnest possible (0.1 mm thick) brass diaphragm. Table 3.1 shows the matrix of tests carried out during this phase, with their mesh type (B or D), impact velocity (v_i) and initial strain rate ($\dot{\varepsilon}_i$). Both mesh types were repeated 3 times each, to study the variability between tests.

Note that throughout this thesis strain rate refers to the engineering strain rate. i.e. the strain rate as calculated using H (the initial height of the sample). The initial strain rate $\dot{\varepsilon}_i$ below refers to the engineering strain rate experienced by the cardboard honeycomb sample at the moment of impact and is defined by Equation 3.1.

$$\dot{\varepsilon}_i = \frac{v_i}{H} \tag{3.1}$$

Table 3.1 Series of performed tests during Phase 2.

Test Ref	Mesh	v_i (m/s)	$\dot{\varepsilon}_i$ (s^{-1})
EDM1	B	5.56	79
EDM2	B	5.80	83
EDM3	B	5.63	80
EDM4	D	5.47	78
EDM5	D	6.45	92
EDM6	D	5.92	85

3.2.2 Sample preparation

Dufaylite was the sole company capable of providing suitable cardboard honeycomb in the UK at the time of purchase. On discussion with their technical department it became apparent that they had previously supplied cardboard honeycomb to the Ministry of Defence for use in the field. The honeycomb supplied to the Ministry of Defence and that used during Phase 1 of the experimental work is constructed from a high grade kraft paper. Being a specialised product, Dufaylite were not able to supply kraft paper honeycomb unless a substantial order was placed, much larger than that required for this project. As an alternative, a recycled cardboard honeycomb was supplied.

The recycled cardboard was expected to be weaker than the kraft paper. However, as the main goal of the experimental testing was to investigate whether internal air pressures play a significant role during dynamic collapse of the cardboard honeycomb and to guide the development of a numerical model, the exact material properties of the cardboard were not important.

The honeycomb arrives in flat pack form from the supplier and a fabrication process is necessary to produce samples which can be tested. Being required to carry

out the fabrication, even with the intent of producing highly repeatable samples to be used in a scientific investigation, gave valuable insight into the inherent variability of the cardboard honeycomb material. The fabrication process was found to be quite difficult, taking several iterations to perfect. Eventually the described methodology was arrived at, consisting of three main tasks:

1. core expansion
2. application of top and bottom liners
3. sample marking and cutting.

The first stage involves expanding the flat packed core to create the hexagonal cellular structure. Two people were required to apply a substantial amount of force when expanding the finer B mesh and it was difficult to avoid damage to the top and bottom of the cell walls when doing so. It was necessary to declare a sacrificial area of damaged cell walls which would not be used to construct samples for testing. Several rounds of stretching, with adjusted hand positions, were performed in an attempt to evenly distribute the lateral expansion force across the honeycomb structure and to create uniform hexagonal cells.

The standard industrial procedure involves a mechanical jig to expand the cardboard honeycomb core. However, as a mechanical jig is not necessarily always available in theatre, the described process was followed to instil a level of geometrical variation which would be characteristic of a non-jig constructed cardboard honeycomb EDM sample.

Figure 3.3 shows the honeycomb core in several stages of the fabrication process. To prevent the honeycomb core from self-contracting the manufacturer suggested spraying with water to cause the cardboard to lose its elasticity and hold its expanded shape. Care was taken to ensure that the volume of water used was kept to a minimum and applied evenly to minimise any influence on the glue used to hold the adjacent cell walls together. The volume of water was also scaled by the average relative density of the mesh type in an attempt to keep the ratio of added water

to volume of cardboard equal. Following spraying, the core was moved away from any standing water and left to dry thoroughly in a well ventilated, warm, area for a minimum of 24 hours **(1)**.

Figure 3.3 Various components of the cardboard honeycomb EDM in several stages of the fabrication process: 1) a drying honeycomb core; 2) a liner sheet immediately after its first coat of PVA; 3) a liner sheet being applied with a second coat of PVA; 4) a honeycomb core after applying the top liner sheet.

A reel of the same recycled cardboard used to construct the cell walls was also supplied with the honeycomb core. This was used for the top and bottom liners and attached with PVA glue. While the honeycomb core was drying, a length of cardboard was cut from the reel. It was then trimmed to be slightly larger than the expanded core to allow for overlap.

A 30 cm ruler was used to apply a coat of PVA glue evenly across the surface of the liner. The cardboard was allowed to absorb this **(2)**, and then a second coat was applied **(3)**; any excess was scraped off to leave a thin even film across the whole surface of the sheet. Judgement was required so that enough glue was used to create the bond between the liner and the end of the cell walls, but not so much that it would flow into the core and set along the length of the cell walls.

The glue-covered liner was then carefully flipped and placed on the core, taking care not to tear the, now, wet sheet. Any wrinkles were removed by smoothing with the palm of a hand to create perfectly flat surface promoting an even and consistent bond between the liner and the cell walls **(4)**.

The PVA glue was allowed a minimum of 48 hours to set, until it was dry to the touch. The core and attached single liner was then flipped and the process repeated to attach the second liner allowing a further 48 hours drying time.

A grid of 250 mm x 250 mm squares was drawn on one liner with sample numbers which, when read, aligned the sample with the glue bonds between the cell walls running top to bottom. The samples were then cut with a sharp cross cut hand saw. Many samples were constructed, about half of which were deemed unfit for testing due to flaws in their macrostructure. All samples were labelled with a letter corresponding to their mesh type and an arbitrary number. Unique of the arbitrary sample numbers: from the pool of constructed samples a batch of those which were deemed the best quality (i.e. well bonded glue, homogeneous conforming macroscale geometry etc) were selected for testing.

3.2.3 Outline of the gas gun apparatus

During each shot, a three stage diving compressor gradually increases the pressure in a reservoir, as shown in Figure 3.4 (a). Covering the outlet to this reservoir is a thin metal diaphragm clamped within a magazine by a circular arrangement of bolts, as shown in Figure 3.4 (b). A rubber O-Ring on both, the front and back face of the magazine, provided an air tight seal preventing air from leaking around the magazine from the pressurised reservoir to the outlet.

At a given pressure the diaphragm bursts, allowing the compressed air to expand along the outlet, shown in Figure 3.4 (a), towards the back face of a piston.

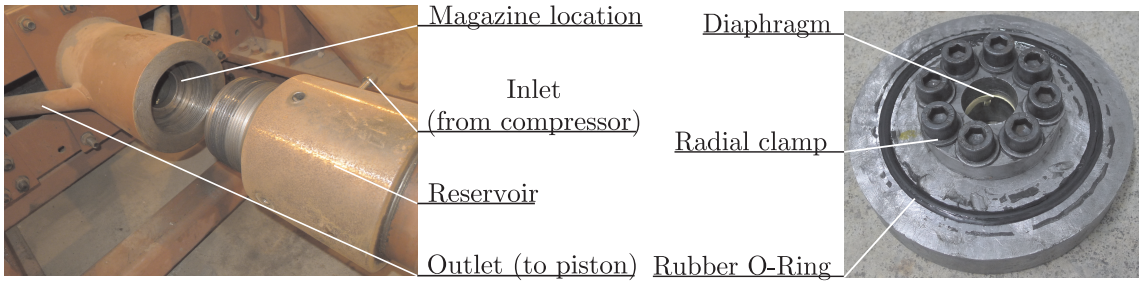

Figure 3.4 Detail of gas gun (a) inlet reservoir arrangement and (b) diaphragm magazine.

The piston, and attached front plate, then accelerates along the barrel shown in Figure 3.5. Two bore-riders (guides) ensure the piston runs true along the centre line of the barrel and two O-Rings provide a seal to prevent the compressed air from escaping between the piston and internal face of the barrel. The combined mass of the travelling piston and plate was measured as 81.4 kg.

The impact event begins when the front plate strikes the top face of the cardboard honeycomb sample. The velocity - and therefore strain rate - of the piston at this point in time can be controlled by adjusting the thickness and material of the diaphragm.

Figure 3.5 Detail of gas gun barrel and projectile components. (a) Barrel, (b) Piston with one white PTFE guide, two black rubber O-Rings and an empty location slot for the second guide, (c) Front plate with connecting bolts.

3.2.4 Measurements and data acquisition

For each test, the following data were recorded:

- Total transmitted load by the cardboard honeycomb sample
- Internal air pressures
- Displacement of the front plate
- High speed video.

During the impact event load is transmitted by the honeycomb through the back plate to the load cell, shown in Figure 3.6 (a). The load cell was custom-built at the University of Sheffield Blast & Impact Laboratory. It was constructed from a short length of steel tube section, capped by end plates at either end. Two orthogonal pairs of Kyowa KSP-2-120-E4 semi-conductor strain gauges were bonded to the outer surface of the hollow tube, linked in such a way as to eliminate bending effects in the output strain and record only axial strain. The strain gauge response was recorded using a Wheatstone bridge circuit. The load-strain gauge output relationships of the cell was calibrated by tests in a UKAS-accredited compression loading rig; the output of the calibrated load cell was accurate to within +/-1kN in the range 0-250kN.

Pressure transducers were placed on the back plate to measure the development of pressures within the honeycomb during impact (Figure 3.6 (b)). Kulite HEM-375 pressure transducers, with natural frequency > 400 kHz and ranges of 0-17 bar for the internal gauges and 0-7 bar for the edge gauge. The pressure gauges act by using a piezoresistive sensor to record the deformation of a diaphragm under a change of pressure. The change of resistance is converted to a voltage through an integral Wheatstone bridge circuit. The gauges were new and the voltage-pressure relationship was calibrated by the manufacturer to an accuracy of $+/-$ 0.5 % full scale output (i.e. 0.5 bar on a 100 bar reading). This accuracy would amount to a worst case error, on the highest measured pressures ($\approx$ 800 bar) of $+/-$ 4 bar.

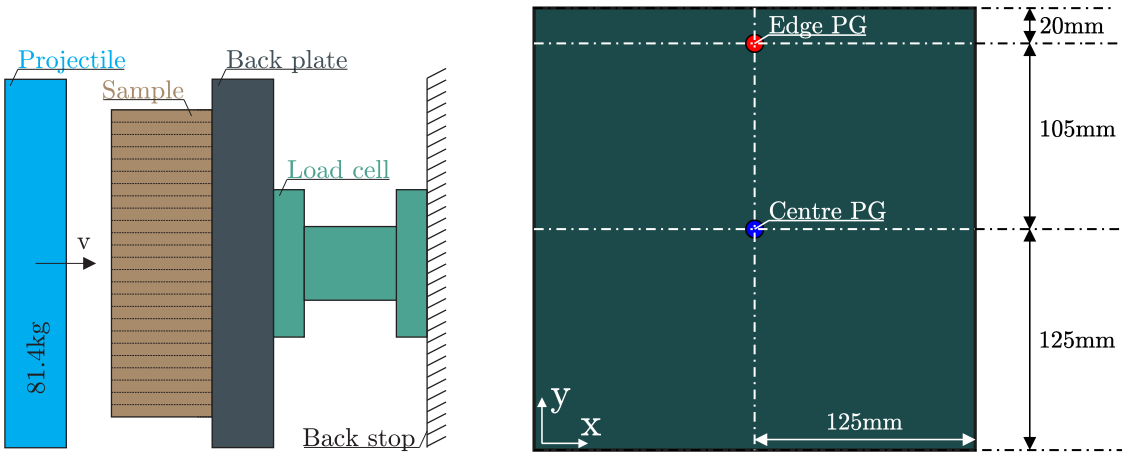

(a) (b)

Figure 3.6 Experimental arrangement of the (a) projectile, load cell, and back plate; and (b) pressure gauges, in relation to the samples tested during Phase 2.

During commissioning of the rig all but two pressure transducers were damaged, either by the shock produced during impact between the front and back plate, or bearing of the cardboard directly onto the gauge diaphragms. The two remaining pressure transducers were placed at positions corresponding to the centre of the sample and 20 mm from the sample edge, in an attempt to capture the effect of distance from the sample edge on the development of internal pressures.

To prevent damage to the remaining two pressure gauges, and subsequent replacements, arrester blocks were used to slow the impactor once the sample had compressed to around 35 % of its original length, thus reducing the loading on the back plate and protecting the pressure gauges from damage. As a consequence, the response of each sample could only be measured up to a strain of around 65 % as beyond this the load was transmitted through the arrester rather than the cardboard honeycomb. However, this approach still yielded useful data over a large proportion of the range of strain of interest.

An M7 laser distance sensor (manufactured by MEL Microelektronik GMBH) was used to record the displacement-time history of the impactor (Figure 3.2). The distance gauge had a bandwidth of 10 kHz, provided a voltage output which varied linearly with the distance from a reflecting surface, and was calibrated in house to

an accuracy of +/− 0.5 mm. This displacement-time history was used to calculate the strain-time history of the sample.

The load cell, pressure gauges, and laser displacement gauge, all produced voltage time histories, which were recorded by a TiePie HS4 USB Handy Scope attached to a laptop. A micro switch trigger was used as the scope trigger source which activated when the front plate began to move. 100 k samples at 195.313 kHz and 16 bit resolution with a 10% pre-trigger ensured that that each impact event was captured with sufficient temporal and voltage resolution. A script was written using an analytical computer package to post-process the data from voltage time history csv files to load, pressure and distance relationships, with sample engineering stress and strain values calculated from these results and the initial cross-sectional area and length of the samples.

3.2.5 Results and conclusions from Phase 2

The total transmitted stress vs strain curves for the three tests performed on B and D meshes are shown in Figures 3.7 (a) and (b). Load recorded after 60% strain has been omitted, since at slightly greater strains, the load was picked up by the timber arrester.

The pressure system, for the loading rig was an existing item of equipment, previously used for dynamic testing where relatively high loads had been used. It was therefore designed to accommodate much higher pressures than those required to generate the energy needed to crush the cardboard honeycomb. The magazine which holds the diaphragm was therefore originally designed to hold thicker diaphragms than those used during this series of tests. This led to difficulties attaining a sufficient clamping force around the edge of the diaphragm which is thought to have contributed to the variance of the impact velocities shown in Table 3.1.

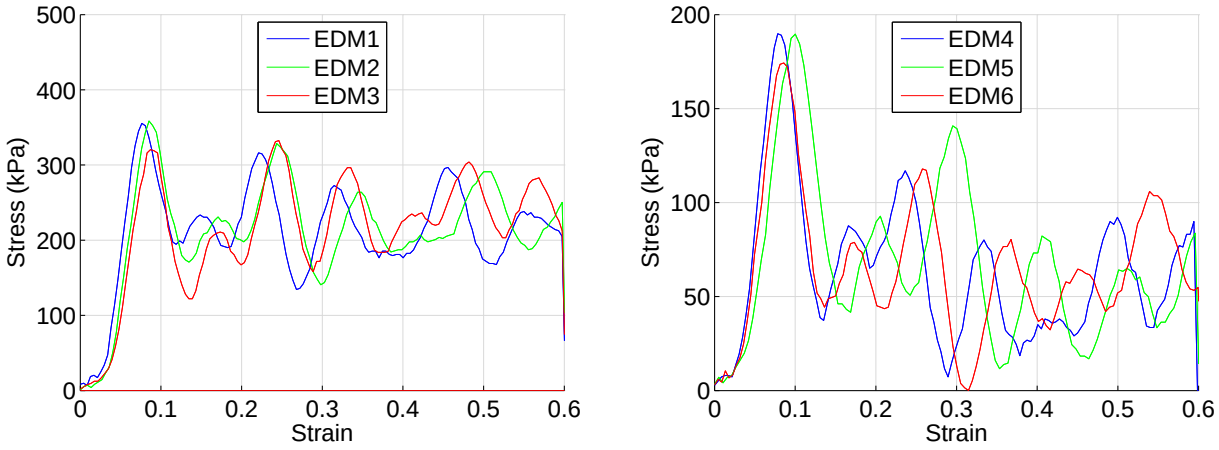

(a) B mesh

(b) D mesh

Figure 3.7 Stress vs strain relationship for all samples tested during Phase 2.

The traces for both meshes display the typical EDM behaviour with a peak followed by a plateau region. The peak to plateau stress ratio was much more pronounced for the D mesh tests. An overlying ringing oscillation, with a frequency ranging between 890-1150 Hz, was still recorded by the load cell. Figure 3.8 shows the load cell traces plotted against time rather than strain, highlighting the fact that the overlying oscillation was imposed from an external dynamic mode, rather than genuine response of the cardboard honeycomb.

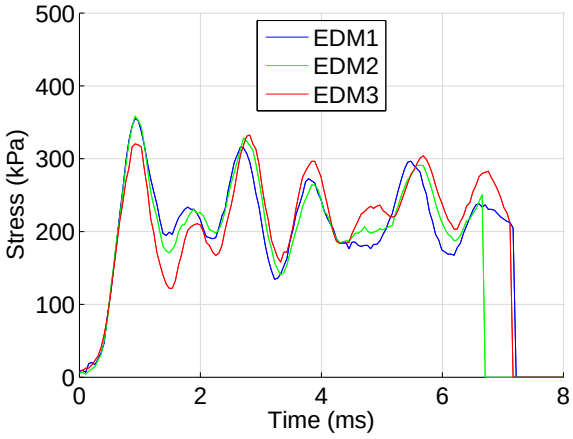

Figure 3.8 Stress vs time for all tested B mesh samples, illustrating the existence of an overlying oscillatory response.

The peak stress was calculated by taking the maximum value for each trace. A single value for the plateau stress was calculated by taking the mean of values from 20% to 60% strain. Table 3.2 shows the mesh type, initial strain rate $\dot{\varepsilon}_i$, peak stress σ_{Peak} and plateau stress $\sigma_{Plateau}$ recorded for the 6 tests performed. Averages for both the B and D mesh samples are shown in bold.

Table 3.2 Phase 2 - Macroscopic response summary. B Avg and D Avg (stated in bold text) refer to the mean values of $\dot{\varepsilon}_i$, σ_{Peak} and $\sigma_{Plateau}$ for three B mesh tests (EDM1-3) and D mesh tests (EDM4-6) respectively.

Test Ref	Mesh	$\dot{\varepsilon}_i$ (s^{-1})	σ_{Peak} (kPa)	$\sigma_{Plateau}$ (kPa)
EDM1	B	79	355	220
EDM2	B	83	356	227
EDM3	B	80	332	242
B Avg		**81**	**348**	**230**
EDM4	D	78	190	56
EDM5	D	92	190	62
EDM6	D	84	174	61
D Avg		**82**	**185**	**60**

The finer B mesh samples transmitted the greatest stress with an average peak and plateau of 348 and 230 kPa respectively, compared to the coarser D mesh with 185 and 60 kPa. The spread in σ_{Peak} between samples was 24 kPa for the B mesh and 16 kPa for the D mesh, the spread in $\sigma_{Plateau}$ was 22 kPa for the B mesh and 6 kPa for the D mesh.

A forensic analysis of the crushed samples was performed by removing the top and bottom liner sheets and observing the cell walls. This showed that:

- de-bonding of the cell walls was very common
- tearing of cell walls was not common. Individual cell walls tended to be folded but intact

- samples were very permeable on one plane only, on the other plane the cell walls were splayed out sideways.

Equation 3.2 relates the pressure P and volume V of a gas before ($_1$) and after ($_2$) an adiabatic expansion or contraction, i.e. an expansion or contraction of a gas whereby there is no transfer of heat out of the system. As shown in Figure 3.8, the impact events last a maximum of 7.5 ms and therefore occur too rapidly for a significant amount of heat to leave the system.

$$P_1 V_1^{\gamma} = P_2 V_2^{\gamma} \tag{3.2}$$

Equation 3.2 was used to produce the dashed black lines in Figures 3.9 (a) and (b), by taking the initial pressure as atmospheric (101.325 kPa), γ as the ratio of specific heats for air ($c_v/c_p = 1.4$) and using strain to calculate the ratio of final to initial volume. The dashed black lines represent the maximum possible internal pressure for a given strain, i.e. the internal pressure that would develop, assuming a perfectly constrained 1 dimensional adiabatic compaction of the air within the honeycomb.

The solid black lines in Figures 3.9 (a) and (b) show the load cell traces for a test performed on a B and D mesh sample respectively and the readings recorded by the central and edge pressure gauges during the two tests are shown in blue and red.

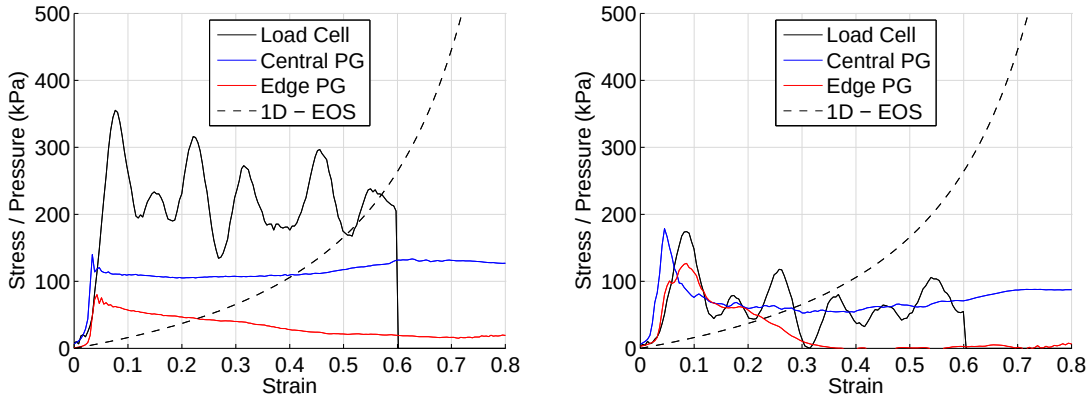

(a) B mesh [EDM1]

(b) D mesh [EDM6]

Figure 3.9 Comparison between maximum possible theoretical internal air pressures and the recorded load cell and pressure gauge traces during compaction of a B mesh (a) and D mesh (b) sample.

As the dashed black line represents the maximum possible internal air pressure, any stress to the left of the dashed black line must have been transmitted by the cell wall structure. This tells us that firstly, the early honeycomb response must be dependent solely on the failure of the honeycomb cell walls, and secondly, the pressure gauges must therefore have been picking up the total load, not just the internal gas pressures. Comparing the similarities between the shape of the central pressure gauge, shown by the blue line in Figure 3.9, with the load cell trace, further enforces this conclusion. Due to this, it was decided that further investigation would be necessary.

3.3 Phase 3 - Gas gun - Further testing

This phase of testing was performed to provide further experimental data on how variations in the mesoscale geometry affect the macroscopic behaviour of the cardboard honeycomb and to collect experimental data on the spacial and temporal development of internal pressures within the cardboard honeycomb during impact. Refinements were made on the experimental methods developed during Phase 2 in

an attempt to eliminate the issues discussed in Section 3.2.5, such as the spurious oscillations recorded by the load cell and structural response recorded by the pressure gauges. The scope and level of detail was also increased by introducing a third mesh type and recording the exact mesoscale geometry of all tested samples.

3.3.1 Scope of Phase 3

All samples were prepared with constant macroscale geometry of 70 mm in height and 250 mm x 250 mm plan area. The cell walls and liners were constructed from a 0.28 mm thick recycled cardboard with a density of 60.7 kg/m^3. Three mesh types were tested, B, D and F. When referring to a mesh type, the letter refers to the average cell wall length $\bar{L}$ and the later the letter, the longer the cell wall. Figure 3.10 shows the mesoscale geometry for a tested sample from each of the three mesh types.

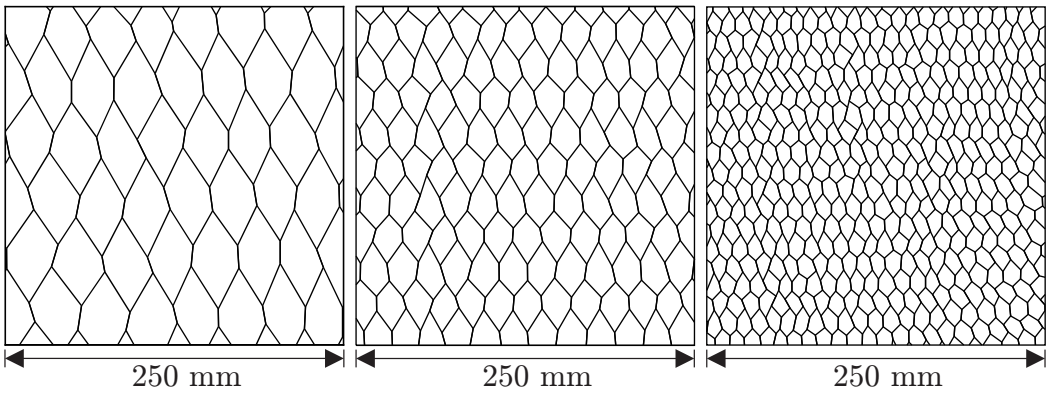

(a) $\bar{L}$ = 24.2 mm (b) $\bar{L}$ = 14.3 mm (c) $\bar{L}$ = 8.0 mm

Figure 3.10 Mesoscale cellular geometry of a tested F (a), D (b) and B (c) mesh sample. These geometries were extracted using the procedure discussed in Section 3.3.5 and refer to sample numbers F25, D27 and B8 respectively.

Table 3.3 details the matrix of tests performed during this phase of testing. Sample references indicate the mesh type followed by a unique number used later to identify the cellular geometry, $\bar{L}$ the average cell wall length and $\dot{\varepsilon}_{avg}$ the average engineering axial strain rate over the impact event.

Table 3.3 Series of performed tests during Phase 3.

Test ref	Sample ref	$\bar{L}$ (mm)	$\dot{\varepsilon}_{avg}$ (s^{-1})
T1	F25	24.7	145
T2	F22	24.3	144
T3	F29	24.2	144
T4	F31	24.3	143
F Avg		**24.4**	**144**
T5	D27	14.3	139
T6	D30	14.4	147
T7	D24	14.2	144
D Avg		**14.3**	**143**
T8	B8	8.0	134
T9	B11	8.1	136
T10	B10	8.0	135
T11	B14	8.0	202
B Avg		**8.0**	**135**

To investigate variability, each mesh type was repeated a minimum of three times while controlling strain rate, during test number 11 (T11) the strain rate was increased by doubling the thickness of the brass diaphragm from 0.1 mm to 0.2 mm. T11 is omitted from B mesh average inter sample strain rate given at the base of Table 3.3.

To both, increase strain rate constancy across all samples and to reduce the computational cost of numerical validation, the impact velocity was increased from that used during Phase 2. The stroke length of the measurable impact event was also extended to 83% strain, allowing the full EDM response to be recorded.

The exact mesoscale geometry of each sample was recorded, so it was known exactly what mesoscale geometry produced a given response. During each impact, time histories were recorded of the total transmitted load and pressures at the 5

internal locations shown in Figure 3.13 (b). To allow calculation of strain and strain rate the displacement time history was recorded with both a laser distance gauge and a high speed video camera.

3.3.2 Amendments to the Phase 2 Methodology

During the sample preparation for Phase 2 it was observed that, even when extreme care was taken to construct highly uniform samples, there were wide variations in the cellular structure between samples of the same mesh type. By recording the mesoscale geometry for all prepared samples it was possible to quantitatively study exactly what geometrical arrangement produced a given experimental response. The geometrical analysis for all tested samples is presented in Section 3.3.5. To emphasize any trends visible in the results a third, coarser, mesh type was introduced.

When commissioning the gas gun rig, several pressure gauges were damaged. The measures which were put in place to protect the remaining gauges limited the maximum experimental strain to 60%. While still providing useful data, this prevented the full EDM response of the honeycomb from being captured. To do so, the samples must be allowed to strain sufficiently, so that they reach the compaction region of EDM stress strain curve.

The honeycomb samples had a footprint area of A_{Trib} = 250 x 250 mm = 62500 mm^2. The geometrical analysis of the cardboard honeycomb samples (Section 3.3.5) yielded an upped bound measurement of the cross sectional area of cardboard cell wall A_c contained within the most dense samples to be $\approx$ 4000 mm^2. Due to the cellular cross section being prismatic over the axial height H these figures could be used to approximate that the most dense samples will consist of approximately 6.4 % solid cardboard material and 93.6 % air. Assuming sufficient porosity, and a perfectly axial compaction, such a sample would consist solely of cardboard at an axial compaction strain of 93.6 %. To protect the pressure gauges from damage, it was imperative that this was not allowed to occur.

Ensuring a sufficient safety factor was included and allowing for the possibility of further testing with deeper samples, it was decided that limiting the strain to 83%

would protect the pressure gauges while providing sufficient data. A 12 mm thick steel collar (with an internal perimeter to match the samples external perimeter) was welded to the back plate. The collar provided a proud rigid surface, which when struck by the edges of the moving front plate, would halt the projectile once the 70 mm deep sample had reached an axial strain of 83%.

During Phase 2, the pressure gauges recorded load that was being transmitted by the cardboard structure, meaning that the recorded traces were not representative of the internal air pressures within the honeycomb. To ensure that the pressure gauges accurately recorded the internal pressures during this phase, several measures were employed. A tool, shown in Figure 3.11, was constructed to pierce the bottom liner of each sample at locations corresponding to the centres of the pressure gauges on the back plate. The pierced holes were then carefully expanded to be slightly larger than the pressure gauge diaphragms, by removing a 5 mm disc of the bottom liner material, while ensuring not to damage the base of the cell walls. If any cell walls were found to interfere with the 5 mm hole they were carefully adjusted to the side. The collar was then used to locate the samples so that the holes lined up exactly with the pressure gauges on the back plate. As an additional precaution, the gauges were wound back, insetting them by 2 mm into the plate, using washers to ensure that an air tight seal was maintained.

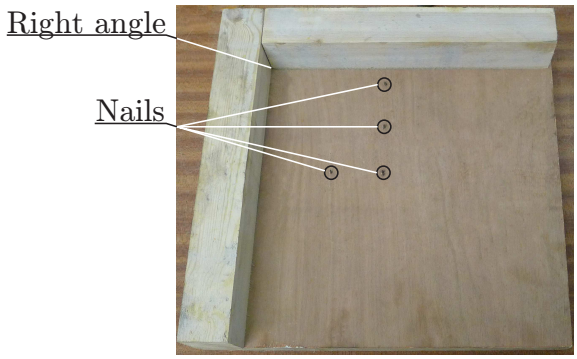

Figure 3.11 Timber sample base piercing tool, consisting of a right angle to locate the top left corner of each sample and nails to pierce the base liner.

It was concluded that the overlying oscillations recorded by the load cell during

Phase 2 may have been the result of a cantilever modal response of the backstop, which provides a solid surface behind the load cell shown in Figure 3.2 and diagrammatically in Figure 3.6. In an attempt to remove this mode and stiffen the backstop system enough, so as to reduce interference between oscillations in any other modes with the true response of the cardboard honeycomb samples, a steel beam section was welded between the top face of the back stop and the reservoir housing arrangement. This steel beam is visible across the top of the experimental general arrangement photo shown in Figure 3.2.

With the aim of attaining a close to constant strain rate over the full impact event, the position of the backstop was adjusted so that full compaction occurred at the end of the piston's travel, allowing the driving force, and therefore acceleration, to drop to minimum. The additional travel time also increased the velocity of the projectile and hence its total kinetic energy on impact with the samples. By increasing the total kinetic energy embodied in the travelling projectile, the proportion kinetic energy removed by each EDM sample was reduced, and a more homogeneous crushing rate was encouraged.

The magazine used during Phase 2, shown in Figure 3.4 (b), was historically used to hold thicker diaphragms than those used during this series of tests. This led to unwanted variation in the impact velocities, visible when looking at the strain rates of test EDM4 and EDM5 in Table 3.2. To eliminate this problem, the new magazine, shown in Figure 3.12, was constructed.

The new magazine consisted of two parts, a cylinder with an external radius matching the magazine location, shown in Figure 3.4 (a), and a threaded plug. The cylinder has a recess which is threaded to match the thread on the plug. During each test a new diaphragm is placed in the threaded recess and the plug is tightened up using the red bar and spanner shown in Figure 3.12 (b). This allowed the application of a much greater and regular clamping force around the edge of the diaphragm, which can be seen in the constancy of the average strain rates (s^{-1}) for tests 1 - 10 in fourth column of Table 3.3.

(a) (b)

Figure 3.12 Redesigned diaphragm magazine with threaded plug and recess (a) and tightening method recruiting leverage to provide a large even clamping pressure around the edge of each diaphragm (b).

3.3.3 Instrumentation and data acquisition

The flat front face of the projectile provided a forced axial displacement on the flat top face of each sample at velocity v. The back face was held stationary on the back plate causing the sample to axially compact (strain). As each sample was crushed, internal load carrying mechanisms transmitted load through the cellular structure to the back plate, this load was then transmitted through the back plate and recorded by the load cell shown in Figure 3.13 (a).

Internal air pressures were recorded at the locations shown in Figure 3.13 (b). Samples are orientated on the back plate, using the label that was added during construction to ensure that the double cell walls are aligned with the y axis.

Pressure gauges have two ratings, the maximum pressure they are capable of recording (their sensitivity) and the pressure which, if exceeded, will cause damage. The damage threshold pressure is normally double the maximum recordable pressure. Matching the sensitivity of pressure gauges with the maximum experimental pressure, while not exceeding the damage threshold will ensure the best signal to noise ratio. The highest pressures were expected to occur in the centre of each sample, a highest possible pressure was estimated but it was unclear exactly what

pressures would be generated by 83%. Gauges 1 and 2 were rated to 7 and 17 bar, while gauges 3 and 4 were rated to 35 bar.

The displacement time history of the projectile was recorded using both a laser displacement transducer aimed at the back face of the front plate, and with high speed video recorded using a Phantom v4.2 monochrome video camera running at 5000 frames per second with a 10 μs exposure.

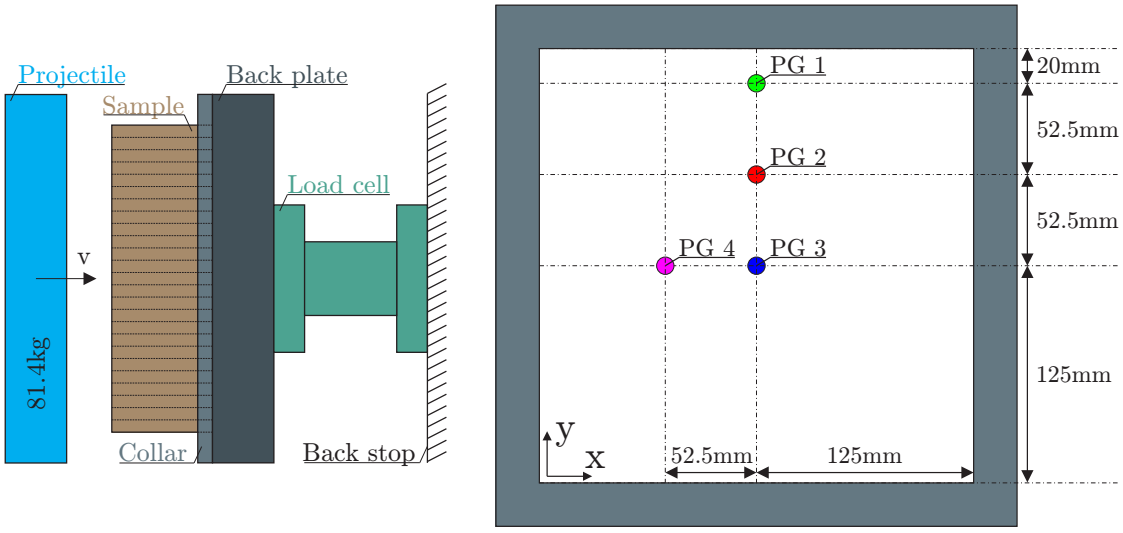

Figure 3.13 Experimental arrangement of the (a) projectile, load cell, and back plate; and (b) pressure gauges, in relation to the samples tested during Phase 3. Comparison with the arrangement used during Phase 2 (Figure 3.6) shows the addition of a protective steel collar, and the inclusion of two additional pressure gauges (PG2 and PG4).

Figure 3.14 shows a detail of how the pressure transducers (gauges) were mounted in the back plate. At each pressure gauge location, a recess was drilled in the back plate from the far face. A mount hole matching the diameter of the pressure gauge was then drilled to full depth and threaded. The pressure gauges were then inserted from the rear and tightened so that an air tight seal was formed; thus, isolating the indicated void and air contained within each sample.

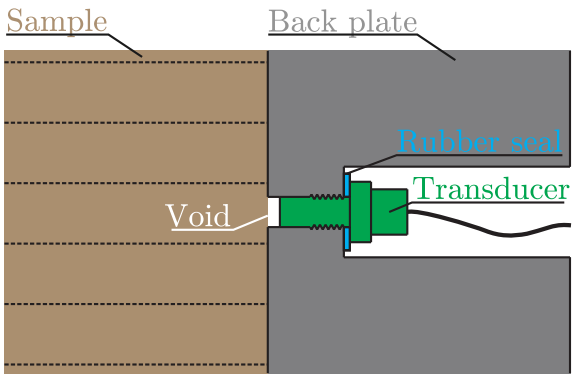

Figure 3.14 Detail showing how the pressure transducers were installed in the back plate.

A diagrammatic representation of the instrumentation arrangement is given in Figure 3.15. For a constant powering voltage the pressure gauges, strain gauges (on the load cell) and laser displacement gauge, all produced a change in voltage proportional to the change in variable they were measuring. The voltages were then digitally recorded at discrete points in time and converted to pressures, loads and displacements.

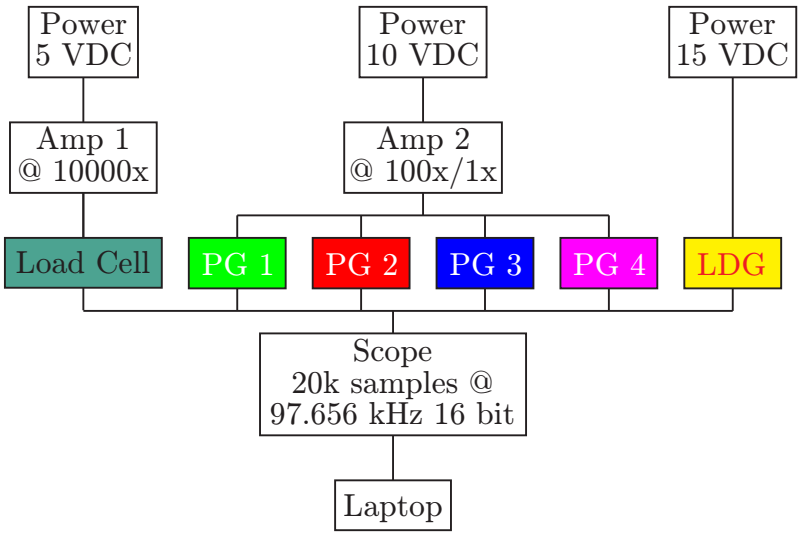

Figure 3.15 Instrumentation schematic with the load cell, pressure gauges (PG) and laser displacement gauge (LDG) highlighted with colour.

Amplifiers were used to distribute power to the instrumentation and to increase the true signal to electrical noise ratio by providing amplification. One amplifier

powered the load cell at an excitation of 5 Volts direct current (VDC). A second amplifier was used to provide 10 VDC to the pressure gauges. A bench power supply provided a stable source of DC power to the two amplifiers at 5 and 10 VDC.

Initially, semiconductor strain gauges were used to measure the strain of the load cell wall. The shock generated by abruptly arresting the projectile with the steel collar was enough to damage the semiconductor gauges. It was necessary to change to less sensitive, but more robust electrical resistance foil gauges.

The output from the load cell, laser displacement gauge and all four pressure gauges, was recorded by two combined TiePie HS4 USB Handy Scopes attached to a laptop. The event was captured with 20 k samples at 97.656 kHz in 16 bit resolution providing 0.2 s of recording time and 65536 voltage intervals. The scope was triggered by the laser displacement gauge when the front plate reached set position prior to impact and a pre trigger of 10% to capture the projectiles pre impact trajectory.

3.3.4 Post processing methods

Matlab was used as a platform to perform post processing on the raw data. Once imported, the first step was to apply conversion factors to the traces, converting them to pressures, load and displacement. Any initial zero shift was also removed from each channel by subtracting an average of the data points pre impact.

After some research into numerical filtering techniques it was possible to remove most of the electrical noise, while maintaining the true signal. The noise was composed of frequencies much higher than each true data trace so a low pass filter was required to remove it, maintaining (passing) the true low frequency components and removing the noise high frequency components. The most basic, and therefore easily applicable, low pass filter is a moving average. When applied to this data set, with a span long enough to remove sufficient noise, a moving average was found to severely clip the amplitude of genuine peaks and troughs.

Figure 3.16 (a) shows a brick wall low pass filter. This filter passes all frequencies below a cut off frequency F_c with their original amplitude and stops all frequencies

above the cut off frequency. A brick wall low pass filter was implemented by decomposing each signal into their frequency components using a Fast Fourrier Transform (FFT), zeroing the amplitude of all frequencies above F_c and then performing an inverse FFT.

The brick wall low pass filter was much better at maintaining peaks and troughs than the moving average but it introduced spurious oscillations close to regions where there was a sharp change in gradient. Research showed that this was the Gibbs Phenomenon [54], caused when sharply removing frequencies above a certain value, leaving their now unbalanced counterparts in the passband. Figure 3.17 shows the effect of applying a brick wall filter to a raw trace. Note the emergence of spurious oscillations as the cutoff frequency (F_c) is reduced below 10kHz.

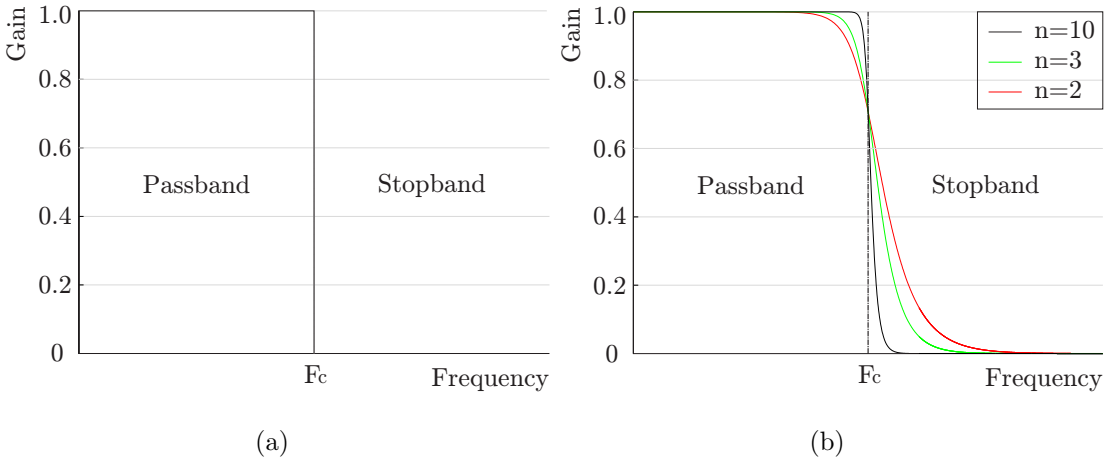

Figure 3.16 The brick wall (a) and graduated Butterworth (b) low pass filters.

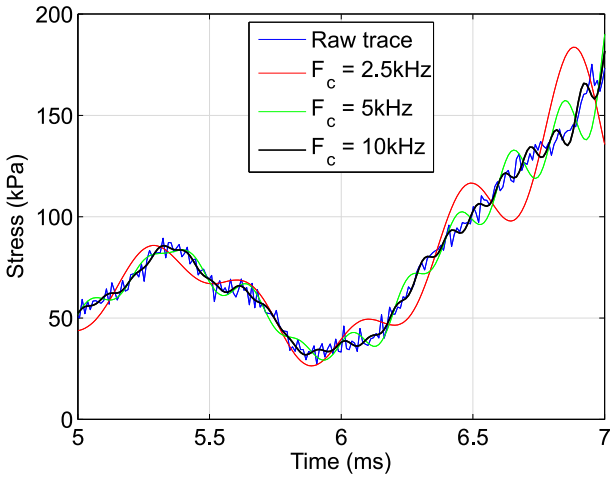

Figure 3.17 An example of the Gibbs phenomenon. Showing a raw trace, and the raw trace after being filtered with several low-pass brick wall filters of varied cut off frequency F_c.

Butterworth [55] discovered that the use of a graduated low pass filter with a normalised cut off frequency to 1 radian per second was capable of eliminating high frequencies without generating numerical ringing via the Gibbs Phenomenon. Figure 3.16 (b) shows three Butterworth low pass filters, created using Equation 3.3, of varying order n where the gain G of the passed frequency is a function of the normalised angular frequency $\frac{\omega}{\omega_c}$ and angular frequency ω is related to normal frequency F by $\omega = 2\pi F$.

$$G(\omega) = \sqrt{\frac{1}{1 + (\frac{\omega}{\omega_c})^{2n}}} \tag{3.3}$$

This filter was implemented using the in built `butter` function in Matlab. With slight variation between tests a filter of order $n = 5$ and cut off frequency $F_c = 2$ kHz was found remove a sufficient amount of noise, while maintaining the true trace with little clipping of peaks and no added ringing due to the Gibbs Phenomenon.

A smooth, second order polynomial was fitted to the displacement time data, allowing the velocity time history to be calculated by differentiation. A displacement time history was also extracted from the high speed video and compared to the laser

displacement time history to identify the data point at which impact occurred. The time and displacement axis were shifted, setting the impact point as the origin which enabled the calculation of axial strain over the impact event. The total transmitted stress σ was also calculated by dividing the total transmitted load by the plan area A = 0.0625 m^2.

3.3.5 Geometrical analysis of samples chosen for testing

During sample preparation a photograph was taken of the exposed mesh. A second photograph was taken once the top liner, with grid, was attached. Using Adobe Photoshop the two images were corrected for lens distortion and perspective, then overlaid. Figure 3.18 shows one of the images produced using this process, revealing the internal geometry of samples B9 to B14. After selecting the batch of samples to be tested, their geometry was imported into AutoCAD and digitized, allowing a geometrical analysis to be performed.

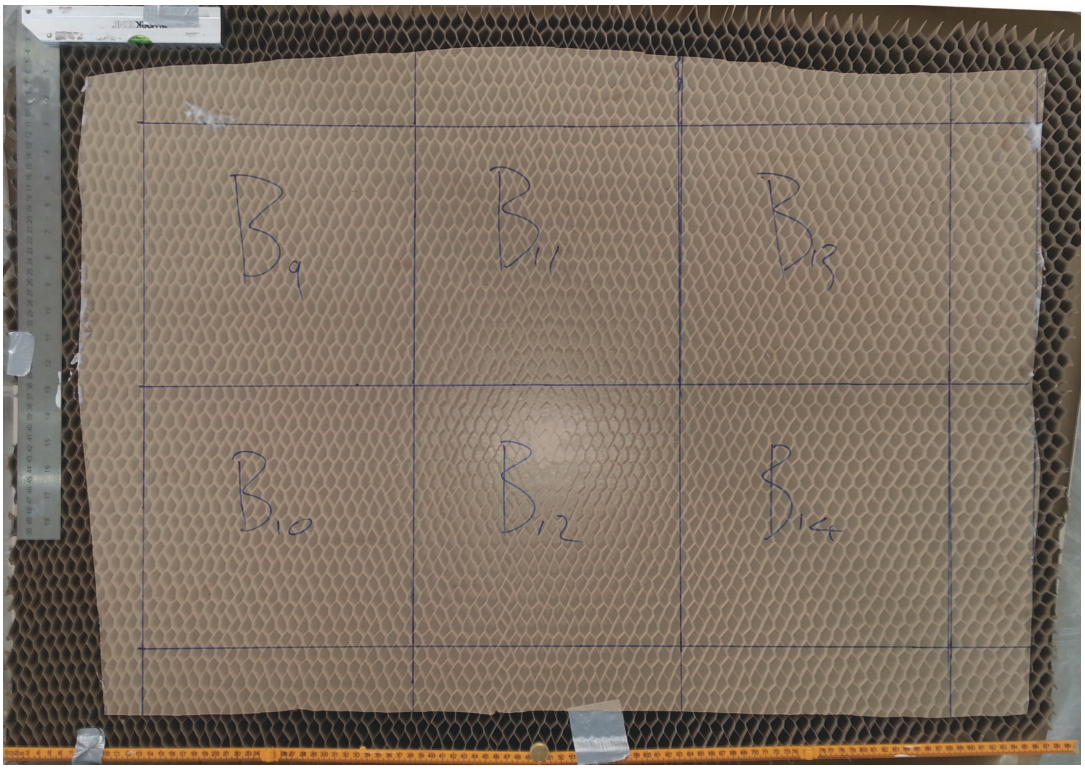

Figure 3.18 Overlaid images revealing the internal geometry of samples B9 to B14.

The cellular geometry of the cardboard honeycomb is created by sticking many layers of cardboard together with strips of glue. During sample preparation the top and bottom layers are pulled apart, resulting is a tessellation of hexagonal cells, each with four single and two double-thickness (glue bonded) cell walls.

Figure 3.19 (a) shows the internal geometry for sample F29 with single cell walls coloured blue and double cell walls red. The lengths of a single and double cell wall are indicated by L_{1t} and L_{2t} respectively.

Alternating black and pink lines in Figure 3.19 (b) show each continuous cell wall. The shaded cells are complete i.e. the air within them is confined by six complete cell walls. Two adjacent cell walls enclose a strip of cells and complete cells belonging to the same strip are shaded with the same colour.

It is worth note, that the digitised sample geometries were marginally idealised by discounting the curvature of the cell walls close to the vertices. This was felt to be a reasonable omission as any deviation between the photographs and the digitised geometries was marginal. The inclusion of any curvature in the digitised geometries would have substantially increased the time taken to carry out the digitisation and added complexity to any subsequent numerical modelling.

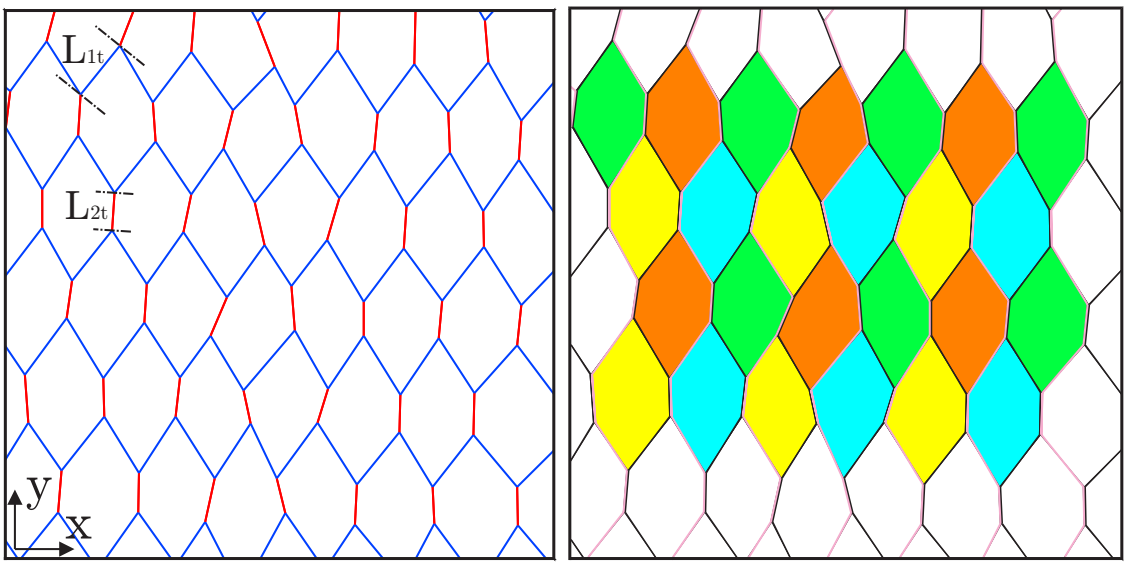

(a) (b)

Figure 3.19 Cellular structural components of sample F29. (a) Layout of double (red) and single (blue) cell walls. (b) Layout of adjacent, continuous, cell walls marked with alternating black and pink lines. All fully sealed (complete) cells are shaded and those which lie between the same pair of cell walls are shaded with the same colour, the air within being separated by only glue bonds.

The arrangement of cell walls causes anisotropy (on plan), which can be idealised by two planes along the x and y axis as indicated by the axis labels in Figure 3.19 (a). The x plane is orientated in the direction of pull used to expand the honeycomb mesh during construction, the y plane is perpendicular to this. The y plane is also parallel to the average direction of the glue bonds. During the tests carried out in Phase 2 all samples exhibited global anisotropic behaviour. Outwards lateral drift of the cell walls, along the x plane, occurred for all tests, while there was no drift in the y plane. In addition, a zone of bond failure was visible for almost every pair of double cell walls and the crushed samples were significantly more permeable along the y plane when compared to the x plane.

Geometrical variation was introduced by testing samples from three mesh types. However, even with a tightly controlled construction process, additional inter-sample variations were introduced.

An idealised cell is displayed in Figure 3.20 (a), symmetrical about both axis with four single cell walls of equal length L_{1t}, four double cell walls of equal length L_{2t} and θ is the angle of expansion. L_{1t} and L_{2t} are pre-set by the manufacturer for a given mesh type and the angle θ is dependent upon the applied expansion force. In reality, during expansion of the core, any initial geometrical manufacturing errors are magnified, causing all six individual angles and cell wall lengths to vary for each cell. As the expansion load is applied, it is transmitted along the stiffest path, being continually redistributed through geometrical alterations as the core is pulled apart.

An idealised cellular arrangement is shown in Figure 3.20 (b) where all cells are aligned with their double cell walls parallel to the y axis. As the honeycomb structure is a perfect tessellation (no empty space between cells), the aforementioned variations in the cellular geometry also force variations in the cellular arrangement, producing an irregular mesh. This irregular mesh causes variations in the meso-scale geometry between samples cut even from the same honeycomb core.

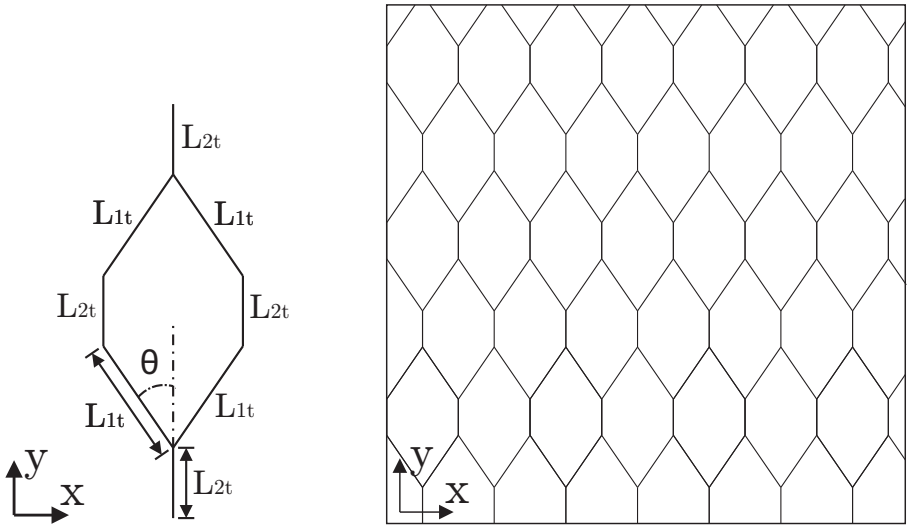

(a) (b)

Figure 3.20 Idealised honeycomb cellular geometry (a) and layout (b).

Table 3.4 displays a summary of the mesoscale geometrical parameters for the tested samples including the total cross sectional area of the cardboard cell walls A_c, average single cell wall length $\bar{L}_{1t}$, average double cell wall length $\bar{L}_{2t}$, quotient

of total length of double cell wall to total length of single cell wall $\Sigma L_{2t}/\Sigma L_{1t}$ and the total number of complete cells ncell. To remove any bias caused by outlying half-cut cell walls, only complete cells were used in the calculation of $\bar{L}_{1t}$, $\bar{L}_{2t}$, and $\Sigma L_{2t}/\Sigma L_{1t}$. Wide variations between all internal angles for all cells reduced the significance of stating an experimental value for θ. The total length of cardboard cell wall ΣL within each sample can be calculated by dividing A_c by the thickness of the cell wall material $t = 0.28$ mm.

Table 3.4 Detailed mesoscale geometrical parameters for all samples tested during Phase 3.

Test ref	Sample ref	A_c (mm^2)	$\bar{L}$ (mm)	$\bar{L}_{1t}$ (mm)	$\bar{L}_{2t}$ (mm)	$\Sigma L_{2t}/\Sigma L_{1t}$	ncell
T1	F25	1205	24.7	32.7	15.4	0.41	28
T2	F22	1149	24.3	30.5	17.2	0.49	25
T3	F29	1146	24.2	29.8	17.9	0.53	25
T4	F31	1145	24.3	29.0	19.1	0.60	27
F Avg		**1161**	**24.4**	**30.5**	**17.4**	**0.48**	**26**
T5	D27	1990	14.3	17.3	11.1	0.61	104
T6	D30	1947	14.4	17.0	11.7	0.65	92
T7	D24	1993	14.2	16.4	12.0	0.69	112
D Avg		**1977**	**14.3**	**16.9**	**11.6**	**0.65**	**103**
T8	B8	3776	8.0	8.3	7.7	0.91	367
T9	B11	4032	8.1	8.2	7.9	0.96	400
T10	B10	3832	8.0	8.3	7.7	0.90	361
T11	B14	3569	8.0	8.8	7.1	0.79	353
B Avg		**3880**	**8.0**	**8.3**	**7.8**	**0.92**	**376**

Average values have been calculated for each mesh type. Test T11 was performed at a higher strain rate and is therefore not a direct comparison with the other 10 tests, so the geometry of sample B14 has been discounted from calculation of the average B mesh parameters. Any analysis considering T11 will refer to sample B14's individual geometry.

By fixing the macroscale geometry several mesoscale geometrical parameters are coupled. A shorter cell wall reduces the cell size, which results in an increase in the both the number of cells and area of cardboard material (A_c) within the fixed 250 x 250 mm square macroscopic plan area. A_c increases with the ratio 1.0: 1.7: 3.3 across the three mesh types from F: D: B. A_c varied by just 60 mm^2 and 46 mm^2 for the F and D mesh samples but by a much larger 463 mm^2 for the B mesh. $\bar{L}$ is very consistent for each mesh and decreases with the ratio 3.1: 1.8: 1.0 from F to B, an almost direct inverse relationship to A_c.

For all samples, the glued double cell walls $\bar{L}_{2t}$ were shorter than the single cell walls $\bar{L}_{1t}$. The quotient between the total length of double and single cell wall $\Sigma L_{2t}/\Sigma L_{1t}$ increased as $\bar{L}$ decreased with the ratio 1: 1.4: 1.9. Meaning that the proportion of bonded double to single cell wall for the B mesh was almost double that of the F mesh.

The number of complete cells is an inverse function of the area of each cell and is therefore an inverse square relationship to the cell wall length, increasing with the ratio 1.0: 4.0: 14.5 from the F mesh to the B mesh. The variation also increases as the cell size reduces, as more cells will be cut per row and column if the sample boundary is drawn through their centre.

The highly variable mesh could then be expressed with the idealised geometry shown in Figure 3.20. Using the average values of $\bar{L}_{1t}$ and $\bar{L}_{2t}$ from Table 3.4, as constants for L_{1t} and L_{2t}, an algorithm was written to calculate which value of θ would result in the recorded value of A_c within the 250 mm $\times$ 250 mm square. Idealised geometrical parameters for each mesh type are given in Table 3.5 and the resulting idealised cellular geometry is displayed in Figure 3.21. The idealised F cell is also shown tessellated as an idealised F mesh in Figure 3.20 (b), which can be compared by eye to the geometry of sample F29 shown in Figure 3.19.

Table 3.5 Mesoscale geometrical parameters of the representative F, D and B mesh idealised cells.

Mesh	A_c (mm^2)	L_{1t} (mm)	L_{2t} (mm)	$\theta°$
F	1161	30.5	17.4	34.5
D	1977	16.9	11.6	36.3
B	3880	8.3	7.8	37.5

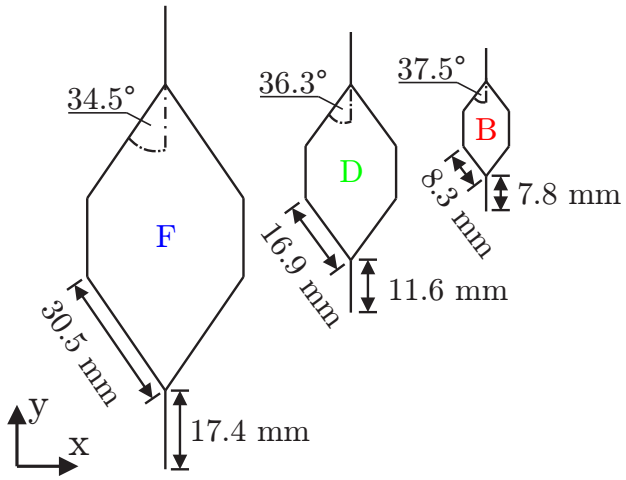

Figure 3.21 Diagrammatic illustration of the representative average F, D and B mesh idealised cells [To scale].

The relationship between θ and A_c for a known macroscale geometry and given cell wall lengths could then be computed. Figures 3.22 (a), (b) and (c) display how A_c varies with θ within a 250 mm $\times$ 250 mm square, for the three mesh types tested in this piece of work. The average geometry of samples selected for testing has been marked with an X.

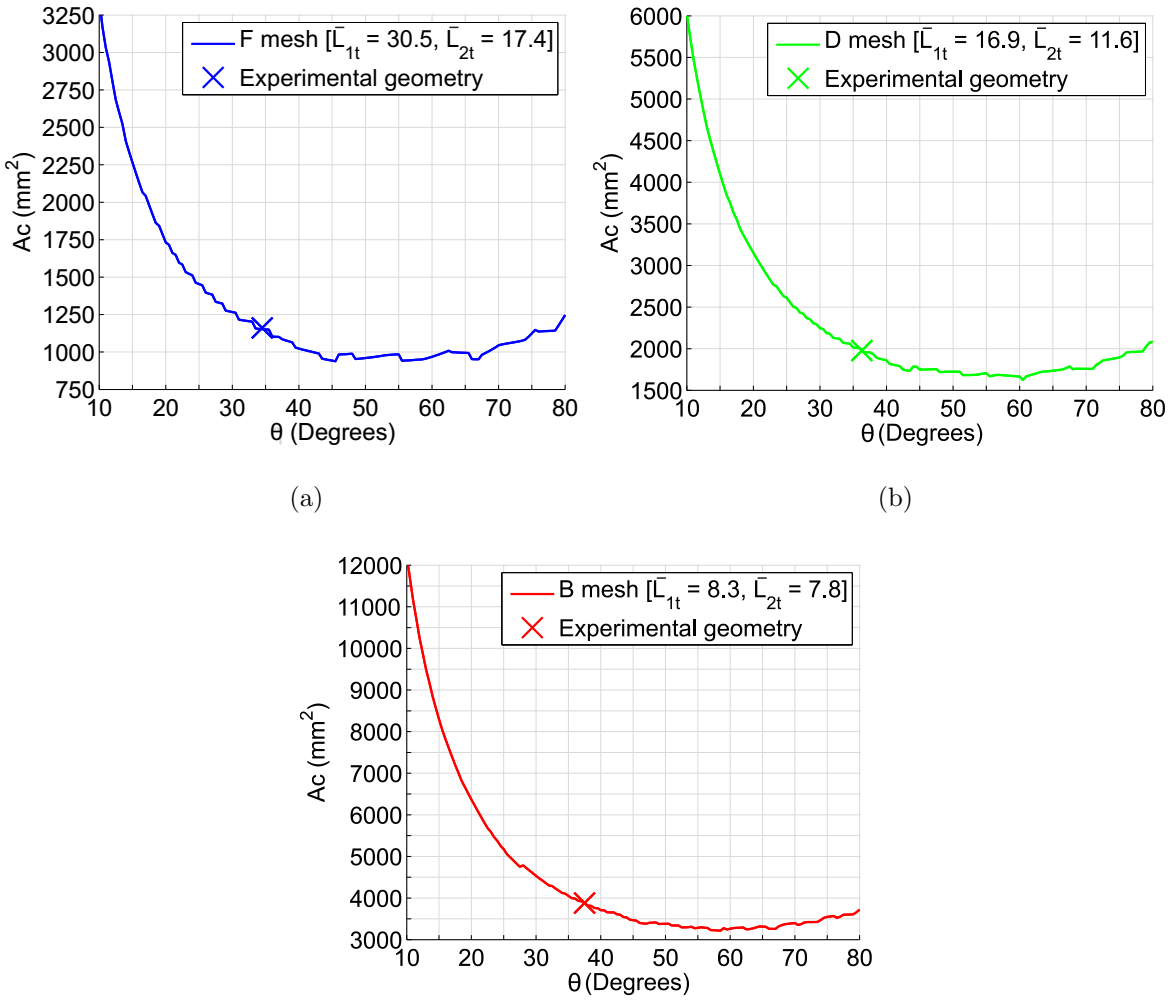

Figure 3.22 Relationship showing how the total cardboard cross sectional area A_c changes with the expansion angle θ within the 250 x 250 mm square for the F mesh (a) D mesh (b) and B mesh (c), recorded values of the tested samples are marked with an x.

3.3.6 Matrix of measured loading rates

Table 3.6 displays the loading rate information for all tests, where v_i and v_f are the initial and final velocities over the impact stroke and $\dot{\varepsilon}_i$ and $\dot{\varepsilon}_{avg}$ the initial and average strain rate.

For T1-7 (all non B mesh samples) there was an increase in the velocity of the

projectile over the impact stroke, meaning that the projectile must have still been driven by pressure on its rear face through the impact. For T8-10 the projectile slowed over the impact stroke, meaning that the B mesh samples must have removed more kinetic energy from the projectile than was being added by the driving force. There was sufficient driving force for the high strain rate test T11 to accelerate the projectile through the B mesh sample.

For each mesh type $\dot{\varepsilon}_{avg}$ was extremely consistent. During the F mesh T1-4 and D mesh T8-10 $\dot{\varepsilon}_{avg}$ varied by 2 s^{-1}, while still only varying by 8 s^{-1} between 139 and 147 for T5 and 7. The greater resistance provided by the B mesh samples was also visible from a reduced $\dot{\varepsilon}_{avg}$.

Table 3.6 Phase 3 - Detailed loading rate information.

Test ref	Sample ref	v_i (m/s)	v_f (m/s)	$\dot{\varepsilon}_i$ (s^{-1})	$\dot{\varepsilon}_{avg}$ (s^{-1})
T1	F25	9.58	10.76	137	145
T2	F22	9.48	10.64	135	144
T3	F29	9.46	10.63	135	144
T4	F31	9.45	10.61	135	143
T5	D27	9.48	9.91	136	139
T6	D30	9.70	10.91	139	147
T7	D24	9.48	10.67	135	144
T8	B8	9.86	8.85	141	134
T9	B11	9.72	9.28	139	136
T10	B10	9.96	8.97	142	135
T11	B14	13.70	14.58	196	202

3.3.7 Results - Macroscopic transmitted load

The stress vs strain relationship represents the global response of the cardboard honeycomb as a unit, the total transmitted load for a given strain being a function of the stiffness provided by the internal load carrying mechanisms at that point in

time. The measured stress vs strain relationships, for all tested samples, are shown in Figures 3.23 (a) F mesh, (b) D mesh, (c) B mesh and (d) T11 - B mesh (higher strain rate). Refer to Table 3.3 in Section 3.3.1 for the complete test series detail.

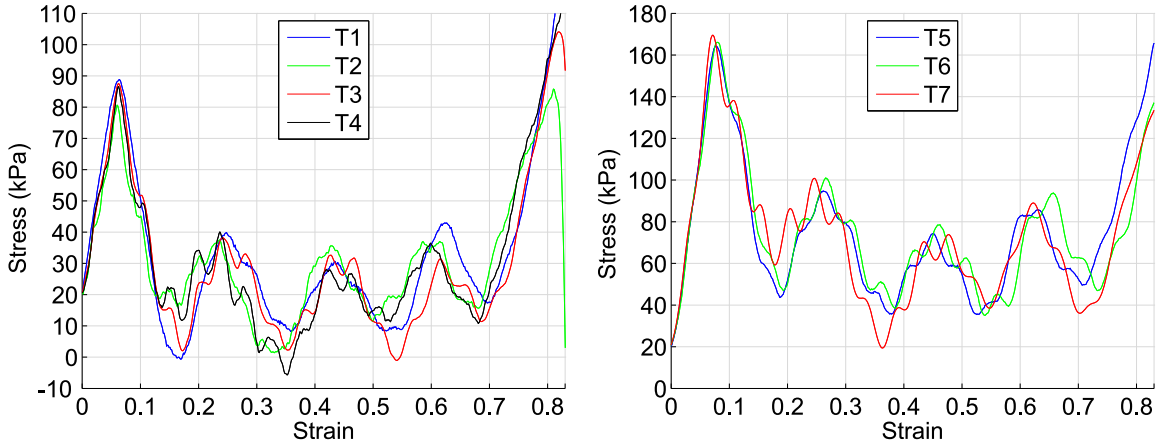

(a) F mesh

(b) D mesh

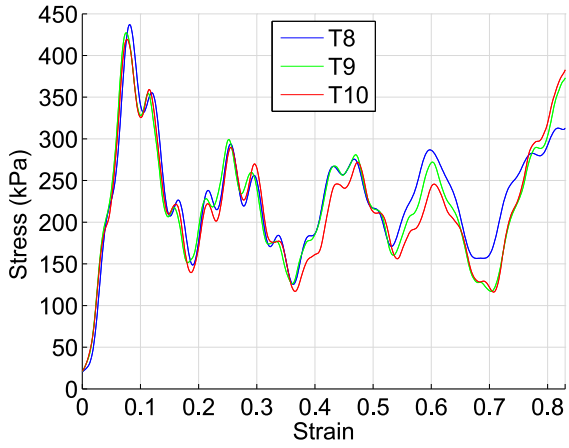

(c) B mesh

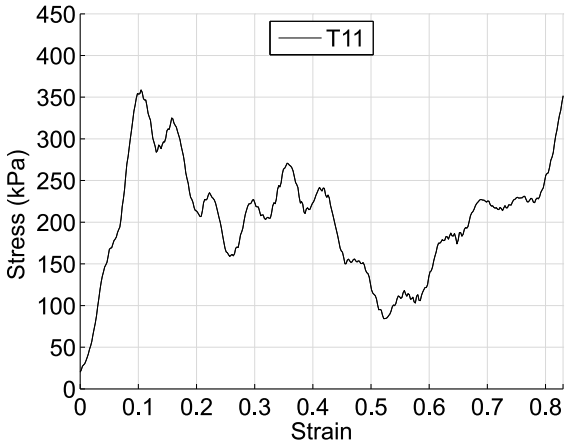

(d) T11 B14

Figure 3.23 Stress vs strain relationship for all samples tested during Phase 3, (a) F mesh, (b) D mesh, (c) B mesh and (d) a B mesh sample with increased strain rate.

Pre impact, a gradually rising 1.2 kN load was recorded by the load cell, which is thought to be the leading pressure wave generated by the rapidly accelerating (a ≈ 250 ms^{-2}) front plate.

Stiffening the backstop did not remove the overlying oscillations (ringing) encountered during the previous two phases. The ringing frequency varied between 680-860 Hz, a reduction on the 890-1150 Hz ringing frequencies observed during Phase 2. Studying the load cell traces, shown in Figure 3.23 (a), generated when testing the F mesh samples, provides verification that the ringing was not a genuine component of the cardboard honeycomb response. Zero load is recorded at 15%, 35% and 55% strain for several tests and at 35% strain for T4 the load cell even registered a negative (tensile load). There was no bond between the base of each sample and the back plate, so it was not possible to transfer any tensile force from the cardboard honeycomb to the load cell. Positive internal air pressures were also recorded by several of the pressure gauges, so it is known that a compressive load was being applied to the back plate, finally both the high speed video and laser displacement gauge verified that the sample was being axially compressed during the whole impact event.

The spurious oscillations could not be removed through filtering because it consisted of frequency components in the same band as the true data. It is likely that the origin on the spurious oscillations is due to the dynamics of the sample supporting structure. For any load to be recorded by the load cell, the heavy back plate must be moved. The net effect of this, at these dynamic loading rates, is that the inertial response of the back plate would have reduced the rate at which load was transmitted to the load cell wall. Thus, causing the rising limb of the recorded load-time histories to appear less steep than the true load-time histories transmitted through the cardboard honeycomb samples. The subsequent oscillations, following the initial peak, could then be explained by the oscillatory response of the back plate and sample supporting structure.

Reducing the mass of the back plate was not an option due to the fact it needed to posses sufficient structural integrity to remain rigid during the violent impact event. Attempts were made to quantify the dynamic properties of the back plate and sample supporting structure, however due to the unknown characteristics of the connections (welds and bolts) this was found to be a time consuming task, so much

so that it was deemed to lie outside the scope of this thesis.

All tested samples exhibited the classical EDM behaviour, three regions characterised by a peak stress σ_{Peak}, a plateau region and a stiffening limb. The exact shape of the true trace in the plateau region is unclear due to the overlying oscillations, although it is not unreasonable to assume they oscillate about the true data. The average stress between 20% and 60% strain has been used as a single value to characterise the plateau stress $\sigma_{Plateau}$ transmitted by each sample. Values of average strain rate $\dot{\varepsilon}_{avg}$, σ_{Peak} and $\sigma_{Plateau}$ for all samples are displayed in Table 3.7.

Table 3.7 Phase 3 - Macroscopic response summary.

Test Ref	Mesh	$\dot{\varepsilon}_{avg}$ (s^{-1})	σ_{Peak} (kPa)	$\sigma_{Plateau}$ (kPa)
T1	F	145	88.9	21.7
T2	F	144	80.7	21.4
T3	F	144	87.6	18.6
T4	F	143	86.6	18.2
F Avg		**144**	**86.0**	**20.0**
T5	D	139	164.3	61.0
T6	D	147	166.1	62.9
T7	D	144	169.6	59.4
D Avg		**143**	**166.7**	**61.1**
T8	B	134	437.2	221.7
T9	B	136	427.4	217.5
T10	B	135	419.5	206.8
B Avg		**135**	**428.0**	**215.3**
T11	B	202	358.6	180.5

Both σ_{Peak} and $\sigma_{Plateau}$ increase as the mesh density increases. Average values of σ_{Peak} increase from 86.0 kPa for the most coarse F mesh to 166.7 kPa for the D mesh and 428.0 kPa for the most dense B mesh. Likewise, $\sigma_{Plateau}$ increases from 20.0 kPa for the F mesh to 61.1 kPa for the D mesh and 215.3 kPa for B mesh

samples.

T11 was performed at the higher strain rate of 202 s^{-1}, compared with $\dot{\varepsilon}_{avg}$ = 135 s^{-1} used for the other three B mesh samples (T8-10). When comparing the recorded stress strain curves of T8-10, Figure 3.23 (c), to T11, Figure 3.23 (d), there is a reduction of the peak stress from $\bar{\sigma}_{Peak}$ = 428.0 kPa to 358.6 kPa. Further work would need to be carried out to identify if there is a strain rate effect contributing to the reduction in load. The geometrical analysis presented in Table 3.4 shows that the sample used for T11 had lower values of A_c = 3569 mm^2, $\Sigma L_{2t}/\Sigma L_{1t}$ = 0.79 and ncell = 353 than the average values of the samples used in T8-10 of A_c = 3880 mm^2, $\Sigma L_{2t}/\Sigma L_{1t}$ = 0.92 ncell = 376, which may account for the reduction in load.

It worth noting that at the higher strain rate, there is more interference on the true load trace from the spurious oscillations, because the time period of each oscillation is a greater proportion of the total time taken for each impact event. This is illustrated in Figure 3.24, which graphs the transmitted stress for all four B mesh samples against time rather than strain. As the stress vs time graph for T11 exhibits a similar shape to the lower strain rate tests and strain is not linearly proportional to time between the two strain rates, the dynamic overlying mode must be distorting the shape of the recorded stress strain curves in time. It must therefore be understood that the gradient of the initial rising limb, which defines time to peak (and associated strain to peak), and stiffening limb are dependent upon the response in the dynamic mode and not solely representative of the cardboard honeycomb samples.

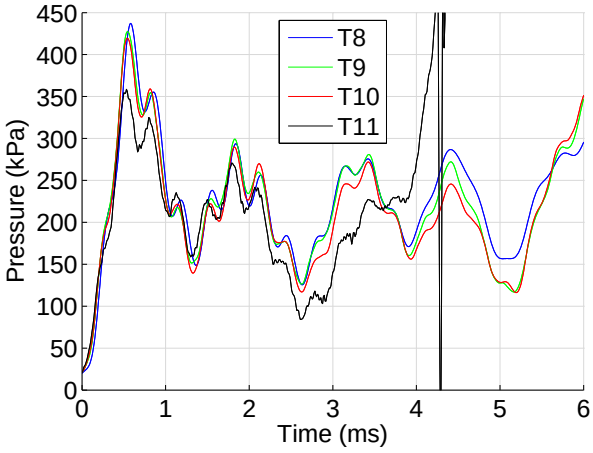

Figure 3.24 Transmitted stress vs time for all B mesh samples, comparison between the trace recorded by the load cell for T8-10 $\dot{\varepsilon}_{avg}$ = 135 and T11 $\dot{\varepsilon}_{avg}$ = 202 to highlight the distortion caused by the overlying oscillatory response.

3.3.8 Results - Mesoscopic internal air pressures

Figures 3.25 (a), (b), (c) and (d) show the recorded internal air pressures and their locations within each sample for the four F mesh samples, T1-4. An instrumentation fault resulted in no reading for pressure gauge 2 (PG2) during T1. The pressure gauge locations were shown in Figure 3.13 (b), their respective distance from the y and x edges (dy and dx) being, PG1: dy = 20 mm dx = 125 mm, PG2: dy = 72.5 mm dx = 125 mm, PG3: dy = 125 mm dx = 125 mm and PG4: dy = 125 mm dx = 72.5 mm.

The predominant shape of the traces recorded by gauges 2-4 is a gradual linear rise in pressure to a plateau beginning at 30% strain, followed by a slight dip, into an exponential rise which starts around 60% strain. For T1-4, gauge 1 recorded no marked increase in pressure until an exponential rise beginning between 60-70% strain. Variations on this shape include a less pronounced dip in T1 and a shorter plateau in T4.

The magnitude of internal pressure is dependent on the distance from the sample edge, with the highest pressures being recorded by the central pressure gauge (PG3)

and lowest pressures by the edge pressure gauge (PG1). The intermediate gauges (PG2 and PG4) recorded very similar pressures for T2 and T3 and sat between the pressures recorded by the central and edge gauge for all tests. There was a brief period, during T4, between 40 and 60% strain, where the pressure recorded by PG3 dropped, equalising with the pressure recorded by PG2.

For T1-3 the central gauge recorded a fairly consistent plateau pressure of 50 kPa while the intermediate gauges recorded a pressure of about half that, around 25 kPa. The maximum pressures were recorded by PG3 at 83% strain reaching 224 kPa for T4. During T3 and T4 the maximum pressure recorded by the edge pressure gauge PG1 equalled that recorded by the intermediate gauge PG4.

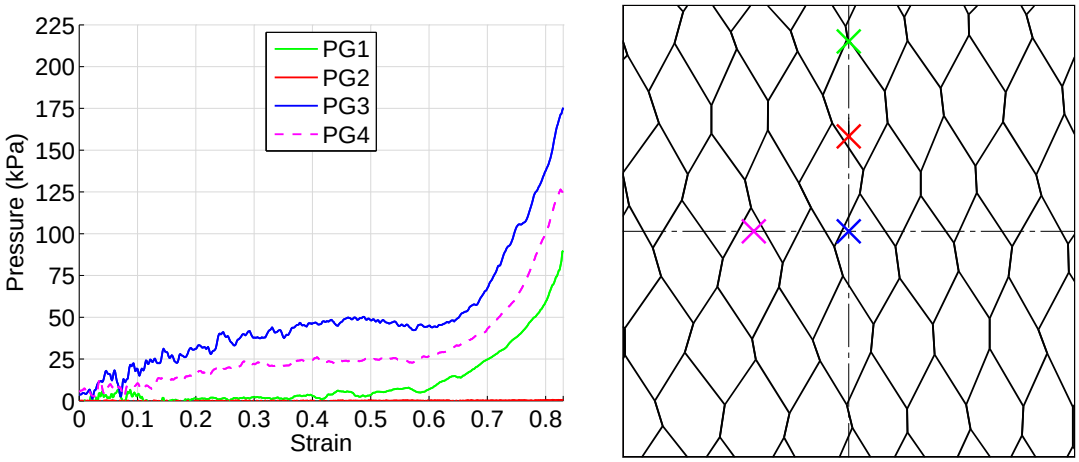

(a) Test T1, Sample F25.

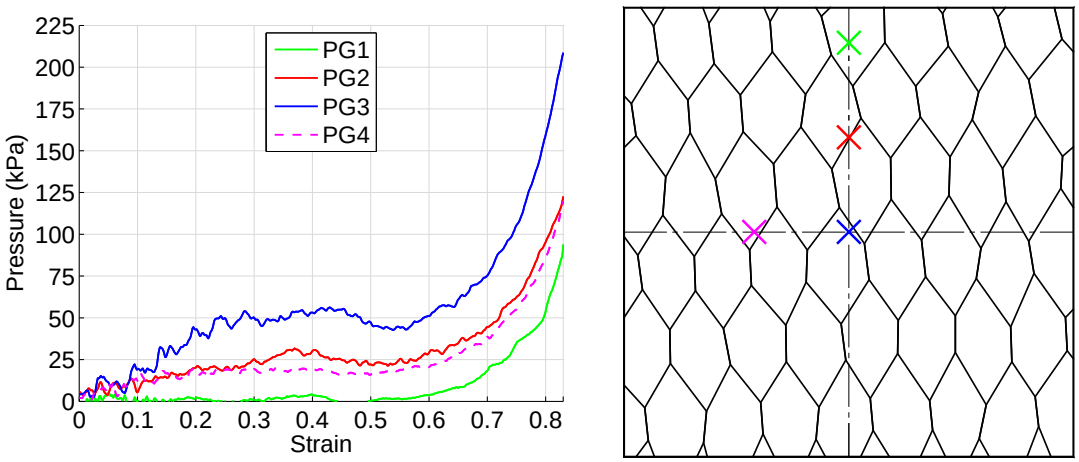

(b) Test T2, Sample F22.

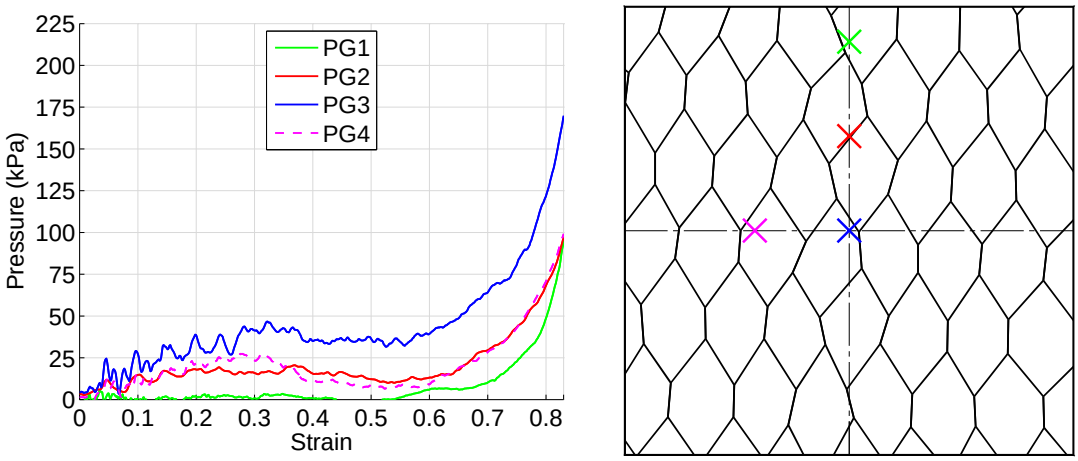

(c) Test T3, Sample F29.

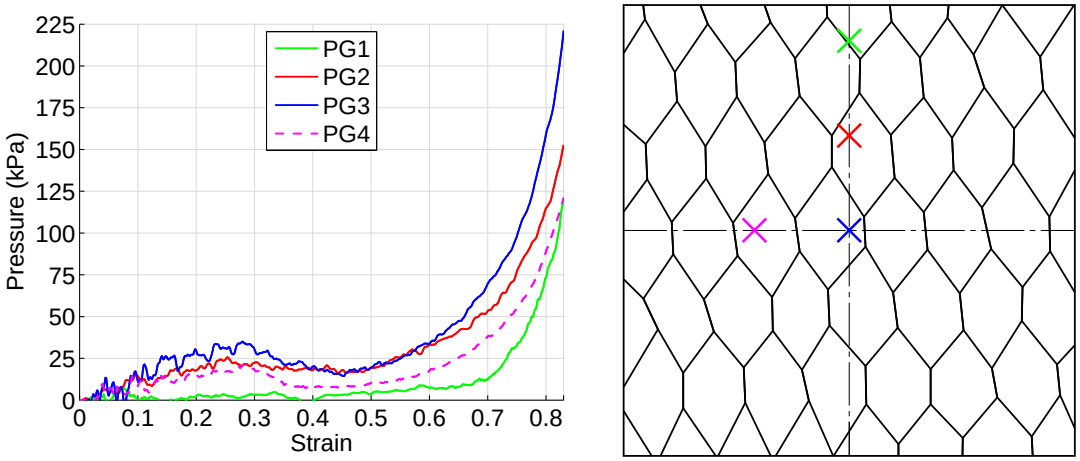

(d) Test T4, Sample F31.

Figure 3.25 Internal air pressures vs strain and the locations that they were recorded within all four tested F mesh samples.

For T1-4 the edge pressure gauge was not located within a complete cell, but still recorded pressure during all four tests. Consequently, during crushing, the buckling cell walls must have created a sealed volume, trapping the air around PG1, allowing it to be compressed and increase in pressure. It is also worth noting that due to the coarse irregular mesh PG1-3 did not always lie within the same strip of cells.

Towards the centre of each sample there is an increase in both the amount of cell wall material surrounding the internal gas, and the path length to the perimeter

free air boundary. The amount of cardboard, and how it is distributed, differed between the x and y plane. On a cross section through the F mesh samples on the y plane (top to bottom) there were a maximum of 3 complete sealed cells, on a cross section on the x plane there were between 5 and 6 complete cells. The magnitude of internal air pressures recorded by the two intermediate gauges (PG 2 and 4) was similar, which suggests that the number of complete cells between any given cell and the perimeter is not the controlling factor in the magnitude of air pressure development.

Assuming a symmetrical internal air pressure distribution, a linear change in pressure between the gauges and zero pressure at the perimeter, it was possible to use the traces recorded by gauges 1-3 to plot an estimated internal spacial pressure distribution for each sample. Figure 3.26 shows contours of internal pressure which developed at various levels of strain ε, during T2, on a cross section through the centre of sample F22. Crosses indicate the location of each pressure gauge. Before 40% strain the rate of pressure increase is directly proportional to the distance from the sample edge, resulting in a triangular pressure distribution through the sample, with a pressure differential between the all three gauges in the region of 25 kPa. After 40% strain the rate of pressure increase at the centre dramatically increases and by 83% strain the pressure differential between the central and intermediate gauges is 86 kPa, while the differential between the edge and intermediate gauge is still only 29 kPa. Between 40 and 60% the total pressure across the sample remains almost constant, after 60% the pressure on all gauges begins to rapidly increase, including the pressure being recorded by the edge gauge.

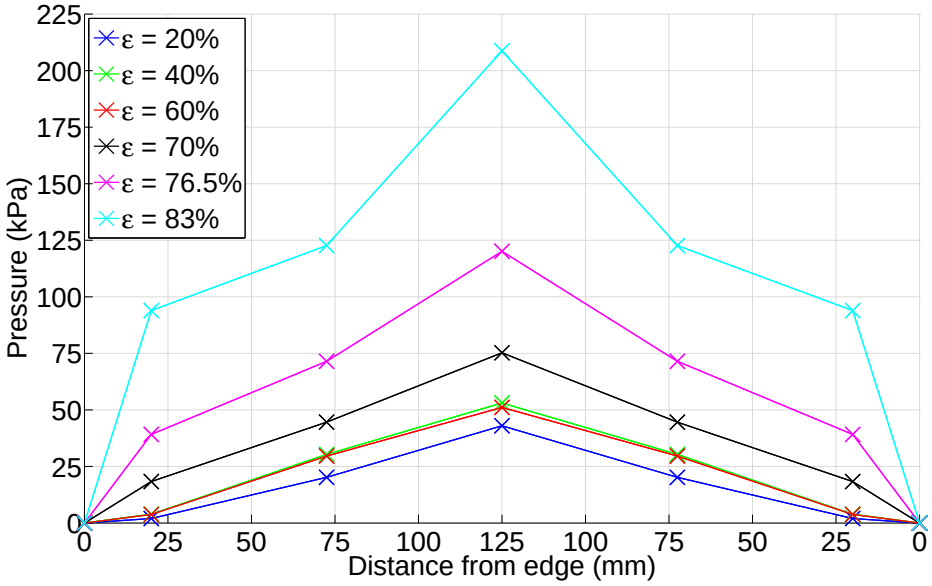

Figure 3.26 Internal pressure distribution, for varying levels of strain on a cross section through the centre of sample F22, Test T2.

Figures 3.27 (a), (b) and (c) show the recorded internal air pressures for T5-7 and their locations within the three tested D mesh samples. Three prevailing features were visible on the traces recorded by the internal pressure gauges for T5-7, a linear increase, changes in gradient of the linear increase and an exponential increase. The exponential increase began at around 70% for almost all traces. The changes in linear gradient were visible on all the internal traces (PG2-4), an example of which can be seen in T6 on the trace recorded by PG3 at 47% strain.

The general trend was for an increase in the magnitude of pressure with an increase in distance from the sample perimeter, although Figure 3.27 (b) shows that from 60 % strain onwards the pressure in the centre and at the intermediate gauges was very similar. For all three tests the pressure recorded at the sample edge was lower than the pressures recorded internally. During T6, the edge pressure gauge increased to 25 kPa but then dropped off, suggesting a venting of the entrapped pressurised air. For all three D mesh tests, at 70 % strain the pressure began to increase at the sample edge. The highest pressure which was recorded within the D mesh samples was during T5 by the central gauge, its magnitude was 248 kPa

(marginally higher than the maximum 224 kPa recorded within the F mesh samples). The pressure recorded by the edge pressure gauge (during the late response) was actually lower than what was recorded during crushing of the F mesh samples, it is thought that this may somehow be due to interference between the cardboard structure and the steel collar as the potential exists for localised sealed volumes to be created at large deformations.

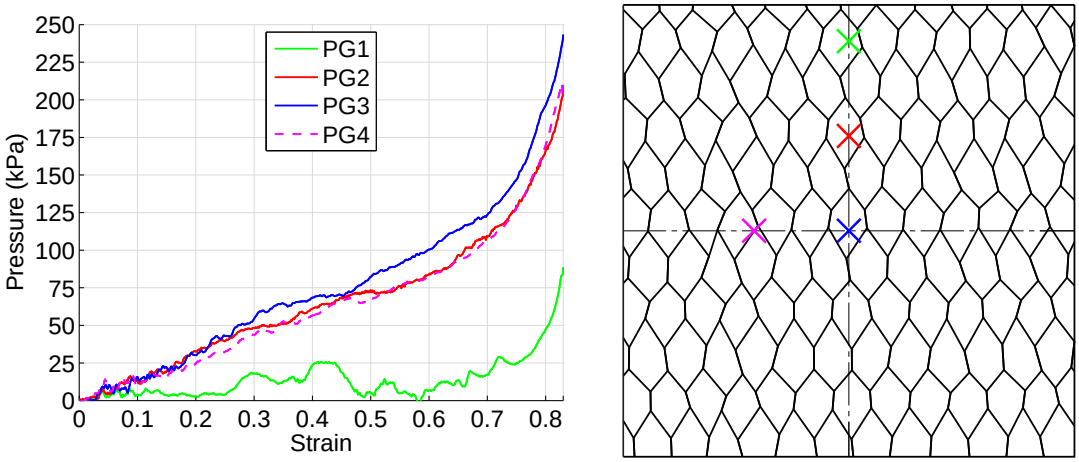

(a) Test T5, Sample D27.

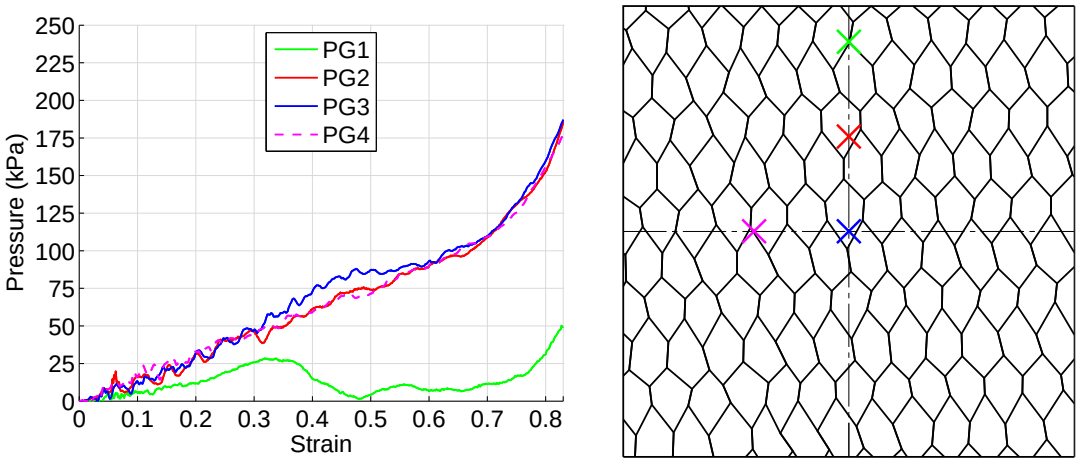

(b) Test T6, Sample D30.

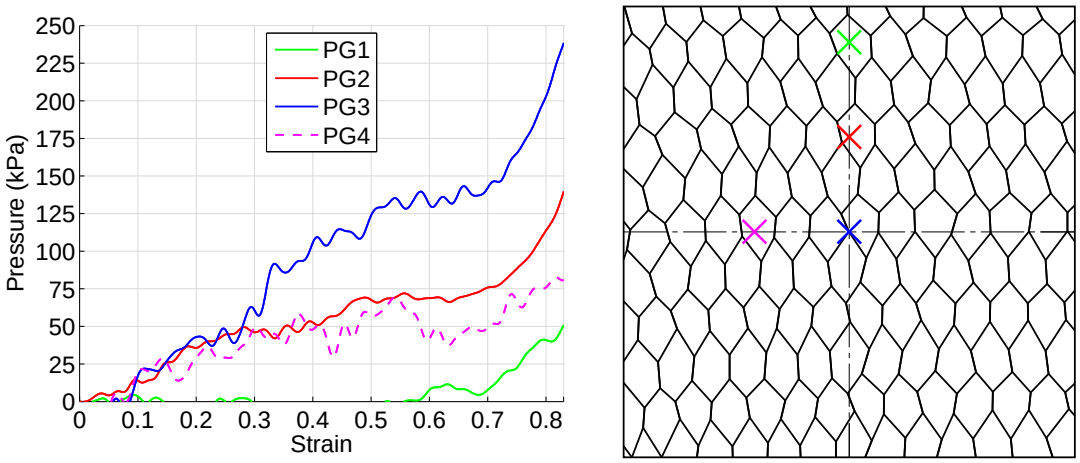

(c) Test T7, Sample D24.

Figure 3.27 Internal air pressures vs strain and the locations that they were recorded within all three tested D mesh samples.

Figure 3.28 shows the pressure distribution, for various levels of strain, through the centre of the sample D27 used in T5. At 20 % strain the pressure was equal on both the central and intermediate gauge forming a region of higher equal pressure across the central 100 mm. After 20% strain the pressure contour began to take on a parabolic shape. By 83% the central high pressure region still existed with only a 25 kPa differential pressure between the central and intermediate gauge, outside of the high pressure region there was a rapid drop off in pressure towards the sample edge. Between 20 and 60% strain the rate of total pressure increase through the sample was almost constant, after 60% strain the total pressure began to exponentially increase. The pressure recorded by the edge gauge steadily increased between 20 and 76.5% strain, but then began to rapidly increase at almost the same rate as was observed on the traces recorded by the central and intermediate gauges.

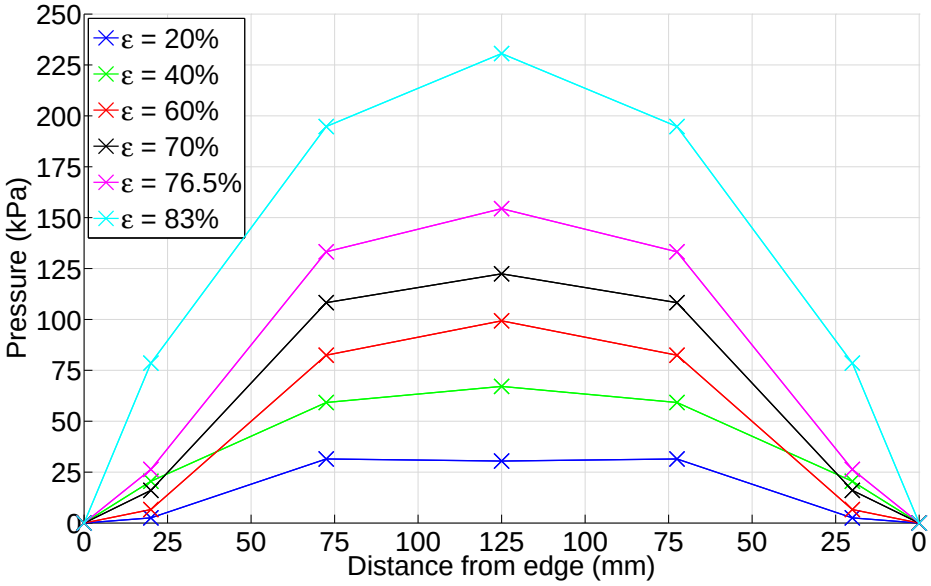

Figure 3.28 Internal pressure distribution, for varying levels of strain on a cross section through the centre of sample D27, Test T5.

Figures 3.29 (a), (b), (c) and (d) show the recorded pressures and their locations within the four tested B mesh samples during T8-11. T11 was performed at a higher strain rate of 202 s^{-1} than that used during T8-10 of 135 s^{-1}.

The pressure recorded by PG3 during T8, shown by the blue line in Figure 3.29 (a), was clipped to 610 kPa by the amplifier. The predominant shape of the traces recorded by PG2-4 was a smooth exponential rise from 0 to 83% strain. The gradient of the exponential rise was dependent on the distance from the sample centre. For T9, the edge pressure gauge also followed this trend but began decreasing at 45 % strain, this behaviour was also visible, to a lesser extent, during T8. The pressures recorded by the two intermediate gauges (PG2 and PG4) were very close for T8 and T9, but began to separate at 65% strain during T10 and 50% strain during T11. The maximum pressure, recorded by the central gauge, was very consistent and reached close to 800 kPa for T9-T11.

There was no obvious strain rate effect when comparing T11 to T8-10, the development of pressures was very similar between all four tests. It is worth remembering that the sample used during T11 also had slightly lower geometrical properties than

the samples used during T8-T10, having a lower values for Ac = 3569 mm^2 and ncell = 353, compared to the averages Ac = 3880 mm^2 and ncell = 376, which will affect the response. The pressure recorded by PG4 during T11 was the highest of the four B mesh tests, and T11 was the only test which saw a drop in the pressure recorded by PG2. The usual final exponential rise recorded by PG1 was more gradual and began earlier than the three lower strain rate tests.

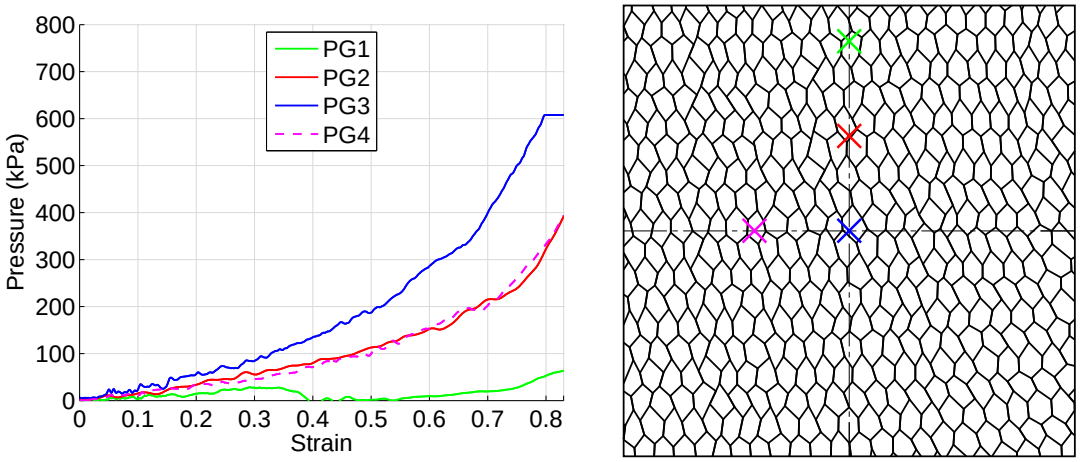

(a) Test T8, Sample B8.

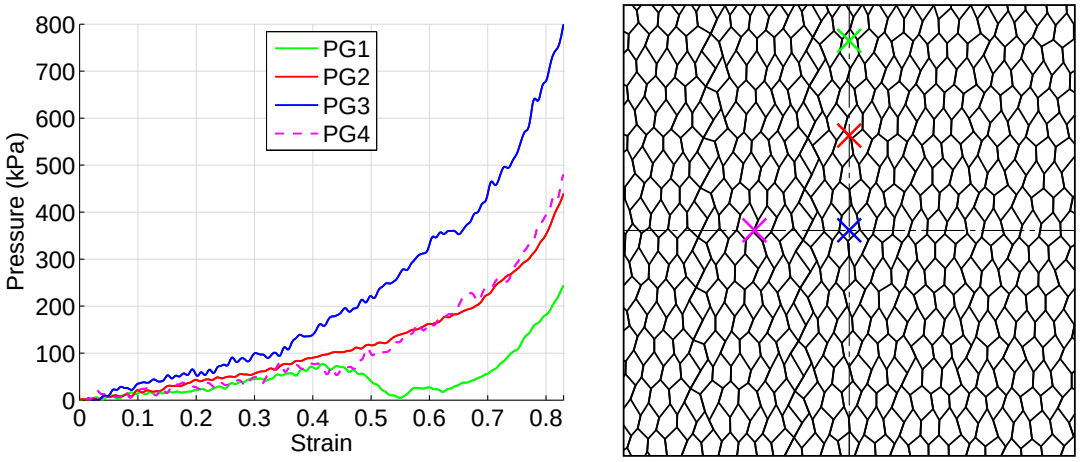

(b) Test T9, Sample B11.

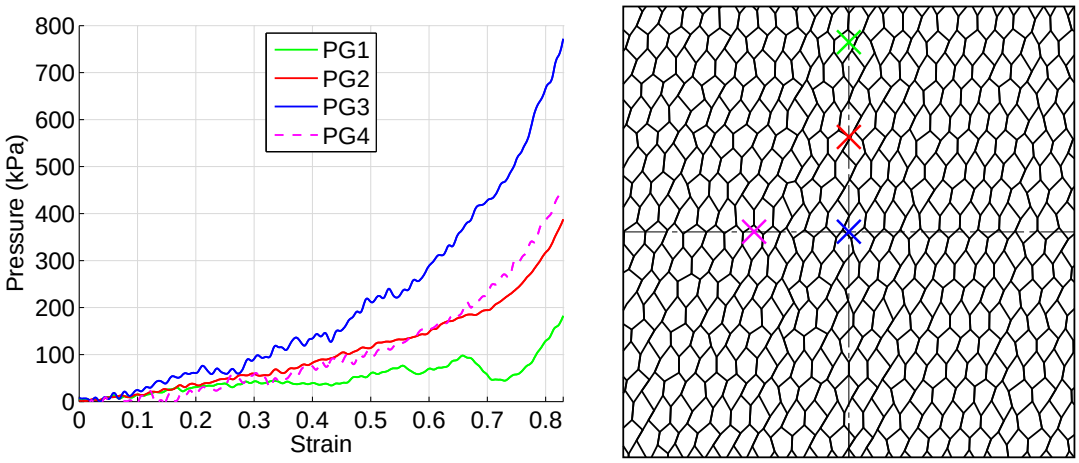

(c) Test T10, Sample B10.

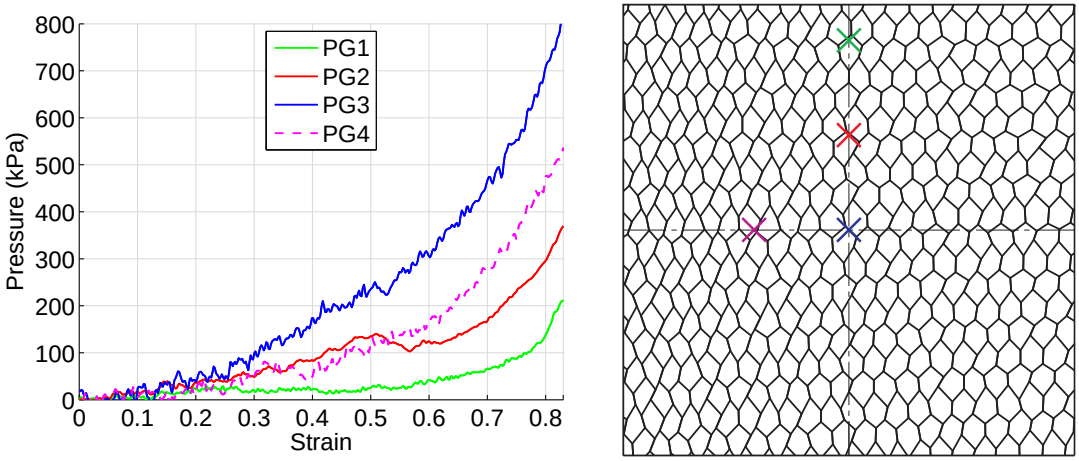

(d) Test T11, Sample B14.

Figure 3.29 Internal air pressures vs strain and the locations that they were recorded within all four tested B mesh samples. T11 was performed at the higher strain rate of $\dot{\varepsilon}_{avg} = 202$ in comparison to $\dot{\varepsilon}_{avg} = 135$ for T8-10.

Figure 3.30 shows contours of internal pressure, for varying values of strain, through the centre of sample B11. Like the other two mesh types, the rate of increase in pressure is dependent on the distance from the edge, being highest in the middle of the sample. The pressure profile develops in a similar manner to that observed within the F mesh, rather than the parabolic distribution present in the D mesh samples. The pressure distribution is almost triangular at 20% strain with a singular gradient from the centre to edge pressure gauge, with increasing strain

the pressure gradient between the central and intermediate gauge steepens quicker than the gradient between the intermediate and edge gauge, resulting in a peaked shape by 83% strain. Comparing the gaps between the contours, the total pressure can be seen to be rising constantly at an exponential rate.

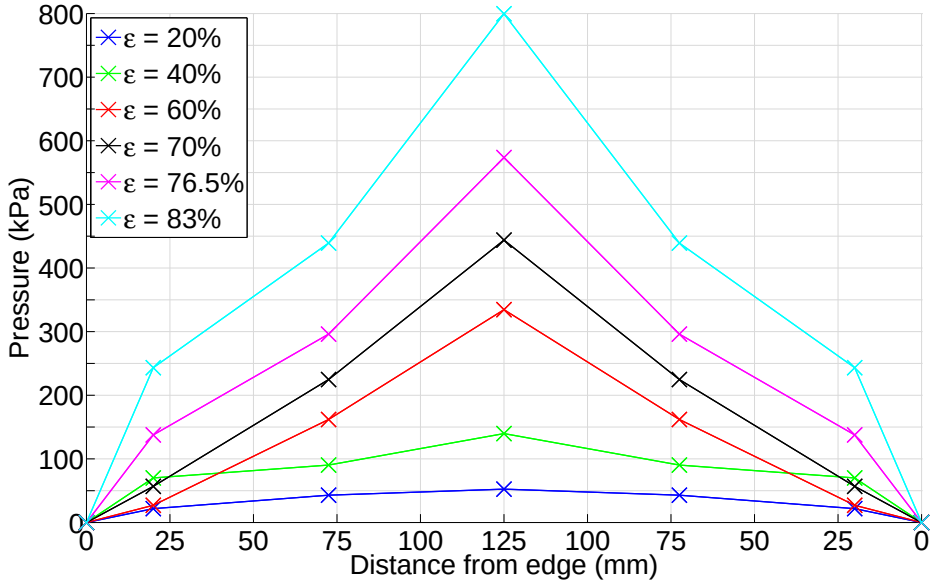

Figure 3.30 Internal pressure distribution, for varying levels of strain on a cross section through the centre of sample B11, Test T9.

To estimate the total load transmitted by the internal pressures, it was necessary to identify a reasonable 2D pressure distribution across the base of each sample. It was assumed that the pressure would be equal within each individual cell, meaning that the pressure would be applied over discrete areas rather than a smooth linear distribution. The complex cellular geometry was idealised by discretising the 250 mm long cross section into a series of bars. Note that the true honeycomb geometries are anisotropic in the x and y direction and therefore not symmetrical. For the purpose of this approximate projection, for each mesh type, a number of bars was chosen to represent a characteristic value for the number of complete cells which would form a complete path through the y axis.

The previously extracted linear pressure profiles were then used to identify the pressure at locations corresponding to the centre of each discretising bar. Figures

3.31 (a),(b) and (c) show the estimated distribution of pressure on a cross section through the centre of an F, D and B mesh sample at 83% strain.

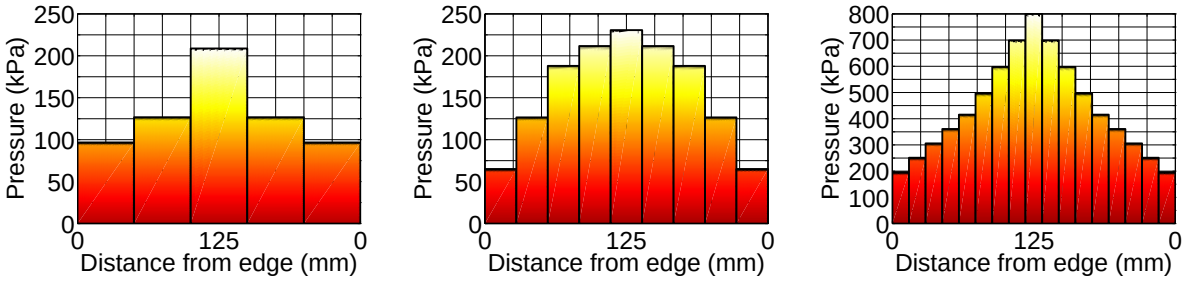

(a) Test T2, Sample F22. (b) Test T5, Sample D27. (c) Test T9, Sample B11.

Figure 3.31 Discretization of pressures at 83 percent strain for a sample from each mesh type.

Similarity in the magnitude of recorded air pressures by gauges 2 and 4 suggested that the internal air pressure profile took on a degree of symmetry about both the x and y axis, with the magnitude of pressure being proportional to the distance from both sample edges. To obtain an estimation of the total load transmitted by the internal air pressures, the pressure profile derived from pressure gauges 1, 2, and 3 was projected in two dimensions through the sample, forming a four sided pyramid-like pressure distribution with its peak located at the sample centre. It was then possible to calculate the total load by multiplying each individual pressure by the area it acted upon.

Figures 3.32 (a), (b) and (c) show the estimated total stress transmitted by the internal air pressures σ_{Air}, for tests performed with the F, D and B mesh samples. Several features were common to the development of σ_{Air} within samples of the same mesh type. The development within the F mesh samples can be characterised by two regions, a plateau of 10 kPa and an exponential increase beginning between 50 and 60 % strain. For the D mesh samples there were three features, a steady rise to a plateau of about 40 kPa at 40% strain, a short plateau and finally an exponential rise beginning at 60% strain, there was no plateau during T7. For the B mesh samples there were also three visible features: a steady rise to about 75 kPa at 50%

strain, a dip in pressure and finally the exponential rise beginning at 60% strain.

An estimated σ_{Air} vs strain relationship, shown in Figure 3.32 (d), was calculated for the F, D and B meshes by averaging the values of σ_{Air} for a given strain for all individual tests of each mesh type. The value of σ_{Air} was dependent on the mesh density, with the most load being carried by air pressures in the B mesh samples. The air pressures carried the least load in the F mesh samples and the D mesh was between the two. At 80% strain the value of σ_{Air} for the F mesh increased to match that for the D mesh; this is due to the final rapid rise in pressure recorded by the edge pressure gauge which was characteristic of the F mesh samples.

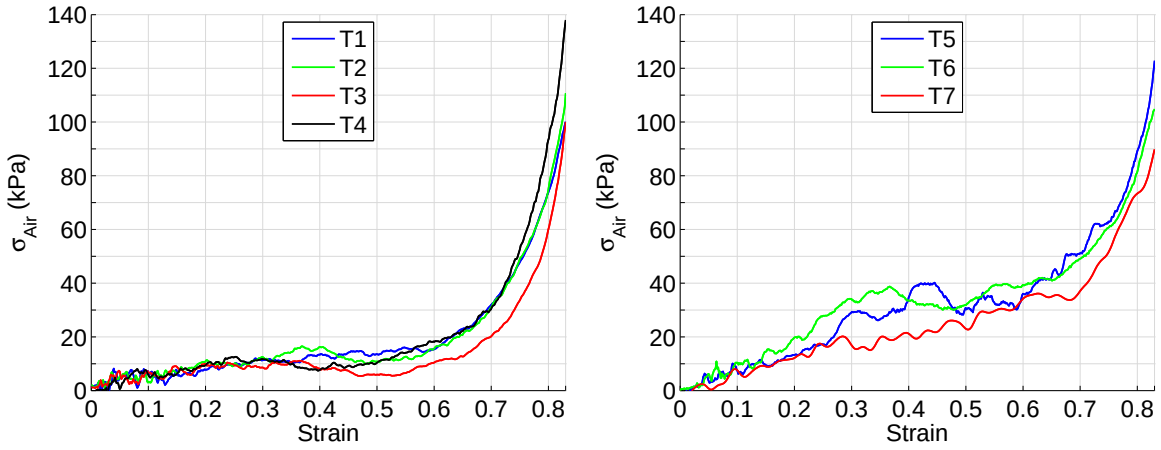

(a) F mesh

(b) D mesh

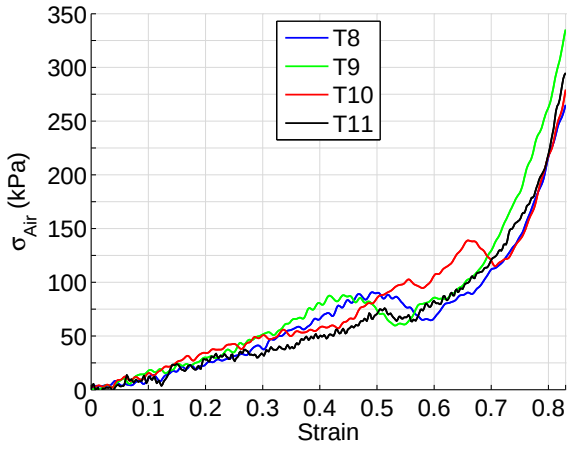

(c) B mesh

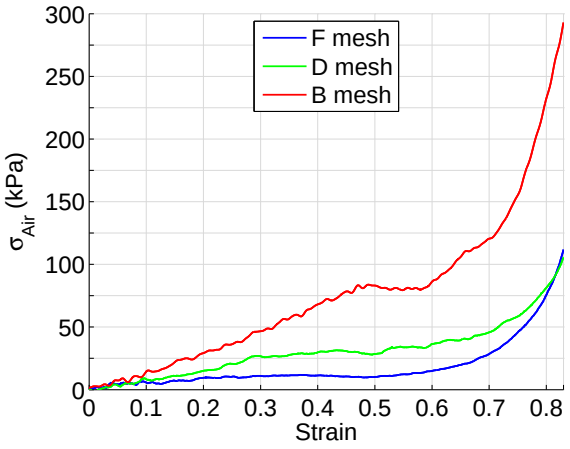

(d) F, D and B mesh type avg

Figure 3.32 Estimated total stress transmitted by the internal air pressures σ_{Air} vs strain for all individual tests, F mesh (a), D mesh (b), B mesh (c) and mesh type averages (d).

Figures 3.33 (a), (b) and (c) show the total stress recorded by the load cell σ_{Total} and the estimated stress transmitted by the internal air pressures σ_{Air} for a sample from the each of the three mesh types. At any value of strain, the difference between σ_{Total} and σ_{Air} (taking into account the spurious oscillations) must be the total stress being transmitted by the cardboard structure. The internal air pressures act as a significant load carrying mechanism for all three mesh types. The early response

is controlled by the cardboard structure, but as the sample is compacted and the internal pressures develop, the proportion of the total load being carried by the air pressures significantly increases.

While σ_{Air} increased as the cell size was reduced, its proportion of σ_{Total} reduced. Looking at the response of sample F22 shown in Figure 3.33 (a), at 40% strain almost all of the stress is being carried by σ_{Air}, in comparison to the response of sample B11 shown in Figure 3.33 (c), where at 40% strain σ_{Air} is just less than half of the σ_{Total}. For all samples, the stiffening limb shown by the sharp increase beginning at 70% strain on the σ_{Total} curves appears to be solely controlled by the exponential rise in the internal air pressures.

It was observed that the magnitude of internal pressure increases with distance from the sample edge. It was also observed that within each sample there was a development of an area of high pressure surrounded by a rapid drop off towards the sample edge. If the plan area was increased, it follows that the magnitude of internal pressure would increase, and the area of high pressure would expand, resulting in an increased value of σ_{Air} and an increased proportion of σ_{Total} being carried by air.

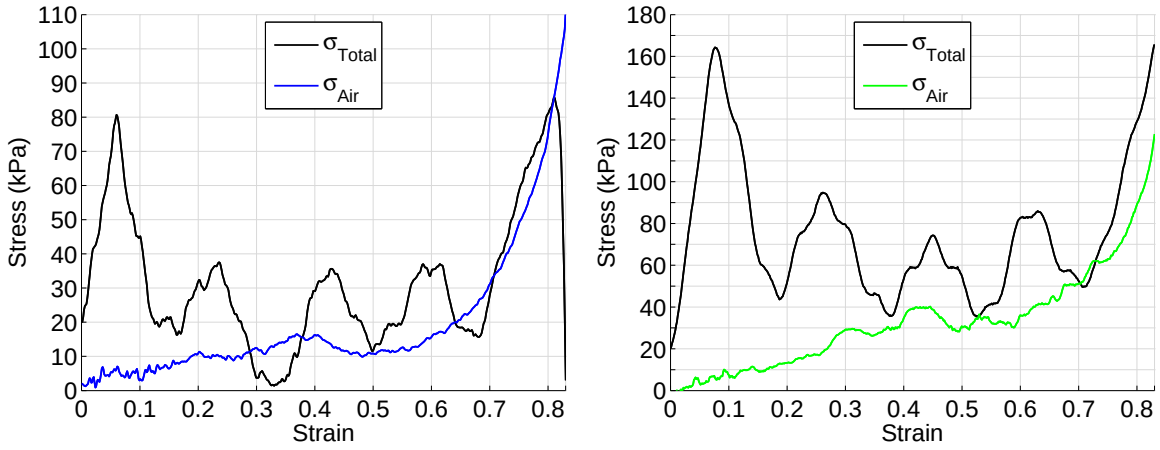

(a) Sampe F22, Test T2

(b) Sample D27, Test T5

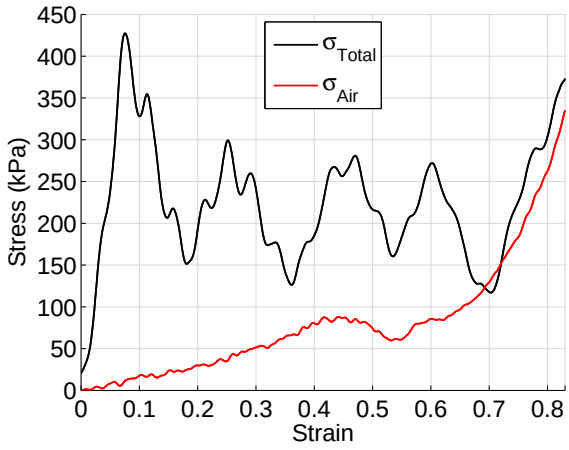

(c) Sample B11, Test T9

Figure 3.33 Total recorded transmitted stress σ_{Total} and proportion transmitted by the internal air pressures σ_{Air} vs strain, for a sample from each mesh type.

3.3.9 Analysis of experimental data

The value of A_c is a function of all mesoscale parameters and is therefore a useful value to quantify the geometry of each sample. Figures 3.34 (a) and (b) show σ_{Peak} and $\sigma_{Plateau}$ plotted against A_c. Blue crosses indicate experimental values, through which it was possible to fit two second order polynomials shown by the solid blue lines. Both lines must pass through the origin because when A_c is equal to zero, no stress will be transmitted. Equations 3.4 and 3.5 relate σ_{Peak} (Pa) and σ_{Plat} (Pa)

to A_c (mm^2).

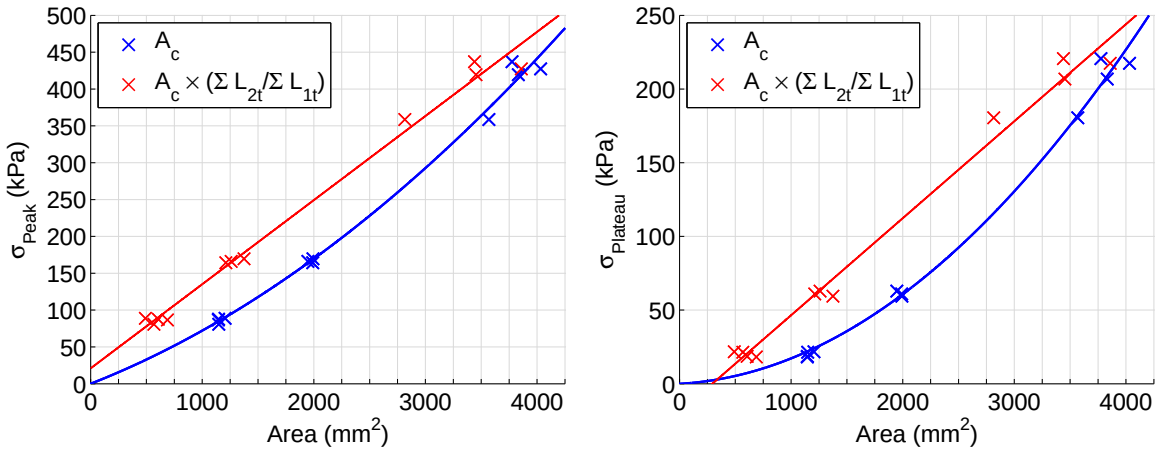

(a) (b)

Figure 3.34 Peak σ_{Peak} (a) and plateau $\sigma_{Plateau}$ (b) transmitted stresses for all samples vs A_c (blue) and A_c after application of the double to single cell wall quotient $\Sigma L_{2t}/\Sigma L_{1t}$. Recorded data is indicated with $\times$.

$$\sigma_{Peak} = 0.0128A_c^2 + 59.33A_c \tag{3.4}$$

$$\sigma_{Plateau} = 0.0132A_c^2 + 4.05A_c \tag{3.5}$$

During the geometrical analysis it was observed that the proportion of double to single cell wall, expressed by the quotient $\Sigma L_{2t}/\Sigma L_{1t}$, increases as the cell size reduces. When the quotient was applied to the A_c of each recorded data point, as shown by the red crosses, it was possible to fit a straight line through the experimental data, suggesting that the second order relationship between stress σ_{Peak}, $\sigma_{Plateau}$ and A_c may be due to the changing proportion of double to single cell wall. This agrees with the literature, as the static transmitted peak and plateau stresses are known to be dependent upon the yield stress of the cell wall material [29, 51]; and the bonded double cell wall has been reported to have a greater yield stress due to the presence of the glue [51]. The red lines are used to simply illustrate a trend in

the data set, their actual positioning holds little meaning as the material properties of the single and double cell walls are unknown.

Each cluster of blue data points represents a mesh type, the cluster at 1200 mm^2 being the F mesh, 2000 mm^2 the D mesh and 3900 mm^2 the B mesh samples. The spread between points in each cluster indicates the effect of the geometrical variations generated during sample construction. The F and D mesh samples are very tightly clustered, while the B mesh samples are more spread out, meaning that the inter-sample variations have little effect on the response for the F and D mesh, but and have a more pronounced effect the finer B mesh. This is most likely due to the added difficulty encountered during construction of the B mesh samples, when having to apply a very large force to expand the core, it was difficult to unify the magnitude of expansion across the core. Also, since the B mesh core was more dense than the D and F cores, a given percentage of variation will result in a larger actual variation of A_c.

Figure 3.35 (a) shows both σ_{Peak} (blue) and $\sigma_{Plateau}$ (red) plotted against the average cell wall length $\bar{L}$ of each sample, Figure 3.35 (b) also shows σ_{Peak} and $\sigma_{Plateau}$, but plotted against the number of complete cells, ncell. A negative correlation is visible between the average wall length and the transmitted stresses. However, the correlation is a much weaker than the correlations observed between the cross sectional area of cardboard and transmitted stress.

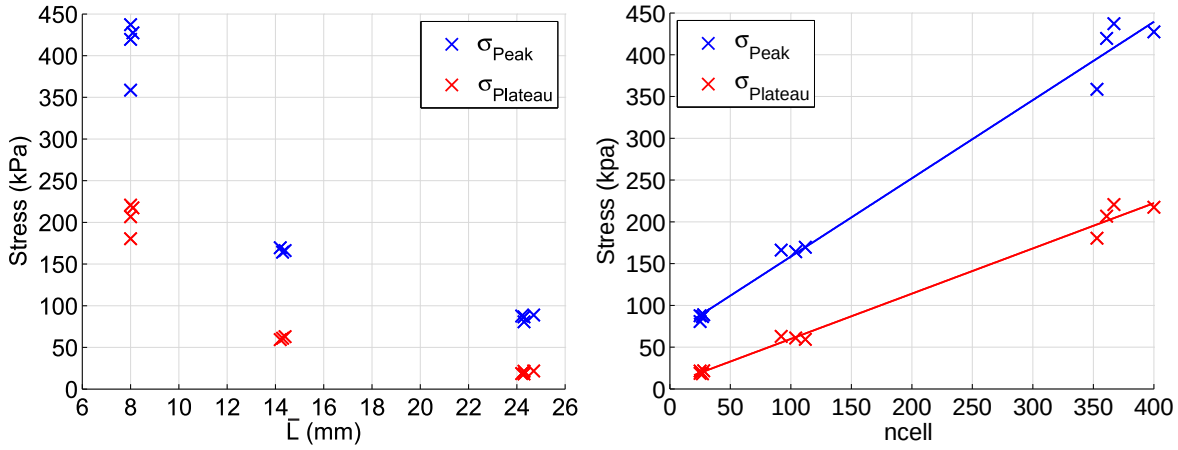

(a) (b)

Figure 3.35 Peak σ_{Peak} (blue) and plateau $\sigma_{Plateau}$ (red) transmitted stresses for all samples vs the average cell wall length $\bar{L}$ (a) and number of complete cells ncell (b). Recorded data is indicated with $\times$.

Like A_c, the value for ncell is a function of the other geometrical parameters. Also like A_c, there is a strong positive correlation between ncell and the transmitted stresses. Equations 3.6 and 3.6, valid over the region $25 <$ ncell < 400, relate ncell to σ_{Peak} and $\sigma_{Plateau}$.

$$\sigma_{Peak} = 937ncell + 6.477 \times 10^4 \tag{3.6}$$

$$\sigma_{Plateau} = 542ncell + 5.711 \times 10^3 \tag{3.7}$$

If a volume of air, of equal volume to the tested samples (250x250x70 mm^3), was confined at its perimeter by a rigid boundary and axially compressed at the rates used in this series of tests, the column of air would effectively be undergoing adiabatic 1D compression. The resulting increase in pressure and therefore stress transmitted by that volume of air $\sigma_{Air,1D}$, for a given value of strain ε, is given by equation 3.8, where atmospheric pressure $P_{Atmospheric} = 101.325kPa$ and the ratio of specific heat capacities for air $c_p/c_v = 1.4$.

$$\sigma_{Air,1D}(\varepsilon) = \frac{P_{Atmospheric}}{(1-\varepsilon)^{c_p/c_v}} - P_{Atmospheric} \tag{3.8}$$

This equation is displayed graphically by the dashed black line in Figure 3.36 (a), on the same graph the estimated σ_{Air} for each of the three tested mesh types is also shown. At 83% strain, $\sigma_{Air,1D}$ reaches a value of 1109 kPa. The exponential shape of the $\sigma_{Air,1D}$ curve is echoed in the traces of σ_{Air}, with a reduction of gradient as the cell size is increased. During the impact event, the top and bottom face of the sample are held flat against the front and back plate and the displacement of the top face is controlled, meaning that any deficit between σ_{Air} and $\sigma_{Air,1D}$ must either be due an increase in internal volume by expansion of the plan area or a loss of gas from within the initial volume. Observations of sudden dips in pressure, made in Section 3.3.8, specifically on the edge pressure gauge and changes in gradient on all gauges combined with the fact that inspection of the crushed samples showed an expansion in the x direction, suggest that the deficit is actually caused by both.

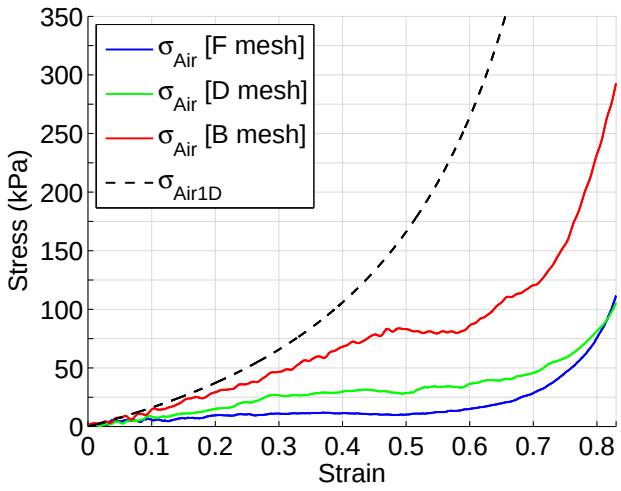

Figure 3.36 Stress which would be transmitted by the internal air pressures if the honeycomb sample provided 100% lateral confinement $\sigma_{Air,1D}$ and average stress transmitted by the internal air pressures for the three tested mesh types σ_{Air} vs strain.

If the air within the cardboard honeycomb samples was perfectly confined during

the crushing event, and the volumetric compressive strain it experienced was solely due to an axial 1 dimensional axial compression of magnitude ε, σ_{Air} would be equal to $\sigma_{Air,1D}$. In reality σ_{Air} is less than $\sigma_{Air,1D}$ and so the quotient between the actual and maximum possible air pressures can be defined as the honeycombs confinement quotient ϕ_{Conf}, where

$$\phi_{Conf} = \frac{\sigma_{Air}(\varepsilon)}{\sigma_{Air,1D}(\varepsilon)} \tag{3.9}$$

which when combined with Equation 3.8 gives

$$\sigma_{Air}(\varepsilon) = \left[\frac{P_{Atmospheric}}{(1-\varepsilon)^{c_p/c_v}} - P_{Atmospheric}\right] \times \phi_{Conf}. \tag{3.10}$$

Figures 3.37 (a), (b) and (c) show the recorded σ_{Air} curves with coloured solid lines and the calculated σ_{Air} (from Equation 3.10) using dashed black lines for the three mesh types B, D and F respectively. It was found that by using a maximum and minimum value of ϕ_{Conf} for the B and D meshes, two forms of Equation 3.10 could be generated which were good fits to the early (B mesh: $\varepsilon < 40\%$ and D mesh: $\varepsilon < 30\%$) and late (B mesh: $\varepsilon > 70\%$ and D mesh: $\varepsilon > 75\%$) regions of the mesh average σ_{Air} curves. Within this envelope, lies a transition period where ϕ_{Conf} reduces with increased strain, i.e. the confinement of the honeycomb reduces, either from loss of the pressurised air or from outwards lateral expansion of the honeycomb structure.

Figure 3.37 (c) shows that it was not possible to accurately fit the same model to the σ_{Air} F mesh type average. The early section is very short and the gradient of the curve in the late section, after 70% strain is much steeper than the transformed $\sigma_{Air,1D}$ curve. In Section 3.3.8 it was observed that the steep increase is due to the contribution from the late development of high pressures at the sample edge.

The maximum values of ϕ_{Conf} represent the initial confinement provided by the honeycomb structure, the values for the B and D meshes were 0.667 and 0.417 respectively, meaning that the B mesh structure provided about 50% more confinement than the D mesh structure. Over the transition zone between the two dashed black lines, the degree of confinement changes due to lateral expansion and venting

of the internal gas. The transition zone was shorter for the finer B mesh than the D mesh. This may be due to the finer mesh, with more cardboard cell wall material, providing less opportunity for air to escape and internal air pressures to adjust the structure, before the lateral permeability reduces and lateral stiffness increases (due to folded cell walls), trapping the air, and entering the final stage. During the final stage ϕ_{Conf} reduced to 0.264 and 0.094 for the B and D mesh respectively which is a 60% reduction in ϕ_{Conf} for the B mesh and a 77% reduction for the D mesh.

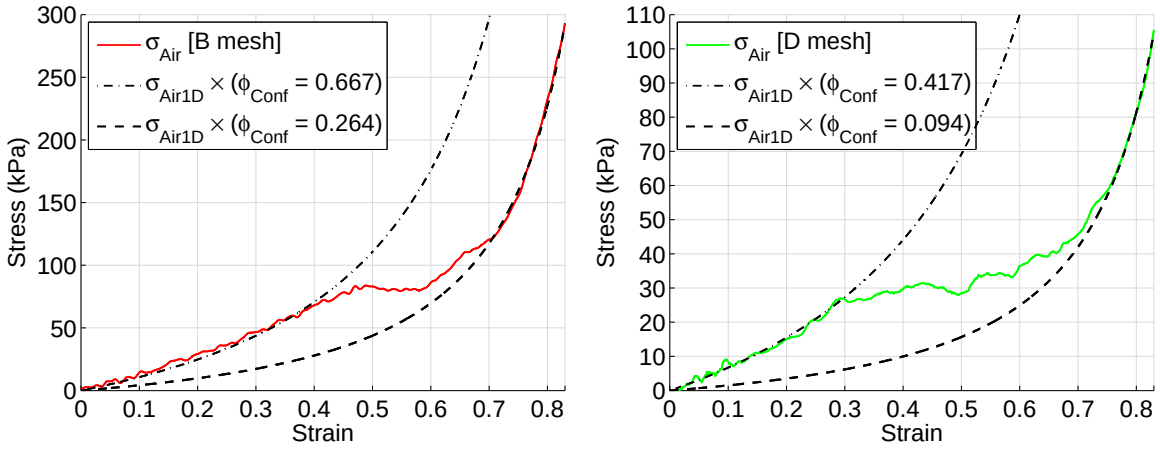

(a) B

(b) D

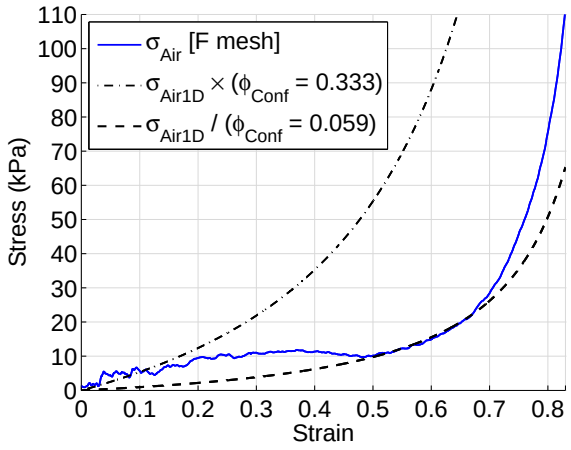

(c) F

Figure 3.37 Solid coloured lines show the experimental σ_{Air} vs strain for the B (a), D (b) and F (c) meshes and the black dashed lines show analytical representations created by applying different values of the confinement quotient ϕ_{Conf} to Equation 3.10.

3.3.10 Conclusions from Phase 3

Impact tests on samples of various geometries, has shown the cardboard honeycomb dynamic response to be sensitive to variations in the geometrical arrangement of the cell walls. A geometrical analysis of the tested cardboard honeycomb samples revealed that, even when extreme care was taken during sample preparation to

produce repeatable samples, variations and manufacturing imperfections were still present in the cellular geometry. The geometry of individual cells, within each sample, was observed to vary widely, but when an average cell geometry was taken, the geometrical variation between two samples of the same mesh type was small.

Any inter-sample variation appeared to be controlled mostly by the expansion angle, i.e. the amount of force used to expand the flat pack core during sample construction. One observed trend, was that as the cell size (mesh type) was reduced from F to B, the proportion of double-ply to single-ply cell wall material increased; this has potential significance on the cardboard honeycombs impact response because the increase in proportion of double to single cell wall also means that there is an increase in the volume of glue (i.e. non-cardboard material) within the cardboard honeycomb sample.

The overlying oscillations, which have been confirmed as spurious, were still present on the load cell traces and while they disguised the exact shape of the EDM stress strain response, it was still possible to extract single values for the peak and plateau transmitted stresses for each sample.

It was shown that an increase in the cross sectional area of cardboard material, number of complete cells, and a reduction in the average cell wall length, caused an increase in both the peak and plateau transmitted stresses; empirical formulae were presented. It was also observed that the proportion of double to single cell wall material affected the peak and plateau stresses.

In agreement with the observations made by Ripperger and Briggs [8], the internal air pressures do indeed act as a significant load carrying mechanism during the cardboard honeycombs dynamic response. The internal air pressures increase with strain, the early response is dominated by the structure, whereas the late response is composed of both load transmitted through the structure and the internal air pressures.

Simultaneous measurement of the internal air pressures, at three locations on one plane, allowed the pressure profile, and its evolution with strain, to be observed (Figures 3.26, 3.28 and 3.30). The magnitude of the air pressure at a point within

the honeycomb was dependent on the distance from the sample edge, with the highest pressures occurring in the centre. The rate of pressure increase was also dependent on the distance from the sample edge, with pressures increasing more rapidly towards the sample centre. Within the D and B mesh samples, at low degrees of axial compaction (below 20%) a central plateau of equal pressure was observed. As axial strain increased, this plateau reduced and the edge-centre pressure gradient increased in steepness.

As the cell size was reduced, the magnitude of internal pressures increased. The maximum recorded pressure at the centre of each F mesh sample was around 180 kPa, whereas the maximum recorded pressure at the centre of the B mesh samples was in the region of 800 kPa. Furthermore, the *total* stress transmitted by the air pressures increased as the cell size was reduced (Figure 3.32 (d)); However, the significance of the internal air pressures (in comparison to the structural response) reduced with reduced cell size (Figure 3.33).

It was discovered that the total stress transmitted by air pressures within a sample of cardboard honeycomb can be expressed by applying a reduction coefficient to the equation of state, which would describe a rapid 1-D compaction of a perfectly restrained sealed volume of air, where the coefficient represents the total lateral confinement provided by the cellular structure at a given strain and reduces as the cross sectional area expands outwards and/or pressurised air escapes via blowout.

It was decided that measuring the high strain rate compressive response of the cardboard would be an extremely challenging task and therefore outside of the scope of this thesis. The practicalities themselves posed problems, such as forming solid samples of the cell wall material, which could actually be tested, would change the nature of the cardboard and, in doing, so reduce the scientific validity of any results. Equipment was not available to perform high strain rate tensile testing of the cell wall material and it was not possible to source samples identical to the single and bonded cell walls for testing.

Valuable insight has been gained into the mesoscopic mechanics of the dynamic cardboard honeycomb response. It has been shown that the spatial and temporal

development of internal air pressures is dependent on the geometrical arrangement of the honeycomb cell walls. Higher pressures have been observed to occur towards the honeycomb centre and within samples with a smaller cell size; however, coupled geometrical parameters such as cell size, wall length, number of cells, and area of cardboard mean that further research must be performed to isolate the role of each parameter in determining the magnitude of the response.

Chapter 4

Development, verification and validation of a numerical model

To further investigate the high strain rate impact response of the cardboard honeycomb, without the economical and physical limitations imposed by experimental methods, a numerical model was constructed. The measurements made during Chapter 3, were limited by the cost and availability of instrumentation, for instance pressure measurement was limited to four discrete points. Additionally, tests could only be performed on samples of cardboard honeycomb which could be sourced, limiting the scope of possible material and geometrical parameters.

By constructing a numerical model, it was possible to view the full spatial and temporal evolution of the internal air pressure and structural load carrying mechanisms, for any given set of material and geometrical parameters, thus yielding a much more complete view of the cardboard honeycomb high strain rate impact response. This chapter details the main tasks which were performed to develop the modelling capability necessary to capture the axial impact response of a gas-filled honeycomb structure akin to the cardboard honeycomb.

The numerical modelling platform of choice was LS-Dyna, a commercial, explicit, finite element package, which specialises in high strain rate non-linear structural dynamics; crucially, LS-Dyna also provided the ability to model the rapid compression and transport of gasses, and their interaction with the cellular structure.

While the computational technology was readily available, its use requires a high level of expertise; before each individual modelling technique could be employed it was essential to ensure that it was verified. In addition, numerical stability and computational cost were both factors which were incredibly onerous; all utilised modelling techniques were not only required to be individually accurate, but also to be compatible with each other. When combined to produce a full scale model, these techniques needed to be computationally efficient enough to allow the numerical analyses to be completed within an acceptable time frame.

As complexity was increased through the gradual inclusion of additional numerical components, existing literature was used to provide analytical verification. Sections 4.1 and 4.2 detail the independent development of the structural (Lagrangian) and gas (Eulerian) components. In Section 4.3 fluid structure interaction was investigated to allow the transfer of forces between the Lagrangian and Eulerian components. Finally, in Section 4.4, the individually verified components were combined to produce a full scale, fully coupled model of the cardboard honeycomb and confined air. Two impact events, from Chapter 3, were replicated, and validation was achieved by comparison between the resulting numerical responses and experimental data.

4.1 Development of the Lagrangian numerical modelling techniques required to capture the structural response

This section details the development and analytical verification of a numerical model capable of capturing the axial buckling behaviour of the honeycomb cell walls. Consideration is given to the mechanisms which contribute to both the peak and plateau regions of the macroscopic EDM response.

Timoshenko and Gere [56] calculated the Euler critical buckling load P_{Crit} for a rectangular plate subject to an even uni-axial compressive load along two opposite

simple supported edges, with the other two **free**, as

$$P_{Crit} = \frac{\pi^2 D}{L^2}\left(\frac{L}{H} + \frac{H}{L}\right)^2 \tag{4.1}$$

where L is width of loaded edge and H the height of the plate. D is the flexural rigidity of the plate (its stiffness in bending), which is a product of its thickness t and the Elastic modulus E and Poisson's ratio ν of the plate material

$$D = \frac{Et^3}{12(1-\nu^2)}. \tag{4.2}$$

Young and Budynas [57] presented Equation 4.3, an adaptation of Equation 4.1, which describes the critical buckling stress of a plate subject to an even uniaxial compressive load along two opposite simply supported edges, with the other two **clamped**,

$$\sigma_{Crit} = \frac{5KE}{(1-\nu^2)}\left(\frac{t}{L}\right)^2 \tag{4.3}$$

where the factor K is dependent on the fixity of the plate edges and, for this case, is equal to 5.73 when $\frac{H}{L} \geq 2.1$ [57].

By assuming each individual cell wall within the honeycomb is a simply supported top and bottom, and laterally restrained by the adjacent cell walls, and the displacement of the top of all cell walls is equal (they all reach the buckling load at the same time), Zhang and Ashby [29] used Equation 4.3 to develop Equation 4.4, which states the maximum peak stress which will be transmitted by a honeycomb before the cell walls collapse due to Euler buckling.

$$\sigma_{PeakEul} = \frac{5KE}{(1-\nu^2)\cos\alpha(1+\sin\alpha)}\left(\frac{t}{L}\right)^3 \tag{4.4}$$

where $\sigma_{PeakEul}$ is the critical buckling stress, i.e. the maximum load transmitted through the cell walls, prior to buckling, divided by their total contributory area (as shown in Figure 4.1.) and $\alpha = 90 - \theta$ where θ is the expansion angle discussed in Chapter 3 and for a regular hexagon $\alpha = 30°$. Equation 4.4 has been used by

E and Wang [43, 44] to express the peak stress, σ_{Peak}, transmitted by cardboard honeycombs.

In the paper by Zhang and Ashby [29] it was also discussed that the critical buckling load may be controlled by crushing of the cell wall material, and in that case

$$\sigma_{PeakCru} = \sigma_{Yield} \frac{2}{\cos\alpha(1+\sin\alpha)} \left(\frac{t}{L}\right) \tag{4.5}$$

gives a second expression for the peak stress $\sigma_{PeakCru}$ where σ_{Yield} is the yield stress of the honeycomb cell wall material.

Post buckling, the honeycomb cell walls enter a progressive plastic alternate folding phase, which causes the drawn out plateau region of the macroscopic stress strain curve. McFarland [28] assumed that the progressive alternate folding mechanism propagated via in-plane shear of the cell walls. By considering the mechanics of the in-plane shear mechanism McFarland made an initial prediction of the plateau stress, transmitted by a honeycomb, during axial progressive buckling.

Later, work by Wierzbicki [22] superseded McFarland's model by showing that the main energy dissipation mechanism was not provided by in-plane shear, but by rolling of the cell walls over a travelling hinge with a toroidal geometry. The predictions made by Wierzbicki were found to give good correlation with both the transmitted plateau stresses and deformed shapes observed during experimental crushing tests on metallic honeycombs; published by McFarland [28] and Magee and Thornton [58]. The analytical model presented by Wierzbicki predicted that the average wavelength λ of each fold would be

$$\lambda = 1.642\sqrt[3]{tL^2} \tag{4.6}$$

and the total number of folds at full compaction n_f is given by $n_f = {}^{H}/_{\lambda}$.

Additionally, the force transmitted to the base of the cell walls P_{Plat} during each fold was given as

$$P_{Plat} = 8.61\sigma_0 t^{5/3} H^{1/3} \tag{4.7}$$

where σ_0 is the stress required to maintain plastic deformation (i.e. the flow stress of the material). For elastic, perfectly plastic materials $\sigma_0 = \sigma_{Yield}$.

E and Wang [51] modified the folding mechanism adopted by Wierzbicki to allow its application to cardboard honeycombs, by incorporating the observed yield strength differential between single and double-ply cell wall material (parameter k), and allowing length variations of the horizontal hinge lines to account for the destruction of the glue bond. The result was Equation 4.8 which gives the transmitted macroscopic plateau stress σ_{PlatAn} as a function of the single-ply cell wall yield stress $\sigma_{Y,t1}$, a quotient of the double to single-ply cell wall yield stress $k = {}^{\sigma_{Y,t2}}/_{\sigma_{Y,t1}}$ and the thickness to length ratio of the cell walls (t/L), during a *quasi-static* axial crushing event

$$\sigma_{PlatAn} = \sigma_{Y,t1} D_1(k) \left(\frac{t}{L}\right)^{\frac{5}{3}} + \sigma_{Y,t1} D_2(k) \left(\frac{t}{L}\right)^{2} \tag{4.8}$$

where constants D_1 and D_2 are calculated using

$$D_1(k) = 1.427(2k+1)^{\frac{2}{3}}(4k+1)^{\frac{1}{3}}, \qquad D_2(k) = 0.3849(2k-1). \tag{4.9}$$

For the honeycomb samples tested by E and Wang [51], the value of k was found to be dependent on the relative humidity (RH) and varied from 1.572 at 30% RH to 1.301 at 95% RH with the average value being $k = 1.41$.

4.1.1 A corner element model

A regular hexagonal honeycomb mesh can be divided into a series of equal sized segments. Each segment, as shown in Figure 4.1, is centred on a vertex and is defined by a triangular boundary, which bisects the three adjoining cell walls and connects the centres of the three surrounding cells.

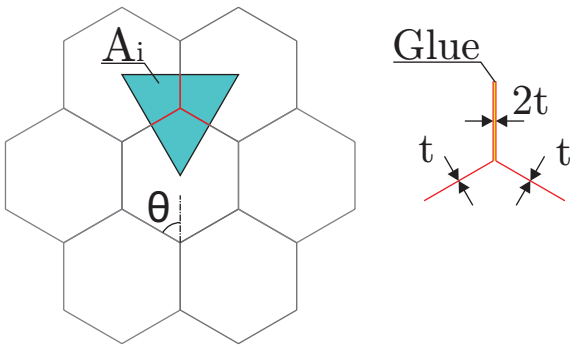

Figure 4.1 An illustration of how a regular hexagonal honeycomb structure ($\theta = 60°$), can be discretised into a series of identical corner elements, each with a tributary area A_i.

The three half length cell walls within each segment are comprised of two sheets, folded at the vertex and bonded along the length of a shared cell wall. This segment of the cellular structure can be treated as a self contained individual corner element that is laterally supported by its neighbouring corner elements. For impact problems where the internal air pressures are not significant, such as is the case, when considering the early region of the response, all of the load transmitted within the contributory area A_i is transmitted through the cell wall material. At a given strain the magnitude of load being transmitted through the corner element $P_i(\varepsilon)$ is dependent on its current axial stiffness; how the axial stiffness changes with strain is a function of its axial crushing response. The total stress being transmitted by each segment of the honeycomb is the load $P_i(\varepsilon)$ being carried by the corner element cell walls divided by its contributory area A_i and so the total macroscopic stress being transmitted by the full honeycomb for a given strain $\sigma_{Total}(\varepsilon)$ is

$$\sigma_{Total}(\varepsilon) = \sum_{i=1}^{n} \frac{P_i(\varepsilon)}{A_i}. \tag{4.10}$$

where n is the total number of corner elements. Given angle θ and the lengths of the single L_{1t} and double cell walls L_{2t}, A_i can be calculated with

$$A_i = L_{1t} L_{2t} \sin\theta + L_{1t}^2 \sin\theta \cos\theta \tag{4.11}$$

or with equation 4.12 when $L_{1t} = L_{2t}$

$$A_i = L^2 \left(\sin\theta + \sin\theta\cos\theta\right). \tag{4.12}$$

The first step to numerically capture the physics involved during compaction of a whole honeycomb structure was to accurately model the axial buckling response of a single corner element. A component schematic of a corner element numerical model is presented in Figure 4.2. A total of four separate parts, identified by their part identification numbers PIDs, were necessary to model the two connected sheets, two parts representing the single-ply cell walls (`PID 1` and `PID 2`) and two parts representing the bonded cell walls (`PID 801802` and `PID 802801`). The notation used to label each bonded cell wall refers, firstly, to the sheet it belongs to `80`**`(1)`**`802` and secondly the sheet it is bonded to `80180`**`(2)`**.

With the aim of removing any unnecessary initial complication, model parameters expressing the physical problem in its simplest form were chosen. Figure 4.2 (a) shows three equal length cell walls, separated by three equal angles of 120°, representing a segment from a regular hexagonal mesh. In Chapter 3 cell wall lengths were observed to vary between 7.1 and 32.7 mm, for this test a length of $L = 10$ mm was chosen for the three cell walls. A macroscale height of $H = 70$ mm was used, which was consistent with the tested samples.

As was shown in Figure 4.1, the corner element is just one segment of a continuous cellular structure. To realise this numerically, symmetrical boundary conditions were applied to the ends of each half cell wall (a distance of L/2 from the vertex) by restraining displacements parallel to the axis running along the length of each cell wall and by allowing only rotations perpendicular to the same axis. The symmetrical boundary conditions were applied along the full height H of the three edges, effectively reflecting the cellular structure about a plane perpendicular to the end of each cell wall. The base of the cell walls were restrained, preventing rigid body translational displacement in the z axis.

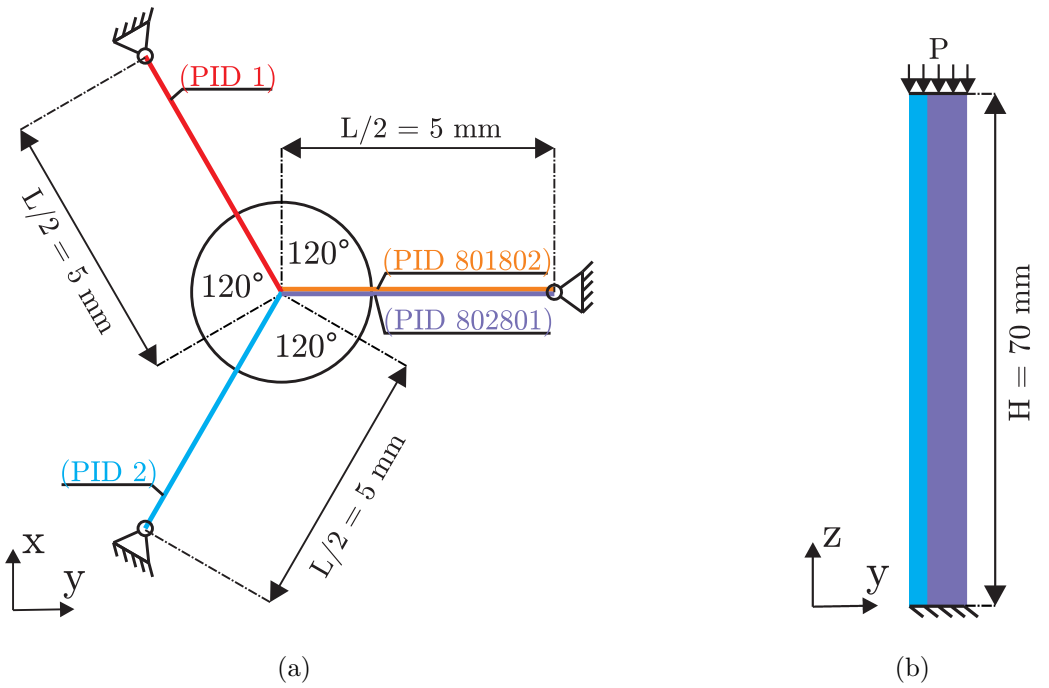

Figure 4.2 Schematic of the (initial) corner element numerical model, showing: (a) plan view with mesoscale geometry and (b) side elevation with macroscopic height.

The cell wall material is much thinner in its thickness dimension than the other two, in plane, dimensions and so the stresses perpendicular to the cell wall surfaces and their resulting strains are negligible in comparison to the in plane stresses. Shell element formulations omit the out of plane normal stress σ_{zz}, and are therefore suitable to this problem. This omission of σ_{zz} also reduces the computational cost required to solve the kinematic equations making shell elements a cheaper alternative to solid elements. Shell elements also carry the advantage of being easier to work with, making meshing easier, and being able to undergo large deformations while still maintaining numerical stability.

There are many shell elements formulations available for use within LS-Dyna, each with their advantages and disadvantages. To model this problem there were three key criteria:

1. Due to the extreme structural deformations that occur during crushing of the honeycomb structure, it was necessary for the chosen element formulation to be highly robust.

2. It was also desirable to keep the computational cost to a minimum, to allow for a high volume of elements in the full scale model.

3. The alternate folding progressive collapse mode [22] meant that the elements close to each vertex would undergo high degrees of warping which must be accommodated for in their formulation.

The default Belytschko-Lin-Tsay [59] element type is computationally efficient due to its use of co-rotational coordinates, single point integration and the use of the standard Cauchy stress within the formulation. Use of the standard Cauchy stress removes the need for additional conversion calculations, because the constitutive relationships within LS-Dyna are in the format of Cauchy stress vs displacement [60]. The Belytschko-Lin-Tsay element formulation assumes a perfectly flat planar element and therefore can't accurately capture warpage. The solution to this problem lay in activating the computationally efficient Wong-Chiang modifications, which allow all four nodes to displace normal to the element mid-plane, and add warping stiffness terms, which control the magnitude of these non planar displacements [61].

At this point it is worth noting that keywords are the form of input used to call upon specific subroutines in LS-Dyna; also, each line of a keyword is known as a card and contains the values necessary for the called upon subroutine. The Belytschko-Lin-Tsay shell element with the Wong-Chiang modifications (implemented by specifying `ELFORM = 10` on the `*SECTION_SHELL` keyword), with four integration points through its thickness, was found to give good results at modest cost, while maintaining numerical stability under extreme deformations.

While being highly efficient, single point integration allows unhindered oscillations of hourglassing modes, i.e. these are deformation modes which have a net-zero displacement at the central point and are therefore not resisted by the element formulation [62]. These oscillations can grow exponentially removing a substantial proportion of energy from the simulation and cause spurious displacements which interfere with the real kinematics of the objects being modelled.

Hourglass modes can not be fully restrained, as they may contribute to a pro-

portion of the genuine structural response. Flanagan and Belytschko [62] developed a stiffness-based hourglass control, which applies resistance to the hourglass forces to prevent them from growing out of control. This stiffness-based hourglass control, with a stiffness coefficient of $Q = 0.05$, was found to keep hourglass energies to a minimum and was enabled for the shell elements by setting `IHQ = 4` on the `*HOURGLASS` keyword attached to the parts defining the cell walls.

When developing a numerical model, the choice of mesh size is a compromise between computational cost and physical accuracy. The computational cost of this model was relatively low in comparison with the larger scale models discussed later in the thesis. With this in mind, the opportunity was taken to use a very fine mesh, it was found that a mesh size of $\delta_{ELv} = 0.271$ mm vertically gave the smallest mesh, which still resulted in acceptable simulation times (during this early stage of model development, where many simulations were required, 24 hours was decided to be an acceptable simulation time. A thorough discussion of the variation simulation times is given later in the thesis); this size was increased to δ_{ELh} 0.278 mm in the horizontal direction to fit exactly 18 elements in the 5 mm span. Table 4.1 displays a summary of the corner element model geometrical properties.

Table 4.1 Corner element model geometrical parameters.

H	L	$\theta°$	δ_{ELv}	δ_{ELh}
70 mm	10 mm	60°	0.271 mm	0.278 mm

4.1.2 Determination of cardboard material properties

The literature discussed in Sections 2.5 and 2.4 indicated that the mechanics of the cardboard honeycomb axial crushing response are dependent on the elastic modulus E, yield stress σ_{Yield}, single to double-ply cell wall yield stress ratio k, and the Poisson's ratio ν (see Table 2.1). This suggests that the mechanical behaviour of an axially crushed honeycomb is mostly dependent on the pre-yield region of the cell wall's constitutive model.

Literature specific to the mechanics of cardboard honeycombs during an axial

crushing response, has neglected any orthotropy of the cardboard cell wall material, and been found to give good agreement between experimental observations and semi-empirical predictions of cardboard honeycomb's quasi-static energy dissipating characteristics [44]. Perhaps unsurprising, since it is logical that during an axial crushing event the material properties parallel to the direction of loading, and hence direction of buckling / progressive folding, would govern the magnitude of the mechanical response. Furthermore, cardboard exhibits elastic-plastic behaviour with parabolic strain hardening, a good approximation of the constitutive material model can sometimes be achieved with an almost linear curve [47].

Taking the above findings into consideration, it was decided that a piecewise-linear elastic-plastic constitutive model, would provide an appropriate approximation of the real, cardboard cell wall material; thus, allowing the physical mesoscopic mechanisms to be studied without adding additional, unknown, complexities. The effects of a more complex, comprehensive material model can be studied at a later date. A diagrammatic representation of the piecewise-linear elastic-plastic constitutive model, used during the numerical simulations is shown in Figure 4.3, in the pre-yield elastic region stress is coupled to strain by

$$\sigma_{Elastic} = E\varepsilon. \tag{4.13}$$

and in the plastic region

$$\sigma_{Plastic} = E\varepsilon_{Yield} + E_t\varepsilon_p. \tag{4.14}$$

where ε_{Yield} is the strain at the yield point, ε_p is the plastic strain, and E_t is the tangent hardening modulus which controls the rate of post-yield strain hardening.

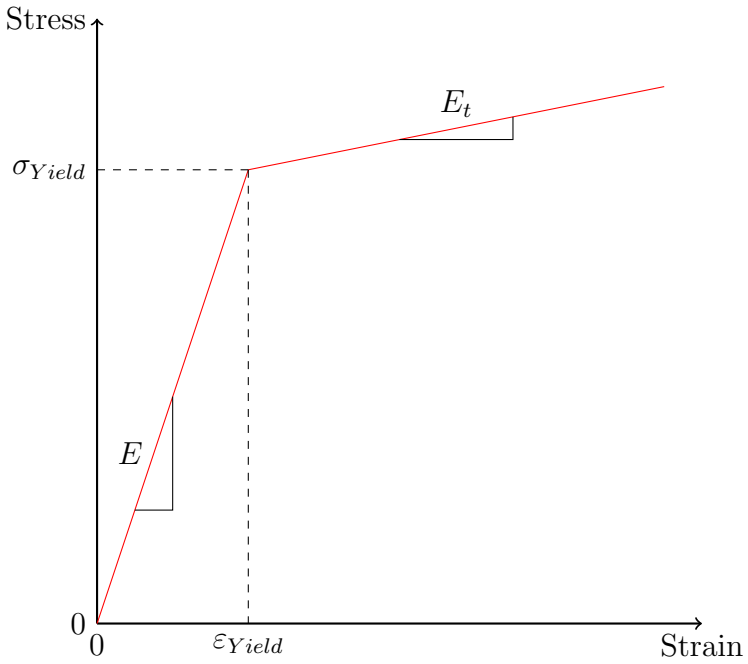

Figure 4.3 Piecewise linear elastic-plastic constitutive model used for the cell wall material, (for specific values see Table 4.2).

A material parameter study is presented in Chapter 5 which investigates, in detail, how variations in the constitutive model parameters affect the macroscopic dynamic response of the cardboard honeycomb. For this model, the literature was used as guidance to attain initial realistic estimations of the material parameters and to ensure that any numerical modelling methods were suitable to the cardboard honeycomb problem. From quasi-static tensile tests of a cardboard honeycomb cell wall material Wang and E [44] determined values of $\sigma_{Yield} = 7.21$ MPa and $E = 2.44$ GPa, a further series of testing by Wang, Wang, and Liao [42] gave lower values of $\sigma_{Yield} = 4.25$ MPa and $E = 0.89$ GPa (see Table 2.1). The chosen values for this numerical model were $\sigma_{Yield} = 5$ MPa and $E = 2$ GPa, which both sit between the reported values and are convenient round figures.

E and Wang [51] discovered that the double-ply, bonded, cell wall material had a higher yield stress than the single cell wall material, the quotient between the two being

$$k = \frac{\sigma_{Y,t2}}{\sigma_{Y,t1}} \tag{4.15}$$

where $\sigma_{Y,t2}$ and $\sigma_{Y,t1}$ are the yield stresses of the double and single cell wall material. Values of k were found to vary depending on the relative humidity, the average value being 1.41.

Szewczyk [53] and Schulgasser [52] reported values of ν for several paper types between extremes of 0.2 and 0.375 with an average of about 0.3, which was chosen for the numerical model.

An initial value of 0.2 MPa was used for E_t, a factor of 10000 less than E, with the intention of providing a modest degree of strain hardening to aid in numerical stability, but being low enough so that strain hardening would not interfere with the collapse mode, allowing a direct comparison between the numerical model and the analytical relationships from the literature.

The cardboard material used to construct the tested samples was of 170 gm^{-2} weight and has a measured average thickness of 0.28 mm, therefore its average density was $\rho = 607$ kgm^{-3}.

The linear elastic plastic constitutive model was implemented in LS-Dyna using the `*MAT_PIECEWISE_LINEAR_PLASTICITY` keyword, a summary of the chosen values is given in Table 4.2.

Table 4.2 Corner element model material parameters.

σ_{Yield}	k	E	E_t	ν	ρ
5 MPa	1.0	2 GPa	0.2 MPa	0.3	603 kgm^3

4.1.3 Structural contact algorithms

Contact algorithms allow numerical bodies to touch, and prevent unwanted penetrations, by allowing the transference of force. They can also be used to simulate frictional interfaces, and specify permanent or conditional attachment between objects. There are many contact algorithms available within LS-Dyna (a comprehen-

sive guide is given by Hallquist [60]), those which were found to be effective for this model are presented here.

A contact algorithm must be defined for every interface that the user wishes to incorporate in the model, i.e. between all elements that are likely to meet, and must not penetrate each other, during the simulation. This would be extremely time consuming to do individually; in practice contact is applied to, and between, groups of elements. Conveniently, in the corner element model, the elements were already arranged in groups, by their part id number. During collapse, there was a possibility for elements from all parts to meet each other, and so it was necessary to define contact between all combinations of parts, including self-contact between elements of the same part. It was also possible to model the cohesive interface between the double cell walls by using a tie break contact algorithm.

Ascertaining a compatible combination of contact algorithms, that generated all the desired contact interfaces and provided the cohesive bond between parts 801802 and 802801, was challenging. Table 4.3 shows the array of contact algorithms that were implemented in this model.

Table 4.3 The contact algorithms and associated parts used in the (initial) corner element numerical model, where A = "Automatic surface to surface", B = "Automatic single surface" and X = "Automatic one way surface to surface tie-break".

PID	1	2	801802	802801
1	B	A	A	A
2	A	B	A	A
801802	A	A	B	X
802801	A	A	X	B

Compatibility issues arose when using tie-break contact algorithms (to model the cohesive bond) in conjunction with the normal automatic surface contact algorithms. Simplistically, there was interference between the repulsive force generated by the automatic surface contact and the attractive force generated by the tie-break

contact. The solution lay in placing the bonded cell walls on top of each other and then using `OPTION = 2` to enable the bond for nodes which are initially in contact and `PARAM = 1` to ignore the shell surface offsets when calculating the penetration distance on the `*CONTACT_AUTOMATIC_ONE_WAY_SURFACE_TO_SURFACE_TIEBREAK`. This method also required that the shell normals, of the bonded elements, face each other; when the tie-break fails and the shells separate, the initially stacked nodes will move towards the tail end of the normal vector.

During the initialization stage of an analysis the LS-Dyna executable searches for initial penetrations and tries to remove them in a single time step by applying nodal forces. Setting `PENCHK = 1` and `IGNORE = 1` on the `*CONTACT_AUTOMATIC_SINGLE_SURFACE` keyword circumvented this by instructing Dyna to ignore the initial penetrations and apply no repulsive force to the stacked nodes until the tie-break was broken and they moved outside of the single surface contact envelope which surrounded the shells. These modifications would not interrupt the desirable self-contact provided by the single surface algorithm, because adjacent nodes of the same part would still surrounded by the contact surface.

4.1.4 Response to compressive axial ramp load

The cell walls were subject to a uniform axial compression by applying the linearly increasing axial load, shown in Figure 4.4, to the nodes at top of the cell walls (at z= 70mm). The existing literature suggested that the magnitude of peak and plateau stresses transmitted during the axial crushing response was a function of the cell wall thickness (t) and cell wall length (L), specifically the quotient between the two (t/L). The cell wall thickness to length quotient (t/L) was varied by holding L constant and changing t. To keep the relative loading rate constant for different (t/L) values, an estimated critical buckling load P_{Crit} was calculated by taking the minimum value of Equation 4.4 and 4.5 and multiplying by A_c. The gradient of the ramp load was set so that the applied load passed through P_{Crit} at 0.1 ms; thus, providing a rapid rate of loading, characteristic of an impact event.

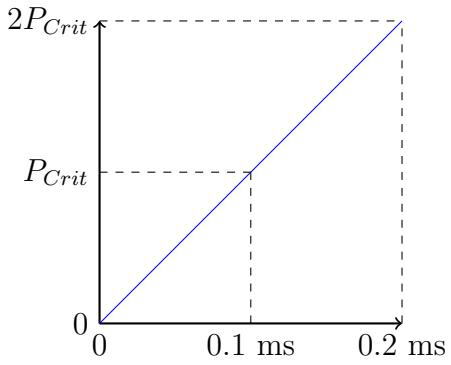

Figure 4.4 Time dependent axial compressive load vs time.

The peak transmitted stress was calculated by summing the vertical reaction forces of every node at the base of the cell walls and dividing by the tributary area of the corner element A_i. The shape of the numerical transmitted stress strain curves took on one of two forms; diagrammatic representations of both are given in Figures 4.5 (a) and (b).

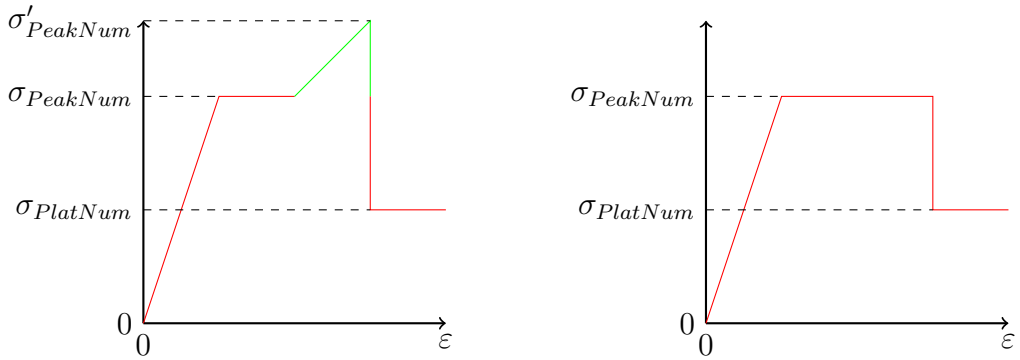

(a) (b)

Figure 4.5 The two numerical model responses, (a) double peaked and (b) the single peaked.

Recorded values of the initial peak stress $\sigma_{PeakNum}$ (red) and, if existent, the secondary peak stress $\sigma'_{PeakNum}$ (green) for (t/L) values from between 0.005 and 0.03 are shown in Figure 4.6. Equations 4.4 and 4.5, which analytically describe the maximum transmitted stresses before collapse due to Euler buckling or material failure, were used with the model material and geometrical parameters to give

Equations 4.16 and 4.17

$$\sigma_{PeakEul} = 4.847 \times 10^{10} \left(\frac{t}{L}\right)^3 \tag{4.16}$$

$$\sigma_{PeakCru} = 7.698 \times 10^{6} \left(\frac{t}{L}\right) \tag{4.17}$$

which have also been plotted on Figure 4.6 with solid and dashed black lines.

As the load was ramped up, so was the stress within the cell walls. Once the stress reached a critical value, the structure buckled and the load dropped. Theoretically, the critical value would be decided by the buckling mechanism that required the lowest load.

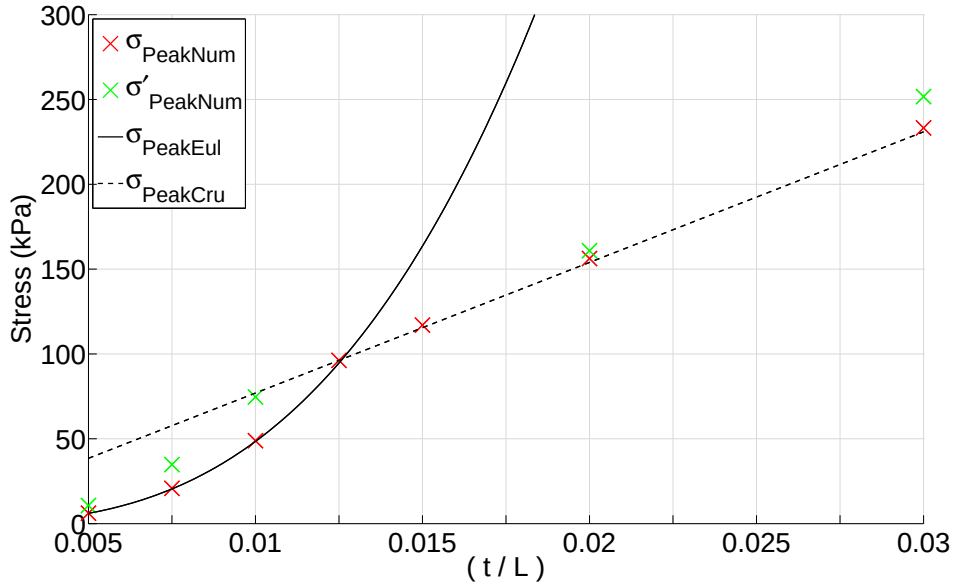

Figure 4.6 Analytical peak stress predictions $\sigma_{PeakEul}$ (Equation 4.4) and $\sigma_{PeakCru}$ (Equation 4.5) with numerical peak stresses $\sigma'_{PeakNum}$ and $\sigma_{PeakNum}$ (see Figure 4.5) vs varied (t/l) values.

There was very good agreement between the buckling response of the numerical model and the analytical predictions, suggesting that the numerical methods were capturing the physics described by the analytical relationships. For all analysis $\sigma_{PeakNum}$ was almost exactly equal to the dominant of the two buckling mechanisms,

which was $\sigma_{PeakEul}$ to the left of (t/l) = 0.0125 and $\sigma_{PeakCru}$ to the right. For analyses dominated by the Euler buckling mode, there was a double peaked response, where the structure stiffened up after the initial yield to $\sigma'_{PeakNum}$.

The value of (t/L) at which the dominant buckling mode changes can be calculated by taking the intersect of Equations 4.4 and 4.5

$$\xi = \sqrt{\frac{2\sigma_{Yield}(1-\nu^2)}{5KE}} \tag{4.18}$$

where

$$\begin{aligned} \left(\frac{t}{L}\right) < \xi \Rightarrow \sigma_{Peak} \approx \sigma_{PeakEul} \\ \left(\frac{t}{L}\right) > \xi \Rightarrow \sigma_{Peak} \approx \sigma_{PeakCru}. \end{aligned} \tag{4.19}$$

4.1.5 Response to a forced displacement

Once confidence had been gained in the fundamental numerical methods, the top and bottom liner sheets could be introduced, the loading method changed to a forced displacement (simulating that used during the experimental testing) and the crushing stroke extended into the plateau region. The necessary corner element model amendments are shown in Figure 4.7.

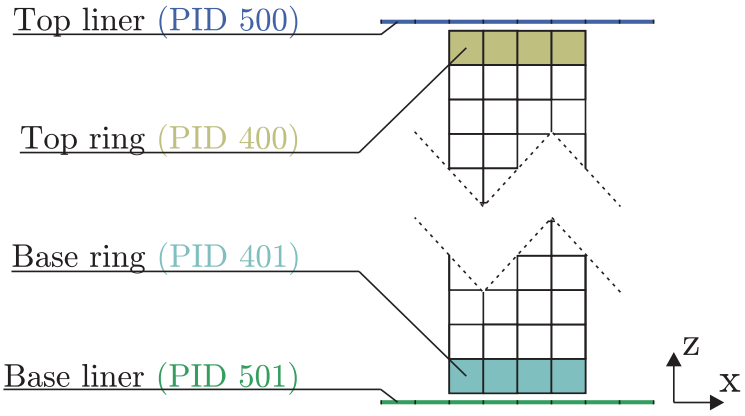

Figure 4.7 Necessary amendments to the corner element model to allow the addition of the top and bottom liner sheets, while also maintaining effective contact and numerical stability.

The top and bottom liners were modelled with the same shell elements used for the cell walls and they were allocated PIDs 500 and 501 respectively. To simulate the bond between the top and bottom of the cell walls and the liners, a bonding method capable of attaching shell edges to shell surfaces was required. At large deformations, many attempted methods resulted in penetration of the shell edges through the liner surface and numerical instability causing a forced analysis termination. The solution was to use a *CONTACT_TIED_SHELL_EDGE_TO_SURFACE_OFFSET contact, defining the shell edge nodes at the top and bottom of the cell walls as a slave node set, and the connecting liner part (PID 500/501) as the master with a 0.05 mm offset.

While this achieved effective contact between the cell wall edges and the liner parts, the nodes at top and bottom edges of the cell walls were now subject to conflicting penalty forces from both the TIEBREAK and new TIED contact algorithms, leading to severe numerical instabilities. To remedy this, it was necessary to move a ring of elements at the top and bottom of each cell wall to separate parts (PIDs 400 and 401). These parts were then omitted from the TIEBREAK contact, effectively releasing just the shell edge nodes to be tied to the liners without conflict.

Table 4.4 shows the resulting array of contact types, which were found to be compatible while providing stable and effective contact during the progressive structural buckling encountered when compacting the hexagonal corner element model to high degrees of strain.

Table 4.4 The contact algorithms and associated parts used in the (amended) corner element numerical model, where A = "Automatic surface to surface", B = "Automatic single surface", X = "Automatic one way surface to surface tie-break" and Y = "Tied shell edge to surface offset".

PID	1	2	801802	802801	400	401	500	501
1	B	A	A	A	A	A	A	A
2	A	B	A	A	A	A	A	A
801802	A	A	B	X	A	A	A	A
802801	A	A	X	B	A	A	A	A
400	A	A	A	A	A	A	A+Y	-
401	A	A	A	A	A	A	-	A
500	A	A	A	A	A+Y	-	-	-
501	A	A	A	A	-	A	-	-

A linear forced displacement was applied to the top liner using the `*BOUNDARY_PRESCRIBED_MOTION`. Three strain rates were chosen which covered the range used in the experimental testing, 50, 100 and 200 s^{-1}, which corresponded to constant impact velocities of 3, 7 and 14 ms^{-1}. Figure 4.8 shows the recorded peak transmitted stress for each strain rate, as (t/L) was varied.

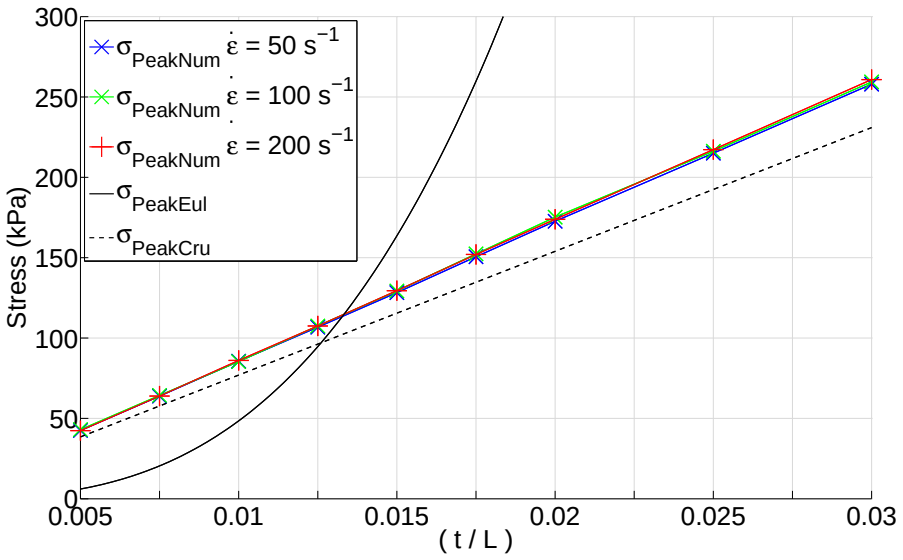

Figure 4.8 Analytical peak stress predictions $\sigma_{PeakEul}$ (Equation 4.4) and $\sigma_{PeakCru}$ (Equation 4.5) with values of numerical peak stresses $\sigma_{PeakNum}$ at varied strain rates ($\dot{\varepsilon}$) and (t/L) values.

There was good agreement between the trend of the quasi-static analytical crushing buckling mode and the numerical results for all simulations. The gradient of the numerical (dynamic) stress-(t/L) relationships were steeper than the quasi-static relationship, suggesting that the enhancement in the dynamic peak stress increases with (t/L). Furthermore, a very marginal strain rate effect begins to emerge as (t/L) increases. It is thought that this strain rate effect may be the emergence of inertial stiffening due to an increase in mass (i.e. wall thickness). Enhancements in the axial crushing stiffness of honeycomb structures due to strain rate have been reported in the literature [23, 24].

At these loading rates, the response appears to be solely governed by the crushing buckling mode. The absence of the Euler buckling effect was thought to be due to the lack of time allowed for the structure to respond. The following calculations give some basis for this assumption. The strain at the yield ε_{Yield} is given as

$$\varepsilon_{Yield} = \frac{\sigma_{Yield}}{E}. \tag{4.20}$$

The vertical displacement of the top liner that causes yield ΔH_{Yield} is

$$\Delta H_{Yield} = \frac{H\sigma_{Yield}}{E} \tag{4.21}$$

and so the time taken for the cell walls to yield T_{Yield} for a given impact velocity v_i can be calculated as

$$T_{Yield} = \frac{H\sigma_{Yield}}{Ev_i}. \tag{4.22}$$

The time taken for a stress pulse to travel to the base of the sample is

$$T_{Wave} = \frac{H}{c} \tag{4.23}$$

where c is assumed to be the 1D longitudinal wave speed

$$c = \sqrt{\frac{E}{\rho}}. \tag{4.24}$$

In order for the structure to buckle under global Euler buckling, its full length must first be subject to compression. The absolute minimum time required for this to occur, is the time taken for a stress wave to travel from the impact point (at the top of the cell walls) to the supported base and back, this time is $2 \times T_{Wave}$. If the time taken for the cell walls to buckle due to yielding of the material is less than $2 \times T_{Wave}$, the buckling mode must be dictated by crushing of the cell wall material and the magnitude of the peak transmitted stress in the region of $\sigma_{PeakCru}$, where

$$T_{Yield} \leq 2T_{Wave} \Longrightarrow \sigma_{Peak} \approx \sigma_{PeakCru}. \tag{4.25}$$

The above relationship can be revised into a more convenient form

$$v_{i,cru} \geq \frac{c\sigma_{Yield}}{2E} \Longrightarrow \sigma_{Peak} \approx \sigma_{PeakCru} \tag{4.26}$$

which allows the calculation of the minimum impact velocity required to ensure that the peak stress will be dictated by yielding of the cell walls, $v_{i,cru}$. For a cell wall material, the minimum value of $v_{i,cru}$ can be obtained by using the maximum

reported value of σ_{Yield} and minimum value of E. For the cardboard honeycomb cell wall material this was $\sigma_{Yield} = 7.21$ MPa [44] and $E = 0.89$ GPa [42], which results in a value of $v_{i,cru} = 4.81$ ms^{-1}. During the experimental impact testing, the minimum recorded impact velocities during Phase 2 and 3 were 5.56 ms^{-1} and 9.45 ms^{-1} respectively. It is therefore not unreasonable to assume that the peak buckling load recorded during all experimental tests was a function of the cell wall crushing buckling mode.

In cases such as this, where the single and double-ply cell walls have equal yield stress, k=1 and Equation 4.8, which gives an analytical prediction of the quasi-static (and homogeneous with axial strain) plateau stress σ_{PlatAn}, becomes

$$\sigma_{PlatAn} = 5.076\sigma_{Yield}\left(\frac{t}{L}\right)^{\frac{5}{3}} + 0.3849\sigma_{Yield}\left(\frac{t}{L}\right)^{2}. \tag{4.27}$$

The dashed black line in Figure 4.9 shows the plateau stress predicted by equation 4.27 for varied (t/L) values with the material yield stress used in the model σ_{Yield}. On the same graph, values of the plateau stress transmitted by the numerical model $\sigma_{PlatNum}$ when crushed at strain rates of 50, 100 and 200 s^{-1}. A solitary value of $\sigma_{PlatNum}$ was calculated for each analysis event by taking the mean transmitted stress from 20 to 50% strain, each of which is indicated on Figure 4.9 with a respective marker.

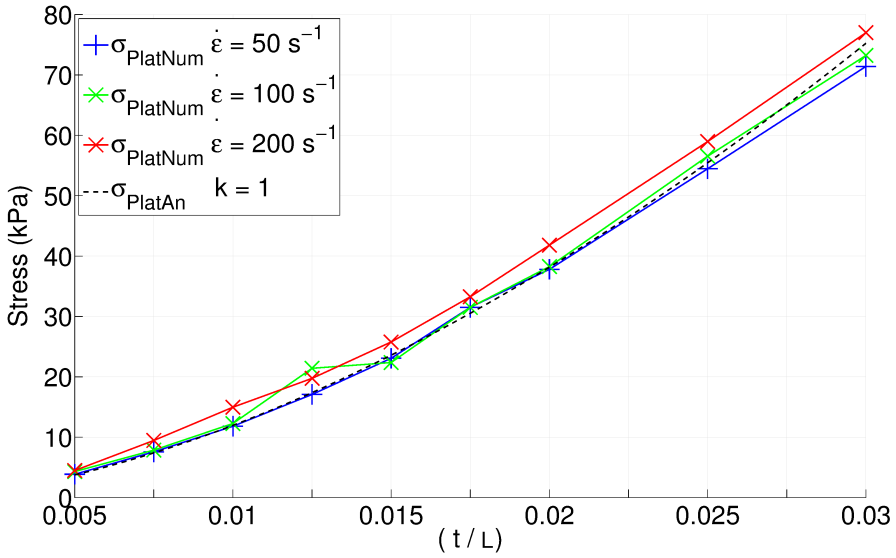

Figure 4.9 Analytical plateau stress predictions σ_{PlatAn} (Equation 4.27) with values of numerical plateau stresses $\sigma_{PlatNum}$ at varied strain rates ($\dot{\varepsilon}$) and (t/L) values.

The numerical model showed excellent consistency with the quasi-static analytical predictions. A small, strain rate effect is visible when comparing the 100 and 200 s^{-1} amounting to an increase of roughly 2.5 kPa for all analyses. As (t/L) increased above 0.02, a second strain rate effect, with increasing magnitude, began to emerge between the 50 and 100 s^{-1} analyses. It is worth note that because there was no strain rate sensitivity included in the utilised cell wall constitutive model, the strain rate effect observed above must be a sole product of the interaction between the loading rate and the mechanics of the folding mechanism.

4.1.6 Mesh study

Consistency between the numerical model and the theoretical predictions (based on observed physical behaviour), suggested that modelling techniques employed so far were capable of capturing the failure mechanisms which contribute to the dynamic crushing response of a cellular honeycomb material. In order to apply the modelling techniques to a full, non-uniform, cellular structure, it was necessary to reduce the required computational cost while maintaining accuracy.

One common method of reducing computational cost is to increase the size of the finite elements. This increases the maximum permissible time step (in agreement with the Courant condition, meaning less time steps are required to advance for the desired analysis time) and reduces the computational cost of each individual time step (as there are less simultaneous equations to solve).

The mesh used for all analyses performed above, that has been found to produce good results, consisted of rectangular elements 0.0271 high by 0.0278 mm wide, giving an average size element size δ_{EL} of 0.275 mm. For this study, two additional meshes were constructed with 0.5 and 1.00 mm square elements, giving 140 and 70 elements respectively, over the 70 mm crushing height, while there were 10 and 5 elements respectively along the 5 mm half length cell wall. To give a direct comparison, both cell wall thickness and strain rate were held constant at 0.2 mm and 100 s^{-1}. Figure 4.10 shows the full transmitted stress vs strain behaviour for all three mesh sizes.

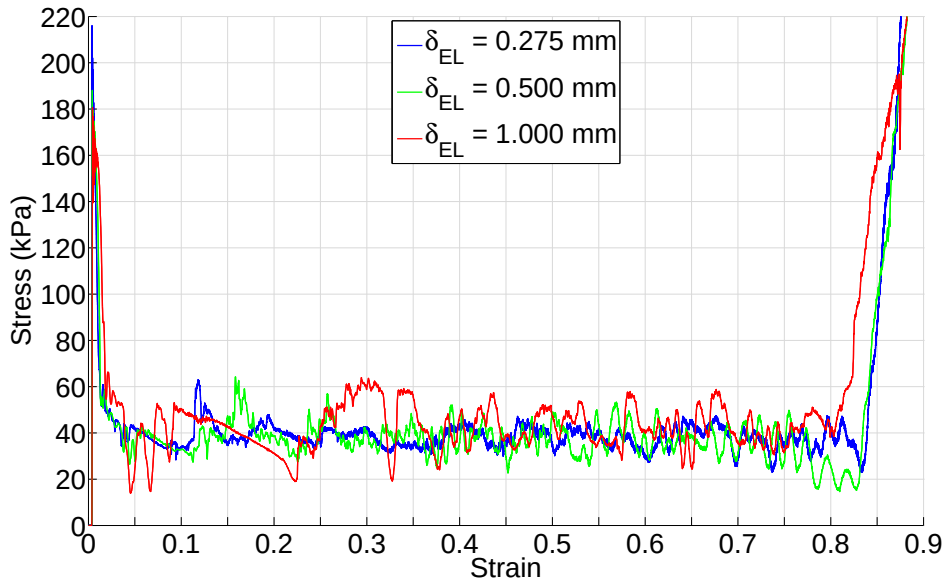

Figure 4.10 Full macroscopic numerical responses (σ_{Total}) for varied mesh size δ_{EL}, produced by the corner element model with (t/L) = 0.02 and $\dot{\varepsilon}$ = 100 s^{-1}.

The overall response of all three mesh sizes was very similar, consisting of a peak, followed by a very level plateau region and finally a sharp increase, once the folds

begin to bear on each other and the structure stiffened up. There were, however, subtle differences, which were most obvious when comparing the response of the most coarse 1 mm mesh (red line) with the response of the two finer meshes (blue and green lines). The oscillations about the plateau are caused by variations in the axial geometrical stiffness as each fold propagates. These oscillations, were much more pronounced and of a lower frequency for the 1 mm mesh. The structure with the 1 mm mesh also reached the stiffening phase slightly earlier than the other two meshes. In Figure 4.11 the x-axis has been adjusted to show a detail of the initial peak.

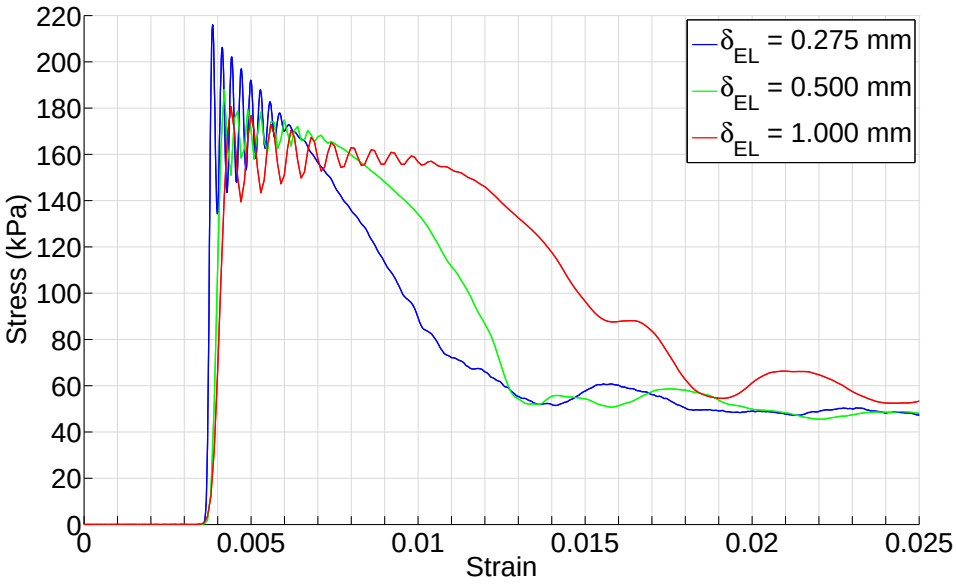

Figure 4.11 Detail of peak macroscopic numerical responses σ_{Total} for varied mesh size δ_{EL}, produced by the corner element model with (t/L) = 0.02 and $\dot{\varepsilon} = 100\ \mathrm{s}^{-1}$.

The early oscillations, including the initial peak, were found to be an artefact introduced by the contact algorithms; the true peak value can be found by taking an average across the oscillatory region. The shape of the softening limb becomes increasingly drawn out and convex as the mesh size is increased. This is thought to be due to the strain required for the first fold to fully form, with a coarser mesh causing a recruitment of a larger region of cell wall material.

Figures 4.12 (a) and (b) show the singular extracted values of the peak (blue)

and plateau (red) stresses against mesh size. On the same graph, the analytical predictions are shown with dashed black lines. The difference between the magnitude of the numerical and analytical peak stresses can be explained by the previously observed strain rate effect. Over the three mesh sizes used, there is a linear reduction in peak stress of 20.7 kPa/mm, which results in a reduction of $\sigma_{PeakNum}$ of 11.7%, when increasing the mesh size from 0.275 to 1 mm. Figure 4.12 (b) shows that there is no significant impact on $\sigma_{PlatNum}$ when increasing the mesh size from 0.275 mm to 0.5 mm. Between a mesh size of 0.5 mm and 1 mm there appears to be a threshold, after which an increase in element size caused in increase of the plateau stress; by a mesh size of 1 mm there was an increase of 8.6% to 43 kPa from the original value of 38 kPa.

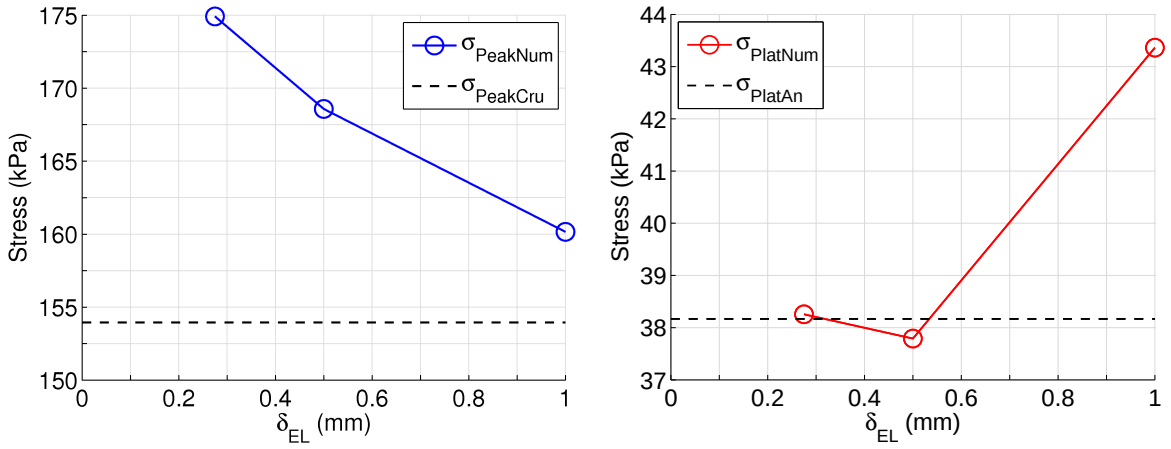

(a) (b)

Figure 4.12 Relationship between (a) $\sigma_{PeakNum}$ and (b) $\sigma_{PlatNum}$ and δ_{EL} for the corner element model with (t/L) = 0.02 and $\dot{\varepsilon} = 100$ s^{-1}. Analytical values $\sigma_{PeakCru}$ and σ_{PlatAn} as predicted by Equations 4.5 and 4.27 are given for reference.

Wierzbicki [22] showed that total length of each fold λ is a function of both the thickness t and length L of the cell walls, where

$$\lambda = 1.642\sqrt[3]{tL^2}. \tag{4.28}$$

It follows that the total number of folds, which will be present in the final crushed

geometry n_{fold}, can be calculated as simply $^{H}/_{\lambda}$. For the model used in the mesh study, Equation 4.28 predicts a λ of 4.46 mm giving a n_{fold} of 16. Figures 4.13 (a), (b) and (c) show the fully crushed, final geometries of the 0.275, 0.5 and 1mm meshes.

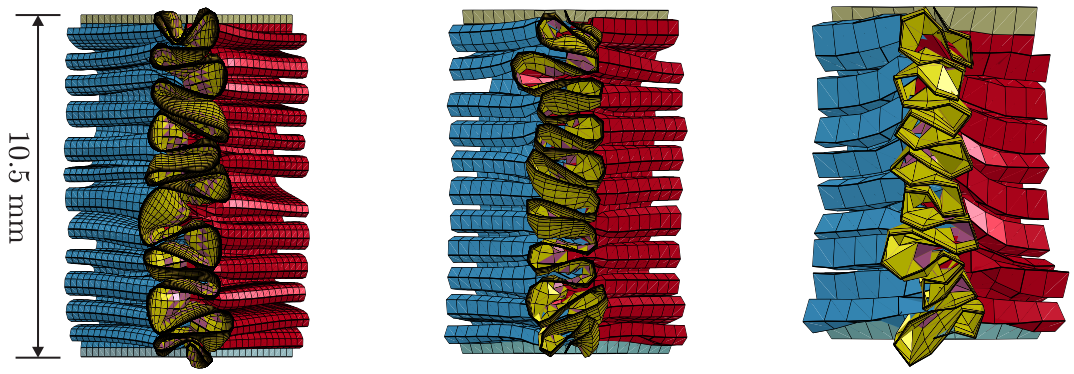

(a) 0.275 mm, $n_{fold} = 18$ (b) 0.5 mm, $n_{fold} = 19$ (c) 1.0 mm, $n_{fold} = 17$

Figure 4.13 Final deformed shapes at 85% strain for the three mesh sizes. Single-ply cell walls are shaded blue and red.

While all three mesh types show slight variation from the predicted 16 folds, they are generally in good agreement. Further research would be required to identify the cause of variation, but for the purpose of this thesis, sufficient confidence has been gained that the physics involved during the folding mechanism are being captured by the utilised numerical techniques. There is no obvious correlation between the number of folds and the mesh size. Comparison of the deformed shape produced by the 1 mm mesh, with the deformed shapes produced by the other two meshes, suggests an explanation of possible threshold that was perceived in Figure 4.12 (b). For both the 0.275 and 0.5 mm meshes there are enough elements to smoothly resolve the shape of a single fold, and so changing the mesh size would have minimal effect on the folding mechanism. For the 1 mm mesh, the folded shape is much rougher, and so logically would provide more resistance. It must be noted that while the overall final deformed geometry produced by the 1 mm mesh does not look realistic, the number of folds and the recorded plateau stress was not significantly different from the response produced by the other two meshes.

The numerical analyses were performed on a Windows 7 desktop PC with 8 GB of RAM and an Intel core i7 2600 CPU clocked at 3.4 GHz. The computational cost for each mesh size can be expressed as a quotient ϕ_{Cost} of the required real time T_{Real} for a numerical run time T_{Num} where $\phi_{Cost} = {}^{T_{Real}}/_{T_{Num}}$. For example, it may take 100 seconds of real time to simulate a numerical event which is a total of 1 second in duration; in this case $T_{Real} = 100$, $T_{Num} = 1$ and ϕ_{Cost} would be equal to 100.

To remove any bias introduced by highly distorted elements, the calculated values of ϕ_{Cost}, given in Table 4.5, were based on the numerical response between 0 and 50% strain.

Table 4.5 Comparison of relative costs ϕ_{Cost} of three corner element model simulations performed using different mesh sizes δ_{EL}.

δ_{EL}	0.275 mm	0.5 mm	1 mm
ϕ_{Cost}	2.2×10^6	1.7×10^5	4.8×10^4

To clarify, 1 second of numerical analysis time with the 0.275 mm mesh would take 2.2×10^6 seconds, or 25.5 days. The relationship between mesh size and computational cost, for this particular model, is non-linear, with the 0.5 and 0.257 mm meshes being a factor of 3.54 and 45.8 times more expensive than the 1 mm mesh. While computational cost was not a limiting factor at this stage in the modelling process, it has been shown that even with a relatively basic model, increasing the mesh size provides a substantial reduction in cost while introducing disproportionately small numerical error.

4.2 Development of the Eulerian numerical modelling techniques required to capture the development of internal air pressures

In order to model the development of pressures within the honeycomb, it was necessary to first identify and verify a numerical modelling method capable of accurately capturing the displacement and deformation (and associated variations in density and pressure) of a gaseous material. Within LS-Dyna there are two primary methods for modelling fluid and gas material: Smooth Particle Hydrodynamics (SPH) and the fully Eulerian finite element method. In terms of LS-Dyna syntax, the fully Eulerian method is a special formulation of the Arbitrary Lagrange Eulerian method, whereby after each time step the fluid mesh is returned to its original position allowing the material to pass between elements.

During the preliminary modelling stage, the feasibility of both methods was investigated; when investigating the use of the SPH method, numerical stability could not be achieved when the SPH expressed air was used in conjunction with highly distorted shell elements, thus, it was discounted early on. Implementation of the fully Eulerian method was not without its difficulties, however, it proved more robust, and through a process of iterative model development a methodology was arrived at, which allowed stable numerical modelling of an air filled cellular structure incurring large structural deformations as a result of high strain rate impact loading.

In Section 3.3.9 of Chapter 3 it was discussed that the air within the cardboard honeycomb is being subject to a rapid, and therefore adiabatic, change in volume; Equation 3.8 gave the **over**pressure which would be generated if a column of air was subject solely to a 1 dimensional adiabatic change in volume by strain ε. Writing Equation 3.8 instead in terms of the final **absolute** pressure P_2 we get

$$P_2 = \frac{P_{Atmospheric}}{(1-\varepsilon)^{c_p/c_v}} \tag{4.29}$$

which states the maximum absolute pressure which will occur within the card-

board honeycomb, for a given strain, if all air is contained throughout and there is no change of the internal cross sectional area, and c_p/c_v is the ratio of specific heat capacities (at constant pressure and constant volume).

During the experimental testing, the maximum recorded internal air pressure was 9 bar; Equation 4.29 predicts that the maximum possible air pressure, well after the useful EDM response (at 90% strain), will be 25 bar. At 300° K and 40 bar, the compressibility factor for air is 0.9917 [63] (the quotient of the actual pressure to the pressure predicted by the ideal gas law), and so at the expected pressures and ambient temperatures, the air within the cardboard honeycomb can be assumed to be acting as an ideal gas.

A form of the ideal gas equation of state (EOS) is given below, which relates the pressure within a region of gas P to its current density ρ, temperature τ and its specific gas constant $R_{Specific}$.

$$P = \rho R_{specific} \tau \tag{4.30}$$

According to Mayers law, $R_{specific} = c_p - c_v$, and so

$$P = \rho \left(c_p - c_v \right) \tau \tag{4.31}$$

where c_p and c_v are the specific heat capacities of a gas when held at a constant pressure and constant volume. A value of $c_v = 722.9$ J/kg.K was obtained for air, at 20° C ($\tau = 293°$ K) from the work published by Magee [64], and the widely accepted value of the ratio of specific heats for air ($\gamma = 1.4$ [65]) was used to calculate a value of $c_p = 1012$ J/kg.K.

The standard atmospheric pressure is 101.325 kPa, at this pressure, with the parameters discussed above, Equation 4.31 yields a density of 1.2 kg/m^3. Table 4.6 shows a summary of the ideal gas properties that were used for the numerical modelling of air.

Table 4.6 Adiabatic ideal gas properties used for air in the numerical analyses.

ρ_0 (kg/m^3)	c_p (J/kg.K)	c_v (J/kg.K)	γ	τ (°K)	$P_{Atmospheric}$ (kPa)
1.2	1012	722.9	1.4	293	101.325

To develop the modelling capability necessary to simulate a rapid change in volume of a body of air, a predictable and simplistic event was required. A column of air, at an initial state representative of an ambient atmosphere, was allowed to double in volume by expanding into an equal sized vacuum. Figure 4.14 shows a schematic of the LS-Dyna numerical model.

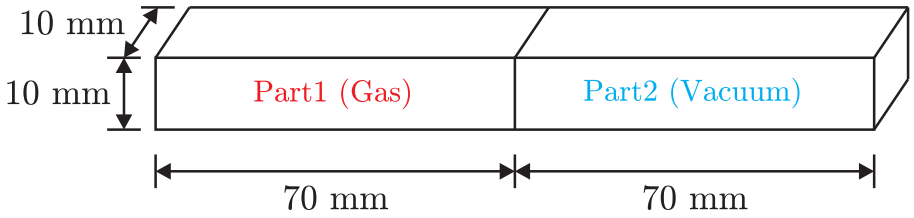

Figure 4.14 Schematic of the model used for verification of the Eulerian numerical methodology.

A geometry of 10 x 10 x 70 mm, for both parts, was chosen to resemble the volume of air contained within the smallest cells observed during the impact testing, that is, the case which was expected to be the most challenging to capture numerically. Verification was achieved by ensuring that the pressure and density of the gas in its final, expanded state, matched that predicted by Equation 4.29. In its final state, the gas expanded to occupy the total internal volume of parts one and two, effectively undergoing a negative strain of 100 %, meaning $\varepsilon = -1$. Substituting into Equation 4.29, the final equilibrium pressure is calculated as

$$P_2 = \frac{101.325 \times 10^3}{(1-(-1))^{1.4}} = 38.4kPa \tag{4.32}$$

and as the mass is constant, for a doubled volume the density will half $\rho_{Fin} = 0.6$ kg/m^3.

Within LS-Dyna two keywords are commonly used to describe the pressure-volume relationship of air, *EOS_LINEAR_POLYNOMIAL and *EOS_IDEAL_GAS. It was discovered, that in problems such as this, where a gas must be transported a large distance relative to its Eulerian domain mesh size, cumulative numerical errors result in the emergence of spurious pressure and density gradients when the *EOS_LINEAR_POLYNOMIAL keyword was used. No such behaviour was observed when using the *EOS_IDEAL_GAS keyword and for that reason it was used for all subsequent numerical analysis involving air.

The *MAT_NULL material model was used in combination with the equation of state, allowing the definition of a material with no shear resistance by instructing the numerical solver to ignore deviatoric stresses. On this keyword viscosity, density and a pressure cut-off are defined. The inclusion of viscosity in this, and all subsequent simulations, was found to be negligible, and so it was omitted from all numerical simulations herein. To prevent the gas from providing any significant tensile resistance to rapid reductions in pressure, a pressure cut-off was defined as an extremely small negative number -1×10^{-15}, which limited the maximum possible negative pressure. It is necessary to define a material type for all parts in LS-Dyna, a material type for the vacuum region (Part 2) was defined using using the dummy material *MAT_VACUUM keyword, with a density of 1×10^{-9} kg/m^3. Both the air and vacuum were allocated a respective *ALE_MULTI-MATERIAL_GROUP, instructing Dyna to prevent mixing and to track the interface between them.

Both parts were defined with solid, 8 noded, 2 x 2 x 2 mm cuboid Eulerian elements, by using the *SECTION_SOLID_ALE keyword. A single point integration multi material element formulation was used, by defining ELFORM = 11, allowing each individual Eulerian element to contain a proportion of both the air and vacuum. Nodes are shared at the interface between the two parts, allowing material to be transported freely across the interface. The fully Eulerian case of the ALE formulation was activated by including the *CONTROL_ALE keyword and turning mesh smoothing off with AFAC = -1, fixing the position of the Eularian mesh in space. The number of cycles between advections was set to 1, ensuring that the original

mesh geometry was restored at the end of each time step with the second order Van Leer advection method.

Boundary conditions were set with single point constraints on the external nodes, restricting only translational displacements in the degrees of freedom perpendicular to each surface. A reduced time step scaling factor of `TSSFAC = 0.5` was used to ensure numerical stability when using the Eularian element formulation.

It was discovered that during this relatively long duration event, the use of a single precision solver resulted in a gradual loss of energy from the model and so double precision was required to maintain accuracy. For short duration events, in the order of milliseconds, single precision was found to be adequate.

Figures 4.15 (a) and (b) show the average pressures and densities of part 1 (red), and part 2 (blue), against time, for the numerical simulation. Values, calculated above, of pressure $P_{An,Fin} = 38.4$ kPa and density $\rho_{An,Fin} = 0.6$ kg/m^3 of the gas in its final expanded state are shown with dashed black lines.

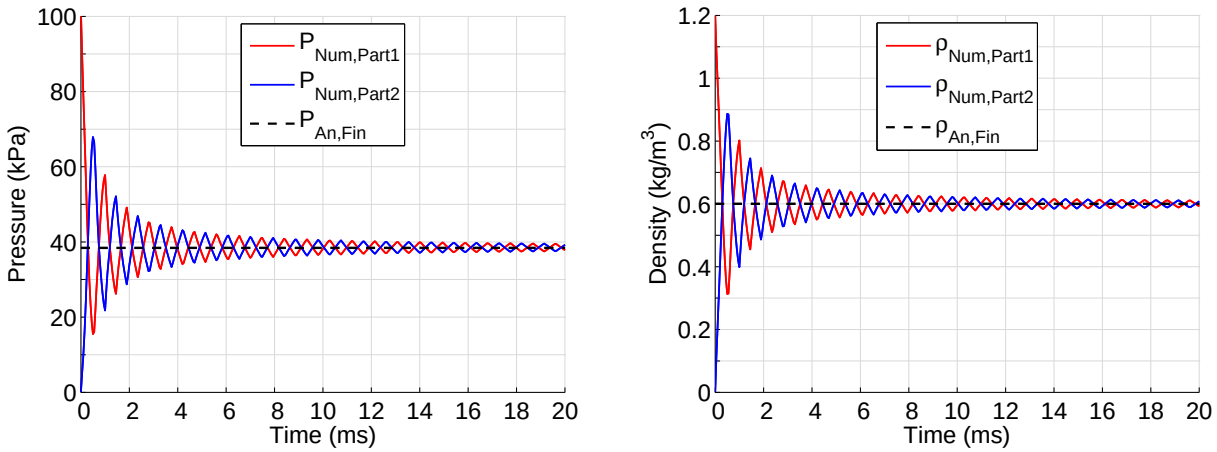

(a) (b)

Figure 4.15 Evolution towards a final equilibrium state following a rapid expansion of air from part 1 (atmospheric) into part 2 (vacuum), (a) pressure and (b) density vs time. $P_{An,Fin}$ and $\rho_{An,Fin}$ indicate the predicted final pressure and density respectively.

There was excellent agreement between the numerical model and the analytical

prediction. A shock front was induced due to the initial sharp change in pressure at the interface between parts 1 and 2. The pressurised gas rushed into the vacuum, causing a rapid increase in both pressure and density in part 2 (to a peak at 0.5 ms), which was matched by an equal drop in pressure and density in part 1. Subsequent reflections caused exponentially decaying oscillations of both the pressure and density about the steady state.

4.3 Development of the numerical modelling techniques required to provide coupling between the cellular structure (Lagrangian) and the internal air (Eulerian) materials

As the internal volume within the cardboard honeycomb reduces, the enclosed air is compressed by movement of the cell walls and, in return, the compressed air distributes a load to the honeycomb structure proportional to the pressure differentials either side of each cell wall. In order to capture this mutual exchange of forces between the enclosed air and the honeycomb structure, it was necessary to develop the capability to numerically couple the Eulerian (air) and Lagrangian (structural) parts.

Effective coupling can be defined as coupling which prevents unwanted leakage of the Eulerian material through the coupled solid surface, does not introduce numerical instability and has a minimal impact on the computational cost. To ensure that effective coupling could be achieved between the Eulerian gas and Lagrangian shell structure, a modification of the event modelled in the previous section was considered; the single point constraints which provided perfect containment at the boundary of part 2 in Figure 4.14, were replaced with a rigid shell container and a coupling definition between it and the rapidly expanding gas.

Figure 4.16 shows the schematic of the modified numerical model. Both parts 1 and 2 were defined in an identical manner to the previous model, with only the

geometry of part 2 being adjusted to allow for the possibility of flow through the shell container. Part 3 was given the same element formulation that was found to give good results when modelling the cell walls during the structural response, (Belytschko-Wong-Chiang). It was found that effective fluid structure interaction (FSI) was much easier to obtain when the shell element size was matched to the Eulerian element size; 2 x 2 mm quadrilateral elements were used for part 3 to match the 2 x 2 x 2 mm hexahedral elements used for parts 1 and 2.

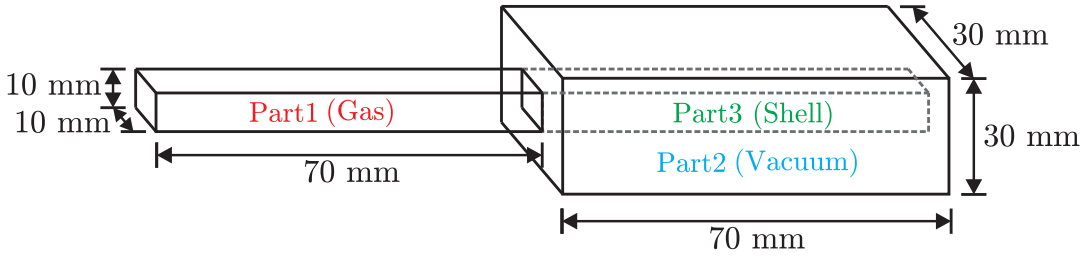

Figure 4.16 Schematic of the model used for verification of the FSI numerical methodology. Part 1 and 2 are Eulerian domains, they consist of Eulerian elements with shared nodes at their interface. Part 3 is a shell container situated within the Eulerian domain defined by Part 2. When successful FSI was achieved, gas flowed from Part 1 into Part 3 but remained within the volume encompassed within the shell container.

In LS-Dyna FSI is activated by inclusion of the `*CONSTRAINED_LAGRANGE_IN_SOLID` (CLIS) keyword, on which constraint and penalty based algorithms can be defined between a slave (Lagrangian) object within the master (Eulerian) domain. Fluids, which are to be coupled within the Eulerian domain, are then identified by setting `MCOUP = -AMMGID`, where `AMMGID` is the ALE multi-material group id allocated to that specific fluid. It is good practice to couple no more than one `AMMG` per CLIS keyword, allowing separate manipulation of each coupling surface and adding clarity when studying their related output (pressures, forces) in the database fluid structure interaction (`DBFSI`) binary output file. In this numerical model, only one coupling relationship was necessary, that was between shell container (part 3) and the air (`AMMG = 1`) within the Eulerian domain (part 2).

Constraint-based algorithms provide FSI by constraining the velocity and/or accelerations of the Eulerian material at the FSI interface; they were found to be extremely unreliable at preventing leakage, when used in this numerical model, and were therefore discounted from any further analysis. Setting the value of `CTYPE = 4` on the aforementioned keyword, activated the penalty coupling method, which was found to give much more reliable results than the constraint method.

Each CLIS keyword generates a coupling surface for the defined Lagrangian parts; these coupling surfaces can then interact with the surface surrounding the defined `AMMG`. This interaction is achieved by tracking the relative position of both the Lagrangian and ALE objects; if, for a given time step, a penetration is detected, then a penalty force is applied to the ALE material of sufficient magnitude to correct for said penetration. In order to effectively detect penetrations, there must be no coupled ALE material beyond the coupling surface at any time, and for this reason the FSI penalty coupling algorithms are one directional.

The single directionality posed two issues which needed to be taken into consideration when modelling this problem; firstly, any relative movement of the ALE material through the coupling surface, in the direction matching the orientation of the contact surface, would be permitted (FSI would not occur); secondly, for FSI to occur it was necessary to ensure that, when defining the initial geometry of a numerical model, there were no instances whereby the coupled `AMMG` was present on both sides of the coupled Lagrangian part, i.e. for the solver to see the coupling surface between the air and shell container, different `AMMG`s needed to be defined on each side of the coupled Lagrangian part.

Coupling surface directions are calculated from the shell normal vectors and the `NORM` value on the CLIS keyword dictates if the fluid is to be coupled to the head `NORM = 0` or tail `NORM = 1` of each vector. For this problem, the easiest solution was to ensure all of the shell normals of part 3 faced inwards and `NORM` was set to 0.

The following parameters were used to produce realistic and effective penalty based coupling between the air material and the shell container: `NQUAD = 2`, creating 2 x 2 coupling points over each shell element; `DIREC = 2`, permitting only

compressive coupling forces normal to each shell element (a variation on the default value of 1 which allows tension, the gas has no tensile strength) and `FRCMIN = 0.1`, a reduction from the default of 0.5 (activating the coupling algorithm when 10 % of an Eulerian element is occupied by the coupled fluid). It was also necessary to set the penalty force scale factor `PFAC` as a linear function of the penetration distance, where the maximum penetration was set at 10 % of the Eulerian element size (0.1 mm) and the maximum coupling pressure as the pressure when leakage was first observed.

Figures 4.17 (a) and (b) show the pressure and density against time for part 1 and the volume contained by the shell container part 3. Black dashed lines show the final state values which were previously calculated in Section 4.2. There was very good agreement with the predictions; following the initial oscillations (also observed in the previous model), the pressure eventually settled to 39.8 kPa and density to 0.615 kg/m^3. Note that these values were slightly higher than the predicted values of 38.4 kPa and 0.6 kg/m^3 (which the previous model began to settle towards), the discrepancy being due to a slight reduction of the internal volume of the shell container caused by the offset coupling surface.

The coupling surface thickness was 0.2 mm which gives a final expanded volume of 1.37 $\times 10^5$ m^3, a predicted final pressure of 39.6 kPa and a predicted final density of 0.613 kg/m^3; this leaves an error of 0.3 % unaccounted for. This 0.3 % is likely due to the fact that in the corners of the shell container the FSI algorithms would have superimposed and therefore activated slightly earlier, effectively extending the contact surface marginally further into the shell container than the 0.2 mm mentioned above.

When comparing the oscillatory response with that which was observed in Figure 4.15, it can be seen that the decay rate is increased when using the penalty surface as the boundary condition over single point constraints; meaning that the penalty coupling algorithm must add a degree of numerical damping when reflecting the shock.

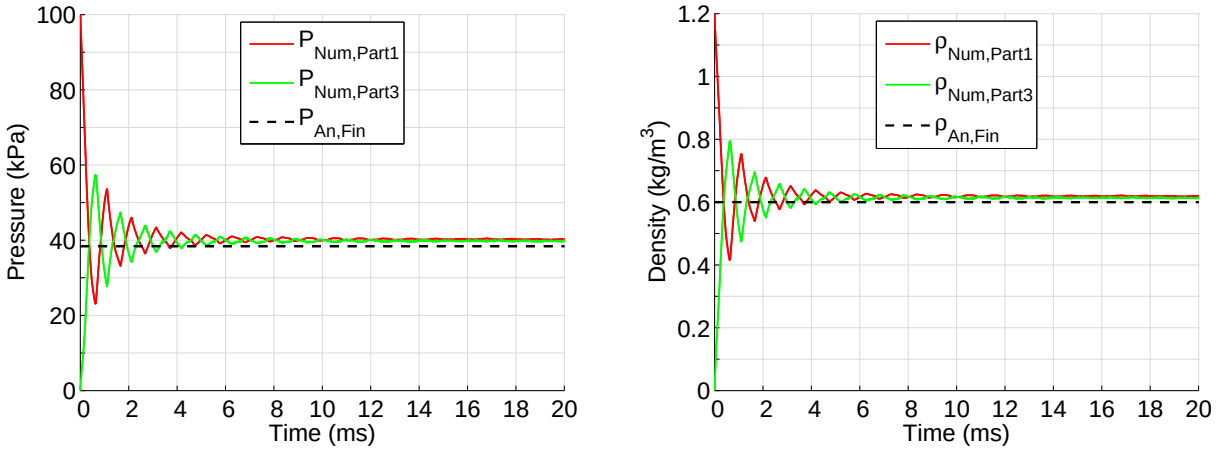

(a) (b)

Figure 4.17 Evolution towards a final equilibrium state following a rapid expansion of air from part 1 (atmospheric) into a rigid shell container part 3 (vacuum), (a) pressure and (b) density vs time. $P_{An,Fin}$ and $\rho_{An,Fin}$ indicate the predicted final pressure and density respectively.

FSI capable of preventing a rapidly expanding pressurised gas from passing through a shell container into a vacuum was realised; indicating that effective FSI could be achieved for the less onerous case (observed during the impact testing), whereby a relatively gradual development of pressure occurs on both sides of each cell wall.

4.4 A fully coupled cardboard honeycomb numerical model

This section details the steps which were required to assemble the modelling techniques, developed in Sections 4.1, 4.2 and 4.3, to create a full scale model capable of capturing the physics involved during the axial impact response of a cardboard honeycomb structure. Comparison between the numerical response and the experimental data presented in Chapter 3, was used to assess the accuracy of the full scale model; to do so, a numerical replication of the experimental tests was achieved

by digitally matching the applied loading, boundary conditions and exact cellular geometry of each sample.

Due to the non-uniform cellular geometries present in the samples used for experimental testing (and therefore lack of symmetry), it was necessary to model the whole structure of each sample to ensure that the response was being accurately expressed; in combination with the fully coupled nature of each analysis and requirement for a large number of self-contact algorithms within the highly distorted geometry, computational cost became a severely limiting factor. To allow the numerical analysis to be completed within a realistic time frame, careful attention was paid to ensure that computational efficiency was a prime consideration when designing the full scale model.

Mechanical properties of the cell wall material were not available, however, a material parameter calibration was possible by firstly selecting values (with guidance from the literature) which gave good agreement with the response of a sample from one mesh type, and then using those values to check the numerical-experimental agreement of a model of a sample from a different mesh type.

4.4.1 Digitisation of the tested samples

To generate the spatially discretised finite element mesh, the following process was performed:

1. Photographs were taken of each honeycomb core before and after the top liner (with square sample grid) was applied

2. Using Photoshop, the photographs were digitally corrected to remove the lens and perspective induced distortion

3. The corrected photographs were then overlaid to reveal the internal cellular geometry of each individual sample

4. The cellular geometry of the samples chosen for testing was imported into AutoCad and digitised, creating 2-D structural cross sections of each tested

cellular arrangement

5. A 3-D geometrical representation of the sample geometries, which were to be modelled, was constructed by extruding the 2-D cross sections and using planar surfaces to represent liner sheets and each cell wall

6. The 3-D surface models were then imported into Altair HyperMesh, which was used to discretise the structural geometry generating a finite element mesh of each structural component

7. The raw finite element meshes were imported into LS-PrePost, allowing any required final formatting to be performed, prior to their use in the numerical analysis.

Stages 1 - 4 were performed as part of the experimental work and are discussed in Section 3.3.5 of Chapter 3, while stages 5 - 7 are novel to the work presented in this section. Two samples were chosen for digitisation, F29 and D27, their average geometrical properties are given in Table 4.7 and dimensions to which they relate are marked on the diagram of an idealised cell in Figure 4.18.

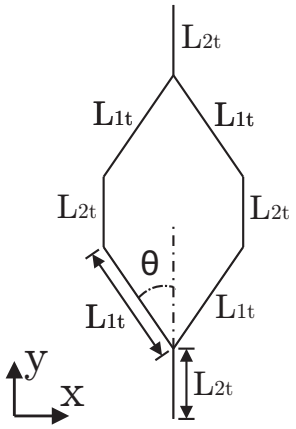

Figure 4.18 The idealised cell.

Sample ref	L_{1t} (mm)	L_{1t} (mm)	$\theta°$
F29	29.8	17.9	36.5
D27	17.3	11.1	35

Table 4.7 Idealised mesoscale geometrical values for samples F29 and D27.

Figures 4.19 (a), (b) and (c) show the geometry of sample D27 at three stages in the mesh generation process; (a), stage 3, an image of the internal geometry is

revealed; (b), stage 5, a 3-D model of the cell walls is created and (c) Stage 6, the 3-D model is discretised using the powerful `2D Automesh` tool, available in Altair HyperMesh.

(a) (b) (c)

Figure 4.19 Three stages of the sample digitisation process. (a) Sample cellular geometry is revealed following image overlay, (b) a 3-D model of the cell wall geometry is created using AutoCad and (c) the 3-D model is discretised using four noded shell elements in Altair HyperMesh.

Figure 4.20 (a) shows a LS-Dyna part schematic of a honeycomb structure with four walls. Solid and dashed lines indicate single and double-ply walls respectively. The part naming convention developed for the (two cell wall) corner element model, in Section 4.1.1, has been followed; that is, each continuous cell wall is given a full integer `PID`, beginning at 1 and incrementing from left to right. Regions of the cell walls which are bonded to adjacent cell walls are named with the convention 801802, where the second and third digits (01) refer to the part number of the cell wall it belongs to, and the fifth and sixth digits (02) refer to the cell wall which it is bonded to.

The suite of solid contact algorithms, which were found to be compatible and to provide good results (Section 4.1.1), required the normals of the double-ply cell walls to face each other, so that when the cohesive bond failed, the cell walls would move apart rather than through each other (shell normal constraint 1). It was also

discovered, in Section 4.3, that the FSI coupling algorithms are one way, meaning that for coupling between the Eulerian gas and Lagrangian cell wall to occur, all shell normals of the Lagrangian parts defined with each CLIS keyword must be uniformly orientated either towards or away from the coupled fluid (shell normal constraint 2). Satisfying both shell normal constraints, was achieved by using the alternating pattern displayed by the arrows, on the internal (blue and orange) cell walls, shown in Figure 4.20 (b).

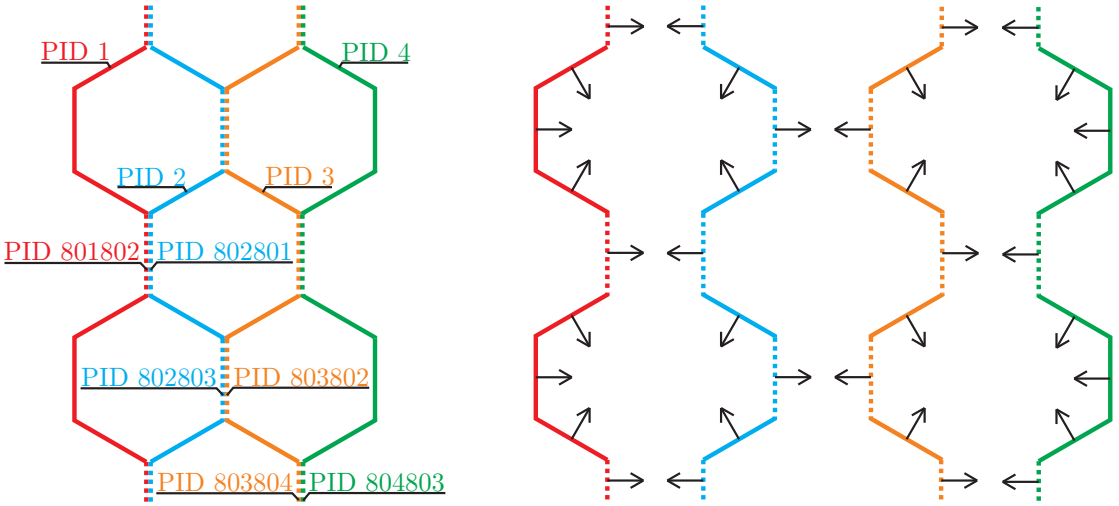

Figure 4.20 Illustration of (a) the part naming convention and (b) shell normal pattern, for a honeycomb cellular model consisting of four complete cell walls.

Figure 4.21 shows a macroscale schematic of the full scale model. The cell wall arrangement is defined as described above, unique to each sample and situated between the top and base liner sheets, (`PID = 500` and `501`). The mesh geometry of the liners conformed to the perimeter of each individual cell; thus, enabling a segment set to be defined encompassing the elements at the base of each cell. These segment sets, allowed each individual cell pressure to be easily extracted during post-processing of the numerical model results. The ring of elements at the top and bottom of all cell walls was moved to parts `400` and `401`, allowing both the tie-break and tied contacts to be used for the cohesive double cell wall bond and contact

between the shell edges and liners, without interference.

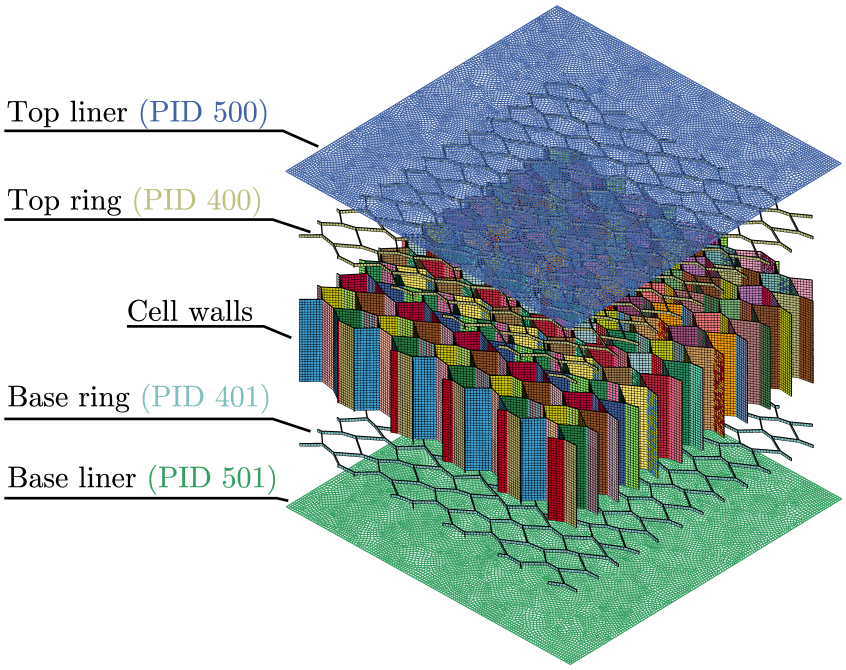

Figure 4.21 Mesoscale schematic of full scale Lagrangian numerical model. For detail of cell walls see Figures 4.19 and 4.20.

The model shown above constitutes the structural components of the honeycomb. To introduce the air, a method was required which would allow the air within adjacent cells to be allocated to different `AMMG`s (necessary for the one-directional FSI coupling algorithms). The irregular cellular arrangement meant that it would be an incredibly onerous task to match the mesh geometry of the Eulerian domain to the internal geometry of each cell; furthermore, the existence of sharp angles at some of the vertices made it impossible to generate a conforming Eulerian mesh without severe impact on the critical time step size.

The solution was to use a background domain of uniform cubic multi-material Eulerian elements and to allocate the gas material at desired locations to different `AMMG`s with the `*INITIAL_VOLUME_FRACTION_GEOMETRY` (IVFG) keyword. The background domain was 325 x 325 mm on plan and 90 mm tall, providing enough clearance to allow flow around the perimeter of the sample, which was situated centrally with the domain.

In combination with the IVFG keyword, a method of defining the geometry and location of each region must be selected. Many methods are available, but due to the irregular honeycomb geometry only two suitable methods were identified: the use of segment sets, or the use of shell elements. At the time of model construction, the most current version of LS-Dyna (for the available license) was revision 6.0.0, with this, the use of segment sets with the IVFG keyword was found to be extremely erratic when defining three different materials in close proximity, and therefore useless for this application.

Fortunately, the use of non-structural, sealed, shell containers (with all shell normals pointing inwards), to encompass the volume within each cell, in combination with the second method IVFG method, was found to give good results. The shell containers which were created for sample D27 are shown in Figure 4.22 (a). For every defined `AMMG` the surface is tracked throughout the numerical analysis, for multiple `AMMG`s the computational cost in both CPU time and memory was found to be substantial. So substantial in fact, that it was necessary to use the minimum of four `AMMG`s (which would ensure the `AMMGID` of gas in adjacent cells was always different) in order to get the model of sample D27 to pass the initialisation phase.

The arrangement of the four `AMMG`s, as defined by parts `901 - 904`, is shown by the four different colours in Figure 4.22 (b). Each vertical strip of colour also identifies a strip of cells (between two adjacent continuous cell walls), the air within them being separated only by the cohesive bond of the double-ply cell walls. To add further efficiency, coupling was only defined between each `AMMG` and the cell walls initially in contact. For reference, the segment set containing the elements at the base of each cell was given a number as shown in Figure 4.22 (b).

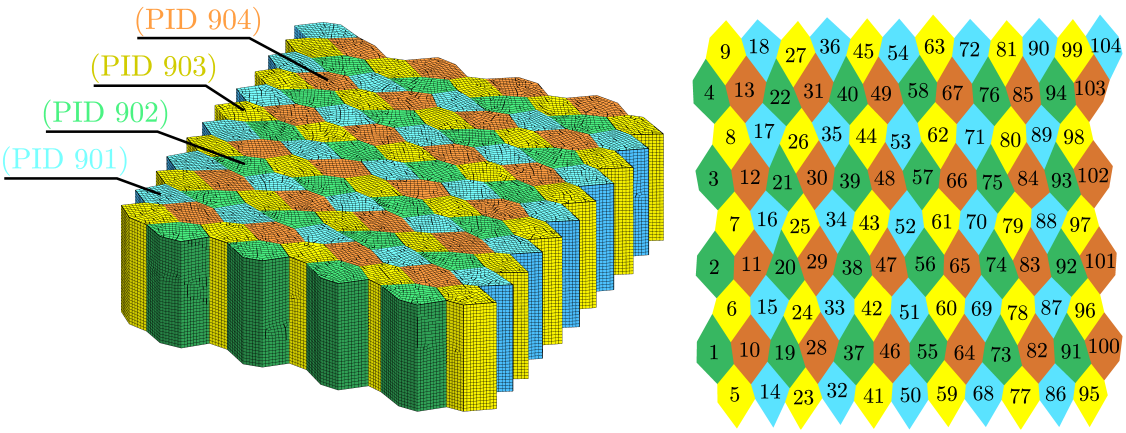

(a) (b)

Figure 4.22 Definition of air within sample D27 (a) non-structural shell containers used to define internal `AMMGs`; (b) complete cells, showing numbering convention.

In an attempt to closely emulate the loading and restraint conditions present during the experimental testing, digital representations of the projectile and back plate arrangements, as shown in Figure 4.23, were constructed to crush and support each sample.

The loading block (`PID 200`) was given identical dimensions to the experimental front plate and was modelled with solid elements and rigid material properties (using the `*SECTION_SOLID` and `*MAT_RIGID` keywords). A value of density was chosen so that when multiplied by its volume, the total mass matched the total projectile experimental mass of 81.4 kg; the elastic modulus was defined so that the internal wave speed matched that in the cell walls, which aided in the achievement of stable contact between the loading block and the top liner, by using the `*CONTACT_AUTOMATIC_SURFACE_TO_SURFACE` algorithm. A displacement time history was then defined, using the `*BOUNDARY_PRESCRIBED_MOTION_RIGID` keyword, to match the displacement time history observed for the projectile during each experimental test

The back plate and load cell were modelled as one combined part (`PID 300`) with elastic, 8 noded, single point integration, solid elements using the `*SECTION_SOLID` and `*MAT_ELASTIC` keywords. A density of 7850 kg/m^3 and elastic modulus of 200 GPa was used, corresponding to mild steel. The collar was defined in an identical

manner and even had shared nodes with (PID 300), but the elements were moved to a different part (PID301) allowing greater control over contact definition with the honeycomb components.

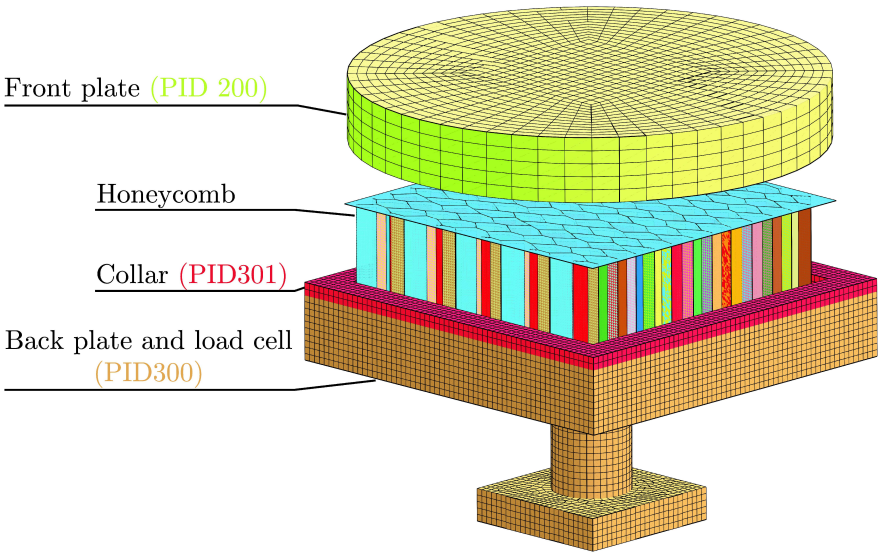

Figure 4.23 Schematic showing sample support and loading conditions. For detail of the honeycomb model see Figure 4.20.

4.4.2 Necessary modifications to add stability

During an explicit numerical analysis, the occurrence of a numerical instability will lead to unrealistic results, and in the majority of cases, a catastrophic premature termination of the simulation. Common forms of numerical instabilities include violations of the critical time step, negative volumes, shooting nodes and uncontrolled oscillations in zero energy hourglass modes. As the complexity of a model is increased, so is the possibility for instabilities to occur; by necessity, the coupled full scale model included many computational components, and was therefore extremely unstable.

Identifying the source of numerical instabilities and determining solutions, proved to be one of the most difficult and time consuming challenges encountered during this thesis; it was not uncommon for numerical instabilities to present themselves in the late stages of an analysis, causing a premature termination after weeks of real

computational time. Minor modifications to the simulation were possible through the restart function (such as deletion of problem elements and nodes), however for any major modifications a full restart, from time 0, was required.

There were two main contributing factors to numerical instability: the requirement for a large number of penalty contact algorithms, and extreme geometrical deformations. The presence of both caused an amplification of their individual adverse effects by enabling situations whereby nodes and AMMGs could be subject numerous conflicting penalty contact forces. In addition, the structural contact algorithms were required to be sufficiently robust, as to prevent penetrations at high degrees of geometrical deformation; one commonly observed mechanism of instability was where a spurious structural penetration would force some of the gas material through a cell wall, effectively trapping it and causing a premature termination by the creation of a negative volume. Reducing the bucket sort frequency to every 5 time steps, using the BSORT variable, was found to help prevent against some, but not all, spurious penetrations.

By default, the penalty contact algorithm in LS-Dyna checks for penetrating slave nodes through master segments and applies correcting penalty forces to each discovered offending node; the penalty stiffness of the node-surface method is independent of the global time step. Segment based contact checks for penetration between surfaces (each of which are defined by four nodes) and distributes the correcting penalty force to all involved segment nodes; the penalty stiffness of the surface-surface method is dependent on the global time step. In most cases, the node-surface method is adequate, and due to its non-dependence on the global time step it is also normally the cheapest. At large deformations, the node-surface method was extremely unreliable at preventing unwanted penetrations, while the surface-surface (segment based contact) method produced very good results; segment based contact was activated by setting SOFT = 2 on the fourth card of each *CONTACT keyword definition.

Hallquist [60] states that for the SOFT = 2 segment based contact, the penalty stiffness κ is inversely proportional to the square of the global time step, $\kappa \propto$

$(1/\Delta t^2_{global})$, where the global time step is a reduction of the critical time step by $\Delta t_{global} = \texttt{TSSFAC} \times \Delta t_{crit}$. Consequently, any reduction of the time step through `TSSFAC` will result in a squared increase in κ. Earlier in this chapter, it was discovered that to maintain numerical stability when using the Eulerian formulation, it was necessary to reduce `TSSFAC` from its default value of 0.9, to 0.5. Thus, dramatically increasing the penalty stiffness (and therefore forces) between the cell walls, to magnitudes which were capable of destroying the cardboard cell wall material without any external loading.

Numerical stability was regained by reducing the penalty stiffness scale factors, of the slave `SFS` and master `SFM` surface (on the third card of each `*CONTACT` keyword), through trial and error to find values which added sufficient stability to permit completion of the analyses, while still provided adequate force to correct spurious penetrations. Values which were found to work best were between 0.09 for contact including the double-ply cell walls and 0.5 for contact between cell walls and the liners.

When coupling was introduced via the `*CONSTRAINED_LAGRANGE_IN_SOLID` (CLIS) keyword, the simulations began to erratically terminate (without any reported errors to guide debugging process), eventually, it was discovered that this was due to the method used to calculate the direction of the applied penalty forces. By default FSI penalty force directions are calculated from normal vectors located at the nodes; setting `NORMTYP = 1` instructed Dyna to alternatively calculate the penalty force directions using segment normals vectors, and in doing so, remedied the erratic, unclassified terminations. It is thought that implementing this modification had such a dramatic positive effect due to increased compatibility with the `SOFT=2` based contact discussed above.

To reduce the CLIS induced numerical instability sufficiently, to allow the desired analysis time to be reached, further modifications to the coupling parameters (developed in Section 4.3) were required. As was the case with the structural contact algorithms, relaxing the magnitude of the penalty forces was found to add stability; this was done by returning the values of `PFAC` and `FRCMIN` to their default values

of 0.1 and 0.5, setting the FSI penalty stiffness to 10 % of the estimated critical penalty stiffness and only activating coupling when 50% of an Eulerian element was filled with the coupled `AMMG`. The relaxation of the FSI contact parameters had a detrimental side effect of allowing leakage to occur; this leakage was eliminated by activating the strong leakage control, by setting the parameter `ILEAK = 2` and using a very small value for the leakage control penalty factor of just `PLEAK = 0.001`.

4.4.3 Material parameter calibration

With the resources available at the time of experimental testing, it was not possible to measure the mechanical properties of cardboard material which constituted the cell walls of the tested samples. In Section 4.1.5, it was shown that a simple linear elastic plastic material model was sufficient to capture both the initial and subsequent progressive buckling mechanisms, which dictate the axial buckling response of a generic cellular honeycomb material. It was also shown that the magnitude of the initial peak is solely dependent on the properties of the cell wall material, and that at the impact velocities $v_i > 9.45$ m/s and cell wall thickness to length ratios $(t/L) > 0.009$ observed during the experimental testing (see Equation 4.26 and Figure 4.9), the magnitude of the initial peak stress σ_{Peak} is likely to be a function of the cell wall yield strength σ_{Yield}; using the known relationship between σ_{Peak} and σ_{Yield} it was possible to determine numerical values for the single $\sigma_{Y,t1}$ and double-ply cell wall $\sigma_{Y,t2}$ yield strengths.

From tensile tests performed on cardboard honeycomb cell wall material, E and Wang [51] reported that the yield strength of the double-ply cell walls $\sigma_{Y,t2}$ was enhanced, by the factor k, in comparison to strength of the single cell walls $\sigma_{Y,t1}$. E and Wang [51] also reported a reduction of $\sigma_{Y,t2}$, $\sigma_{Y,t1}$ and k with increased relative humidity (RH); at 30% RH, k was given as 1.572.

During the impact testing, presented in the previous chapter, the RH of the testing environment was not recorded; however, care was taken to ensure that once constructed all samples to be tested were kept in a dry, heated, environment (next to a radiator), only transported to site on the day of testing and even then placed next

to a halogen space heater, ensuring that the water content within the cardboard material was kept to an absolute minimum.

In the Lagrangian structural analyses presented earlier in this chapter, the glue strength was chosen as to provide a full strength bond between the double cell walls, removing the unquantified de-bonding effect from the simulations. From visual inspection of the experimentally crushed samples, de-bonding was found to be present throughout; thus it was necessary to reduce the strength of the glue σ_{Glue} between the double cell walls to allow de-bonding to occur in the numerical model.

Experimental values for σ_{Glue} were not known; preliminary numerical analysis showed that a reduction in σ_{Glue} caused a reduction in $\sigma_{Plateau}$. A relatively small value of σ_{Glue} was chosen in comparison to an estimated experimental value, allowing de-bonding to occur, while ensuring that any error induced by deviation from the actual experimental value of σ_{Glue} would be visible as a qualitative *reduction* in $\sigma_{Plateau}$.

Using a value of $\sigma_{Glue} = 62.5kPa$ and holding all other material parameters constant (determined in Section 4.1.2), the cell wall yield stresses were scaled (with the proportion $\sigma_{Y,t2} = 1.572\sigma_{Y,t1}$), so that the peak stress transmitted by a Lagrangian-only numerical model, matched the peak recorded by the load cell during the impact response of sample F29; values of of $\sigma_{Y,t1} = 4.2$ MPa and $\sigma_{Y,t2} = 6.6$ MPa were found to give good agreement, this was promising as values attained from tensile testing of cardboard honeycomb cell wall material by Wang and E [44] and Wang, Wang, and Liao [42] were in the region of $5 - 10$ MPa.

Table 4.8 shows the full compliment of material parameters used to model the cellular structure. Red text indicates values which have been adjusted from those determined in Section 4.1.2 (see Table 4.2). Note that only adjustments to the cell wall and glue yield strengths were made. Unless otherwise stated, the parameters in the table below were used for all numerical analyses in this section.

Table 4.8 Structural linear elastic-plastic material properties used for the full scale model, those shown in red were adjusted (from those given in Table 4.2) as a result of the material parameter calibration.

$\sigma_{Y,t1}$	$\sigma_{Y,t2}$	k	E	E_t	ν	ρ	σ_{Glue}
4.2 MPa	6.6 MPa	1.572	2 GPa	0.2 MPa	0.3	603 kgm^3	62.5 kPa

These parameters were then used to perform two simulations, both Lagrangian-only and identical in every respect apart from the structural geometry; one simulation was performed of F29 and one of D27, comparison between the numerical ($\sigma_{Total,Num,[F29,L]}$, $\sigma_{Total,Num,[D27,L]}$), and experimental ($\sigma_{Total,Exp,[F29]}$, $\sigma_{Total,Exp,[D27]}$) macroscopic responses is given in Figures 4.24 (a) and (b).

With such minimal initial modifications to the structural modelling techniques developed in Section 4.1, the correlation with the experimental data was surprisingly good, which suggested that the logic and methodology followed during the model development process was sound. The peak stress of sample F29 was used to scale the numerical response (by **only** adjusting the yield stress of the cell wall material), and so that correlation holds no significance; however, when the same material properties were extrapolated to a model of D27 there was very good agreement between the numerical and experimental peak stresses.

It must be noted that the experimental traces presented below do not represent the true honeycomb response; the recorded initial stiffness is substantially lower, and therefore strain to peak stress substantially higher, due to experimental factors. Factors which were determined to have a detrimental effect on the recorded stiffness were:

- the presence of a pre-impact pressure wave generated due to the rapid acceleration of the front plate, causing a compression of the contiguous cushion of air
- the dynamic, inertial response, of the heavy back plate causing a drawing out of the time base over which the compressive load was transmitted to the load

cell strain gauges

- a possible ringing along the length of the projectile over the initial impact stroke
- slack take up due to bedding of the honeycomb samples.

Discounting the spurious components of the measured response, there is good agreement between the overall shapes of the experimental and numerical responses. Comparing the plateau regions of these initial analyses, there is better agreement with the plateau magnitude for F29 than D27; the reason for this was not clear. The structural only numerical stiffening limbs also occur later than those measured by the load cell, which is not surprising as this region of the macroscopic response has been shown to be dominated by the internal air pressures (which were absent in this model).

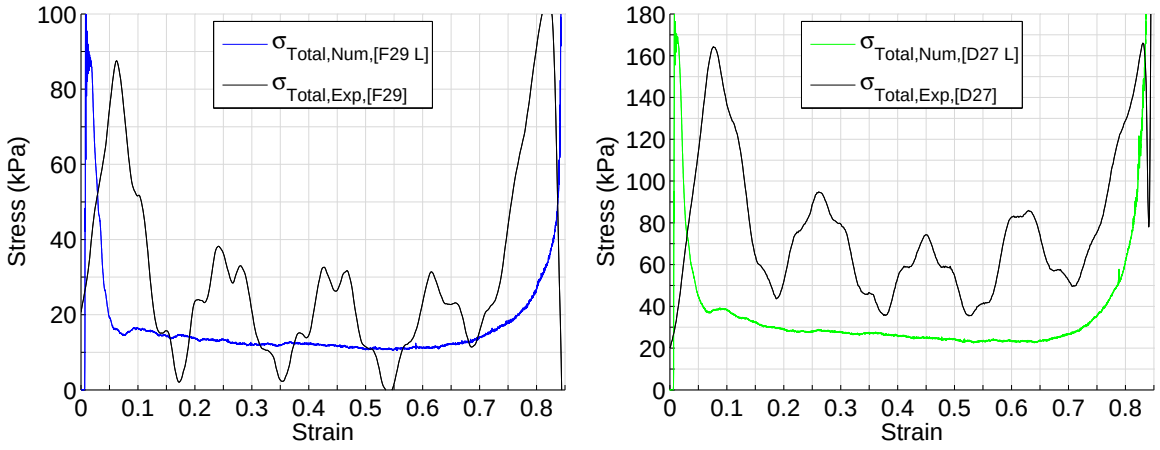

(a) F29 (b) D27

Figure 4.24 Comparison between experimental and Lagrangian only numerical macroscopic responses of samples F29 and D27. $\delta_{EL} = 1$ mm.

A very low value of σ_{Glue}, relative to $\sigma_{Y,t2}$, was used in the above analysis to allow de-bonding and effectively generate a lower bound response. An upper bound was created by repeating the analysis with a full strength bond $\sigma_{Glue} = \sigma_{Y,t2}$; the

actual experimental value of σ_{Glue} must have lay in the envelope between the weak and full strength bond.

To reduce computational time, a 2 mm mesh was used. The results for both Lagrangian-only analyses are shown in Figures 4.25 (a) and (b) for samples F29 and D27 respectively. It can be seen that in these structural only analyses, the full strength bond caused a reduction in gradient of the post peak softening limb, a lift of the plateau stress, and further delay of the compaction limb. The lift in plateau stress was not significant enough to explain the shortfall in plateau of sample D27. Interestingly, the full strength bond also introduces a shoulder to the softening limb, a feature which was also present on the experimental traces, but it was not clear if that was part of the genuine structural response.

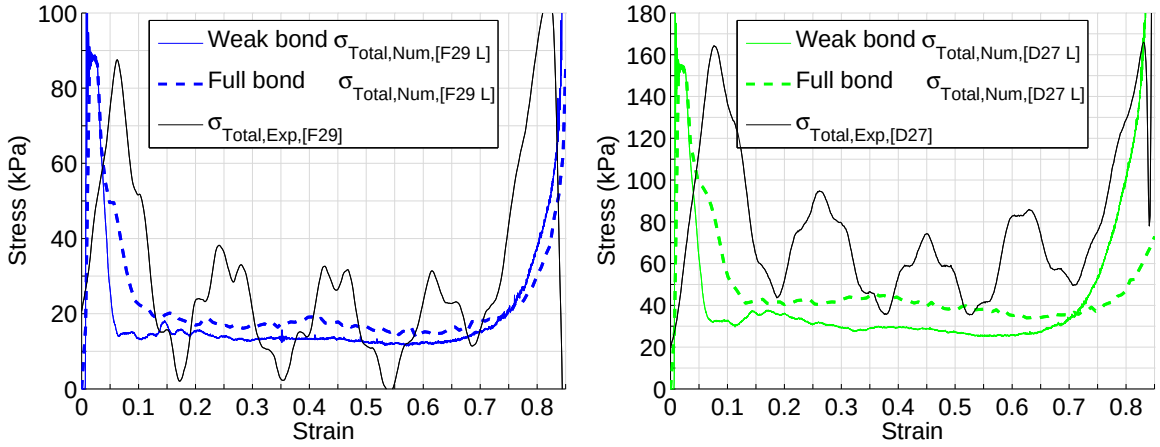

(a) F29 (b) D27

Figure 4.25 Comparison between experimental and Lagrangian only numerical macroscopic responses samples of F29 and D27 using a *weak* ($\sigma_{Glue} = 62.5$ kPa) and full strength *strong* ($\sigma_{Glue} = 6.6$ MPa), glue bonds. $\delta_{EL} = 2$ mm.

Good agreement between the structural only models and the experimental data was achieved with minimal modification to the material properties, suggesting that the chosen Lagrangian numerical modelling techniques were valid. The observed deviations were deemed more than acceptable when considering the omission of air, complexity of the event being modelled, lack of exact material parameters and

uncertainty in the recorded data.

During the impact testing, the magnitude of internal air pressures was observed to increase significantly with increased lateral confinement; it is therefore likely that the accuracy of these Lagrangian-only numerical models is limited to samples which provide similar levels of confinement; and understanding of the mechanisms introduced by the air is required for extrapolation to greater plan areas and finer meshes.

4.4.4 Mesh refinement and numerical validation

In Section 4.1.6 a mesh study was performed to assess the impact of changing the mesh size on the accuracy and computational cost of a simple Lagrangian-only model. It was discovered that a 1 mm mesh provided substantial cost saving, with minimal reduction in the accuracy of the simulation. When scaling up the model and introducing the Eulerian parts, it quickly became apparent that computational cost was going to be a limiting factor. The following work was performed to assess the feasibility of achieving additional reductions in computational cost by further increases in the element size.

For both samples, four meshes were created with δ_{EL}: 6, 4, 2 and 1 mm; each mesh consisted of even square four noded shell elements. These 8 meshes were used to perform 8 otherwise identical Lagrangian-only simulations, using the parameters presented in Table 4.8. Table 4.9 shows a cost comparison of all 8 Lagrangian-only simulations, where T_{Real} is the total real simulation time required to complete each analysis and ϕ_{Cost} is the relative cost for each simulation, where $\phi_{Cost} = {}^{T_{Real}}/_{T_{Num}}$. Note that ϕ_{Cost} provides a decimal rather than sexagesimal number for inter simulation cost comparison.

The cellular structure of sample D27 consisted of a larger number of cell walls than sample F29; to model these additional cell walls it was necessary to define more elements, more parts and more contacts between them. When defining a greater number of computational objects, the system of equations, which describe their position and deformation, expands; the effect of this increase in complexity

is two fold: more physical memory is required to hold the system of equations and more calculation time is required to solve them and advance to the next time step, and so the overall computational cost increases.

Considering the cost of the simulations using the 1 mm meshes it can be seen that the impact of increased scale was substantial; when a 1 mm mesh was used for the simple corner element model, in Section 4.1.6, ϕ_{Cost} was 4.84×10^4; for the same mesh size (and wave speed) applied to the full scale structural simulations of sample F29 and D27 ϕ_{Cost} increased to 4.62×10^6 and 1.36×10^7 respectively, factors of 95 and 281 times more expensive. Additionally, elements were added as the mesh size was reduced; the cost increased relative to the 6 mm mesh with the ratios 1: 2.59: 9.36: 17.36 and 1: 2.33: 4.16: 14.6, (with a decrease of mesh size from 6: 4: 2: 1 mm) for the F29 and D27 models respectively.

This was not an exact comparison as more than one model may have been running on the machine used to perform the analysis. However, due to stability it was necessary to use a shared memory parallel (SMP) solver. The standard practice was to ensure that there was at least 20 % reserve of the maximum memory and CPU load free at all times, limiting the detrimental effect on computational efficiency encountered when throttling resources, and so the relative computational times still provide a good estimate of the relative computational costs.

Table 4.9 Comparison of relative costs ϕ_{Cost} of the full scale Lagrangian-only numerical models, for varied mesh sizes δ_{EL}. Where $\phi_{Cost} = {}^{T_{Real}}/_{T_{Num}}$ and $T_{Num} =$ 6.8 ms.

	F29 L		D27 L	
δ_{EL} (mm)	ϕ_{Cost}	T_{Real} (hh:mm:ss)	ϕ_{Cost}	T_{Real} (hh:mm:ss)
6×6	2.66×10^5	00:30:12	9.30×10^5	01:45:26
4×4	6.91×10^5	01:18:16	2.17×10^6	04:05:23
2×2	2.49×10^6	04:41:41	3.87×10^6	07:18:02
1×1	4.62×10^6	08:43:40	1.36×10^7	25:45:24

The macroscopic response of all 8 Lagrangian-only models are shown in Figures 4.26 and 4.27. Variation of the mesh size had little to no effect on the magnitude of the initial peak, likewise, the plateau stress magnitude was relatively insensitive to changes in the mesh size; the rest of the macroscopic response converged as δ_{EL} was reduced. The convergence was mostly visible in the change of gradient of the post peak softening limb and compaction limb, which indicates the softening and compaction rate. This effect is caused by a limitation on the smallest resolvable fold by a mesh of given δ_{EL}; the occurrence of earlier stiffening for a larger mesh size is due to the presence of less unfolded cell wall at any given strain. As the mesh size was reduced, there were diminishing returns on the added accuracy; in comparison to the additional computational cost, the accuracy gained from reducing the mesh size from 2 mm to 1 mm was very small.

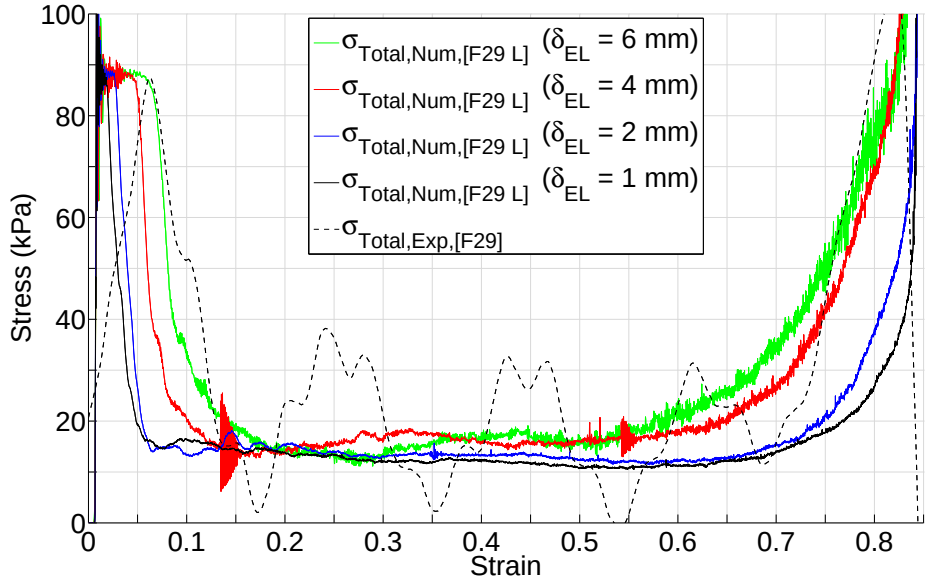

Figure 4.26 Comparison between experimental $\sigma_{Total,Exp,[F29]}$ and full scale, Lagrangian-only (L), $\sigma_{Total,Num,[F29L]}$ numerical macroscopic responses, for sample F29 and varied mesh size δ_{EL} = 1 to 6 mm.

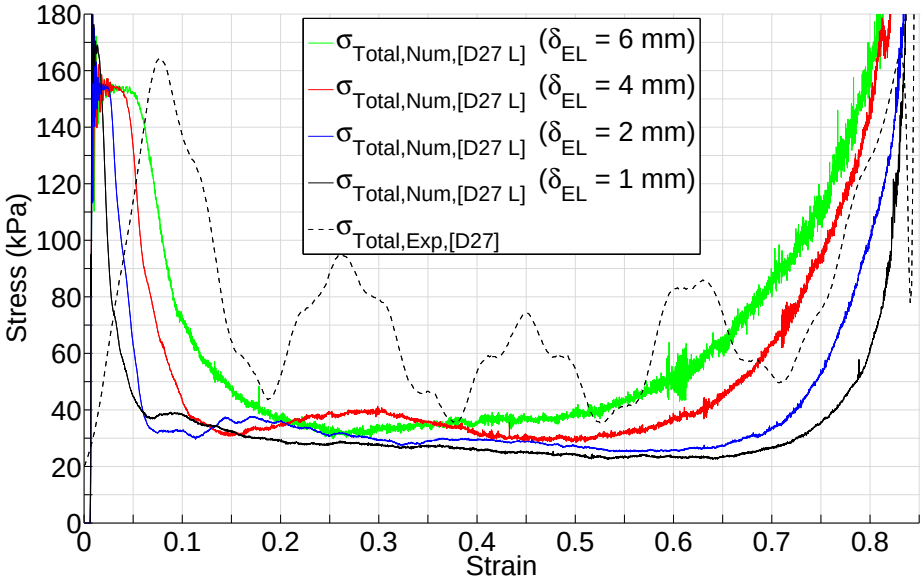

Figure 4.27 Comparison between experimental $\sigma_{Total,Exp,[D27]}$ and full scale, Lagrangian-only (L), $\sigma_{Total,Num,[D27L]}$ numerical macroscopic responses, for sample D27 and varied mesh size $\delta_{EL} = 1$ to 6 mm.

The next step was to introduce the air to the model; the structural meshes were placed centrally within a 325 x 325 x 90 mm cuboid domain mesh. The Eulerian domain was meshed with regular cube elements with dimensions matching each structural mesh. Five ALE multi material groups `(AMMGs)` were defined, one for the background gas, and one for the gas within each of the each of the four alternating strips of cells (identified by green, yellow, blue and orange in Figure 4.22); Table 4.10 displays the computational time and relative costs of all six analyses.

Introduction of the Eulerian domain and the definition of the 5 `AMMGs` with their coupling to the Lagrangian structure substantially increased the computational cost, in comparison to the Lagrangian-only analyses. Comparison between the two Lagrangian-only (L) and two Lagrangian + Eulerian (L+E) simulations performed with 2 mm meshes shows an increase in the cost by a factor of 57 and 79 for samples F29 and D27 respectively.

As the mesh size was reduced, ϕ_{Cost} for the simulation of sample D27 increased with the ratio 1: 2.7: 7 (with respect to the 6 mm mesh); using a 2 mm mesh, the

total required time to complete the necessary 6.8 ms simulation was 579 hours 3 minutes and 4 seconds, which is just over 3 weeks and 3 days. Using the relative cost of the Lagrangian-only simulations as a guide, with the computational power available, it was estimated that using a 1 mm mesh would take a minimum of 6 to 9 weeks; this would have been a substantial investment of time, with no guarantee of full convergence, especially considering that the amount of memory required would have prevented any other simulations from being ran in parallel. An attempt was made at initialising a 1 mm mesh simulation: the machine which was available at the time had 8 GB of RAM, which was not enough.

Table 4.10 Comparison of relative costs ϕ_{Cost} of the full scale, fully coupled Lagrangian and Eulerian (L + E) numerical models, for varied mesh sizes δ_{EL}. Where $\phi_{Cost} = {}^{T_{Real}}/_{T_{Num}}$ and $T_{Num} = 6.8$ ms.

	F29 L+E		D27 L+E	
δ_{EL} (mm)	ϕ_{Cost}	T_{Real} (hhh:mm:ss)	ϕ_{Cost}	T_{Real} (hhh:mm:ss)
6 × 6	5.17×10^6	009:46:15	1.53×10^7	028:54:05
4 × 4	2.57×10^7	048:30:15	4.19×10^7	079:13:14
2 × 2	1.42×10^8	268:56:32	3.07×10^8	579:03:04

Figures 4.28 and 4.29 show comparisons between the fully coupled analyses and recorded traces for samples F29 and D27 respectively. The Lagrangian only analyses converged towards an underly stiff late response, failing to capture the magnitude and timing of the stiffening limb. It can be seen that by introducing the air, the stiffening limb was simulated more accurately; it was shown during the experimental testing that while the early response was controlled solely by the structure, as the crushing progressed, developing air pressures began to dominate.

Reducing the mesh size caused convergence towards a less stiff response with increased gradient of both the (post peak) softening and (compaction) stiffening limbs. Unlike the Lagrangian-only analyses, variations in δ_{EL} had a significant effect on the magnitude and shape of the plateau region, with convergence towards

a lower, flatter plateau with a sharper angle at the transition between the softening limb and plateau. The convergence effect was more pronounced for sample D27, this is visible from the larger gaps between the numerical traces in Figure 4.29 compared to the gaps in Figure 4.28.

Comparison between the dashed black and blue lines in Figure 4.28, shows very good agreement between the experimental $\sigma_{Total,Exp,[F29]}$ and the numerical $\sigma_{Total,Num,[F29L+E]}$ for the 2 mm mesh. Figure 4.29 also shows good agreement between the experimental and numerical responses for sample D27. Numerical models of both samples produced plateau which was lower than the recorded data. This deviation was more pronounced in the model of sample D27 than the model of F29 and was attributed to the variation in the material parameters from the actual experimental values; in these analyses, the lower bound value for σ_{Glue} was used and so it was known for certain that at least one of the numerical material parameters was lower than the experimental values.

It was decided that further material parameter calibration, to remove all numerical-experimental deviations, would be extremely costly and would be of limited use; from the comparisons drawn between the numerical and experimental macroscopic responses, confidence was gained that the modelling techniques were capturing the evolution of the mesoscale mechanisms which contribute to the macroscopic EDM impact response.

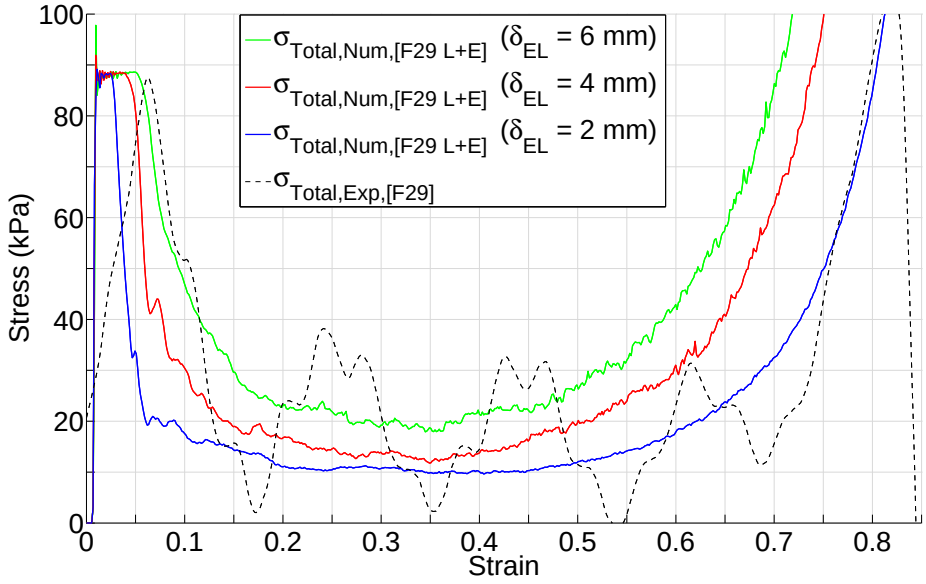

Figure 4.28 Comparison between experimental $\sigma_{Total,Exp,[F29]}$ and full scale, fully coupled Lagrangian and Eulerian (L + E) $\sigma_{Total,Num,[F29L+E]}$, numerical macroscopic responses, for sample F29 and varied mesh size δ_{EL} = 1 to 6 mm.

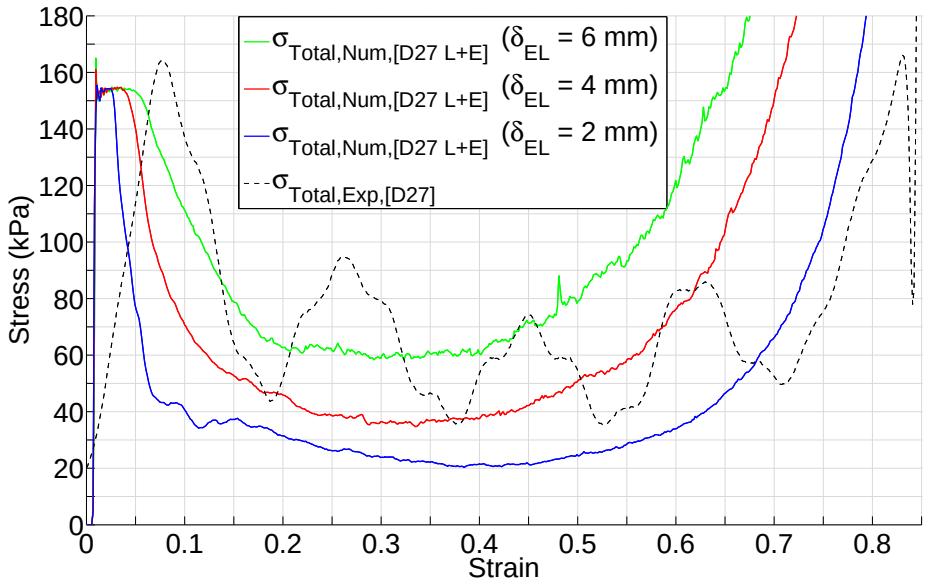

Figure 4.29 Comparison between experimental $\sigma_{Total,Exp,[D27]}$ and full scale, fully coupled Lagrangian and Eulerian (L + E) $\sigma_{Total,Num,[D27L+E]}$, numerical macroscopic responses, for sample D27 and varied mesh size δ_{EL} = 1 to 6 mm.

Figures 4.30 and 4.31 compare the experimental internal pressures, for samples F29 and D27, with those generated during the fully coupled analyses with a 2 mm mesh. Colours identify each pressure gauge, a diagram of their locations within each sample is shown; solid and dashed lines indicate numerical and experimental results respectively.

In Figure 4.30 it can be seen that the edge pressure gauge (PG1) was not initially located within a closed cell for sample F29; there was no recorded pressure on PG1 until 70% strain, after which the pressure began to increase. This feature, which was visible on both the numerical and experimental traces, was due to the creation of a sealed volume between the crushed cell walls and the steel collar.

Both simulations produced internal pressures of a higher magnitude than the recorded experimental pressures, at full compaction the numerical pressures were a factor of 3 to 4 larger than the recorded pressures. While the magnitude was larger, higher pressures developed within the model of D27 than within F29, which agrees with the experimentally observed correlation between degree of confinement and magnitude of developed pressure.

Likeness can also be drawn between the shape of the numerical and experimental traces. During the experimental testing, as lateral confinement was increased, the shape of the pressure traces shifted from a plateau followed by a dip and a transition into an exponential region (F mesh) to a linear increase transitioning into the exponential region (D and B meshes). The shape of the numerical traces resembles the pressure traces recorded within the D mesh samples, whereby there was a linear increase followed by an exponential increase starting around 60% strain.

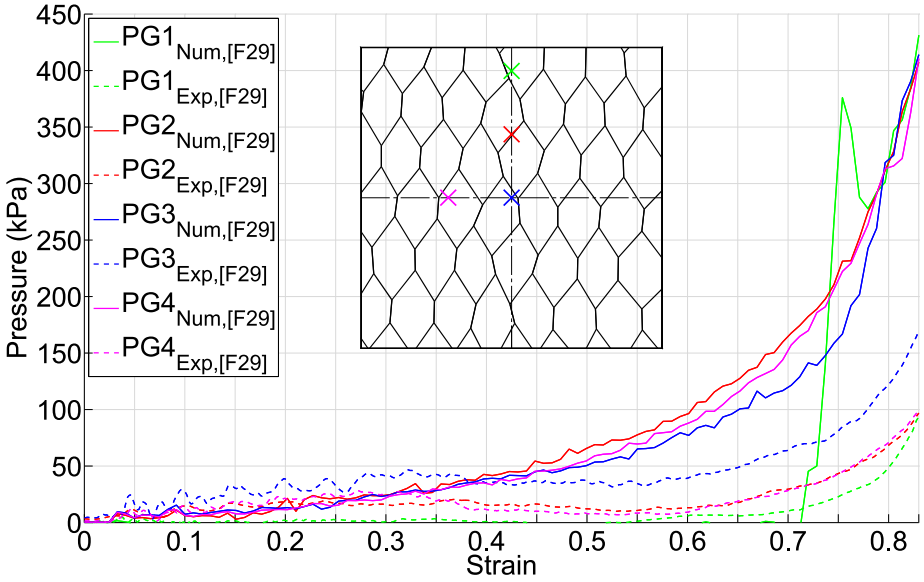

Figure 4.30 Comparison between experimental and numerical pressure gauge readings for sample F29. $\delta_{EL} = 2$ mm.

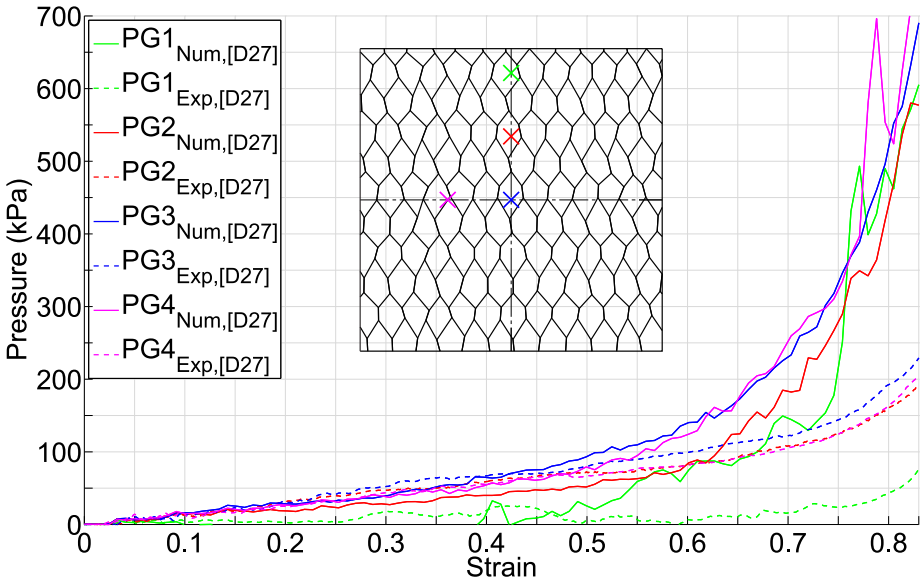

Figure 4.31 Comparison between experimental and numerical pressure gauge readings for sample D27. $\delta_{EL} = 2$ mm.

The discrepancy between the magnitude of the numerical and experimental internal air pressures appeared to be due to a difference in the lateral confinement.

With the additional numerical confinement being due to either: an additional restraint to gas flow caused by the chosen numerical methods or, deviations between the numerical and experimental structural material parameters. In reality, it was likely to be a product of the two, but their exact contributions were to remain elusive without substantial computational time.

One source of spurious numerical confinement can be seen by looking at Figures 4.32 (a) and (b), which show how the development of the pressure at the central pressure gauge changed in response to mesh size, for sample F29 and D27 respectively. Solid coloured lines represent numerical results and the dashed black lines show the experimental traces. There is a clear convergent behaviour towards the experimental trace; it would appear that with the 2 mm mesh size, the simulation has not converged, however, due to the presence of other unknown variables and the previously discussed limitations on computational power, the extent of the non-convergence is unknown.

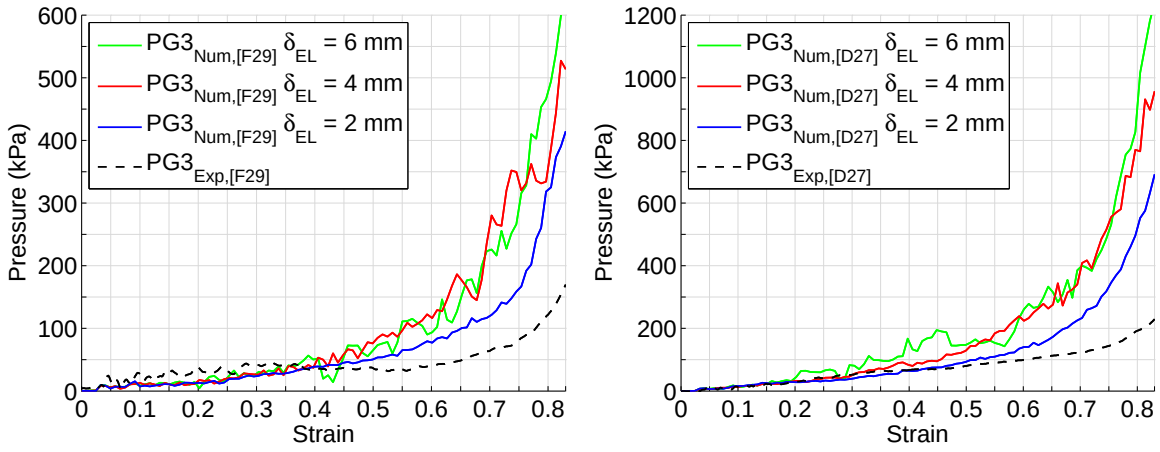

(a) F29 (b) D27

Figure 4.32 Comparison between experimental and numerical central pressures for varied mesh size, showing convergence towards the experimental response with reduced δ_{EL}.

4.5 Discussion

A numerical model capable of capturing the high strain rate axial crushing response of the cardboard honeycomb EDM was constructed. From measurement of internal air pressures during impact tests of the EDM, in Chapter 3, it was shown that the high strain rate crushing behaviour is a function of both the structural response and the development of internal air pressures. Therefore, to capture the resulting micro-structural mechanisms, which dictate the macroscopic cardboard honeycomb EDM behaviour, it was necessary to include numerical representations of both the cell wall structure and the air within each sealed cell.

The modelling capability was developed through using simple problems and existing literature to verify newly introduced numerical techniques. As complexity was gradually increased, issues of numerical stability and computational cost became increasingly onerous, imposing strict limitations on the numerical methods. In Sections 4.1 and 4.2 models of the structure and air were developed independently, in Section 4.3 a method of coupling between them is investigated and in Section 4.4 the verified computational methods are used to create full scale models of samples F29 and D27, which were crushed during the experimental testing. Comparison between their numerical responses and experimental data provided numerical validation.

The cellular structure was constructed from four noded, Lagrangian, Belytschko-Lin-Tsay shell elements with four nodes through their thickness and one on plan; Wong-Chiang variations were activated, adding warping stiffness and allowing the elements to accurately and stably resolve the alternate progressive folding mechanism. The cell wall material was defined with a linear elastic-plstic material model, which was found to give reasonable results.

A suite of various segment based structural contact algorithms was used to prevent spurious self and adjacent penetrations of the cell wall nodes. The glue bonds between the double-ply cell walls were modelled with a simple tie break penalty contact.

The air was modelled using Eulerian multi-material elements and an adiabatic

ideal gas equation of state. The Lagrangian structure was placed centrally within an Eulerian background domain, and non-structural shell containers were used to define the volume within each cell which was to be filled with air; coupling between the air and cell walls was defined using a penalty FSI algorithm.

Computational cost of the fully coupled analyses was very high. The most demanding simulation performed during the work presented in this chapter was of sample D27 using a 2 mm mesh. It required 91 parts, 350 thousand Lagrangian shell elements and 1.2 million Eulerian multi-material solid elements. To complete a 6.8 ms simulation required a total computational time of 579 hours.

While experimental material properties were unknown, using existing literature as guidance a simple material parameter calibration was performed; resulting values were found to give good correlation between the numerical and experimental response. While there were discrepancies, their nature and magnitude suggested that they were due to deviations between the numerical and experimental material properties, and mesh dependent non-convergence, rather than flaws in the applied modelling techniques. These issues were addressed by performing the work presented in the following chapters.

Chapter 5

Material parameter study

This chapter presents an investigation into how variations of the cell wall material parameters affect the macroscopic impact response of an air filled, thin walled, honeycomb structure. To perform the study, a numerical model was created; the numerical model was given a regular hexagonal geometry and material parameters typical of a cardboard honeycomb EDM. Section 5.2 presents an analysis of the spatial internal air pressure development and its effect on the structural response. Section 5.4 investigates the effect of variations in the cell wall material parameters on the macroscopic response, and in Section 5.5 those material parameters, which the macroscopic response was found to be most sensitive to, are considered in more detail.

An idealised, macroscopic, EDM response for the cardboard honeycomb is shown in Figure 5.1. The response can be characterised by four response parameters: peak transmitted stress σ_{Peak}, plateau transmitted stress $\sigma_{Plateau}$, strain to compaction ε_{Comp}, and the energy stored within the EDM at a given strain $U(\varepsilon)$.

Note that this characteristic definition of a dynamic cardboard honeycomb EDM response is subtly different from that of a typical EDM (Figure 2.1). When a classic EDM compacts (such as a steel tube or quasi-statically loaded aluminium honeycomb) there is a sudden sharp increase in the gradient of the stress-strain response. In a dynamically crushed cardboard honeycomb EDM, the internal air pressures superimpose on the structural response, providing a smooth sweeping increase of the

stiffening limb. Note that this behaviour is also is in line with fairly recent observations made on the response of dynamically crushed, sealed, aluminium honeycombs (Figure 2.5 (a))[27]. The original definition of ε_{Comp} will be retained, however it must be stated that the point of compaction may now be dictated by the rate of internal air pressure increase rather than just structural compaction.

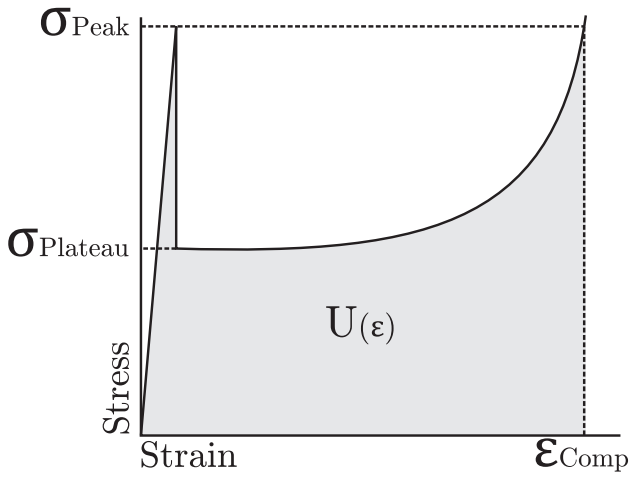

Figure 5.1 An idealised air filled honeycomb macroscopic response curve, showing the four characteristic response parameters: Peak stress, σ_{Peak}; Plateau stress, $\sigma_{Plateau}$; Compaction strain, ε_{Comp} (the strain at which the transmitted stress begins to exceed the initial peak); and Internal strain energy per unit volume $U(\varepsilon)$.

By holding the geometry of the honeycomb structure constant and varying each material parameter individually, their effects on the impact response could be isolated, and by evaluating σ_{Peak}, $\sigma_{Plateau}$, ε_{Comp} and U_ε for each analysis, the magnitude of any effects could be quantified.

5.1 Numerical methodology

To perform the large volume of numerical analysis required for a material parameter study, a computationally efficient numerical model of an air filled honeycomb was needed; by applying the modelling techniques developed in Chapter 4, this was possible. While the majority of the computational methods remained unchanged,

this section identifies modifications which were made to the full scale, air-filled cellular honeycomb models which were used for numerical validation in Section 4.4.

The use of a perfect regular hexagonal structure, allowed computational efficiency to be dramatically increased, by exploiting the quarter symmetry shown in Figure 5.2 (a); thus, allowing the full structural response to be simulated by modelling just one quarter segment with symmetrical boundary conditions along the planes of symmetry. An illustration of the modelled portion, and location of the symmetrical boundary conditions, is shown in Figure 5.2 (b).

Symmetrical boundary conditions were applied along the X-X plane, by using single point constraints, to restrain Eulerian flow and all Lagrangian displacements and rotations across the boundary. For symmetry, it was necessary to locate the Y-Y plane through the bonded, double-ply, cell walls. Restraining structural displacements across the Y-Y plane, using single point constraints, also prevented both the de-bonding and progressive folding mechanisms which occur during buckling.

As a compromise, a wall of rigid solid elements was placed along the Y-Y plane, and contact was defined between this and the cell walls, providing one-directional lateral restraint across the boundary. While this solution allowed progressive buckling and the formation of air flow pathways at the boundary, it imposed limitations due to the fact that it was not actually a perfect quarter symmetry boundary condition and no cohesion of the boundary cell walls could be defined; lack of cohesion of the boundary cell walls was to mean that air pathways could more readily form resulting in the development of lower pressures in cells 43-46 than would occur if the structure had been modelled as a whole.

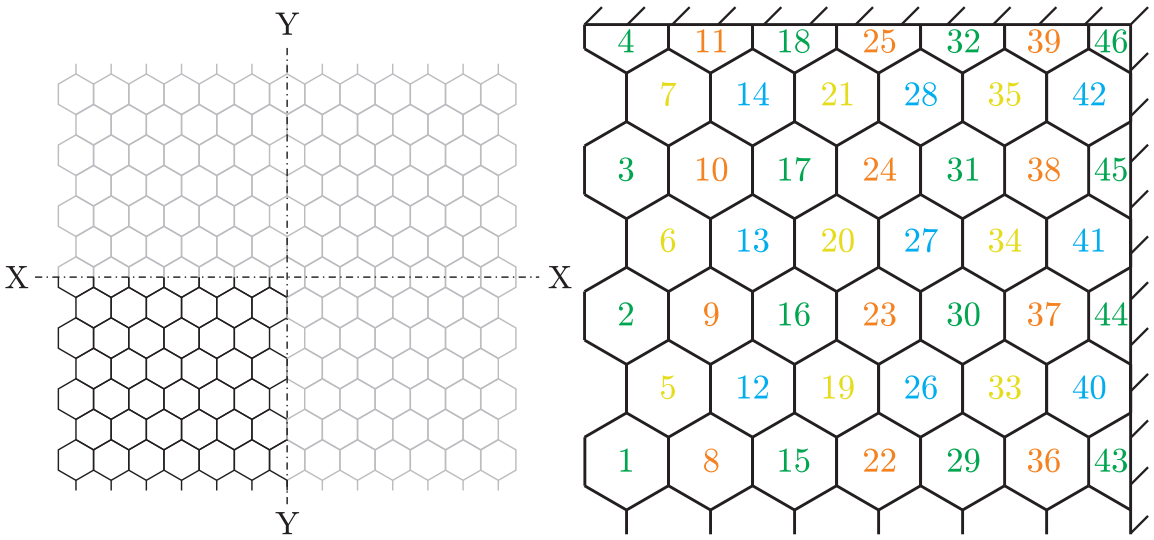

Figure 5.2 Cellular geometry of the numerical model used as a platform for the material parameter study, showing: (a) the full geometry (grey) and planes of symmetry X-X and Y-Y on which symmetrical boundary conditions were imposed, thus allowing the full structure to be modelled with quarter symmetry (black). (b) the modelled quarter portion consisting of 46 closed cells (containing air), air in cells of the same colour was separated only by glue bonds between the adjoining (Y-Y orientated) cell walls.

A 13 x 13 regular cell hexagonal arrangement ensured X-X and Y-Y planes of symmetry passed through a central cell; the full structure consisted of a total of 163 cells (ncell) arranged in 13 rows (nrow) and 25 columns (ncol), an illustration is given in Figure 6.1. In the quarter symmetry model there were a total of 46 cells, 36 whole, 9 half and 1 quarter; the cells were numbered from bottom left to top right as illustrated in Figure 5.2 (b).

The model was 70 mm in height and all cells consisted of six equal cell walls, 10 mm in length (L) and 0.3 mm thick (t), and had an internal angle θ of 60° (see Figure 3.20 (a) for identification of mesoscopic geometrical parameters). The 10 mm cell walls were divided into six equal sized δ_{EL}, 1.667 mm square shell elements; this provided a smaller (and therefore more accurate) mesh than that used for numerical

validation (see Section 4.4.4 of Chapter 4) and allowed the cell walls to be cut exactly in half to create the half cell walls shown at the top and bottom edge of the honeycomb structure, in Figure 5.2 (b). Additionally, the internal area of each hexagon can be calculated from $A_{Hex} = 2L^2(\sin\theta + \sin\theta\cos\theta) = 2 \times 10^2$ mm$(\sin 60° + \sin 60° \cos 60°) = 259.8$ mm^2.

The total footprint plan area A_{Trib} of the quarter symmetry honeycomb structure was calculated from $A_{Trib} = \delta_X \times \delta_Y = 6.5L\sqrt{3} \times 10.5L = 11821$ mm^2. The total cross sectional area of cardboard cell wall within A_{Trib} is defined as A_{Card} and is calculated by multiplying the total cell wall length ΣL by the thickness t. For the default quarter symmetry geometry the total length of one continuous cell wall was 140 mm and there were 13 of these so $\Sigma L = 1820$ mm, multiplied by the default cell wall thickness of $t = 0.3$ mm gives a default $A_{Card} = 546$ mm^2. The proportion of the total footprint area (and also volume, as A_{Card} is constant over the full height H) that is occupied by cell wall material can be calculated from $\phi_{Card} = {}^{A_{Card}}/_{A_{Trib}}$.

A summary of the meso and macroscale geometrical parameters, used for all simulations in this chapter, are given in Tables 5.1 and 5.2.

Table 5.1 Mesoscale geometrical parameters used for the material parameter study.

L	t	$\theta°$	A_{Hex}	δ_{EL}
10 mm	0.3 mm	60°	259.8 mm^2	1.667 mm

Table 5.2 Macroscale geometrical parameters used for the material parameter study.

H	δ_X	δ_Y	ncol	nrow	A_{Trib}	A_{Card}	ϕ_{Card}
70 mm	112.6 mm	105.0 mm	12.5	6.5	11821 mm^2	546 mm^2	4.619 %

A total of six elastic-plastic constitutive material parameters were required to define the cell wall material: yield stress σ_{Yield}, quotient of the double-ply to single cell wall yield stresses k (where k $= {}^{\sigma_{Y,t2}}/_{\sigma_{Y,t1}}$), elastic modulus E, tangent hardening

modulus E_t, Poisson's ratio ν and density ρ. In addition, σ_{Glue} was used to represent the strength of the glue bond between the double-ply cell walls.

Based on the background research and material parameter calibration presented in Sections 4.1.2 and 4.4.3 of Chapter 4, values of the material parameters were chosen which were deemed to be representative of a typical cardboard honeycomb cell wall; these values are given in Table 5.3.

For the purpose of these analyses σ_{Yield} is defined as the yield stress of the single-ply, cardboard only, cell wall material; the factor k represents the amplification in yield strength caused by the inclusion of glue between the double-ply cell walls. From tensile tests on samples of the single and double-ply cardboard cell wall material E and Wang [51] found the average increase in strength of the composite was 41%; a value of k = 1.41 was included in the numerical model, meaning the default yield stress of the double cell walls was: $\sigma_{Y,t2} = 5$ MPa $\times$ 1.41 = 7.05 MPa.

Table 5.3 Default linear elastic-plastic material parameters on which singular variations were made.

σ_{Yield}	k	E	E_t	ν	ρ	σ_{Glue}
5 MPa	1.41	2 GPa	2 $\times 10^5$ Pa	0.3	630 kg/m^3	0.5 MPa

The geometrical and material parameters stated in Tables 5.1, 5.2 and 5.3 define the default numerical model to which variations were applied. In addition, all samples were crushed at the default impact velocity of $v_i = 5$ ms^{-1}, and therefore strain rate of $\dot{\varepsilon} = 71.4$ s^{-1}.

5.2 Analysis of internal air pressure development and its effect on the structural response

Using the geometrical and material parameters given in Tables 5.1, 5.2 and 5.3, two numerical analyses were performed; one with and one without the entrapped air. For the simulation absent of air, at any given value of strain, all load being

transmitted through the honeycomb was carried by the cell walls, its magnitude a function of their material properties and current geometrical arrangement, and so $\sigma_{Total} = \sigma_{Card}$. For the simulation which included air, the pressures which developed due to its compression also carried load, and so $\sigma_{Total} = \sigma_{Card} + \sigma_{Air}$. Herein, the two analyses will be referred to as "structural only" and "fully coupled" respectively.

From comparisons between the responses of the structural only and fully coupled analyses, some insight could be gained into: the mechanisms which control the development of internal air pressures, the air pressure distribution within the honeycomb, and what effect air pressures have on the structural response.

Figure 5.3 shows macroscopic responses of both the structural only (solid) and fully coupled (dashed) analyses. For both analyses black lines indicate the load carried by the cell wall structure; for the fully coupled analysis load which was carried by the air pressures is shown with a red dashed line and the total load is shown with a blue dashed line.

The effect of the air pressures on the macroscopic response can be seen by comparing the solid black line with the dashed blue line. The air provides an overall stiffening of the response, the magnitude of which generally increases with strain as the air pressures build.

Over the plateau region (between 15 and 45 % strain) there was a reduction in σ_{Card} while σ_{Air} continued to increase, meaning that the level of stiffening remained relatively constant; at 19 % there was a sharp downward notch and σ_{Card} drops below the solid black line, reducing at a similar rate to the increase in σ_{Air}. After 55 % strain this softening of σ_{Card} halts, and the structural only and fully coupled structural responses resume their convergence.

Similarities between the two σ_{Card} curves in the early and late responses suggest that the internal air pressures have little effect on the structural response in these regions; the early response is unaffected because the air pressures, which increase with strain, must reach a certain magnitude before being able to significantly affect the structure. During the late response, the cell walls begin to bear on each other and the cellular geometry degrades, in this region the load being transmitted through

the structure becomes progressively less dependent on the geometrical arrangement of the cell walls. Likewise, the effect of any any structural variations (induced by the internal air pressures) on σ_{Card}, would diminish with increased strain causing the two curves to converge.

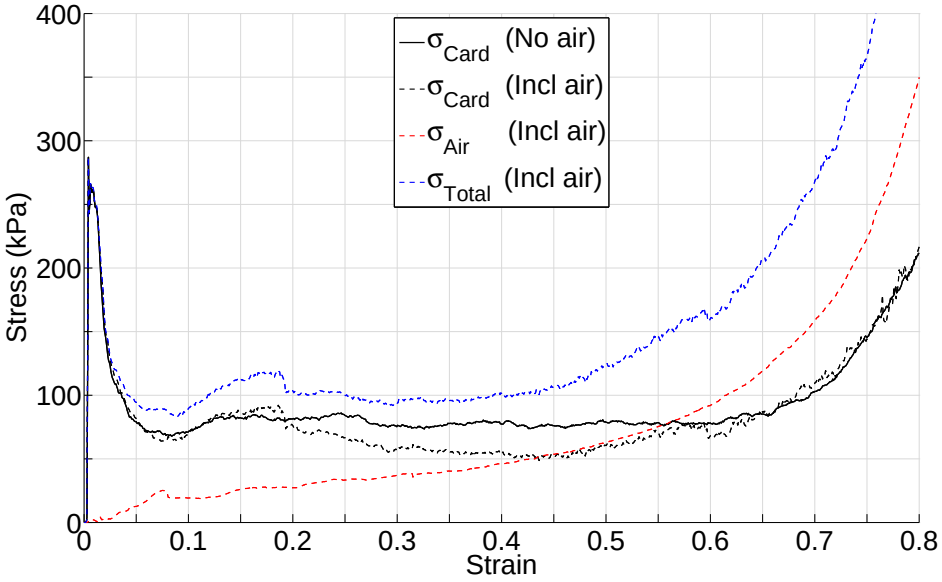

Figure 5.3 Comparison of the response without (solid black line) and with (dashed lines) air included in the simulation. For the simulation including air, the two components of σ_{Total} are given: stress transmitted by the structure σ_{Card} and internal air pressures σ_{Air}.

Figure 5.4 (a-h) shows the deformed shapes of the structural only (a-d) and fully coupled (e-h) analyses at 20, 40, 60 and 80 % strain. The contours illustrate the total lateral displacement (on plan, in the x-y plane); where the contour colour level indicates the magnitude of displacement, ranging from blue showing no displacement ($\Delta_{x,y} = 0$ mm) to red showing the maximum displacement ($\Delta_{x,y} = 30$ mm).

Cells in which the white background can be seen were bounded by walls undergoing the standard progressive buckling mode (illustrated by Figure 4.13 of Section 4.1.6); in cells where the white background is partially or fully obscured, the cell walls have deviated from the progressive buckling mode by moving laterally.

In the structural only analysis (a-d) there was some lateral movement of the

cell walls towards the perimeter, but most of the cell walls followed the progressive buckling mode through the full compression stroke; at 80 % strain (which is a substantial compaction), in all but three of the cells there is a proportion of the white background still visible.

Now looking at the deformed shapes from the fully coupled analysis (e-h), and comparing with (a-d), the effect of the entrapped air on the structural response can be seen. Figures (f-h) all show a dramatic increase in the lateral movement of the cell walls over the equivalent structural only analyses. Furthermore, this lateral drift (which was previously confined to the sample perimeter) was now visible on almost all of the cell walls. Drift occurred on both the x-x (right to left) and y-y (top to bottom) planes, while being most substantial right to left. The magnitude of lateral drift reduced towards the sample centre (top right), where at 80 % strain there were still cells in which the white background was not obscured.

Comparison between the two early deformed shapes at 20 % strain (Figure (a) and (e)), shows that in this early region of the response, any air pressure induced lateral drift is very small (only just beginning at the left hand edge). Additionally, the zone of weakness which developed during the structural only analysis (visible at the bottom centre of Figure (a)), is not present in Figure (e), suggesting that the presence of internal pressures of a relatively low magnitude actually provides a degree of geometrical stiffening, giving lateral restraint to the cell walls, and encouraging the progressive rather than a lateral-global buckling mode.

Re-examining the solid and dashed black lines, which were shown in Figure 5.3, the modification of σ_{Card} can be explained; the small increase, visible at 17 % strain, was due to the removal of the early zone of weakness; while the reduction in σ_{Card} between 19 and 60 % strain was due to a reduction in the geometrical stiffness of the cell wall arrangement due to lateral drift.

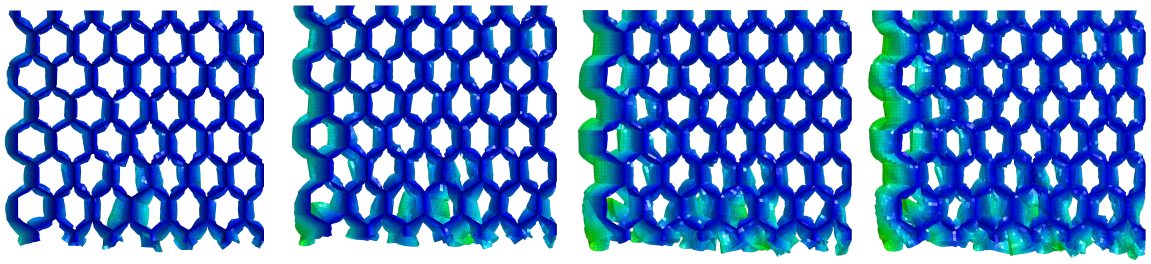

(a) $\varepsilon = 20\%$ (b) $\varepsilon = 40\%$ (c) $\varepsilon = 60\%$ (d) $\varepsilon = 80\%$

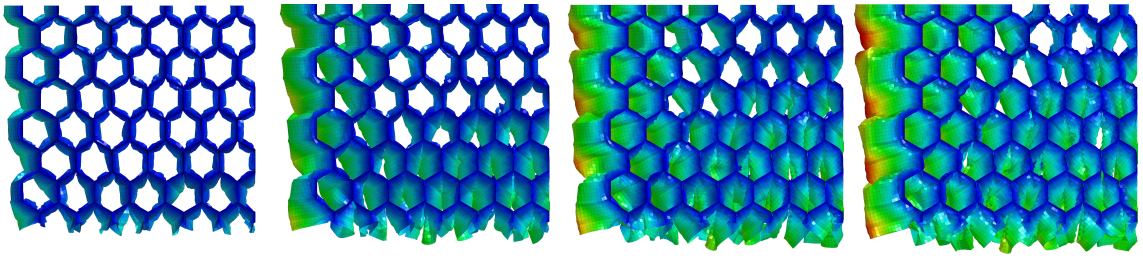

(e) $\varepsilon = 20\%$ (f) $\varepsilon = 40\%$ (g) $\varepsilon = 60\%$ (h) $\varepsilon = 80\%$

Figure 5.4 Plan view of the deformed structure at 20, 40, 60 and 80 % strain, when: (a-d) air **was not** included and (e-h) when air **was** included in the numerical simulation. Contours show the magnitude of lateral displacement (on the x-y plane), where the temperature indicates magnitude; with minimum (blue) being 0 mm and maximum (red) being 30 mm.

For clarity, the rigid body lateral displacement of each cell wall in the x direction Δ_x (right to left being positive) is shown in Figure 5.5 (b). Three cell walls have been identified, as shown in Figure 5.5 (a), and their Δ_x curves plotted with corresponding colours in Figure 5.5 (b). It can be seen that: lateral drift increases with strain; the magnitude of Δ_x is larger in cell walls closer to the honeycomb edge; and the differential of Δ_x between two adjacent walls increases towards the edge.

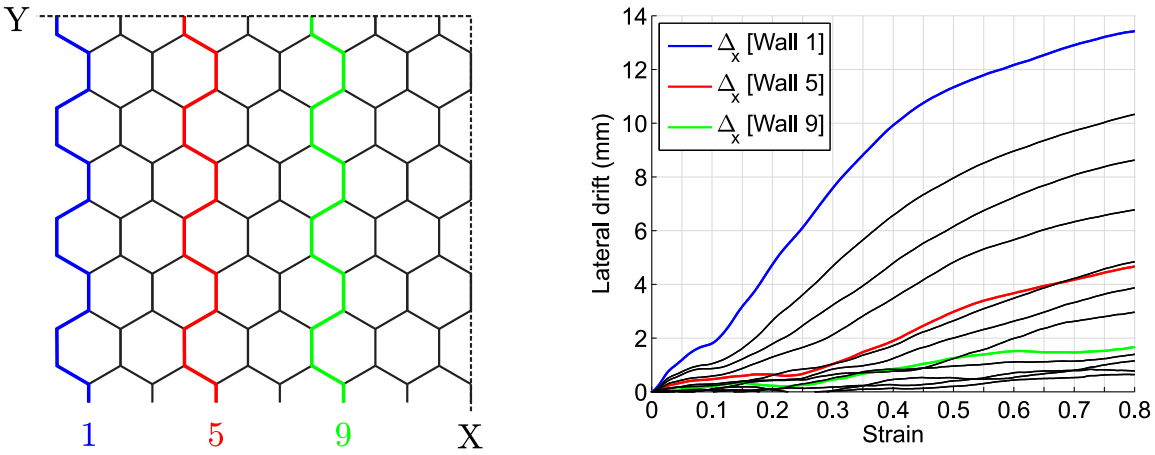

(a) (b)

Figure 5.5 A graphical illustration of the cell wall lateral drift which occurred as a result of internal air pressures. The rigid body x displacement (Δ_x) of all individual cell walls is shown in (b), where walls 1, 5, and 9 have been highlighted using the colours indicated in (a).

In Figure 5.4 it was observed that the cell walls drift laterally due to the inclusion of air. It is also known that each cell wall was fixed at its top and bottom edge to the liner sheets. It is therefore not unreasonable to assume that the deformation mechanism due to drift can be expressed using the geometry shown in Figure 5.6 (a, left), where the solid black line shows the profile of the deformed cell wall due to a rigid body lateral displacement of Δ_x, and the dashed line shows the location of the initial undeformed shape.

The shaded area in Figure 5.6 (a, left) shows the increase in area (on the **vertical plane**), which would result from an average rigid body displacement of magnitude Δ_x (where $2\Delta_x$ is the maximum mid-point displacement of the cell wall at half height). Now if this slice was projected along the full length of the cell wall, the shaded area in Figure 5.6 (a, right) shows the equivalent increase in plan area $\delta A_{\Delta x}$ (on the **horizontal plane**) which would result from the same rigid body displacement; the magnitude of $\delta A_{\Delta x}$, for a cell wall of length L, is simply $\delta A_{\Delta x} = \Delta x \times L$.

Using this mechanism, an estimation for the total increase in equivalent internal

plan area (occupied by gas), due to lateral drift, can be calculated by: assuming that every cell wall is moved to the perimeter (so that they occupy the same location) and then multiplying the average rigid body displacement of all cell walls, $\bar{\Delta}_x$, by the perimeter length of the left edge $13.5L$, giving: $\delta A_{\bar{\Delta}_x} = \bar{\Delta}_x \times 13.5L$; repeating for drift in the y direction: $\delta A_{\bar{\Delta}_y} = \bar{\Delta}_y \times 13L$; and then summing to get the total increase due to lateral drift: $\delta A_{\bar{\Delta}_{x,y}} = \delta A_{\bar{\Delta}_x} + \delta A_{\bar{\Delta}_y}$.

Figure 5.6 (b) shows how $\delta A_{\bar{\Delta}_x}$, $\delta A_{\bar{\Delta}_y}$, and $\delta A_{\bar{\Delta}_{x,y}}$ changed as the fully coupled crushing simulation progressed. The increase in the internal area in the x direction was of a higher magnitude than in the y direction, a difference in magnitude which increased with strain, visible by the relationship between the blue and red curves.

When looking at the black curve which shows $A_{\bar{\Delta}_{x,y}}$ there are three visible points of inflexion at 2, 12 and 25 % strain; after an initial rapid increase, the rate of increase reduced between 2 and 12 % strain, at 12 % strain the gradient sharply increased and then began a smooth reduction which was present during the remaining crushing event.

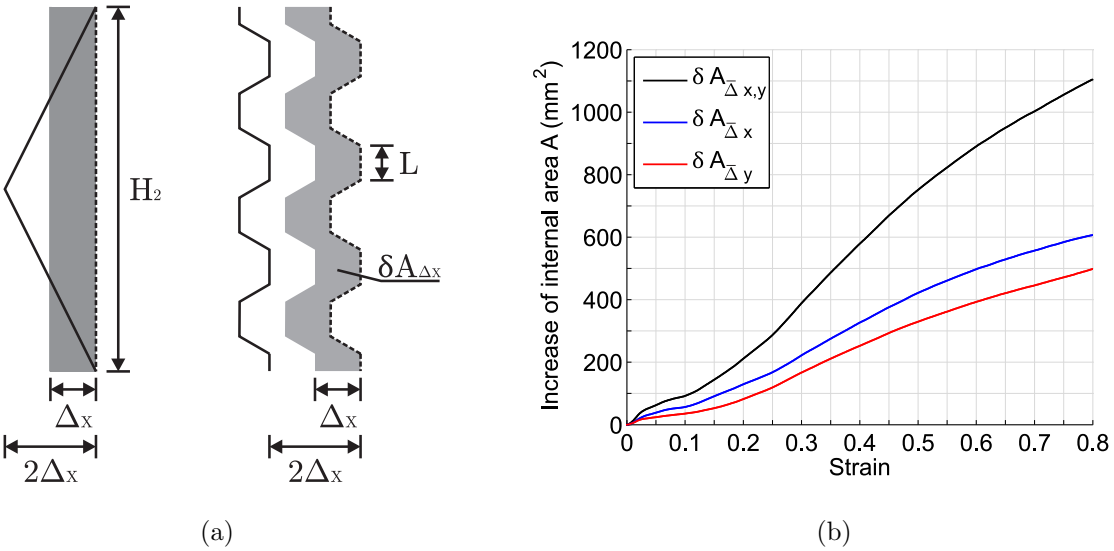

Figure 5.6 (a) The assumed deformation mechanism as a result of lateral drift, showing the net increase of plan area $\delta A_{\Delta x}$ for a lateral rigid body x displacement of Δ_x. (b) Increase of internal plan area during the air filled simulation, due to the average lateral drift of all cell walls in; the x direction $\delta A_{\bar{\Delta}_x}$; y direction $\delta A_{\bar{\Delta}_y}$; and in total $\delta A_{\bar{\Delta}_{x,y}}$.

During the experimental testing work (presented in Chapter 3), samples of cardboard honeycomb were crushed at high strain rates; for each crushing event, air pressures were measured at four internal locations within each sample. Findings included: 1. that the magnitude of pressure was generally proportional to the distance from the sample edge (increasing towards the centre), and 2. an increase in lateral confinement from additional cell walls resulted in higher pressures; pressures at locations other than the four measurement points and therefore the true distribution of pressure and total load carried by the air, was unknown.

Figure 5.7 shows the spatial distribution of internal air pressures, within the honeycomb during the fully coupled analysis, at 20 (a), 40 (b), 60 (c) and 80 (d) % strain. The resulting pressure distribution was a hexagonal grid matching the structural geometry; with no boundary, the air pressure within each cell was able to equalise. When the lateral drift of the cell walls was sufficient to create multiple separated sealed volumes within a single cell, it was possible for that cell to contain

air at different pressures; the pressures shown are those which were present at the base of the honeycomb and are therefore representative of the load transmitted through the sample.

The pressure distribution at 20 % strain (Figure 5.7 (a)) shows a plateau region of equal pressure at $ncol > 3, nrow > 2$, meaning that the rate of pressure increase in the internal cells was equal during the early response. Figure (b) shows that this plateau region had broken down by 40 % strain and a gradient of pressure throughout the sample began to emerge.

It was not possible to include a cohesive bond for the cell walls located on the y-y plane symmetrical boundary (see Section 5.1). As a result, the air pressures which developed in the cells located on the central column ($ncol = 13$) were lower than if a glue bond had been present, this is visible in Figure 5.7 (c).

Higher pressures developed in the cells towards the centre. Cells located at the two perimeter edges ($nrow, ncol = 1$) developed much lower pressures. Furthermore, pressures on $nrow = 1$ were lower than those on $ncol = 1$ with some cells on $nrow = 1$ developing no pressure by 40 % strain.

Comparison between the deformed shapes in Figure 5.4 (e-h), Figure 5.5 and the pressure distributions in Figure 5.7 (a-d), shows that for a given strain, the magnitude of pressure in a given cell is inversely proportional to the lateral displacement of the cell walls, and therefore the total load transmitted by the air is inversely proportional to the average lateral displacement of all cell walls on the x-y plane at a given strain $\bar{\Delta}_{x,y}(\varepsilon)$, and so: $\sigma_{Air} \propto {}^{1}/_{\bar{\Delta}_{x,y}(\varepsilon)}$.

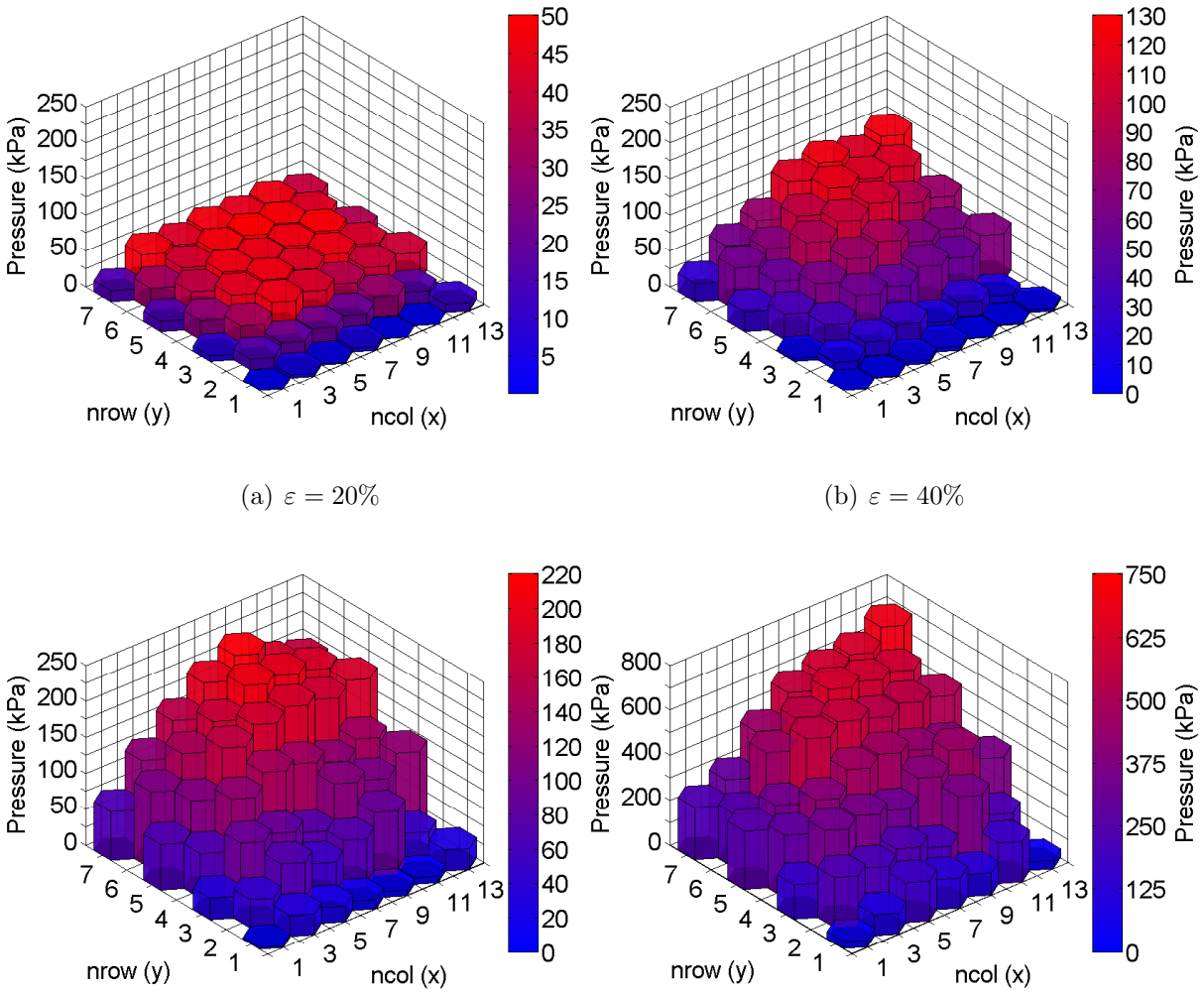

(a) $\varepsilon = 20\%$

(b) $\varepsilon = 40\%$

(c) $\varepsilon = 60\%$

(d) $\varepsilon = 80\%$

Figure 5.7 Spatial development of internal air pressures during the air filled numerical simulation ($\sigma_{Glue} = 0.5$ MPa) at 20, 40, 60 and 80 % strain.

As the air within the honeycomb is undergoing a rapid adiabatic compression, the resulting air pressures are related to the adiabatic equation of state. For a column of air, with perfect confinement, the air pressure which would develop in response to a rapid 1 dimensional strain ε is calculated from Equation 5.1, where $P_{Atmospheric} = 101.325$ kPa and ${}^{c_p}/_{c_v} = 1.4$ for these numerical analyses.

$$\sigma_{Air,1D}(\varepsilon) = \frac{P_{Atmospheric}}{(1-\varepsilon)^{c_p/c_v}} - P_{Atmospheric} \tag{5.1}$$

During analysis of the experimentally recorded air pressures (see Section 3.3.9), it was discovered that for a given strain the load being carried by the air can be related to $\sigma_{Air,1D}$ by: $\sigma_{Air} = \phi_{Conf} \times \sigma_{Air,1D}$, where ϕ_{Conf} is a factor which indicates the current degree of confinement provided by the honeycomb structure; furthermore, ϕ_{Conf} was found to decrease with an increase of axial strain.

Table shows $\sigma_{Air,1D}$ as predicted by Equation 5.1; the maximum cellular pressure, $\sigma_{Air,max}$; the total stress transmitted by the internal air pressures, σ_{Air}; and the confinement quotient ϕ_{Conf} of the fully coupled numerical analysis at 20, 40, 60 and 80 % strain. There are two points of interest here: firstly, the maximum cellular pressure $\sigma_{Air,max}$ was in exceedance of $\sigma_{Air,1D}$ at 20 and 40 % strain; and secondly, in agreement with observed experimental behaviour, ϕ_{Conf} reduced with strain, and so ϕ_{Conf} must be a function of strain: $\phi_{Conf}(\varepsilon)$

Table 5.4 A summary of the pressures which developed during the default fully coupled numerical analysis.

ε (%)	$\sigma_{Air,1D}$ (kPa)	$\sigma_{Air,max}$ (kPa)	σ_{Air} (kPa)	$\phi_{Conf}(\varepsilon)$
20	37	49	27	0.73
40	106	122	46	0.44
60	264	212	92	0.35
80	863	686	320	0.37

Two observations have been made of σ_{Air}, 1: $\sigma_{Air} = \phi_{Conf} \times \sigma_{Air,1D}$, and 2: $\sigma_{Air} \propto {}^{1}/\bar{\Delta}_{x,y(\varepsilon)}$, suggesting that the degree of lateral confinement is a function of the cell wall lateral drift, or more specifically: the change of current internal volume V_2 due to a change of cross sectional area δA. Reconsidering the adiabatic pressure volume relationship

$$P_1 V_1^{\gamma} = P_2 V_2^{\gamma} = K \tag{5.2}$$

where K is constant and $\gamma = {}^{c_p}/_{c_v}$, can be written in the form

$$P_2 = \frac{P_1(H_1A_1)^\gamma}{[(H_1 - \varepsilon H_1)(A_1 + \delta A)]^\gamma} \tag{5.3}$$

which gives final (absolute) pressure P_2 for a volume of air at initial (absolute) pressure P_1 and volume $V_1 = A_1 \times H_1$, subject to a vertical strain ε (where $H_2 = H_1 - \varepsilon H_1$) and change in cross sectional area A_1 area of δA (where $A_2 = A_1 + \delta A$) to create a volume $V_2 = A_2 \times H_2$. Note that for $\delta A = 0$, Equation 5.3 reduces to Equation 5.1 (the 1D adiabatic equation of state).

In addition to a change of internal volume due to δA, a second mechanism was observed to be responsible for a change in $\phi_{Conf}(\varepsilon)$: loss of gas via blow out. Blow out occurred only in the y-y direction, the plane on which the glue bonds were orientated; when the pressure gradient between two adjacent cells in the same column reached a certain magnitude, the high pressure gas formed a pathway by destroying the cohesive bond and separating the double cell walls. The glue bonds could also fail during normal structural deformation, allowing the gas to flow along the ready made pathway. During the crushing event it was also possible for pathways to become re-sealed due to large structural deformations.

The largest possible pressure differential which can develop within the honeycomb is between the over pressure $\sigma_{Air,max}$ and the surrounding 0 kPa over pressure at the honeycomb perimeter. In reality, air in cells close to the perimeter ($nrow = 1$) vented well before $\sigma_{Air,max}$ was reached. Cells close to the perimeter vent first as the pathway to the surrounding ambient air is the shortest and most readily formed. As the row number increases, the air must form a longer (less permeable) pathway to vent. Additional factors, such as structural deformations of the (still bonded) double-ply cell walls and air pressures acting on their back faces from adjacent cells, increase the difficulty for pathways to form.

A third simulation was performed, σ_{Glue} was increased from 0.5 to 7.05 MPa to provide a full strength bond between the double-ply cell walls. Internal pressure distributions at 20, 40, 60 and 80 % strain are shown in Figure 5.8 (a-d).

During this numerical analysis, much less air was able to vent, resulting in higher pressures throughout. In comparison to the pressure distributions which developed

during the original fully coupled analysis (shown in Figure 5.7), a much larger number of cells reached and maintained $\sigma_{Air,max}$. This resulted in the development of an internal pressure plateau which lasted throughout the analysis. The ability of many cells to reach $\sigma_{Air,max}$ suggested that they contained the same volume of air, no air was able to vent from these cells during the impact event.

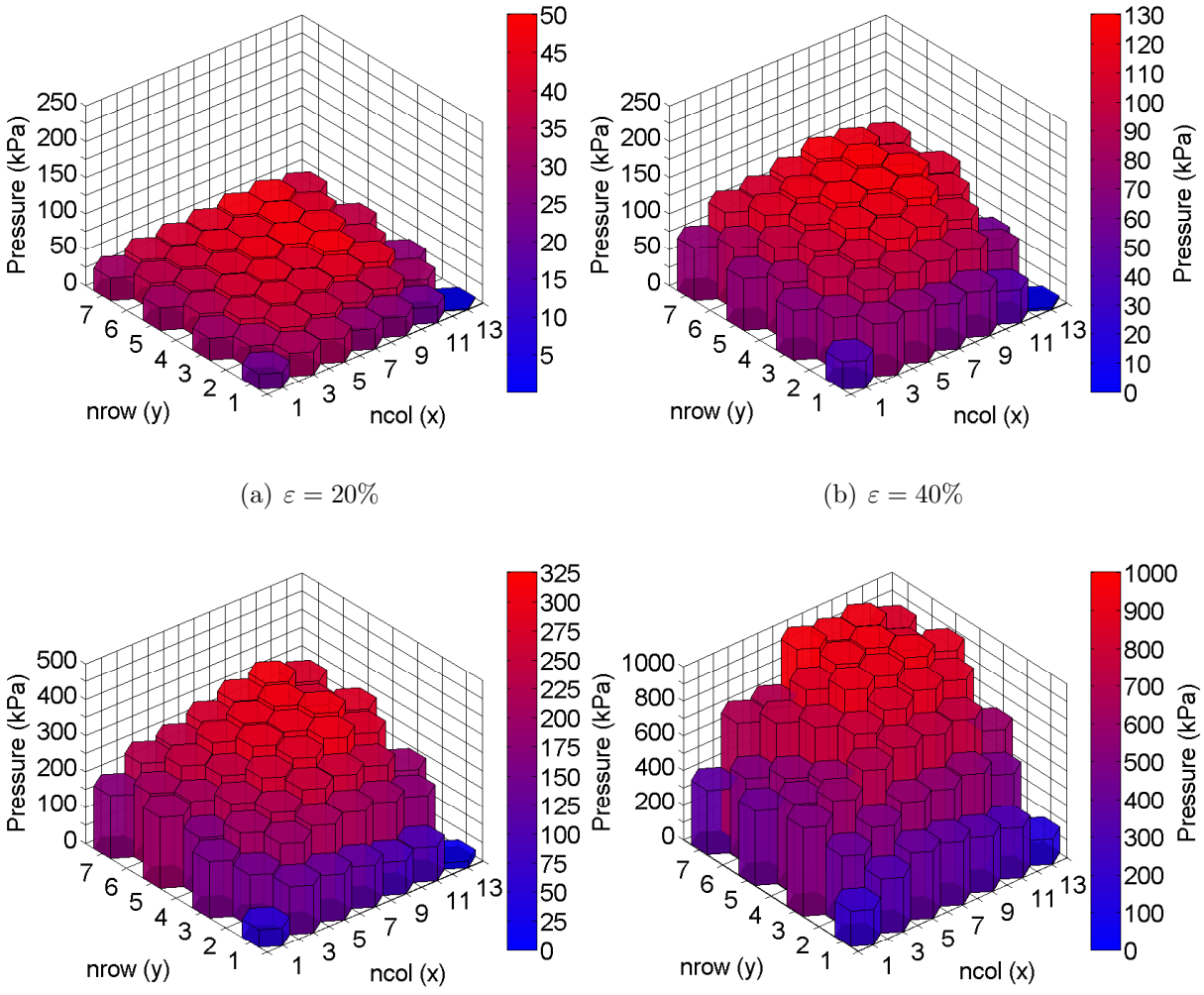

(a) $\varepsilon = 20\%$

(b) $\varepsilon = 40\%$

(c) $\varepsilon = 60\%$

(d) $\varepsilon = 80\%$

Figure 5.8 Spatial development of internal air pressures during a numerical simulation with a full strength glue bond: $\sigma_{Glue} = \sigma_{Y,t2} = 7.05$ MPa (an increase from the default value of $\sigma_{Glue} = 0.5$ MPa used for Figure 5.7).

Table 5.5 compares $\sigma_{Air,max}$, σ_{Air} and $\phi_{Conf}(\varepsilon)$ between the two analyses. An

increase in σ_{Glue} caused $\sigma_{Air,max}$ to exceed $\sigma_{Air,1D}$ during the full impact event, whereas previously this was only the case at 20 and 40 % strain. A reduction in the amount of internal air lost due to venting had a significant effect on $\phi_{Conf}(\varepsilon)$, which dropped at a much slower rate during the analysis with full strength glue bonds, than during the analysis with weaker glue bonds.

Clearly, the development of air pressures within the honeycomb is significantly affected by the volume of entrained air which is retained during the impact event, and therefore: $\sigma_{Air} \propto {}^{1}/_{\kappa_y(\varepsilon)}$, where $\kappa_y(\varepsilon)$ is the permeability of the cellular structure in the y direction at a given strain (with units in $m^3/s/m^2$) i.e. $\kappa_y(\varepsilon)$ is the volume of air which can flow through the area $\delta_X \times H$ where H is the honeycomb height and δx is the width of the honeycomb in the x-x plane. Previously, 1: $\sigma_{Air} = \phi_{Conf} \times \sigma_{Air,1D}$, 2: $\sigma_{Air} \propto {}^{1}/_{\bar{\Delta}_{x,y(\varepsilon)}}$ and now, 3: $\sigma_{Air} \propto {}^{1}/_{\kappa_y(\varepsilon)}$.

Table 5.5 A comparison of the pressures which developed during the two fully coupled numerical analyses, as a result of using the default and full strength glue bonds. All air pressures, $\sigma_{Air,1D}$, $\sigma_{Air,max}$ and σ_{Air} are all given in kPa.

		$\sigma_{Glue} = 0.50$ MPa			$\sigma_{Glue} = 7.05$ MPa		
ε (%)	$\sigma_{Air,1D}$	$\sigma_{Air,max}$	σ_{Air}	$\phi_{Conf}(\varepsilon)$	$\sigma_{Air,max}$	σ_{Air}	$\phi_{Conf}(\varepsilon)$
20	37	49	27	0.73	47	34	0.92
40	106	122	46	0.44	126	85	0.80
60	264	212	92	0.35	307	194	0.73
80	863	686	320	0.37	951	583	0.68

In the cells which developed $\sigma_{Air,max}$ (for the analysis where σ_{Glue} was equal to 7.05 MPa) no venting occurred; the additional pressure $\sigma_{Air,max} - \sigma_{Air,1D}$ can be attributed solely to loss of internal volume to folded cell walls, which develop during the structural deformation; a loss of volume which, can be expressed (like $\delta A_{\bar{\Delta}_{x,y}}$ due to lateral drift) by an equivalent δA. Equation 5.3 can be rearranged to make δA the subject

$$\delta A = \left[\frac{P_1(H_1A_1)^\gamma}{P_2(H_1 - \varepsilon H_1)^\gamma}\right]^{(1/\gamma)} - A_1 \tag{5.4}$$

giving an expression for the change in area δA attributed to a change in pressure from P_1 to P_2 at a longitudinal strain of ε. Substituting atmospheric pressure $P_{Atmospheric}$ and $\sigma_{Air,max}$

$$\delta A_{Loss} = \left[\frac{P_{Atmospheric}(H_1A_1)^\gamma}{(\sigma_{Air,max} + P_{Atmospheric})(H_1 - \varepsilon H_1)^\gamma}\right]^{(1/\gamma)} - A_1 \tag{5.5}$$

we get an equation which gives the equivalent loss of internal area due to structural deformations A_{Loss}, which would generate over pressure $\sigma_{Air,max}$ at a strain of ε. The net change in area $\delta A_{Net}(\varepsilon)$ can then be calculated by summing the growth in area due to lateral drift $A_{\bar{\Delta}_{x,y}}(\varepsilon)$ and the loss of area due to structural deformations $\delta A_{Loss}(\varepsilon)$ (both of which are a function of ε), which can be written simply as:

$$\delta A_{Net}(\varepsilon) = \delta A_{\bar{\Delta}_{x,y}}(\varepsilon) + \delta A_{Loss}(\varepsilon). \tag{5.6}$$

Figure 5.9 shows how $\delta A_{\bar{\Delta}_{x,y}}$ (blue line), δA_{Loss} (red line) and δA_{Net} (black line) changed with strain for the fully coupled analysis with the full strength glue bonds. Comparison between the blue and red lines shows that the rate of change of $\delta A_{\bar{\Delta}_{x,y}}$ was much more constant than the fluctuation δA_{Loss}. Both mechanisms had an equally significant impact on the net change in area; δA_{Net} was negative until 40% strain, after which the cell wall drift began to dominate, resulting in a net expansion of the internal volume.

The significance of the early, strong oscillations visible below 20 % strain on the red line is not clear. In this region, pressures were still very low and so any fluctuations from additional sources would be amplified as their relative size would be large in comparison to the low early pressures. One potential source of this additional early pressure, is a reflecting shock in the air, caused by a sudden forced acceleration of the gas particles on contact between the impactor and the top liner; after 20 % strain (when the air pressures began to become significant) the oscillations has almost completely damped out.

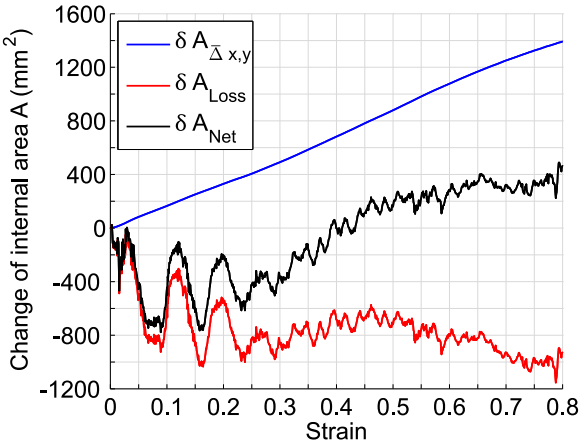

Figure 5.9 Increase of internal area due to outwards cell wall drift $\delta A_{\bar{\Delta}_{x,y}}(\varepsilon)$, decrease of internal area due to structural deformations $\delta A_{Loss}(\varepsilon)$ and net total change of area $\delta A_{Net}(\varepsilon)$ during the air filled analysis with full strength glue bonds.

Substituting δA_{Net} into Equation 5.3

$$\sigma_{Air,\delta V}(\varepsilon) = \frac{P_{Atmospheric}(H_1 A_1)^{\gamma}}{[(H_1 - \varepsilon H_1)(A_1 + \delta A_{Net})]^{\gamma}} - P_{Atmospheric} \tag{5.7}$$

an equation is created which gives $\sigma_{Air,\delta V}(\varepsilon)$, the internal pressure would be generated within the honeycomb solely due to a change of the internal volume from $V_1 = H_1 A_1$, to $V_2 = (H_1 - \varepsilon H_1)(A_1 + \delta A_{Net})$.

Finally, any difference between $\sigma_{Air,\delta V}(\varepsilon)$ and the actual value of σ_{Air} at a given strain ε must be due to loss of gas, and so

$$\sigma_{Air}(\varepsilon) = \sigma_{Air,\delta V}(\varepsilon) - \sigma_{Air,Vent}(\varepsilon) \tag{5.8}$$

where $\sigma_{Air,Vent}(\varepsilon)$ is the drop in pressure which resulted from a loss of internal gas of volume V_{Vent}. Black, blue and red lines in Figure 5.10 show σ_{Air} with its two components $\sigma_{Air,\delta V}(\varepsilon)$ and $\sigma_{Air,Vent}(\varepsilon)$ for the fully coupled analysis with full strength glue bonds.

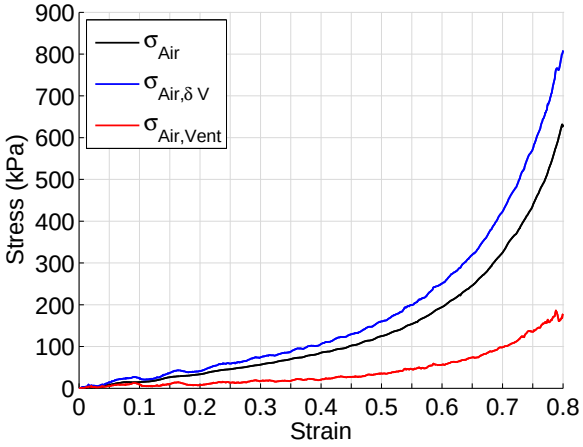

Figure 5.10 Total stress actually transmitted by air the internal air pressures σ_{Air}, stress which would have resulted purely from the change of internal volume (if all air had been retained) $\sigma_{Air,\delta V}$, and the component which was lost due to venting of the air $\sigma_{Air,Vent}$ during the fully coupled analysis with full strength glue bonds. Where: $\sigma_{Air}(\varepsilon) = \sigma_{Air,\delta V}(\varepsilon) - \sigma_{Air,Vent}(\varepsilon)$.

This approach is limited as it relies on the development of $\sigma_{Air,max}$ (which requires a cell absent of any venting) to estimate the current internal volume within the honeycomb. However, insight has been gained into the complicated and highly variable mechanisms which contribute to the development of internal air pressures.

Perhaps the most striking finding is the development of an internal equal pressure plateau of $\sigma_{Air,max}$ (visible in Figure 5.8). If the sample plan area was increased, so would the proportion of cells able to reach $\sigma_{Air,max}$ and in turn σ_{Air} would approach $\sigma_{Air,max}$.

5.3 Material parameter study scope

The numerical simulation was now repeated with singular variations on one of the 7 material parameters given in Table 5.3. The default values, which are in the expected magnitude for a cardboard honeycomb cell wall, were based on those originally determined in Section 4.1.2, with added consideration of the values which were found to give good agreement between the numerical model and the experimental

results in Section 4.4.3.

The matrix of numerical simulations was populated by firstly performing two additional simulations for each material parameter, to assess the sensitivity of the response, and then adding additional simulations (where computational resources allowed) to further study the parameters which were found to be most sensitive.

Effort was made to maintain the magnitude of variation, between parameters, for the initial two additional simulations to allow a fair sensitivity analysis; where possible, variations were made on the default value so that the three simulations possessed values which

1. were in the ratio of 1:2:4
2. and the value used for the default analysis was situated in the middle.

Some parameter variations proved problematic; for example, when density was halved from the default value of 630 kg/m^3 to 315 kg/m^3 numerical stability could not be achieved; and some parameter variations made little engineering sense, such as doubling the default Poisson's ratio from 0.3 to 0.6 (i.e. above that of a perfectly compressible material where $\nu = 0.5$), or halving the yield stress ratio from the default of 1.41 to 0.705 (imposing a lower yield stress for the double than the single-ply cell walls). In these cases it was necessary to relax the two constrains stated above, firstly, by allowing the default analysis to become either the maximum or minimum value while maintaining the 1:2:4 ratio (such as for the density simulations), and secondly, by adopting a more sensible, even, inter-simulation variation (such as for the Poisson's ratio simulations).

Table 5.6 gives a summary of the minimum and maximum values covered in this material parameter study. Note that the range of values investigated for the tangent hardening modulus E_t was particularly large, this was to provide some insight into when and if strain hardening begins to have an effect on the response i.e. at what rate of strain hardening the elastic-plastic material model ceases to be an accurate assumption.

Table 5.6 Scope of the analysed material parameter variations.

Parameter	Minimum value	Maximum value
ν	0.2	0.4
E (GPa)	1.0	4.0
ρ (kg/m^3)	630	2520
k	1.00	1.41
σ_{Glue} (MPa)	0.00	7.05
σ_{Yield} (MPa)	2.5	10.0
E_t (Pa)	2×10^3	2×10^8

5.4 Material parameter study: Macroscopic response results

For all analyses, four response parameters were calculated and in doing so, the sensitivity of the macroscopic response to variations of each material parameter could be quantified. σ_{Peak} was calculated by taking an average of the initial peak and the four following data points, removing any numerically induced oscillations; $\sigma_{Plateau}$ was calculated as the average transmitted stress between 20 and 50 % strain; ε_{Comp} was the strain at which the plateau rises to exceed σ_{Peak}; and $U(\varepsilon)$ was computed for several levels of strain (including ε_{Comp}), by integrating the stress strain curve.

At a given value of strain $U(\varepsilon)$ represents the amount of kinetic energy which has been converted to internal strain energy (per unit volume) by the EDM. $U(\varepsilon)$ consists of two components, energy dissipated by plastic strain of the cell walls (permanent) and energy stored by adiabatic compression of the internal gas (temporary). $U(\varepsilon_{Comp})$ is the total amount of strain energy, per unit volume, within the sample at compaction.

Sections 5.4.1 to 5.4.7 look at the effect of varying each of the material parameters. In each section the macroscopic response curves are presented and then followed by graphs of the four response parameters. In each graph comparing the

macroscopic responses, the response of the default analysis is plotted with a **solid black line**.

5.4.1 Effect of Poisson's ratio (ν) on the macroscopic response

Figure 5.11 shows the numerical macroscopic responses for varied Poisson's ratio. The graphed stress is σ_{Total}, which is a composite of the stress transmitted by both the air and the cardboard structure, $\sigma_{Total} = \sigma_{Card} + \sigma_{Air}$. It was previously observed that the early response was dominated by buckling of the cell wall structure and as strain increased, the dominance moved towards the internal air pressures.

Variations in the Poisson's ratio, caused no obvious trends in the early macroscopic response. When looking at the late response, after 50 % strain, as the Poisson's ratio was increased, the rate of stiffening was reduced. The late response is dependent on the development of internal air pressures; this reduced rate of stiffening could be explained by an increase in the internal volume from an enhanced, net, macroscopic, Poisson's ratio effect of the cellular structure.

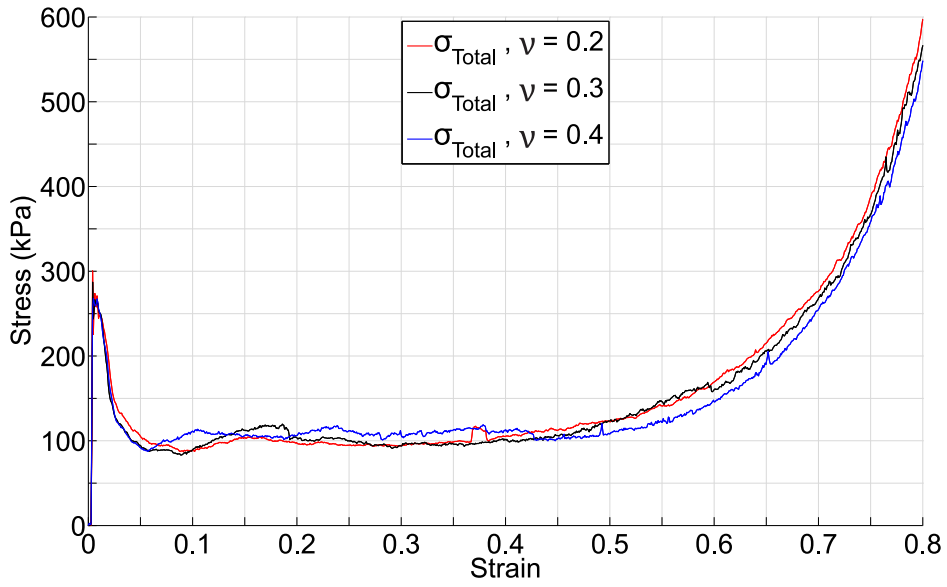

Figure 5.11 Total transmitted stress by the honeycomb σ_{Total} vs axial strain ε during the simulations with varied Poisson's ratio ν.

Figure 5.12 (a) and (b) shows how the peak and plateau transmitted stresses σ_{Peak}, $\sigma_{Plateau}$ (blue and red lines) and the strain to compaction ε_{Comp} (green line), changed due to variations in the Poisson's ratio. The three analyses are plotted with hollow circle markers, a linear connection between them is used to highlight any trends. There was no marked effect on σ_{Peak}, $\sigma_{Plateau}$; while the reduction in the rate of stiffening, discussed above, caused a linear 1.6 % increase in ε_{Comp} when the Poisson's ratio was increased from 0.2 to 0.4.

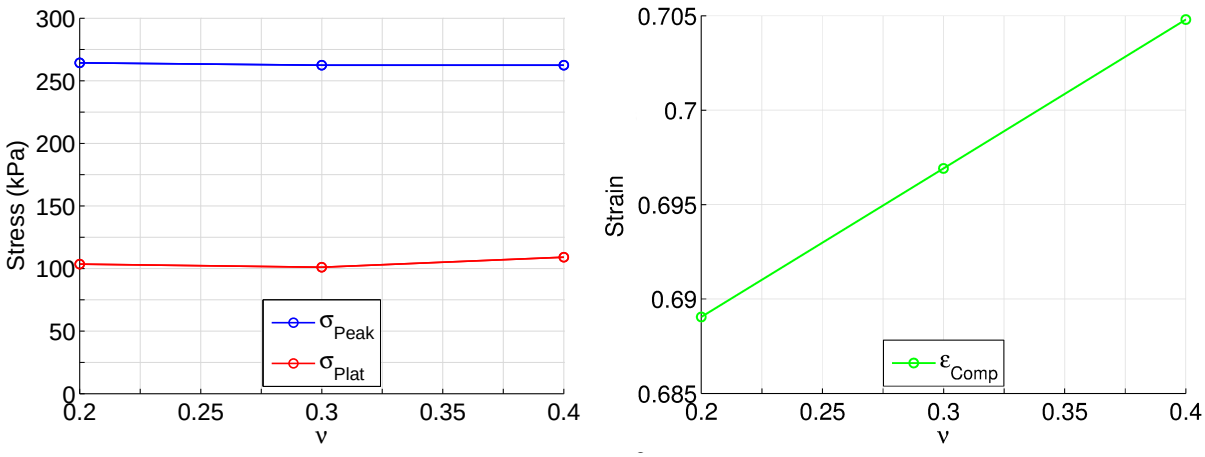

(a) (b)

Figure 5.12 Variations of the macroscopic response parameters (a) σ_{Peak}, $\sigma_{Plateau}$ and (b) ε_{Comp} as a result of variations in the cell wall Poisson's ratio ν.

Figure 5.13 shows how the internal strain energy per unit volume U increased with strain ε, as the Poisson's ratio was varied. In addition, the dashed black line shows U at the point of compaction, i.e. the total kinetic energy converted to strain energy by the honeycomb, during its useful EDM response. There were no discernible, noteworthy trends, the downward slope of 80% strain contour (green line) is just another expression of the singular trend discussed above; also, $U_{\varepsilon_{Comp}}$ is remarkably consistent for all values of ν.

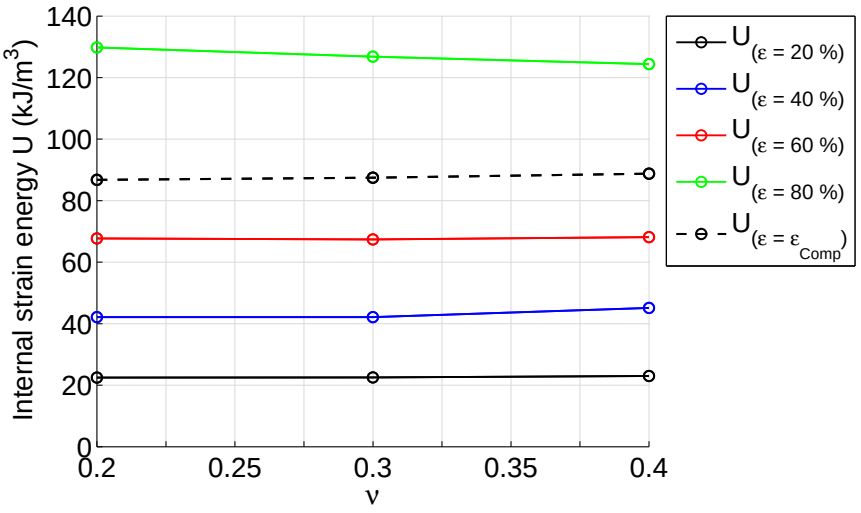

Figure 5.13 Variation of the total strain energy per unit volume $U(\varepsilon)$, at various increments of strain (including ε_{Comp}) as a result of variations in the cell wall Poisson's ratio ν.

5.4.2 Effect of elastic modulus (E) on the macroscopic response

Figure 5.14 shows the numerical macroscopic responses, for varied elastic modulus. The main effect of varying the elastic modulus can be seen between 5 and 25 % strain. In this region there is a transition between the post-peak softening limb and the plateau; the transition zone is characterised by an initial dip, followed by a small peak, before settling to the plateau.

As the elastic modulus was increased, the shape of the transition zone changed; both the peak and dip inflection point moved left and up, shortening the softening limb while reducing the dip severity and increasing the secondary peak magnitude. After the secondary peaks, all three responses linearly converged, reaching equal magnitudes at 40% strain. Finally, there was a marginal reduction in the stiffening rate, between 55 and 70% strain, with increased elastic modulus.

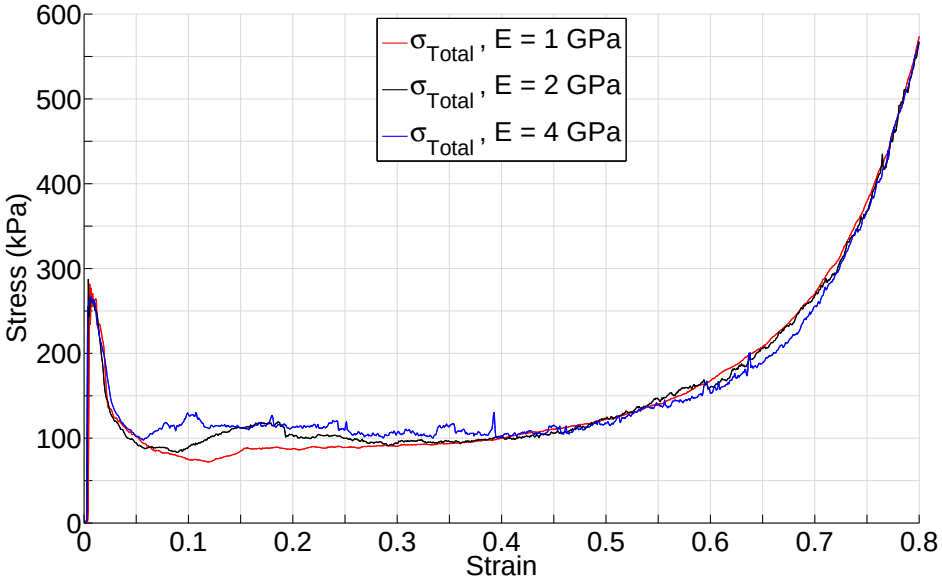

Figure 5.14 Total transmitted stress by the honeycomb σ_{Total} vs axial strain ε during the simulations with varied elastic modulus E.

Figure 5.15 (a) and (b) shows how the peak and plateau transmitted stresses σ_{Peak}, $\sigma_{Plateau}$ (blue and red lines) and the strain to compaction ε_{Comp} (green line), changed with variations in the elastic modulus. Between 1 and 4 GPa there was no marked effect on σ_{Peak}, a small linear increase in $\sigma_{Plateau}$ from 98 kPa to 109 kPa and an even smaller 1% increase in ε_{Comp}.

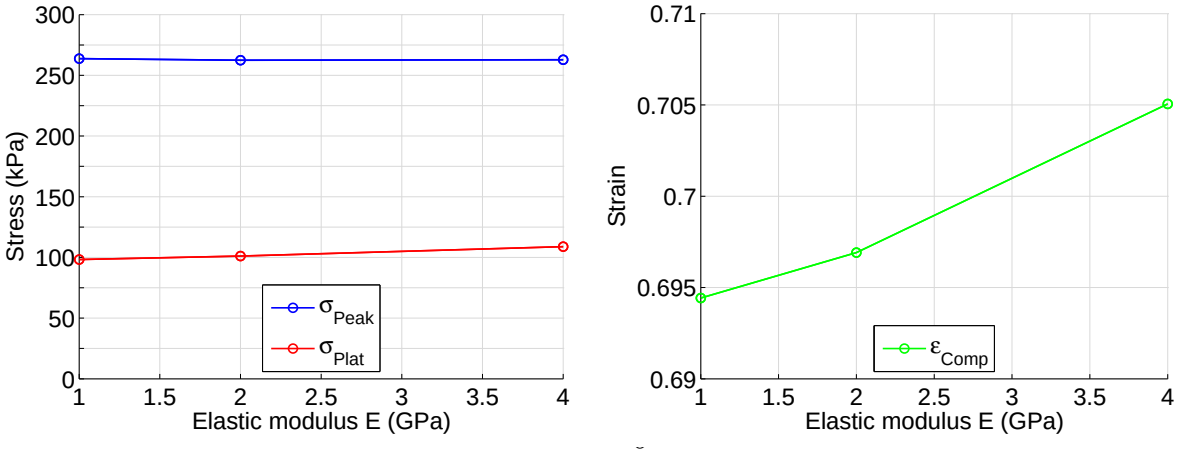

(a) (b)

Figure 5.15 Variations of the macroscopic response parameters (a) σ_{Peak}, $\sigma_{Plateau}$ and (b) ε_{Comp} as a result of variations in the cell wall elastic modulus E.

Figure 5.16 shows how the internal strain energy per unit volume U increased with strain ε, as the elastic modulus was varied. By 40 % strain, the difference in the early macroscopic behaviour had instilled a gradual, almost linear, increase of the internal strain energy per unit volume; U increased by 8.4 kJ/m^3 when E was increased from 1 and 4 GPa; over the same interval, the strain energy per unit volume at compaction $U_{\varepsilon_{Comp}}$ also increased by a total of 8.9 kJ/m^3 from 83.5 to 92.4 kJ/m^3.

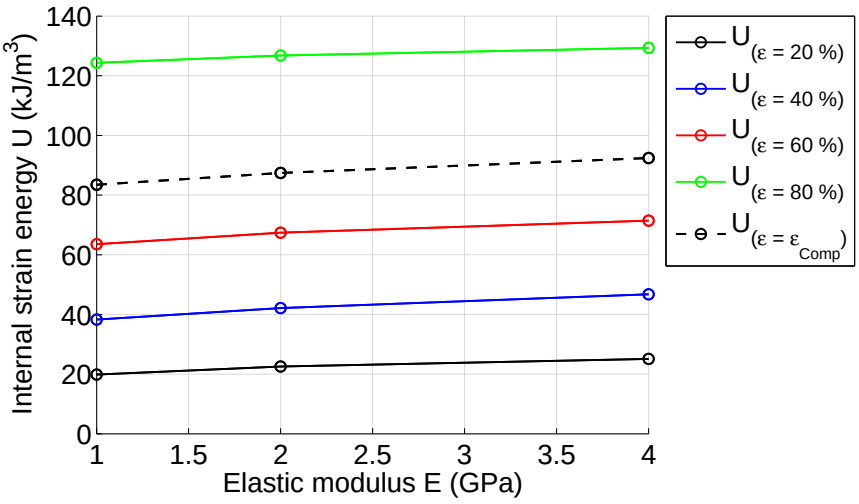

Figure 5.16 Variation of the total strain energy per unit volume $U(\varepsilon)$, at various increments of strain (including ε_{Comp}) as a result of variations in the cell wall elastic modulus E.

5.4.3 Effect of density (ρ) on the macroscopic response

Figure 5.17 shows the numerical macroscopic responses, for varied cardboard density; both the early (0 - 10 % strain) and late (50 % + strain) response was affected by changes in density; there was no significant impact on the central plateau region.

With increased density the rate of softening between the peak and plateau was reduced. With increased density, there was also a smoothing out of the initial dip and peak characteristic to the transition region between the softening limb and plateau. An opposite effect was visible in the late response: stiffening began later with increased density.

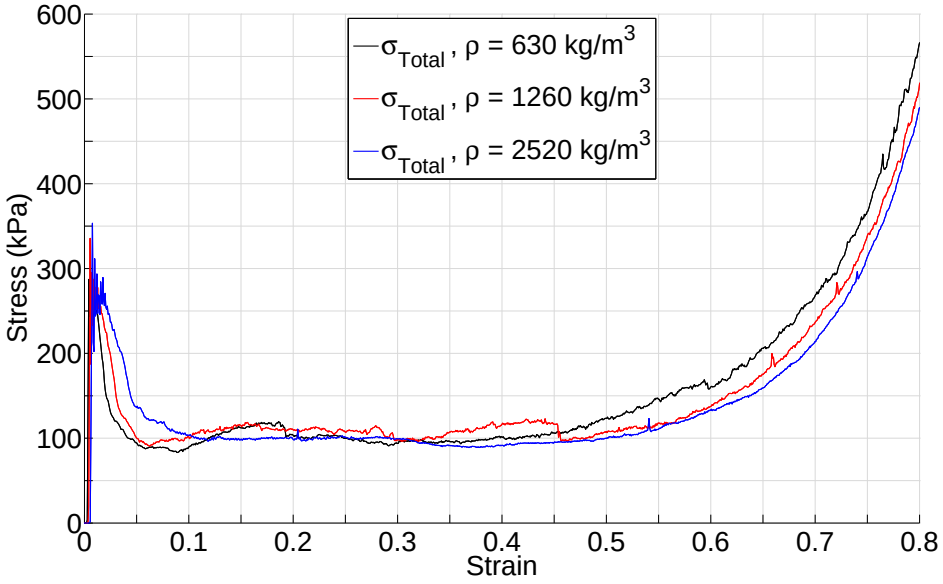

Figure 5.17 Total transmitted stress by the honeycomb σ_{Total} vs axial strain ε during the simulations with varied density ρ.

Figure 5.18 (a) and (b) shows how the peak and plateau transmitted stresses σ_{Peak}, $\sigma_{Plateau}$ (blue and red lines) and the strain to compaction ε_{Comp} (green line), changed with variations of the density. While there was no clear relationship between σ_{Peak} and $\sigma_{Plateau}$ and the density, the simulation with a density of 1260 kg/m^3 produced marginally higher values for both the peak and plateau stresses. The reduction in stiffness of the late response, observed in Figure 5.17, resulted in a later compaction strain as the density was increased, ε_{Comp} increased by 3.2 % as the density was increased from 630 to 2520 kg/m^3.

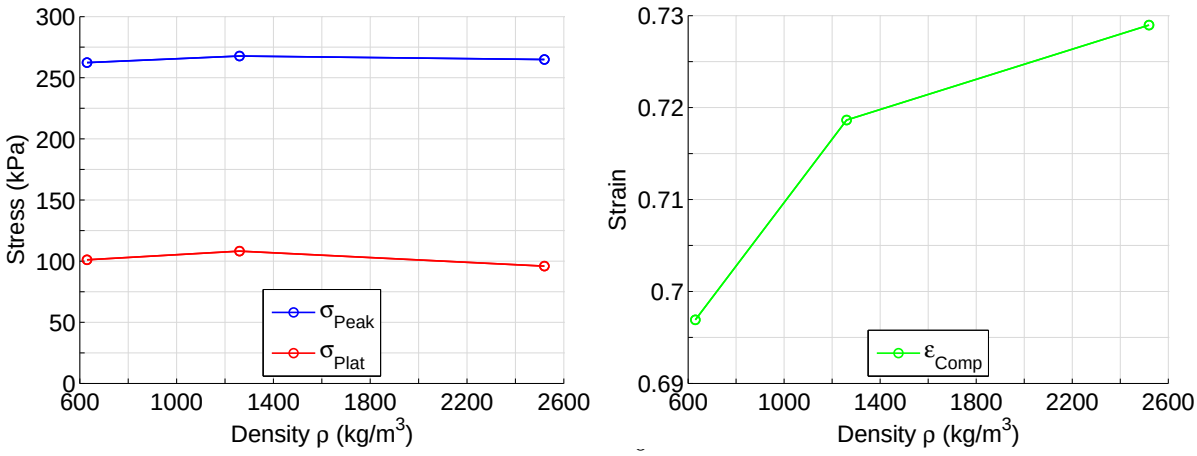

(a) (b)

Figure 5.18 Variations of the macroscopic response parameters (a) σ_{Peak}, $\sigma_{Plateau}$ and (b) ε_{Comp} as a result of variations in the cell wall density ρ.

Figure 5.19 shows how the internal strain energy per unit volume U increased with strain ε, as the density ρ was varied. The effect of density on the early and late responses is visible when comparing the early and late contours. At lower strains, a cell wall with a higher density provides marginally more energy absorption, while at higher strains, the opposite begins to become true. However, by comparing the shape and location of the dashed black line with the green line, it can be seen that, for these analyses the energy absorbed per unit volume at compaction $U(\varepsilon_{Comp})$ is unaffected by late response stiffening induced by a reduction in density.

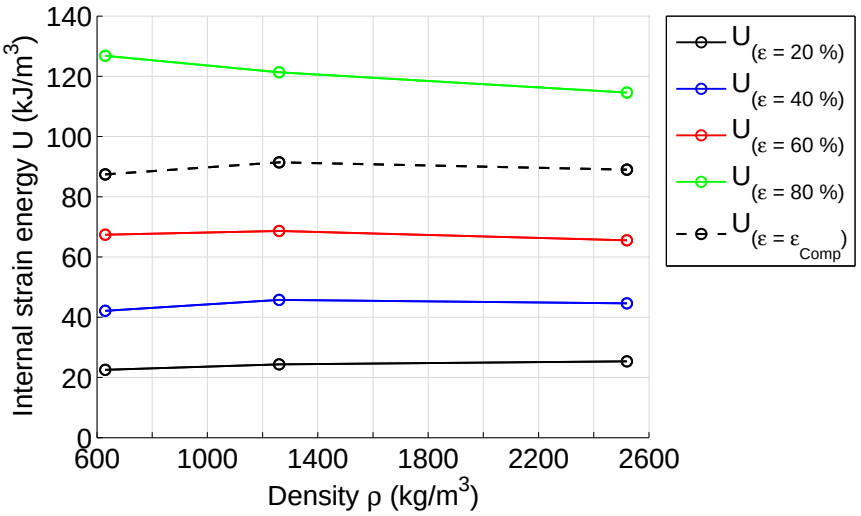

Figure 5.19 Variation of the total strain energy per unit volume $U(\varepsilon)$, at various increments of strain (including ε_{Comp}) as a result of variations in the cell wall density ρ.

5.4.4 Effect of the double-ply yield stress amplification factor (k) on the macroscopic response

Figure 5.20 shows the numerical macroscopic responses, for varied k, (where $k = {}^{\sigma_{Y,t2}}/_{\sigma_{Yield}}$). Analyses were performed with two additional values of k, 1.00 and 1.2 below the default value of 1.41; for k = 1.2 and 1.41 the yield stress of the material constituting the double cell walls was increased by a factor of 20 % and 41 % respectively. The effect was small, however, an increase in k caused a general lift in magnitude across the response.

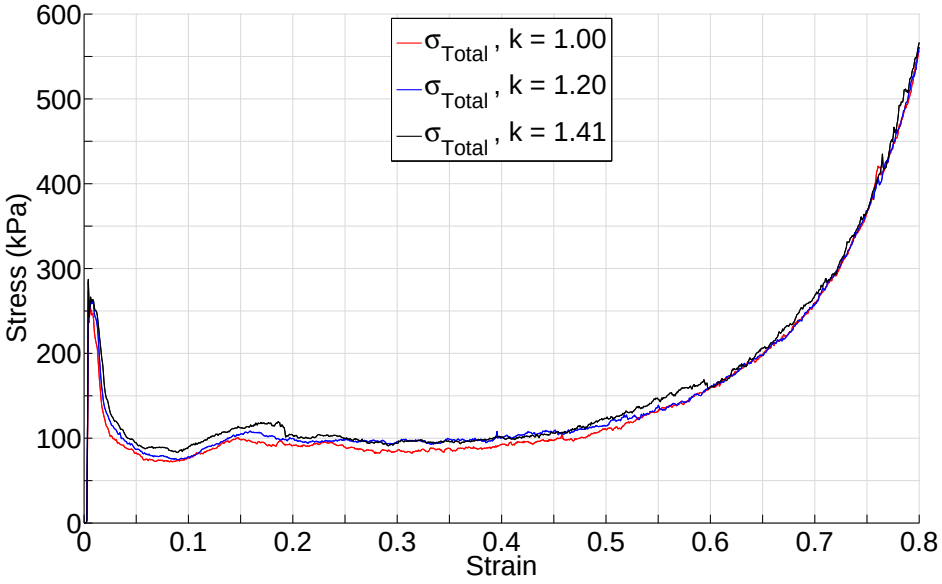

Figure 5.20 Total transmitted stress by the honeycomb σ_{Total} vs axial strain ε during the simulations with varied double to single-ply cell wall yield stress ratio k.

Figure 5.21 (a) and (b) shows how the peak and plateau transmitted stresses σ_{Peak}, $\sigma_{Plateau}$ (blue and red lines) and the strain to compaction ε_{Comp} (green line), changed with k. As k was increased from 1 to 1.41, σ_{Peak} and $\sigma_{Plateau}$ each increased by 10 kPa and 9 kPa, an increase of 4 and 10 % respectively; the effect of varying k on the compaction strain was negligible, illustrated by the extremely tight y axis in Figure 5.21 (b).

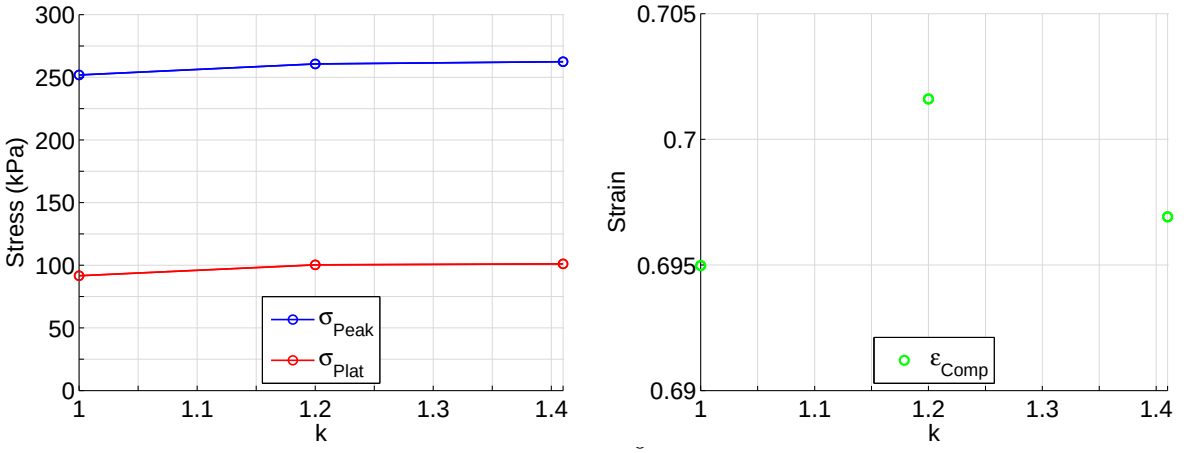

(a) (b)

Figure 5.21 Variations of the macroscopic response parameters (a) σ_{Peak}, $\sigma_{Plateau}$ and (b) ε_{Comp} as a result of variations in the double to single cell wall yield stress ratio k.

Figure 5.22 shows how the internal strain energy per unit volume U increased with strain ε, as k was varied. For plotted levels of strain, there was a linear increase of U with k. The cumulative effect of the general lift in response magnitude with k (observed above) caused an increase in the gradient of the U-k relationship with increased strain; when k was increased from 1 to 1.41, there was a linear increase in U of 3.45 kJ/m^3 at 20 % strain (solid black line) while at 80 % strain (solid green line), this increased to 8.80 kJ/m^3. Over the same interval $U_{\varepsilon_{Comp}}$ increased by 11 % from 78.9 to 87.4 kJ/m^3.

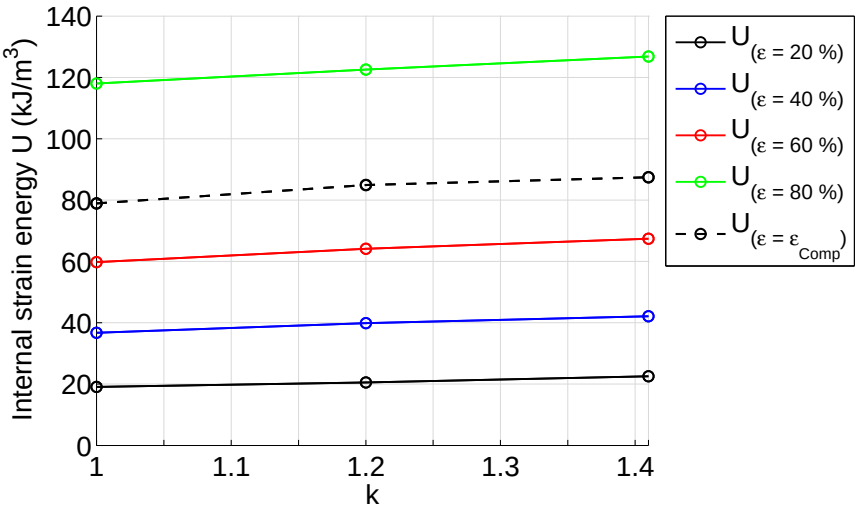

Figure 5.22 Variation of the total strain energy per unit volume $U(\varepsilon)$, at various increments of strain (including ε_{Comp}) as a result of variations in the double to single cell wall yield stress ratio k.

5.4.5 Effect of glue strength (σ_{Glue}) on the macroscopic response

Figure 5.23 shows the numerical macroscopic responses, for varied σ_{Glue}. The glue strength was varied between 0 MPa (no bond) and 7.05 MPa, $\sigma_{Glue} = \sigma_{Y,t2} = k \times \sigma_{Yield}$ (full strength bond).

Two main effects are visible from variations in σ_{Glue}; as the strength of the glue bond was increased, the rate of post-peak softening increased and the plateau shortened. For a full strength bond (green line) the transmitted stress began to lift away from the plateau at 25 % strain; when no bond was used (red line) the sample began to stiffen at 45 % strain. Once stiffening began, the actual shape of the rise was similar for all four analyses.

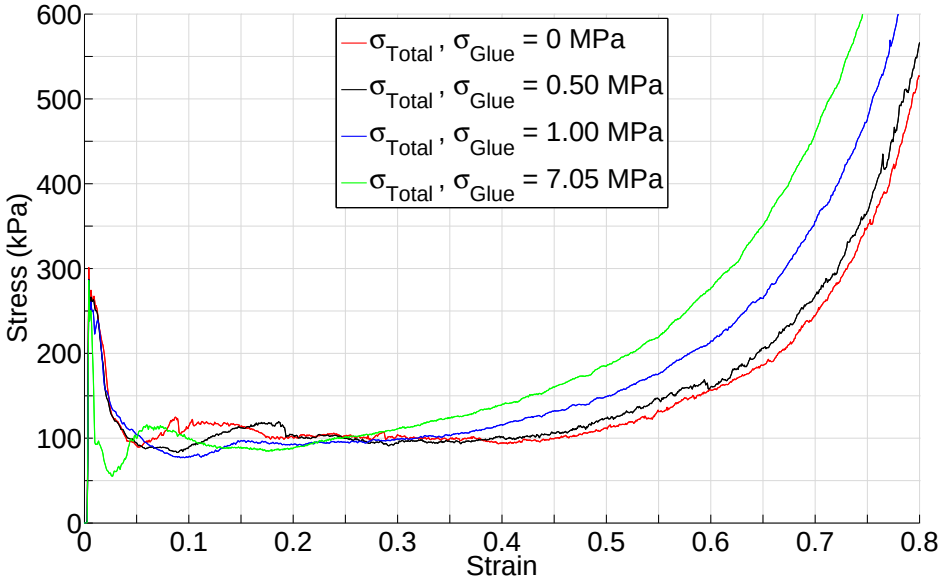

Figure 5.23 Total transmitted stress by the honeycomb σ_{Total} vs axial strain ε during the simulations with varied glue strength σ_{Glue}.

Figure 5.24 (a) and (b) shows how the peak and plateau transmitted stresses σ_{Peak}, $\sigma_{Plateau}$ (blue and red lines) and the strain to compaction ε_{Comp} (green line), changed with σ_{Glue}. An increase in σ_{Glue} from 0 to 7.05 MPa caused a drop in σ_{Peak} of 11 kPa (4 %) and an increase in $\sigma_{Plateau}$ of 27 kPa (27 %). The earlier onset of stiffening (visible in Figure 5.23), with increased σ_{Glue} caused a reduction in ε_{Comp} of from 71 to 58% strain. Sharp changes in gradient, at 1 MPa, visible on the blue, red and green lines in Figure 5.24 (a) and (b) suggested that the sensitivity of the response reduces as σ_{Glue} increases above 1 MPa.

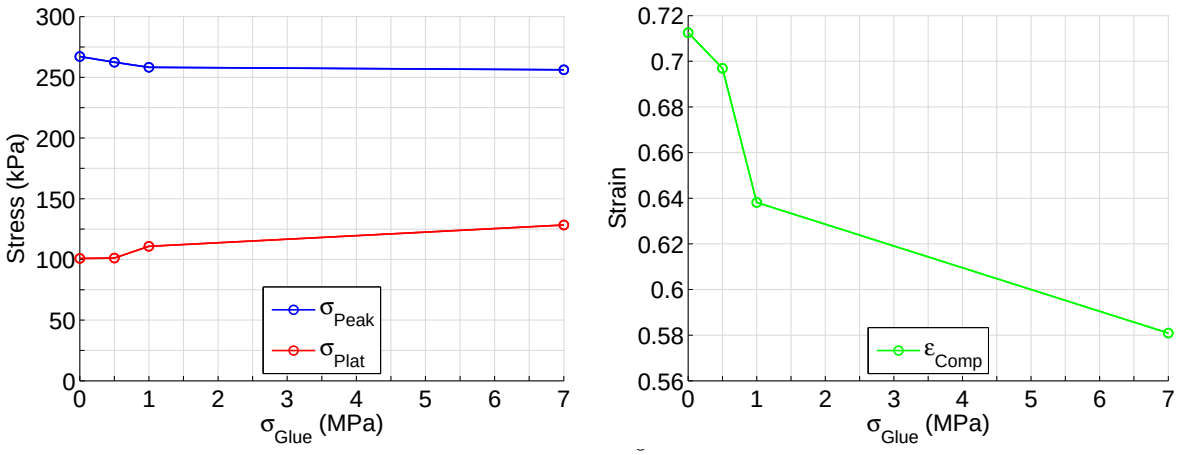

(a) (b)

Figure 5.24 Variations of the macroscopic response parameters (a) σ_{Peak}, $\sigma_{Plateau}$ and (b) ε_{Comp} as a result of variations in the cohesive bond strength between the double-ply cell walls σ_{Glue}.

Figure 5.25 shows how the internal strain energy per unit volume U increased with strain ε, as σ_{Glue} was varied. At low values of strain there was more energy stored when the glue bond was weak. In contrast, by 60 % strain an increase in σ_{Glue} caused an increase in U. The black dashed line shows that for this configuration, an increase in σ_{Glue} from 0 to full strength caused a reduction of $U_{\varepsilon_{Comp}}$ by 17 % from 90 to 75 kJ/m^3.

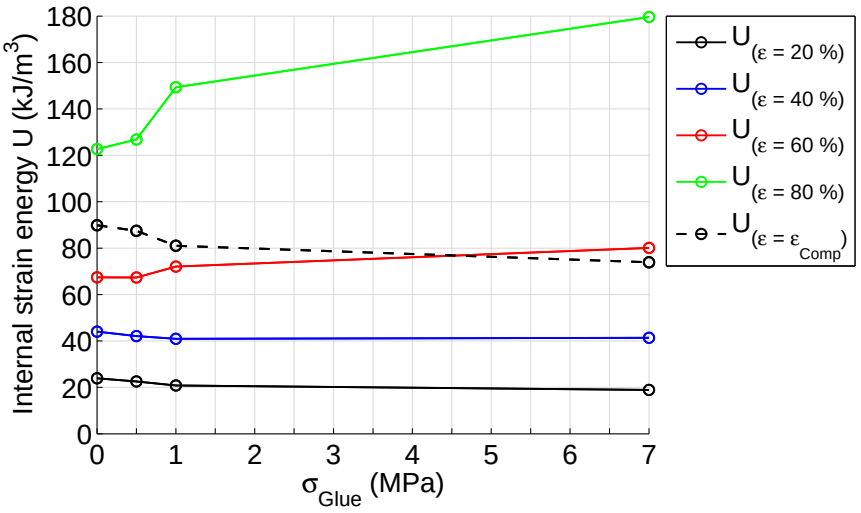

Figure 5.25 Variation of the total strain energy per unit volume $U(\varepsilon)$, at various increments of strain (including ε_{Comp}) as a result of variations in the cohesive bond strength between the double-ply cell walls σ_{Glue}.

5.4.6 Effect of yield stress (σ_{Yield}) on the macroscopic response

Figure 5.26 shows the numerical macroscopic responses, for varied σ_{Yield}. It can be observed that there was a strong relationship between variations in the yield stress and the macroscopic response, an increase of the cell wall yield stress increased the magnitude of load transmitted by the sample in the peak, plateau and compaction region.

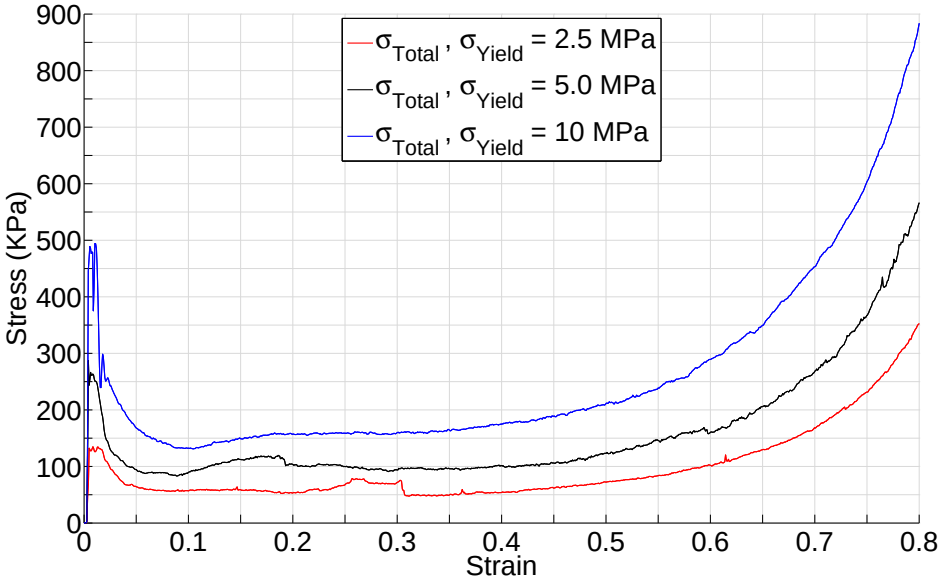

Figure 5.26 Total transmitted stress by the honeycomb σ_{Total} vs axial strain ε during the simulations with varied cell wall yield stress σ_{Yield}.

Figure 5.27 (a) and (b) shows how the peak and plateau transmitted stresses σ_{Peak}, $\sigma_{Plateau}$ (blue and red lines) and the strain to compaction ε_{Comp} (green line), changed with σ_{Yield}.

Three analyses were performed, σ_{Yield} was increased by a factor of 2, from 2.5 to 5 MPa and then again from 5 to 10 MPa; there was an almost perfectly linear relationship between both the values of σ_{Peak}, $\sigma_{Plateau}$ and σ_{Yield}; as σ_{Yield} was increased, the peak and plateau stresses diverged.

Over the first interval ($\sigma_{Yield} = 2.5 \rightarrow 5$ MPa), σ_{Peak} increased from 129 to 262 kPa, a factor of 2, suggesting direct proportionality: $\sigma_{Peak} \propto \sigma_{Yield}$. Over the second interval ($\sigma_{Yield} = 5 \rightarrow 10$ MPa), σ_{Peak} increased from 262 to 494 kPa, a factor of 1.9, suggesting that as the σ_{Yield} is increased the direct proportionality between σ_{Yield} and σ_{Peak} begins to degrade.

Now considering $\sigma_{Plateau}$ (red line), over both the first and second intervals there was an increase by a factor of 1.7, (from 60 to 101 kPa then from 101 to 171 kPa for); this was remarkable when considering that the macroscopic response curves shown in Figure 5.26 were not exact geometrical transformations of each other. An increase

in σ_{Yield} between 2.5 and 10 MPa also increased the compaction strain ε_{Comp} from 65 to 72 %.

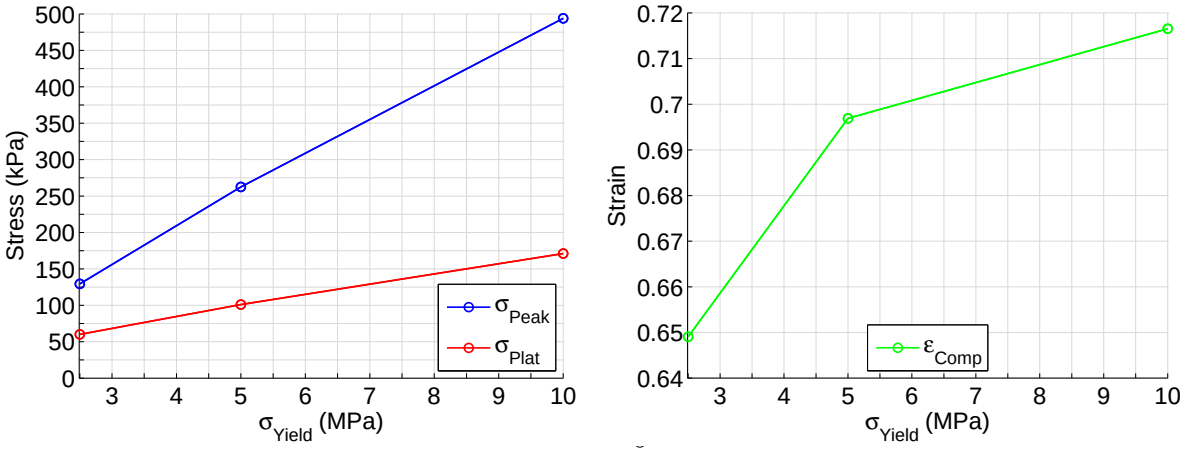

(a) (b)

Figure 5.27 Variations of the macroscopic response parameters (a) σ_{Peak}, $\sigma_{Plateau}$ and (b) ε_{Comp} as a result of variations in the cell wall yield stress σ_{Yield}.

Figure 5.28 shows how the internal strain energy per unit volume U increased with strain ε, as σ_{Yield} was varied. For all levels of strain there was a linear increase in U with σ_{Yield}; the gradient of the U-σ_{Yield} relationship also increased with strain. An increase in σ_{Yield} from 2.5 to 10 MPa caused a total increase in $U_{\varepsilon_{Comp}}$ by a factor of 3.4 from 45 to 155 kJ/m^3.

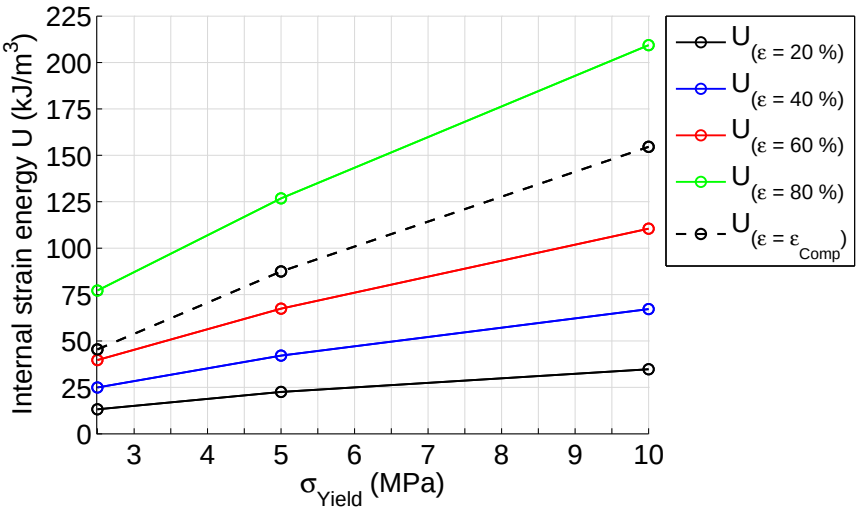

Figure 5.28 Variation of the total strain energy per unit volume $U(\varepsilon)$, at various increments of strain (including ε_{Comp}) as a result of variations in the cell wall yield stress σ_{Yield}.

5.4.7 Effect of tangent hardening modulus (E_t) on the macroscopic response

A graphical representation of the linear elastic-plastic constitutive model was given in Figure 4.3 on which it is shown that the tangent hardening modulus (E_t) is the gradient of the post-yield region. Its magnitude, in comparison to the elastic modulus (E), defines the degree of strain hardening present in the model; for a perfectly linear elastic-plastic material model $E_t = 0$, and for a perfectly linear elastic material model $E_t = E$. By default, a value of $0.0001 \times E$ was used to reduce the effect of strain hardening to a negligible magnitude. Three additional simulations were performed using values of E_t from $E \times 10^{-6}$ to $E \times 10^{-1}$, giving a range of $E_t = 2 \times 10^3 \rightarrow 2 \times 10^8$ Pa.

Figure 5.29 shows the numerical macroscopic responses, for the four simulations with varied E_t. For the default analyses and values below $E_t < 2 \times 10^5$ Pa the effect on the response was negligible; at an unknown value between 2×10^5 and 2×10^7 Pa, E_t began to have a significant effect on the response.

As E_t was increased, there was an increase in the transmitted stress across the full response and the differential between the peak and plateau region was reduced; for a value of 2×10^8 Pa the macroscopic response (green line) no longer resembled the idealistic macroscopic response which was illustrated in Figure 5.1.

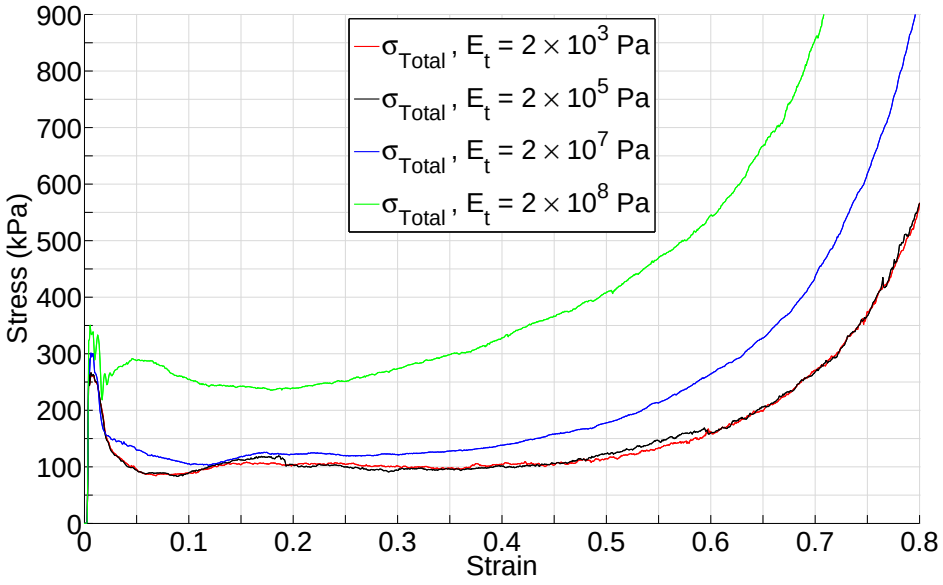

Figure 5.29 Total transmitted stress by the honeycomb σ_{Total} vs axial strain ε during the simulations with varied tangent hardening modulus E_t.

Figure 5.30 (a) and (b) shows how the peak and plateau transmitted stresses σ_{Peak}, $\sigma_{Plateau}$ (blue and red lines) and the strain to compaction ε_{Comp} (green line), changed with E_t. A log scale has been used on the x axis as the values of E_t were spread across many orders of magnitude.

For values of $E_t \leq 2 \times 10^5$ Pa, there was little to no effect on the response. As E_t was increased above 2×10^5 Pa, towards E (2×10^9 Pa), the magnitude (and sensitivity to a given change in E_t) of both σ_{Peak} and $\sigma_{Plateau}$ increased. Additionally, the values of σ_{Peak} and $\sigma_{Plateau}$ converged as E_t was increased towards E.

As ε_{Comp} was dependent on the difference between σ_{Peak} and $\sigma_{Plateau}$, their convergence as E_t was increased from 2×10^5 to 2×10^8 caused a rapid reduction in ε_{Comp}, from 69 to 41 %.

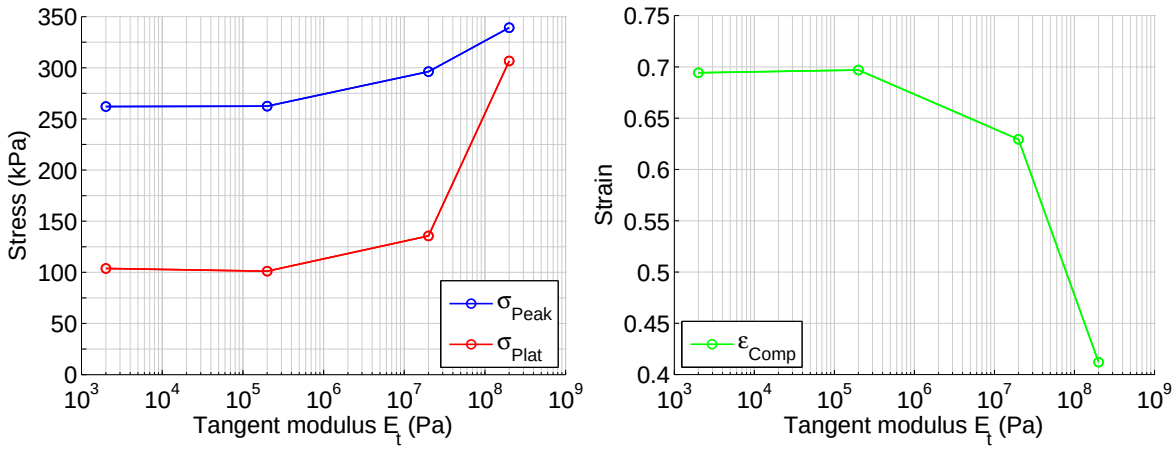

(a) (b)

Figure 5.30 Variations of the macroscopic response parameters (a) σ_{Peak}, $\sigma_{Plateau}$ and (b) ε_{Comp} as a result of variations of the cell wall tangent hardening modulus E_t.

Figure 5.31 shows how the internal strain energy per unit volume U increased with strain ε, as E_t was varied. As E_t was increased over the interval $2{\times}10^5 \rightarrow 2{\times}10^8$ Pa there was an increase in both the magnitude of U and its rate of increase with respect to E_t and ε. In comparison, $U_{\varepsilon_{Comp}}$ was relatively consistent, while still increasing by 29% (25 kJ/m^3) over the full interval.

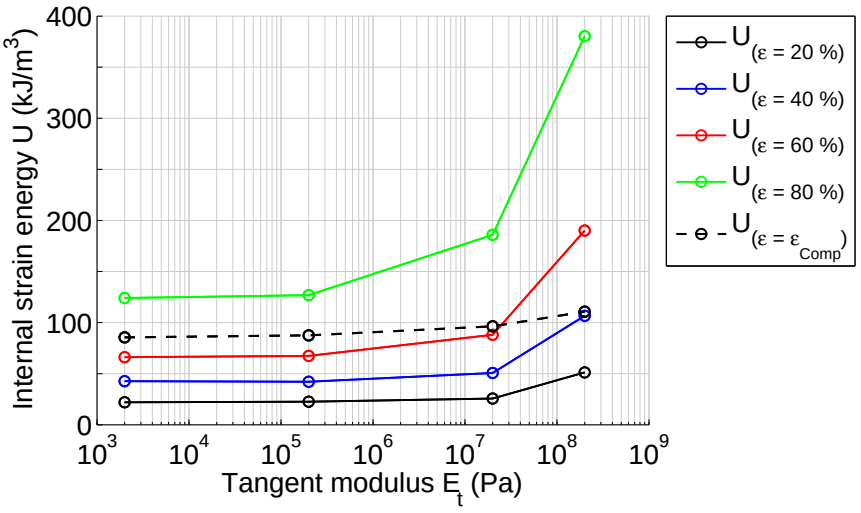

Figure 5.31 Variation of the total strain energy per unit volume $U(\varepsilon)$, at various increments of strain (including ε_{Comp}) as a result of variations in the cell wall tangent hardening modulus E_t.

5.4.8 Summary of the material parameter study macroscopic response results

Within the scope of analyses performed during this chapter (see Table 5.6) the material parameters which had the least effect on the honeycomb response were:

- Poisson's ratio (ν)
- Elastic modulus (E)
- Density (ρ)
- Yield stress ratio (k)

and those which were found to have a more significant effect on the response were:

- Glue strength (σ_{Glue})
- Yield stress (σ_{Yield})
- Tangent hardening modulus (E_t).

While it may be a true that ν, E, ρ and k are capable of significantly influencing the honeycomb response when increased outside of the boundaries imposed by the initial sensitivity analysis, or when used in combination with a different set of other parameter values, this further investigation must be reserved for future work.

5.5 Analysis of the effect of dominant material parameters on the structural and air pressure load carrying mechanisms

This section presents further investigation into how variations of the glue strength, yield stress and tangent hardening modulus affected the macroscopic response. This is done by identifying how each parameter variation affected the load carried by the cardboard cell wall structure σ_{Card}, and the internal air pressures σ_{Air} (the two components from which the macroscopic response is composed). Consideration is also given to what effect the resulting variations of σ_{Card} and σ_{Air} had on their corresponding energy absorption capacities U_{Card} and U_{Air}.

5.5.1 Effect of variations in glue strength (σ_{Glue}) on the mesoscopic load carrying mechanisms

Figure 5.32 shows macroscopic response for the four analyses with varied glue strength σ_{Glue}. The total transmitted load has been decomposed into its two constituents; each analysis is identified by a unique colour; the load transmitted by the cell walls σ_{Card} is plotted with solid lines, and load transmitted by the internal air pressures σ_{Air} is plotted with dashed lines. On the same graph, $\sigma_{Air,1D}$ has been plotted for reference (as calculated from Equation 5.1); $\sigma_{Air,1D}$ is the pressure which would develop if no gas was lost via blow out and there was no change of internal volume due to structural deformations.

For the most part, variations in the glue strength had no significant effect on σ_{Card}. However, when a full strength glue bond was used the initial post peak

structural deformation was distributed throughout the full height of the structure, causing a much more rapid softening than was present in the other three analyses, whereby the the deformations were concentrated around the creation of the first progressive fold. This behaviour can be seen in Figure 5.32, below 5 % strain, by comparison of the much steeper solid green curve with the other three less steep curves.

The analyses shown with green and black lines (σ_{Glue} = 0.5 and 7.05 MPa) were both discussed in detail during Section 5.2. To summarise, three overlying mechanisms have been observed to control the magnitude of internal air pressure development; 1. volume increase due to cell wall drift; 2. volume reduction due to structural deformations; and 3. loss of gas via venting. For air to vent from a given cell, a pathway must be formed from that cell to the perimeter. To form, a pathway must pass through at least one pair of initially bonded double-ply cell walls. An increase of σ_{Glue} increases the stress required to separate the double-ply cell walls, less pathways are able to form, less air is vented and as a result higher pressures develop.

With increased σ_{Glue}, σ_{Air} approached $\sigma_{Air,1D}$, but even with a full strength glue bond the honeycomb provided less than full restraint to the entrained air and $\sigma_{Air,1D}$ was not reached. Additionally, increases of σ_{Glue} had diminishing returns, increasing σ_{Glue} from 0.5 to 1 MPa (an interval of 0.5 MPa) had a larger effect on σ_{Air} than increasing from 1 to 7.05 MPa (an interval 6.05 MPa).

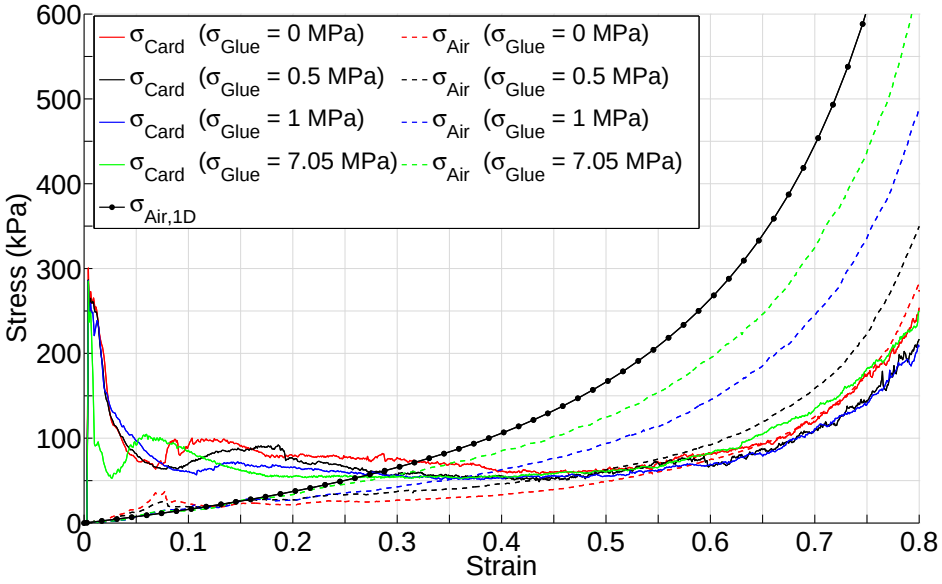

Figure 5.32 Stress transmitted by the cell wall structure σ_{Card} and internal air pressures σ_{Air} vs axial strain ε during the simulations with varied glue strength σ_{Glue}. In addition, $\sigma_{Air,1D}$ (as given by Equation 5.1) has been plotted, illustrating the stress which would be transmitted through the air if it were perfectly constrained and subject to an axial strain of ε.

Figure 5.33 shows how the two components of internal strain energy changed with variations in σ_{Glue}; U_{Card} is permanently stored in non-reversible plastic strain of the cell walls and U_{Air} is temporarily stored by reversible compression of the entrained air.

Variations of σ_{Glue} had little effect on U_{Card}, it is worth nothing that the energy absorbed during the peak stress region was insignificant in comparison to the magnitude of energy absorption provided by the plateau. Counter intuitively, U_{Card} was higher for the analysis with no glue bonds. During the early response there was no effect on U_{Air}, but after 30 % strain an increase of σ_{Glue} caused a significant increase of U_{Air}; U_{Air} more than doubled from 48 to 111 kJ/m^3 when the glue bond was increased from zero to full strength.

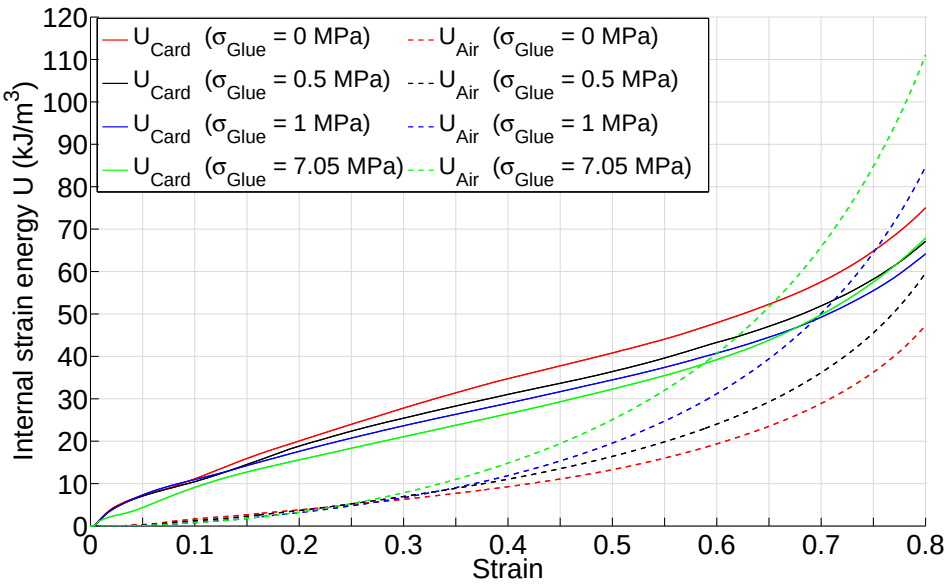

Figure 5.33 Energy per unit volume which was stored permanently as plastic strain energy in the cell walls U_{Card} and temporarily in compression of the internal air U_{Air} vs strain ε during the simulations with varied glue strength σ_{Glue}.

5.5.2 Effect of variations in yield stress (σ_{Yield}) on the mesoscopic load carrying mechanisms

Figure 5.34 shows σ_{Card} and σ_{Air} for the three analyses with varied yield strength σ_{Yield}. An increase of σ_{Yield} caused an increase in both σ_{Card} and σ_{Air}. For all three analyses, the structural response took on a similar shape, its magnitude was scaled in line with a variation of σ_{Yield}. Likewise, the gradient of σ_{Air} increased towards $\sigma_{Air,1D}$ as the yield stress was increased.

The point at which the structure and air were of equal stiffness ($\sigma_{Card} = \sigma_{Air}$) shifted later in the crushing response; as σ_{Yield} was increased from 2.5 to 5 to 10 MPa the point of equal stiffness moved from 35 to 44 to 52 % strain respectively. This suggested that as σ_{Yield} is increased, the significance of the internal air pressures (in comparison to the structural response) diminishes; even more so when considering that σ_{Air} will reach an upper limit (of $\sigma_{Air,max} \approx \sigma_{Air,1D}$), and σ_{Card} will not. It appears that the geometrical and material parameters, typical of a cardboard hon-

eycomb, place it in a region where the magnitude of load transmitted by the internal air pressures, is comparable to the magnitude of load transmitted by the cellular structure.

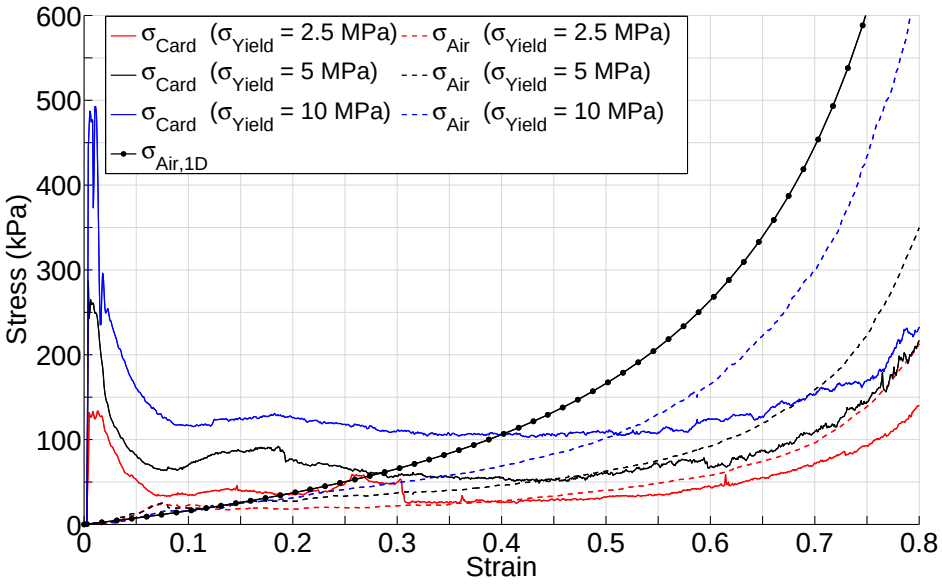

Figure 5.34 Stress transmitted by the cell wall structure σ_{Card} and internal air pressures σ_{Air} vs axial strain ε during the simulations with varied cell wall yield stress σ_{Card}. In addition, $\sigma_{Air,1D}$ (as given by Equation 5.1) has been plotted, illustrating the stress which would be transmitted through the air if it were perfectly constrained and subject to an axial strain of ε.

Figure 5.35 shows how U_{Card} and U_{Air} were affected by variations in σ_{Yield}. After the initial sharp increase caused by the peak stress, the U_{Card} curves were almost linear throughout the whole response, their gradient increasing with increased σ_{Yield}. During the early analysis U_{Air} was unaffected, at 25 % strain the curves began to diverge, an increase of σ_{Yield} increasing the rate of pressure development and therefore amount of energy stored in U_{Air}.

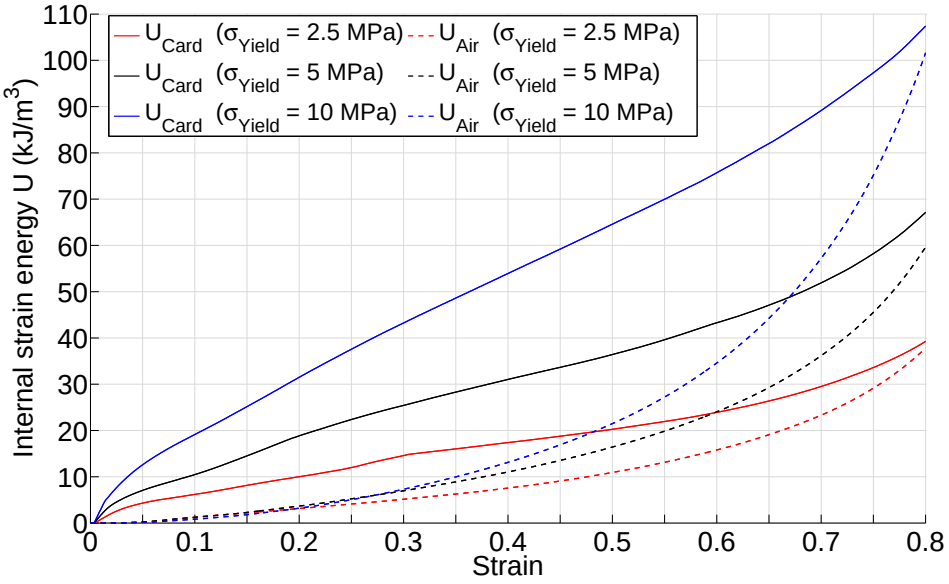

Figure 5.35 Energy per unit volume which was stored permanently as plastic strain energy in the cell walls U_{Card} and temporarily in compression of the internal air U_{Air} vs strain ε during the simulations with varied cell wall yield stress σ_{Yield}.

5.5.3 Effect of variations in tangent hardening modulus (E_t) on the mesoscopic load carrying mechanisms

Figure 5.36 shows how the stresses transmitted by the cardboard structure and internal air pressures were affected when the tangent hardening modulus E_t was varied. While the elastic modulus E is the gradient of the *pre-yield* limb of the stress strain constitutive model, the tangent hardening modulus E_t is the gradient of the *post-yield* limb, and therefore controls the magnitude of post-yield strain hardening present in the model. Note, that for all analyses the elastic modulus had a value of 2×10^{9} Pa.

When E_t was less than $0.001E$ i.e. when the tangent hardening modulus was less than 2×10^{6} Pa, any variation in its value had little effect on the honeycomb response. As the tangent hardening modulus was increased above 2×10^{6} Pa, the load being transmitted by both the structure and internal air pressures began to be affected, resulting in a general increase of σ_{Air} and σ_{Card} with an increase of E_t.

σ_{Air} increased when the tangent hardening modulus was increased from 2×10^5 Pa and 2×10^7 Pa, however when the tangent hardening modulus was increased above 2×10^7 Pa, to 2×10^8 Pa any further increase in σ_{Air} was marginal.

There was a notable increase of σ_{Card} as the tangent hardening modulus was increased above 2×10^6 Pa; additionally, the sensitivity of σ_{Card} to variations in the tangent modulus increased as its value approached the elastic modulus, increasing both the magnitude of structural stiffening and modifying the shape of the structural response. For the simulation where the tangent hardening modulus was a tenth of the elastic modulus (i.e. $E_t = 2 \times 10^8$ Pa), the plateau had risen to be almost equal to the peak stress, resulting in a structural response which was no longer characteristic of a typical EDM.

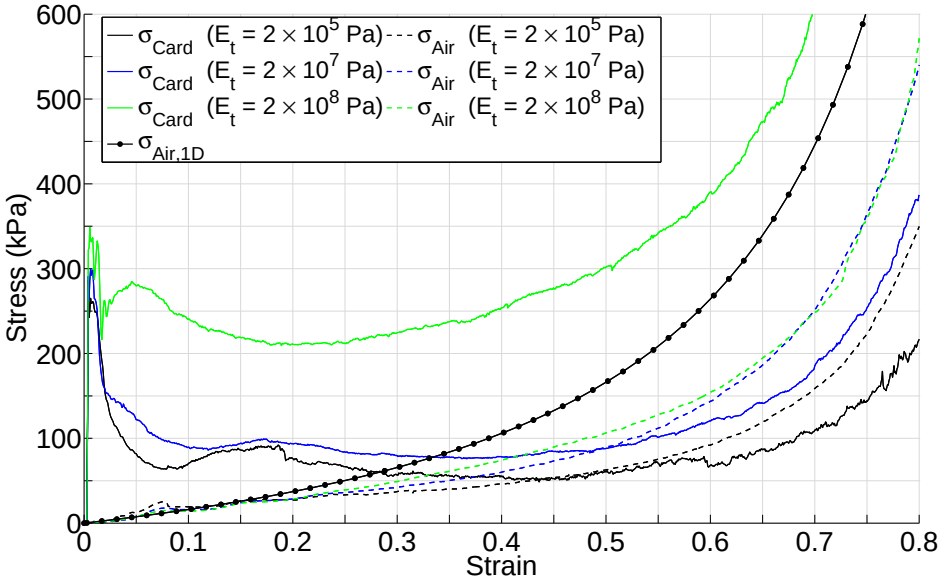

Figure 5.36 Stress transmitted by the cell wall structure σ_{Card} and internal air pressures σ_{Air} vs axial strain ε during the simulations with varied cell wall tangent hardening modulus E_t. In addition, $\sigma_{Air,1D}$ (as given by Equation 5.1) has been plotted, illustrating the stress which would be transmitted through the air if it were perfectly constrained and subject to an axial strain of ε.

The reason behind this stiffening can be understood by revisiting the basic mechanics behind the structural response. At any given strain, the load being trans-

mitted by the structure is a function of the material properties and the current geometrical arrangement. When the cell wall material has no strain hardening, the maximum stress which can be present within the cell walls is limited to σ_{Yield}. At the point just prior to impact the geometrical arrangement is at its stiffest, and so when impact occurs the internal stress increases to its maximum $\leq \sigma_{Yield}$, causing a macroscopic peak stress of σ_{Peak} to be transmitted through the honeycomb.

Immediately following σ_{Peak}, the internal stress can increase no more, the structure is forced to buckle, assuming the geometrically less stiff, but kinematically stable progressive buckling mode, and the macroscopic transmitted stress falls to $\sigma_{Plateau}$. The progressive buckling mode then propagates until the cell wall is exhausted and the honeycomb compacts causing the macroscopic transmitted stress to rise from σ_{Peak} as the honeycomb stiffens up.

When strain hardening was included, the stress within the cell walls was no longer limited to σ_{Yield}, and so when the internal stress reached the yield stress, in addition to buckling, the internal stress was able to then increase above σ_{Yield} at a rate proportional to the tangent hardening modulus and the rate of deformation. Consequently, rather than the whole structure being forced into a progressive buckling mode (concentrated at one point along the cell wall height), once a region of cell wall was deformed by a certain amount it stiffened up and the load began to act on the next region of the cell wall.

As E_t was increased towards E, a greater proportion of cell wall material was recruited, and stiffened to a greater magnitude, to provide resistance during the post peak deformation. As a resultthe plateau stress was no longer reliant solely on a change in geometrical stiffness (with a limit on the internal stress) and rose towards σ_{Peak}.

Figures 5.37 (a) and (b) show the deformed shapes, at 5 % axial strain (i.e. just after the initial peak stress), of the simulations with minimal and maximum strain hardening. The responses of these two simulations were shown with black and green lines in Figure 5.36. The behaviour discussed above is clearly illustrated; Figure 5.37 (a) shows a region of concentrated extreme deformation at the base of the cell walls

(and another beginning to form at their top) with the vast majority of the cell wall material unfolded; while Figure 5.37 (b) shows an evenly distributed deformation pattern, with the full height of cell wall being recruited and numerous simultaneous folds (of lesser magnitude) beginning to emerge.

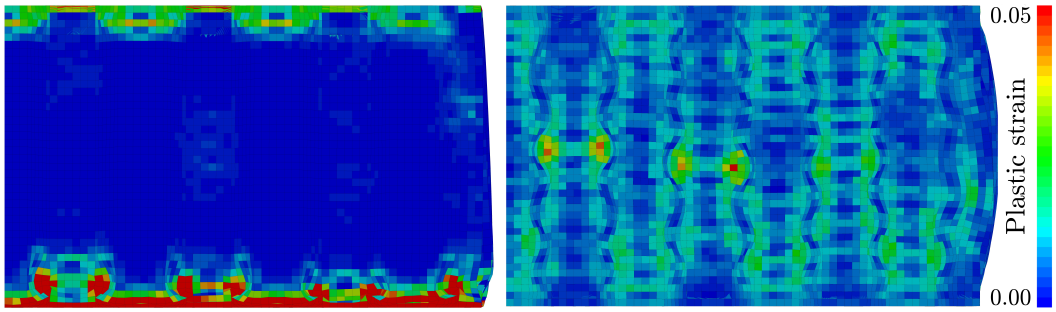

(a) $E_t = 2 \times 10^5$ Pa (b) $E_t = 2 \times 10^8$ Pa

Figure 5.37 Side elevation (camera is looking at the left edge of the geometry shown in Figure 5.2) showing the deformed shape of the honeycomb at 5 % axial strain for the simulations with minimum (a) and maximum (b) (strain hardening). Contours illustrate the magnitude of plastic strain of the cell wall material.

Figure 5.38 shows how U_{Card} and U_{Air} were affected by variations in E_t. While there was an increase of U_{Air} when E_t was increased from 2×10^5 to 2×10^7, the major effect was on the structural response; when E_t was increased above 2×10^7, U_{Card} increased dramatically, rapidly becoming the dominant energy absorption mechanism.

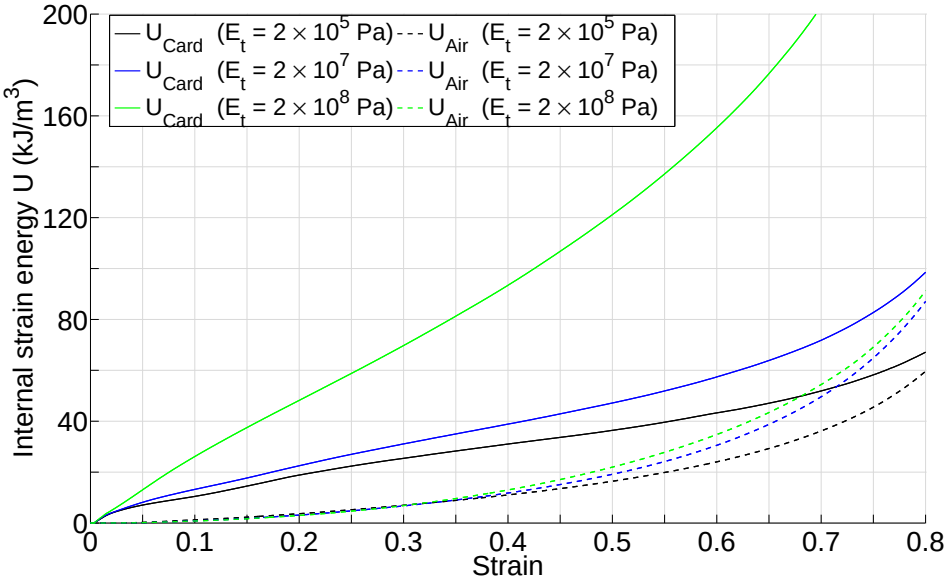

Figure 5.38 Energy per unit volume which was stored permanently as plastic strain energy in the cell walls U_{Card} and temporarily in compression of the internal air U_{Air} vs strain ε during the simulations with varied cell wall tangent hardening modulus E_t.

The reduction of the differential between the peak and plateau stresses suggest that it may be advantageous for a user to select a cell wall material which has a greater degree of strain hardening; meaning that when the peak and plateau transmitted stresses are equal, the honeycomb will provide a maximum energy absorption capacity for a given maximum design transmitted stress. In this case, the concept of compaction becomes irrelevant and the user would be required to decide a maximum permissible stress, which once reached, a known amount of energy absorption will have have been provided.

However, by considering the extreme case where the rate of post-yield strain hardening is increased to such an extent that $E_t = E$ (the cell wall becomes perfectly elastic). In this case, no yielding would occur and the transmitted stress would tend towards infinity with increased strain, i.e. the honeycomb would no longer function as an EDM. Thus, there must be a limit after which any further increases in the rate of post-yield strain hardening no longer have a desirable effect on the response.

Furthermore, by considering the fact that the internal stress is allowed to exceed σ_{Yield}, to what extent being dependent on the amount of time that the structure has to respond (i.e. the rate of loading and rate of strain hardening), it is clear that increasing the tangent hardening modulus must be also introducing a degree of strain rate sensitivity.

5.6 Conclusions

By performing numerical simulations of an air filled, cellular honeycomb structure subject to high strain rate axial crushing, it has been possible to study the mechanisms which occur during the non-linear, air-structure coupled, impact response of the cardboard honeycomb EDM. The numerical simulations have allowed the response to be observed with a much higher spatial resolution than what is realistically possible with experimental methods; thus, providing a novel insight into the mesoscopic mechanisms which compose the cardboard honeycomb macroscopic response. Furthermore, the numerical model was used as a platform to isolate the effects of variations in the cell wall material parameters on the structural and air pressure load carrying mechanisms, which together comprise the macroscopic EDM honeycomb response.

In Section 5.2 the role of the entrained air was studied. Comparison between simulations of the honeycomb with and without the air showed that the internal air pressures, while causing a temporary reduction in the stress transmitted by the cell walls, provided a substantial secondary load carrying mechanism and resulted in a net increase of the total macroscopic transmitted stress. The presence of pressured air within the honeycomb also modified the structural deformation mode, causing the cell walls to drift outwards, with a magnitude proportional to the distance from the honeycomb centre; a graphical representation of this behaviour is shown in Figure 5.5.

In Chapter 3 it was discovered that the internal air pressure distribution is non-uniform, with higher pressures developing towards the honeycomb centre; however,

as the pressure was only recorded at four discrete points the exact internal pressure distribution was unknown. The numerical modelling revealed that the internal pressure distribution is discretised by the cell walls, the air within each cell being of equal pressure and its magnitude dependent on the distance of that cell from the honeycomb perimeter; Figures 5.7 and 5.8 show the pressure distributions which developed during two separate numerical simulations.

It was observed that at any point during the response, there is a maximum possible internal air pressure. Its magnitude is dependent on the current volumetric strain provided by both the loss internal volume due to the axial strain and the loss of internal volume due to the volume occupied by the folded cell walls. If provided with sufficient lateral confinement by the honeycomb structure (such as for cells towards the centre), the pressure within any given cell will reach this maximum pressure; however, when the air pressure exceeds the provided lateral confinement (such as for cells towards the perimeter) it deforms the structure, causing the aforementioned outwards cell wall drift, and/or where a pathway to the perimeter can be formed, vents via blow out, reducing the internal pressure below the maximum.

The result (which is shown in Figure 5.8) is an internal pressure distribution where those cells capable of reaching the maximum pressure form a plateau of equal pressure, surrounded by cells containing air at a lesser pressure of reducing magnitude towards the honeycomb perimeter. As the axial strain is increased, so is the magnitude of internal air pressure, the pressure gradient between more cells becomes capable of exceeding its restraint and the plateau region shrinks.

As the maximum internal pressure increases, so does the gradient between it and the surrounding atmospheric pressure. As the pressure gradient increases, the air in more and more cells begins to reach pressures of magnitudes that allow it to overcome the resistance provided by both the structure and the bonded cell walls and create a blow out pathway. It may also be the case, that the pressure gradient required to form a pathway between some cells and the perimeter, is so high that no air is able to escape, from these cells, during the impact response.

Theoretically, as 4.6% of the macroscopic volume consisted of cardboard (see

Figure 5.2), once the structure had reached 95.4 % strain there would be no air remaining within the honeycomb. However, it may be the case that the air pressures reach such a high magnitude that they cause the impacting object to spring back. Although for the samples tested during the experimental tests, once the projectile was halted by the collar (at 83% strain), the internal air pressures rapidly vented (within ms).

To identify the effects of variations in the cell wall material parameters and evaluate their effects on the EDM behaviour of the cardboard honeycomb, four response parameters were calculated for each simulation: peak transmitted stress, plateau stress, strain at which compaction occurs and absorbed energy per unit volume. Over the scope of simulations performed (see Table 5.6) three material properties were found to have a significant effect on the response, these were: the double-ply glue bond strength, cell wall yield stress and the cell wall tangent hardening modulus.

An increase in the glue strength (while not having a noteworthy effect on the structural response) was found to significantly increase the volume of air retained within the honeycomb, resulting in much higher cellular pressures and therefore higher total stress transmitted through the air. This resulted in an increase of the energy absorbed per unit volume, at the compaction point by 29 %, when the glue bond strength was increased from zero to full strength (i.e. equal to the double cell wall yield stress).

An increase in the cell wall yield stress increased the stress transmitted by both the structure and the internal air pressures. The peak stress was an almost linear function of the yield stress, with the peak stress being a product of the yield stress and the cross sectional area of cardboard cell wall. The absorbed energy per unit volume at compaction increased by 340 % when the yield stress was increased from 2.5 to 10 MPa.

An increase in the magnitude of strain hardening, via an increase in the tangent hardening modulus, had no effect on the response when it was below a thousandth of the value of the elastic modulus (0.001E); above this, an increase in the tangent

modulus began to modify the response, lifting both the peak and plateau stress, but at different rates, causing the peak and plateau to converge. The mechanism behind this behaviour was shown in Figure 5.37; an increased amount of strain hardening, allowed the cell walls to stiffen above the yield stress and pass on load to the next section of the cell wall, the result was a structural response where a much larger proportion of the cell wall height was recruited to resist the impact loading.

5.6.1 Implications of the material parameter study for an end user

Due to the relatively cheap cost of cardboard, the limiting design factor is likely to be volume, possibly followed by weight if a significant amount cardboard was required; cost is unlikely to be a factor. In this case, the design process would roughly consist of:

1. Decide maximum permissible transmitted stress
2. Decide required magnitude of energy absorption (e.g. amount of kinetic energy to be removed from a falling object)
3. Determine the height and plan area available for the EDM
4. Select a honeycomb which conforms to the above criteria

The ideal cardboard honeycomb EDM will therefore be required to provide a maximum amount of energy absorption for the maximum permissible stress (normally the peak stress), while conforming to the permissible plan area and height. At the point at which the honeycomb stiffens up enough for the transmitted stress to exceed the initial peak stress, the honeycomb is deemed to be compact. With this in mind, the total strain energy per unit volume at the compaction strain is a good metric of the cardboard honeycombs EDM efficiency.

Considering the significant potential of the internal air pressures to provide free energy absorption capacity (air costs and weighs nothing in comparison to the cardboard), it may be advantageous for the user to utilise this capacity by specifying a

honeycomb configuration where the maximum permissible stress occurs not during the early structural response, but during the late exponential phase. In this case, the honeycomb would be acting as a hybrid airbag, possessing the late impact behaviour of an airbag, but with additional energy absorption capacity provided by the cell wall structure.

In Figures 5.32, 5.34 and 5.36 the curve $\sigma_{Air,1D}$ shows the maximum possible stress which can be exerted solely by the air pressures when subject to a 1 dimensional strain, this can also be used as an approximation for the maximum stress which an airbag could exert if it were perfectly restrained against lateral expansion. If the designer used a weak enough structure so that the maximum permissible stress occurred during the late exponential increase region, but with enough confinement so that the maximum air pressures were able to develop, everything above the $\sigma_{Air,1D}$ curves would be additional bonus resistance (and therefore energy absorption capacity), which the designer would not be able to access by selecting an air bag.

The simulations presented in this chapter show that the bias towards an air dominated response can be created by providing full strength glue bonds between the double ply cell walls and reducing the cell wall yield stress. Furthermore, in Section 5.5.3 it was shown that an increase in the rate of strain hardening caused the peak and plateau stresses to converge, causing the cardboard structure to provide a much greater amount of energy absorption for a given permissible stress.

The work presented in this chapter suggest that if it were possible to tightly control the material properties, an air filled honeycomb structure has the potential to be deployed as an extremely efficient EDM. In practice, it will be much easier to control the response of the cardboard honeycomb through a combination of adjustments in both the material and the geometrical parameters; thus, Chapter 6 contains an investigation into the effects of geometrical modifications, of the honeycomb geometry, on the cardboard honeycombs EDM response.

Chapter 6

Geometrical parameter study

This chapter presents an investigation into how variations of the meso and macroscale geometry affect the macroscopic impact response of an air-filled, thin-walled cellular honeycomb. The quarter symmetry numerical model (discussed in Section 5.1 of Chapter 5) was used as a basis for the study. By holding the cell wall material parameters constant and introducing solitary variations in one of six independent geometrical parameters it was possible to isolate each geometrical parameter's individual effect.

The numerical methodology is discussed (Section 6.1), followed by an outline of the analysed geometrical variations (Section 6.2). The effect of variations in the cellular geometry, on the cardboard honeycomb dynamic response, are then studied (Sections 6.3 to 6.8), and findings summarised, with consideration given to potential implications for the end user (Section 6.9).

6.1 Numerical methodology

There are six fundamental geometrical parameters, which define the honeycomb structure; three of which are mesoscopic, describing the geometry of each individual cell: cell wall thickness t, cell wall length L and internal expansion angle θ. Two are macroscopic, defining the global dimensions of the honeycomb sample: axial height (H), number of rows (nrow), and number of columns (ncol); nrow and nncol define

the minimum number of cells required to complete a path through the honeycomb from one edge to its opposite, on the X-X and Y-Y planes respectively. Figure 6.1 gives a graphical representation of each parameter and how they correspond to the cellular geometry of the quarter symmetry numerical model.

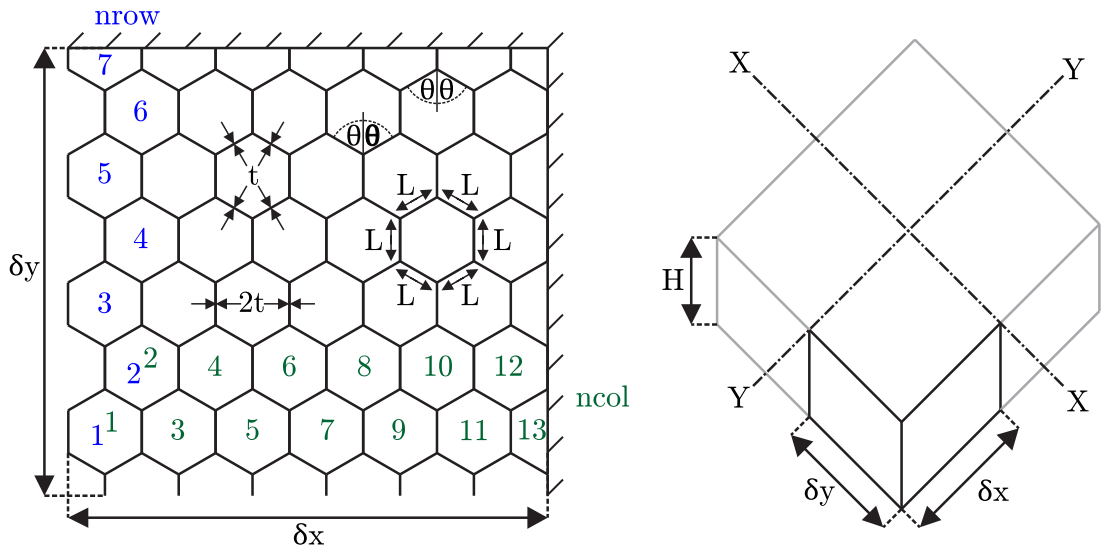

Figure 6.1 Geometry of the quarter symmetry numerical model with annotations showing the fundamental geometrical parameters. Footprint dimensions δ_x and δ_y have also been included to provide reference between the meso and macro scale.

Values of the fundamental geometrical parameters corresponding to the default cellular geometry are given in Table 6.1. Each of these six fundamental geometrical parameters can be varied independently with no effect on the other five. These six geometrical parameters form the basis of this parameter study, each one was varied in turn, while the others remained constant at their default values given below.

Table 6.1 The independent, fundamental, geometrical parameters which describe the honeycomb structure, for details see Figure 6.1. These values define the default cellular geometry on which variations were made; this geometry was also used for all analyses presented in Chapter 5.

t (mm)	L (mm)	$\theta°$	H (mm)	ncol (full)	nrow (full)
0.3	10	60	70	12.5 (25)	6.5 (13)

Variations of the *independent* geometrical parameters caused subsequent variations of *dependent* parameters. Values of eight dependent geometrical parameters, for the default quarter symmetry cellular arrangement, are given in Table 6.2, they are: δ_X and δ_Y, the dimensions of the honeycomb footprint in the X-X and Y-Y plane; A_{Trib}, the total footprint area i.e. the full tributary area from the full cellular structure; ΣL, the total length of cell wall within A_{Trib}; A_{Card}, the total cross sectional area of cardboard cell wall; ϕ_{Card}, the percentage of A_{Trib} which is composed of cardboard material; A_{Hex}, the internal plan area of one hexagonal cell; and A_{Air}, the total cross sectional area of entrained air; and, total macroscopic volume of the honeycomb V.

To ensure a fair comparison between simulations, when an independent parameter variation resulted in an increase of the plan area, the loading block was scaled in accordance. As the loading block was given more than enough energy to provide a forced displacement, this scaling of its size was mainly to ensure that the honeycomb was crushed evenly.

Table 6.2 The dependent geometrical parameters which are functions of those given in Table 6.1. Values given are for the default cellular geometry, on which variations were made. For details see Figures 6.1 and 6.2.

ncell	δ_X (mm)	δ_Y (mm)	A_{Trib} (mm^2)	ΣL (mm)	A_{Card} (mm^2)	ϕ_{Card} (%)	A_{Hex} (mm^2)	A_{Air} (mm^2)	V (m^3)
40.75	112.6	105.0	11821	1820	546	4.62	250.8	10220	8.27×10^{-4}

Figure 6.2 shows a simple two cell honeycomb, with annotations to clarify the identification for the four areas referenced in the table above.

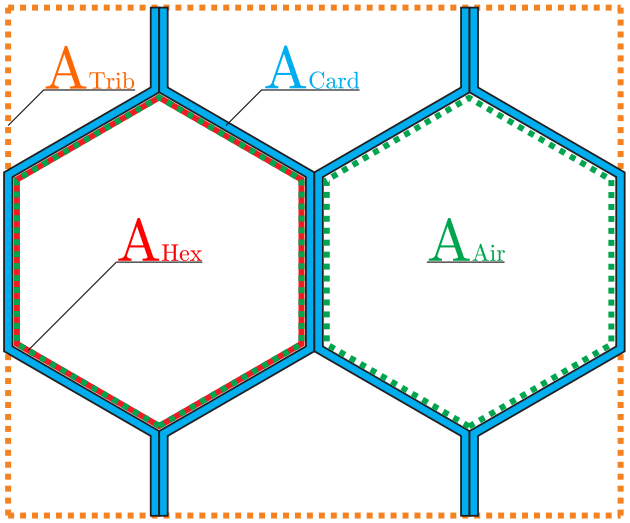

Figure 6.2 An illustration showing the four dependent areas for a honeycomb consisting of two cells, where: A_{Card} is the cross sectional area of cardboard cell wall, A_{Hex} the internal area of one cell, A_{Air} the total area of enclosed air within the honeycomb and A_{Trib} is the total footprint tributary area.

The arbitrary initial geometry prevents a simple relationship between nrow, ncol and the number of cells ncell from being defined (for this application it was quicker and easier to just count the cells); however, some useful relationships between the independent and dependent parameters can be drawn:

$$\delta_x = (ncol + 0.5)L\sin\theta \qquad \delta_y = (nrow + 0.5)(L\cos\theta + L) \tag{6.1}$$

$$A_{Hex} = 2L^2\left(\sin\theta + \sin\theta\cos\theta\right) - 3tL \tag{6.2}$$

$$\Sigma\, L = 2\, L(nrow + 0.5)(ncol + 0.5) \tag{6.3}$$

which can be used to calculate the remaining dependent parameters

$$A_{Trib} = \delta_x\delta_y \qquad A_{Air} = ncell{\cdot}A_{Hex} \qquad A_{Card} = \Sigma L{\cdot}t \qquad \phi_{Card} = {}^{A_{Card}}/_{A_{Trib}}. \tag{6.4}$$

Note that $\phi_{Card} \neq {}^{A_{Card}}/_{A_{Air}}$ because A_{Air} only includes air sealed within cells. Finally volume V is calculated by multiplying A_{Trib} by height H; likewise, due to

the honeycomb cross section being homogeneous over its height H, A_{Card}, A_{Hex} and A_{Air} can be converted to volumes by simply multiplying by H.

Table 6.3 gives values of the material parameters which were used for all analyses. To provide ongoing consistency they matched the default material parameters used during the material parameter study (presented in Chapter 5).

Table 6.3 The material parameters which were used for all analyses presented in this chapter and are consistent with the default material parameters used during Chapter 5, they are: yield stress, σ_{Yield}; double to single cell wall yield stress ratio, k; elastic modulus, E; tangent modulus, E_t; Poisson's ratio, ν; density, ρ; and cohesive bond strength, σ_{Glue}.

σ_{Yield}	k	E	E_t	ν	ρ	σ_{Glue}
5 MPa	1.41	2 GPa	2 $\times 10^5$ Pa	0.3	630 kg/m^3	0.5 MPa

The numerical results were analysed in a similar manner to Chapter 5, for each analysis the four response parameters (shown in Figure 5.1) were evaluated and used as metrics to identify and quantify any trends caused by each geometrical variation. Additionally, as cardboard is a relatively cheap and light material and the cardboard honeycomb mostly consists of air ($\phi_{Card} = 4.62\%$ in Table 6.2), volume rather than weight (and cost) is likely to be the limiting design factor. With this in mind, the response parameters will continue to be presented in the format of stresses and energy per unit volume, effectively treating the cardboard honeycomb as an EDM unit of macroscopic dimensions $V = \delta_x \cdot \delta_y \cdot H$.

6.2 Geometrical parameter study scope

Table 6.4 shows the range of variations performed for each independent geometrical parameter. The ranges of variation for t, L, θ and H were chosen to cover a range of known possibilities which would be typical for a cardboard honeycomb mesh; values recorded for the samples used during the experimental testing of L and θ were given

in Tables 3.3 and 3.21, minimum and maximum observed values for L were 8 to 24.7 mm, and average values for θ were shown to vary between 34.5° and 37.5° and the cell wall thickness t was measured as 0.28 mm. L was increased from the standard of 70 mm to a maximum of 140 mm, to study the effect of using a deeper honeycomb and the number of rows and columns were reduced from the original geometry which consisted of 13 rows and 25 columns. The values shown for ncol and nrow reference the number of columns and rows in the full honeycomb structure.

Table 6.4 Range of variations used for each independent geometrical parameter.

Parameter	Minimum value	Maximum value
t	0.15 mm	0.9 mm
L	5 mm	30 mm
θ	30°	90°
H	70 mm	140 mm
ncol	9	25
nrow	5	13

6.3 Effect of cell wall thickness (t) on the response

The cell wall thickness was varied from 0.15 to 0.9 mm, Table 6.5 shows the dependent parameters which were affected and how they varied as a result. The cross sectional area A_{Card} increased proportionally with t from 273 to 1638 mm^2, in turn, the proportion of total area which consisted of cardboard ϕ_{Card} to increase from 2.31 to 13.9 %, while the area of entrapped air A_{Air} reduced by 8.8 % from 10403 to 9487 mm^2.

Table 6.5 Secondary geometrical variations which resulted from variations in the cell wall thickness t.

t (mm)	A_{Card} (mm^2)	ϕ_{Card} %	A_{Hex} (mm^2)	A_{Air} (mm^2)
0.15	273	2.31	255.3	10403
0.30	546	4.62	250.8	10220
0.60	1092	9.24	241.8	9853
0.90	1638	13.9	232.8	9487

6.3.1 Effect of variations in t on the macroscopic response

Figure 6.3 shows the numerical macroscopic responses for the simulations with varied cell wall thickness. A general stiffening with increased cell wall thickness can be observed with σ_{Total} being increased across the full response; an increase of t caused an increase in the peak stress, an increase in the plateau and earlier compaction.

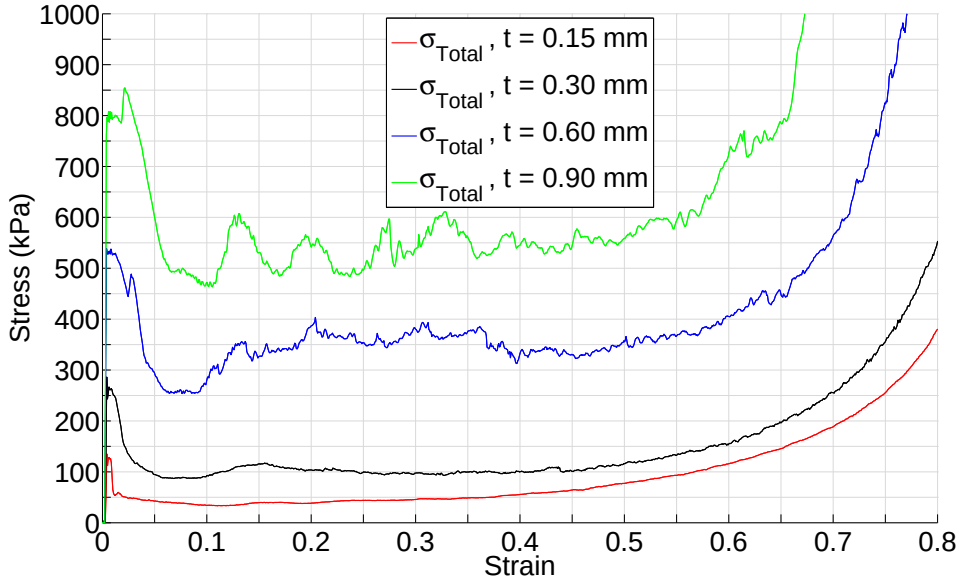

Figure 6.3 Total transmitted stress by the honeycomb σ_{Total} vs axial strain ε during the simulations with varied cell wall thickness t.

Figure 6.4 (a) and (b) shows how the peak and plateau transmitted stresses

σ_{Peak}, $\sigma_{Plateau}$ (blue and red lines) and the strain to compaction ε_{Comp} (green line), changed with variations of the cell wall thickness. As t was increased from 0.15 to 0.9 mm, σ_{Peak} increased linearly from 126 to 847 kPa; σ_{Plat} increased almost linearly, with equal rate to σ_{Peak} between 0.3 and 0.6 mm and at a slower rate below 0.3 and above 0.6 mm; ε_{Comp} reduced linearly from 70.6 to 66.2 % between 0.3 and 0.6 mm, but for the simulation with 0.15 mm thick cell walls the stiffening limb reached the peak stress uncharacteristically early causing a ε_{Comp} of 61.7 % strain.

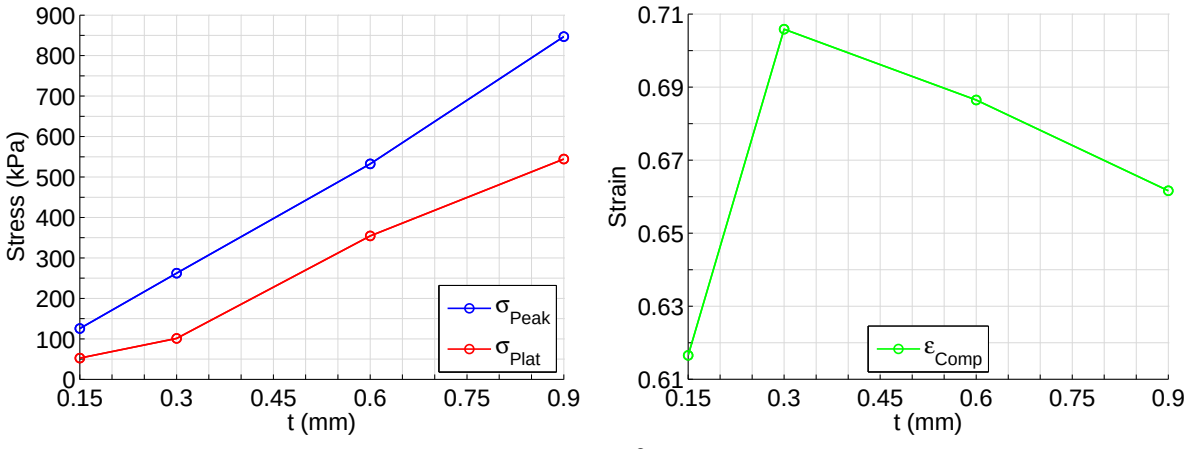

(a) (b)

Figure 6.4 Variations of the macroscopic response parameters (a) σ_{Peak}, $\sigma_{Plateau}$ and (b) ε_{Comp} as a result of variations of the cell wall thickness t.

Figure 6.5 shows how the internal strain energy per unit volume U increased with strain ε, as t was varied. For all levels of strain, an increase of t resulted in a larger value of U. The gradient of the $t - U$ relationship increased with an increase of ε, this was caused by the cumulative stiffening effect observed in Figure 6.3. At 20, 40, 60 % and ε_{Comp}, the $t - U$ relationship was linear for over 0.3 mm $< t <$ 0.9 mm; while for the 0.15 mm analysis the values of U sat above the projected linear trends. Increasing t from 0.15 to 0.9 mm resulted in an increase of the energy absorbed at compaction $U_{\varepsilon_{Comp}}$ from 40 to 385 kJ/m^3, a factor of 9.6.

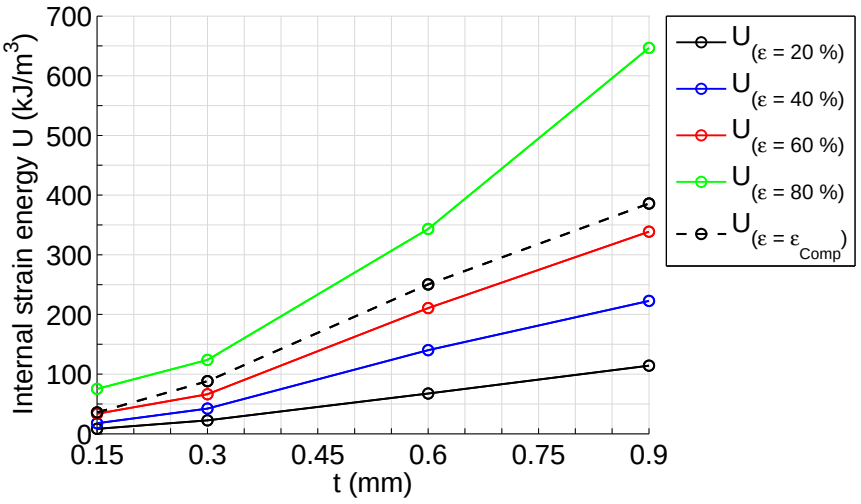

Figure 6.5 Variation of the total strain energy per unit volume $U(\varepsilon)$, at various increments of strain (including ε_{Comp}) as a result of variations in the cell wall thickness t.

6.3.2 Effect of variations in t on the mesoscopic load carrying mechanisms

Figure 6.6 shows how the stress carried by the structure σ_{Card} and the stress carried by the internal air pressures σ_{Air} were affected when the cell wall thickness was varied. Changing the cell wall thickness had no effect on the honeycomb footprint area; any variations in the transmitted stresses are also direct representation of the magnitude of transmitted load.

Comparison between the solid lines shows a general increase of σ_{Card} in response to an increase of t. An increase of t also caused the structure to compact earlier and with increased rate, this can be observed by comparison between the point at which structural compaction began to occur on the blue and green solid lines at 70 and 65 % strain respectively.

The red and black dashed lines show that σ_{Air} was mostly unaffected when the cell wall thickness was reduced below 0.3 mm, above 0.3 mm σ_{Air} increased with t towards the upper limit of $\sigma_{Air,1D} \approx \sigma_{Air,max}$, by the simulation with a cell wall

thickness of 0.9 mm, σ_{Air} was very close to (and may have reached) this upper limit.

Comparison between the σ_{Card} and σ_{Air} curves, for each analysis, shows a shift in the dominant load carrying mechanism as the cell wall thickness is varied. During crushing of the honeycomb with 0.15 mm thick cell walls, the point at which $\sigma_{Air} = \sigma_{Card}$ occurred at a very low strain of 15 % and from then on $\sigma_{Air} > \sigma_{Card}$; during crushing of the honeycomb with 0.9 mm thick cell walls, σ_{Air} was less than σ_{Card} for the full event.

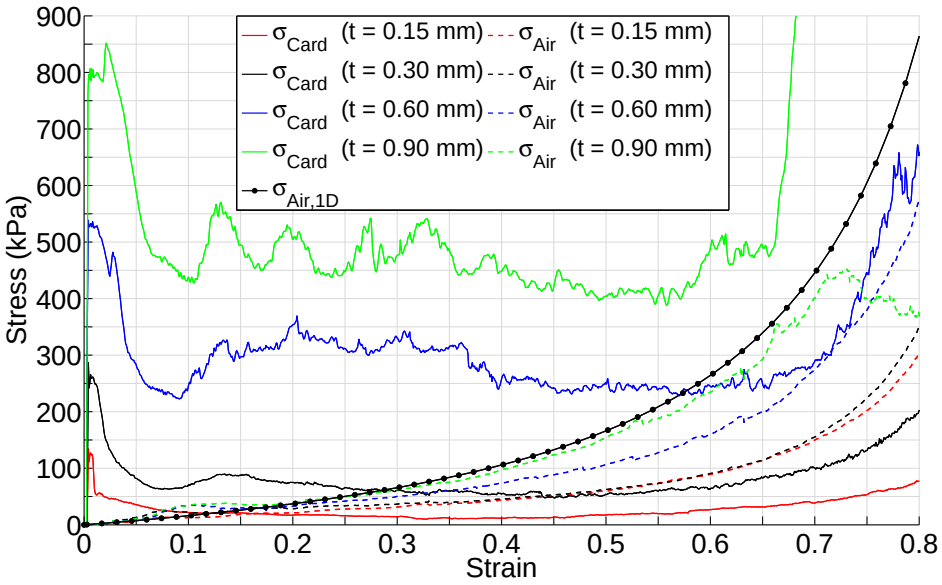

Figure 6.6 Stress transmitted by the cell wall structure σ_{Card} and internal air pressures σ_{Air} vs axial strain ε during the simulations with varied cell wall thickness t. In addition, $\sigma_{Air,1D}$ (as given by Equation 5.1) has been plotted, illustrating the stress which would be transmitted through the air if it were perfectly constrained and subject to an axial strain of ε.

Figure 6.7 shows how U_{Card} and U_{Air} were affected by changes in the cell wall thickness t. U_{Card} increased for each increase of t. The greater spacing between the black and blue solid lines than the spacing between the blue and green solid lines shows that the rate of increase was mostly affected when increasing t from 0.3 to 0.6 mm than for the same increment when increasing from 0.6 to 0.9 mm. As t was increased between 0.3 and 0.9 mm, so did U_{Air}, while between 0.15 and 0.3 mm

there was almost no effect.

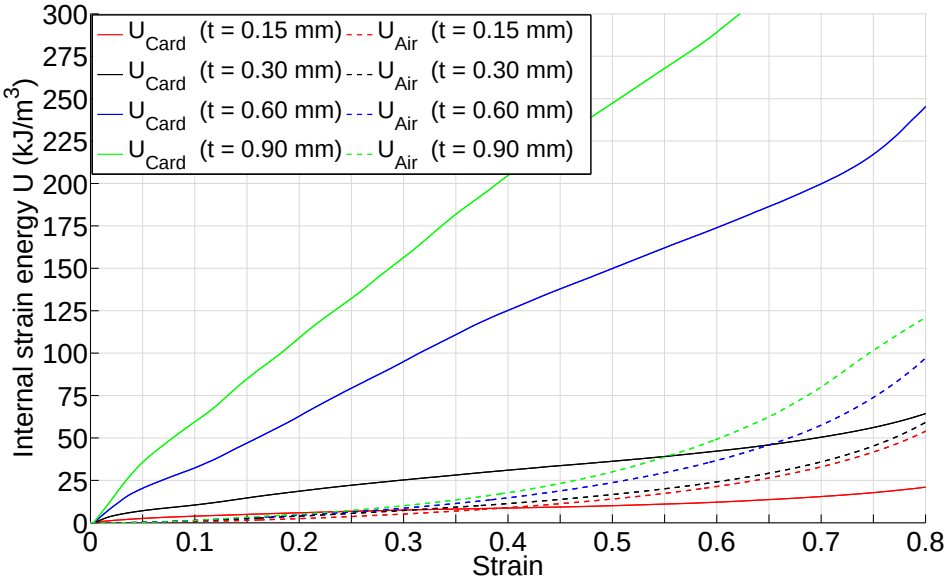

Figure 6.7 Energy per unit volume which was stored permanently as plastic strain energy in the cell walls U_{Card} and temporarily in compression of the internal air U_{Air} vs strain ε during the simulations with varied cell wall thickness t.

6.4 Effect of cell wall length (L) on the response

Four simulations were performed with varied cell wall length (L) 5, 10, 20 and 30 mm, Table 6.5 shows the dependent parameters that were affected and how they varied as a result; changing L caused variations in every dependent parameter. Figure 6.8 compares the four (full) cellular geometries which resulted as a variation of the cell wall length.

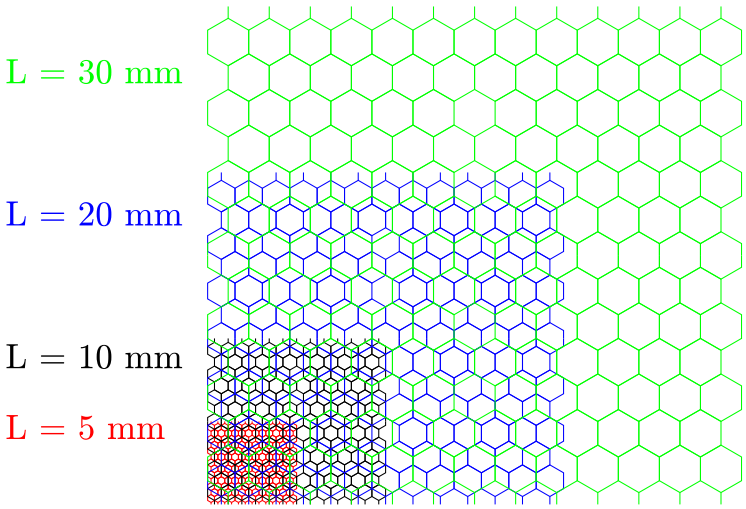

Figure 6.8 Comparison between the four tested cellular geometries, which were generated by variations in the cell wall length L.

As the cell wall thickness was held constant, varying the cell wall length caused a linear variation in the cardboard cross sectional area; because the cell wall thickness was held constant, an increase of the cell wall length L, by a factor of 6 (from 5 to 30 mm,) also caused an increase in the total cross sectional area of cardboard A_{Card} by a factor of 6. In contrast, the area over which the cardboard cross section acts was a square function; when L was increased by a factor of 6 from 5 to 30 mm, A_{Trib} increased by a factor of 6^2. Consequently, as the cell wall length was increased the proportion of cardboard to air reduced.

This resulted in a reduction of ϕ_{Card}; the honeycomb volume consisted of 9.24 % cardboard for a cell wall length of 5 mm, while this reduced to 1.54 % when the cell wall length was increased to 30 mm. Over the same interval, the cross section of air increased by a factor of 38, slightly more than the A_{Trib}; the volume of A_{Hex} occupied by the cell wall thickness (the $-3tL$ from Equation 6.2) became proportionally less with increased L.

Table 6.6 Secondary geometrical variations which resulted from variations in the cell wall length L.

L (mm)	δ_X (mm)	δ_Y (mm)	A_{Trib} (mm^2)	ΣL (mm)	A_{Card} (mm^2)	ϕ_{Card} (%)	A_{Hex} (mm^2)	A_{Air} (mm^2)	V (m^3)
5	56.3	52.5	2955	910	273	9.24	60.5	2463	2.10×10^{-4}
10	112.6	105.0	11821	1820	546	4.62	250.8	10220	8.27×10^{-4}
20	225.2	210.0	47285	3640	1092	2.31	1021.2	41615	3.31×10^{-3}
30	337.7	315.0	106376	5460	1638	1.54	2311.3	94184	7.45×10^{-3}

6.4.1 Effect of variations in L on the macroscopic response

Figure 6.9 shows the macroscopic responses for the simulations with varied cell wall length L. As L was increased from 5 to 30 mm, there was reduction in the stiffness of the early response and an increase in the late response. Additionally, as L was increased, the gradient of the plateau region, between 10 and 60 % strain, shifted from negative to positive.

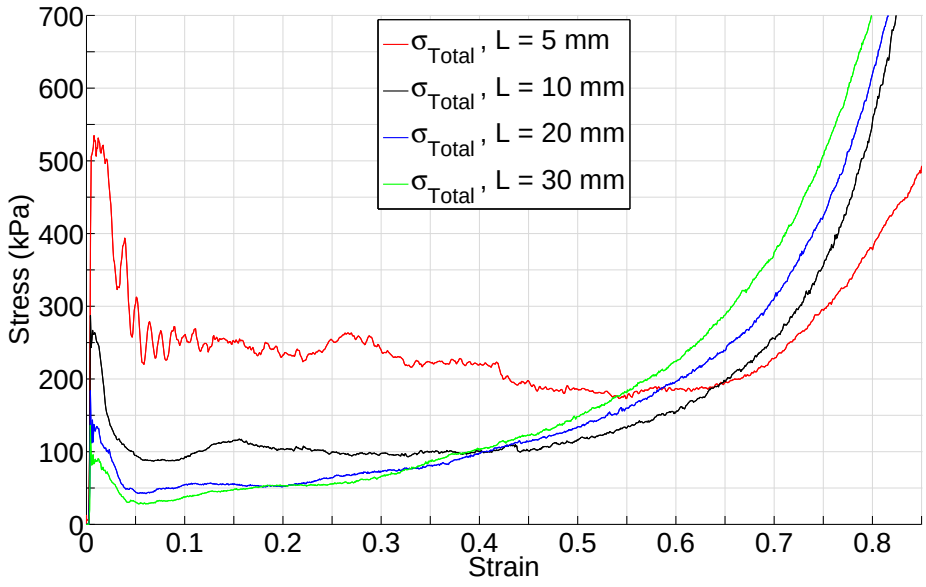

Figure 6.9 Total transmitted stress by the honeycomb σ_{Total} vs axial strain ε during the simulations with varied cell wall length L.

Figure 6.10 (a) and (b) shows how the peak and plateau transmitted stresses σ_{Peak}, $\sigma_{Plateau}$ (blue and red lines) and the strain to compaction ε_{Comp} (green line), changed with variations of the cell wall length. σ_{Peak} σ_{Plat} and ε_{Comp} all reduced as L was increased. σ_{Peak} was inversely proportional to L; when L was doubled from 5 to 10 and then 10 to 20 mm, σ_{Peak} roughly halved reducing from 520 to 261 kPa and then 261 to 138 kPa respectively. By applying lines of best fit in the form $f(x) = ax^b + c$ to the numerical data, it was possible to produce the empirical relationships given by Equations 6.5 and 6.6 relating both σ_{Peak} and $\sigma_{Plateau}$ to L (in metres).

$$\sigma_{Peak} = 1.645 \times 10^3 L^{-1.077} + 2.676 \times 10^4 \tag{6.5}$$

$$\sigma_{Plat} = 4.328 \times 10^{-3} L^{-3.258} + 8.686 \times 10^4 \tag{6.6}$$

Note that as L is increased, the values of σ_{Peak} and σ_{Plat} converge; a behaviour which was partly observed in Figure 6.9 by the early softening and late stiffening with increased L, i.e. a shift in stiffness towards the late response. A result of this shift was that ε_{Comp} occurred much sooner for analyses with a longer cell wall, however as the initial peak becomes less onerous in comparison to the plateau, ε_{Comp} begins to lose its significance as a design response parameter.

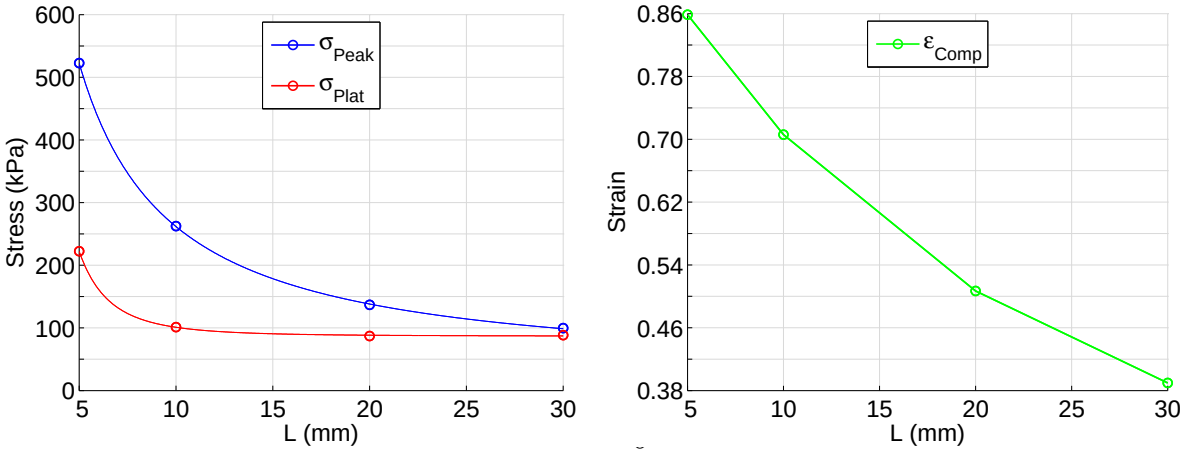

(a) (b)

Figure 6.10 Variations of the macroscopic response parameters (a) σ_{Peak}, $\sigma_{Plateau}$ and (b) ε_{Comp} as a result of variations of the cell wall length L.

Figure 6.11 shows how the internal strain energy per unit volume U increased with strain ε, as L was varied. An increase of L caused a reduction in U for all but the 80% strain contour. For all levels of strain, the honeycomb with a 5 mm long cell wall stored the most internal strain energy. The reduction of ε_{Comp} observed in Figure 6.10 (b) was mirrored in the $U_{\varepsilon_{Comp}}$ curve, which shows a dramatic reduction in the energy absorbed at compaction with increased L.

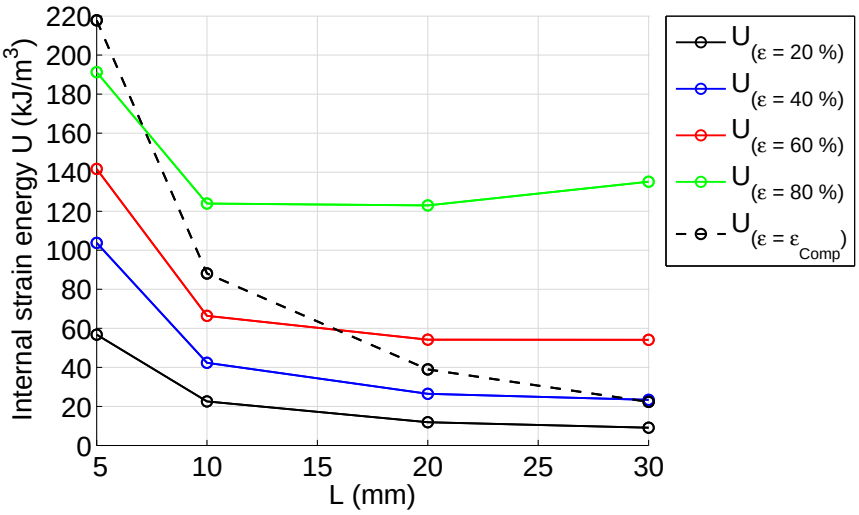

Figure 6.11 Variation of the total strain energy per unit volume $U(\varepsilon)$, at various increments of strain (including ε_{Comp}) as a result of variations in the cell wall length L.

6.4.2 Effect of variations in L on the mesoscopic load carrying mechanisms

Figure 6.12 shows how the stress carried by the structure σ_{Card} and the stress carried by the internal air pressures σ_{Air} were affected when the cell wall length was varied; a reduction L caused an increase of σ_{Card} and a reduction of σ_{Air}.

As L was increased, the dominant load carrying mechanism shifted towards σ_{Air}. For the analysis with 5 mm long cell walls, σ_{Card} was greater than σ_{Air} during the full analysis. While during the analysis with 30 mm cell walls, σ_{Air} was greater than σ_{Card} from 6 % strain onwards; during the 30 mm analysis, at 12.5 % strain the load being transmitted through the honeycomb was almost fully carried by the air pressures while the structural component was negligible and so the honeycomb was effectively acting as a column of air. As L was increased, an early development of pressure above that predicted by the 1D equation of state $\sigma_{Air,1D}$ began to occur, this is visible in the region below 20 % strain on the σ_{Air} curves.

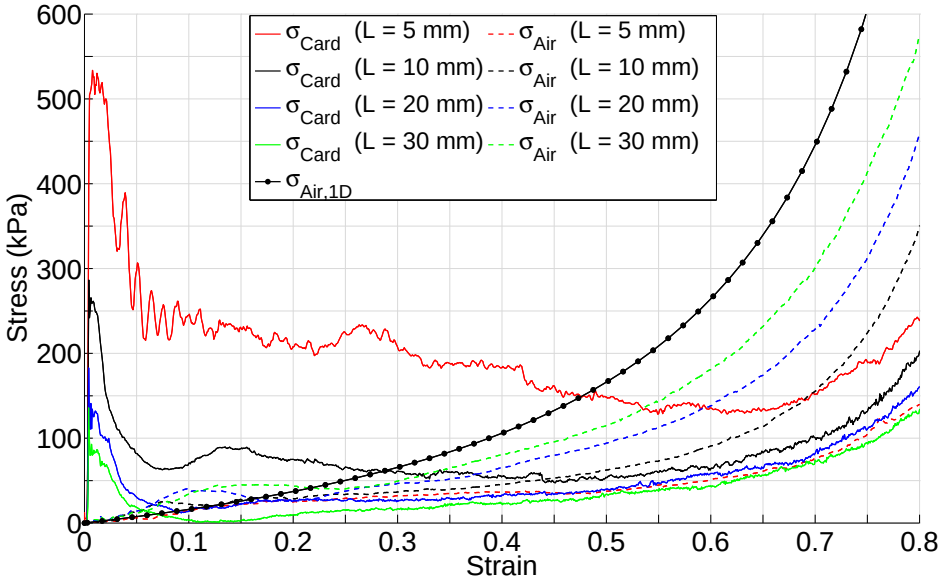

Figure 6.12 Stress transmitted by the cell wall structure σ_{Card} and internal air pressures σ_{Air} vs axial strain ε during the simulations with varied cell wall length L. In addition, $\sigma_{Air,1D}$ (as given by Equation 5.1) has been plotted, illustrating the stress which would be transmitted through the air if it were perfectly constrained and subject to an axial strain of ε.

Figure 6.13 shows how the energies per unit volume, absorbed permanently by the cell walls U_{Card} and temporarily by the air U_{Air}, were affected by changes in the cell wall length L. As L was increased, U_{Card} reduced and U_{Air} increased. When L was increased from 5 to 30 mm, the energy stored within the air at 80% strain increased from 32 to 108 kJ/m^3, an increase by a factor of 2.38; while over the same interval, the energy stored in the structure reduced from 158 to 30 kJ/m^3, a reduction by a factor of 5.27.

The difference in the sensitivities of U_{Card} and U_{Air} to a given change in L resulted in responses of a dramatically different natures, whereby for a short cell wall most of the energy is absorbed by the cardboard material $U_{Card} : U_{Air} = 5 : 1$ (at 80% strain for L = 5.0 mm) and for a long cell wall majority of the energy is stored in compression of the air $U_{Air} : U_{Card} = 3.6 : 1$ (at 80% strain for L = 30 mm).

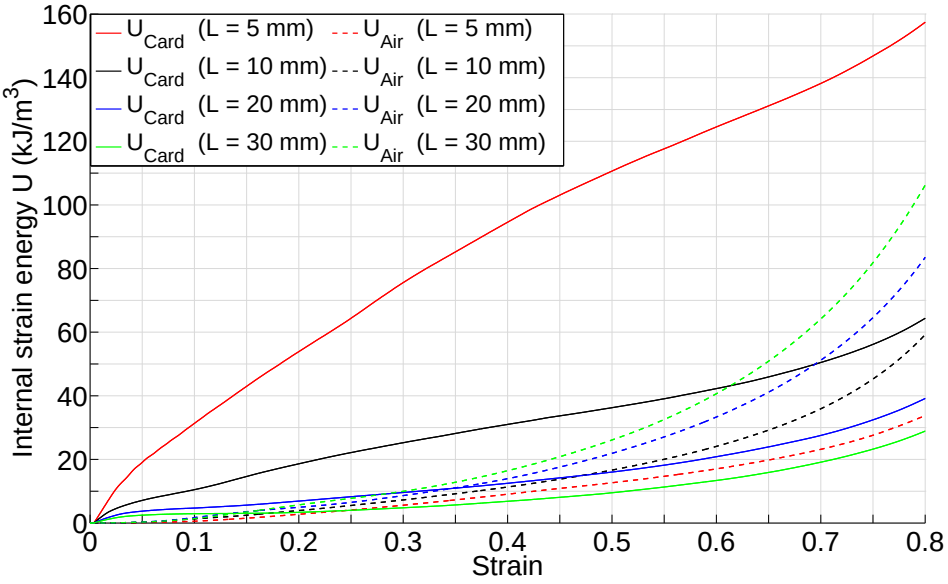

Figure 6.13 Energy per unit volume which was stored permanently as plastic strain energy in the cell walls U_{Card} and temporarily in compression of the internal air U_{Air} vs strain ε during the simulations with varied cell wall length L.

6.5 Effect of internal angle (θ) on the response

Three analyses with varied internal expansion angle θ were performed; one with the default regular hexagonal geometry, where $\theta = 60°$; one at a lower degree of expansion, where $\theta = 30°$; and one at the maximum possible degree of expansion, where the hexagons have been drawn out to form rectangles of dimensions $L \cdot 2L$, and so $\theta = 90°$. The three resulting cellular geometries are illustrated in Figure 6.14.

These three meshes represent common variations which are likely to occur during the fabrication process. In Chapter 3 the internal expansion angle was observed to be highly variable even between cells of the same sample; however, average values of 34.5°, 36.3° and 37.5° were determined for the F, D, and B mesh types during Section 3.3.5.

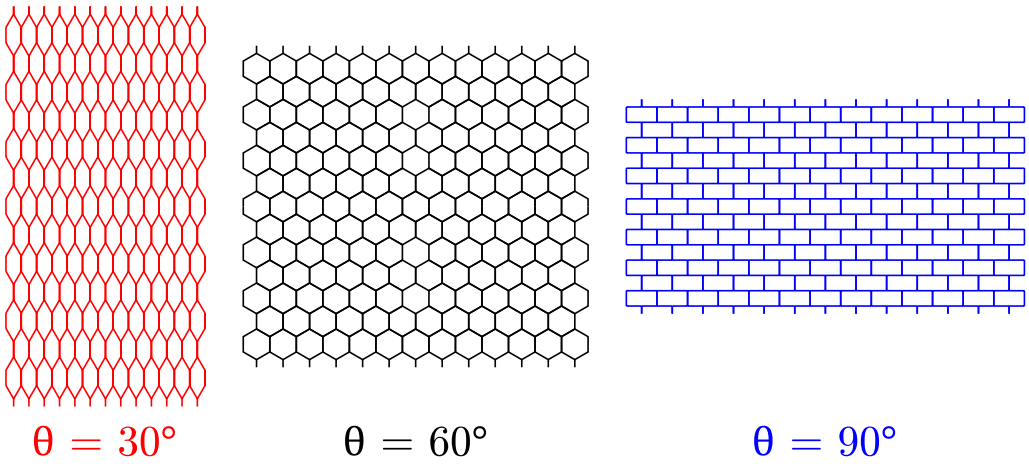

Figure 6.14 Comparison between the three tested cellular geometries which were generated by variations of the internal expansion angle θ.

Table 6.7 shows the dependent parameters which were affected and how they varied when the internal expansion angle was changed. When changing θ, the amount of cell wall material remained constant, while the footprint and volume of air within each cell changed. Equation 6.2 relates A_{Hex} to θ via the trigonometric expression $(\sin\theta + \sin\theta\cos\theta)$; the maximum value of A_{Hex} occurs at 60°, however $(\sin\theta + \sin\theta\cos\theta)$ is not symmetrical about this point, so: $A_{Hex,30°} < A_{Hex,90°}$. The ratio between the resulting tributary areas was $A_{Trib} = 1.00 : 1.07 : 1.39$ for $\theta = 30° : 90° : 60°$, causing the proportion of A_{Trib} consisting of cardboard to reduce at the ratio $\phi_{Card} = 1.39 : 1.07 : 1.00$.

Table 6.7 Secondary geometrical variations which resulted from variations of the internal expansion angle θ.

θ (°)	δ_X (mm)	δ_Y (mm)	A_{Trib} (mm^2)	ϕ_{Card} (%)	A_{Hex} (mm^2)	A_{Air} (mm^2)	V (m^3)
30	65.0	130.6	8490	6.43	177.6	7237	5.94×10^{-4}
60	112.6	105.0	11821	4.62	250.8	10220	8.27×10^{-4}
90	130.0	70.0	9100	6.00	191.0	7783	6.37×10^{-4}

6.5.1 Effect of variations in θ on the macroscopic response

Figure 6.15 shows the macroscopic responses for the simulations with varied internal expansion angle θ. A higher stress was transmitted through the honeycombs with an internal angle of 30° and 90° than was transmitted through the regular hexagonal honeycomb with an internal angle of 60°.

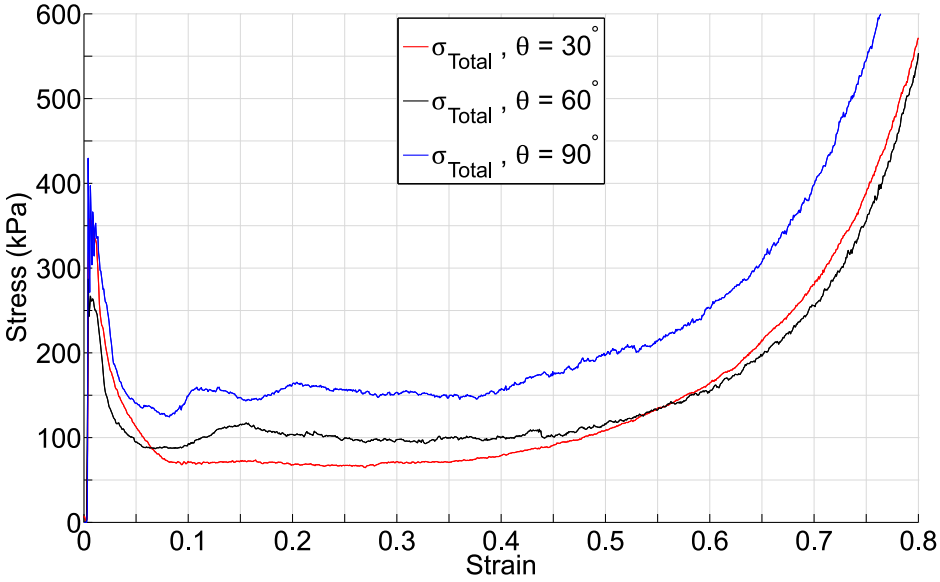

Figure 6.15 Total transmitted stress by the honeycomb σ_{Total} vs axial strain ε during the simulations with varied internal expansion angle θ.

Figure 6.16 (a) and (b) shows how the peak and plateau transmitted stresses σ_{Peak}, $\sigma_{Plateau}$ (blue and red lines) and the strain to compaction ε_{Comp} (green line), changed with variations of θ. The 60° simulation produced the lowest value of σ_{Peak} at 262 kPa while the 30° and 90° simulations transmitted higher values of 354 and 357 kPa respectively. σ_{Plat} increased with θ, lifting from 78 to 161 kPa as theta was increased from 30° to 90°. An increase of θ also caused a linear reduction in the compaction strain ε_{Comp} with the plateau rising to match the peak stress at 73.7 % strain for 30° analysis and 5.7 % earlier, at 68.0 % strain for the 90° analysis.

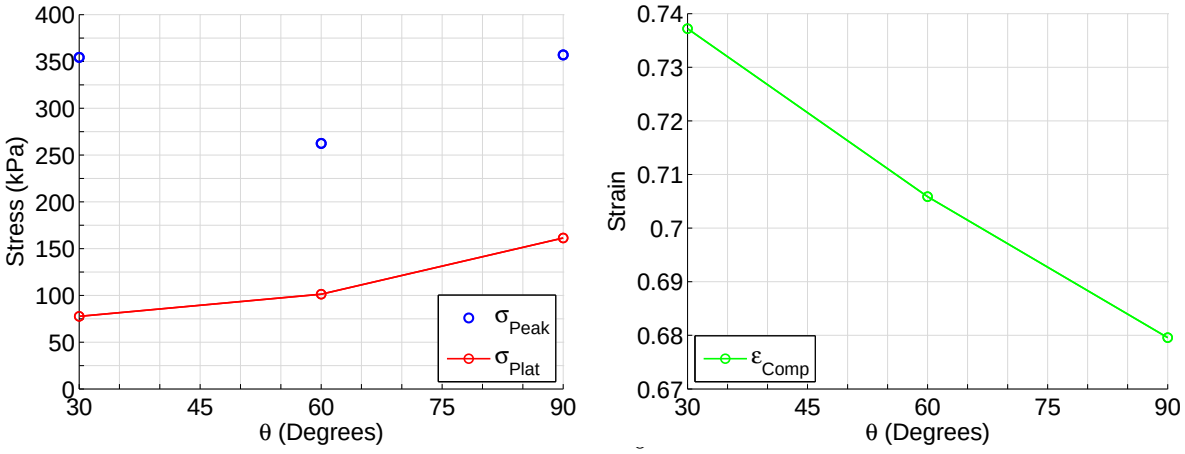

(a) (b)

Figure 6.16 Variations of the macroscopic response parameters (a) σ_{Peak}, $\sigma_{Plateau}$ and (b) ε_{Comp} as a result of variations of the internal expansion angle θ.

Figure 6.17 shows how the internal strain energy per unit volume U increased with strain ε, as θ was varied. For each constant value of strain there was an increase of U with an increase of θ; the greatest effect was observed when increasing θ from 60° to 90°, i.e. when over-expanding the honeycomb past the regular hexagonal geometry. There was no significant variation of the internal energy per unit volume at the compaction point $U_{\varepsilon_{Comp}}$ between the 30° and 60° analyses; however, when θ was increased from 60° to 90°, $U_{\varepsilon_{Comp}}$ increased by 44 %, from 88 to 127 kJ/m^3.

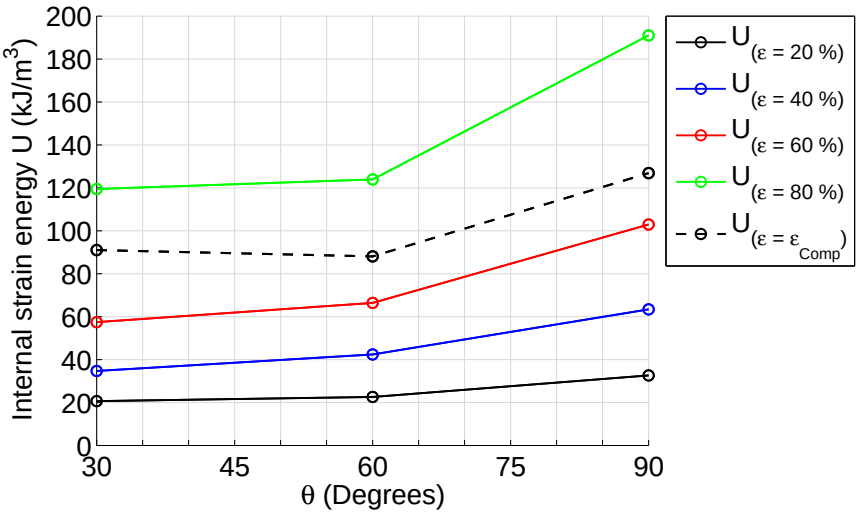

Figure 6.17 Variation of the total strain energy per unit volume $U(\varepsilon)$, at various increments of strain (including ε_{Comp}) as a result of variations in the internal expansion angle θ.

6.5.2 Effect of variations in θ on the mesoscopic load carrying mechanisms

Figure 6.18 shows how the stress carried by the structure σ_{Card} and the stress carried by the internal air pressures σ_{Air} were affected when the internal expansion angle θ was varied.

The solid blue line shows that σ_{Card} transmitted by the 90° honeycomb was highest over the full response. The relative stiffness between the 30° and 60° honeycombs varied with strain; during the plateau region ($10\% < \varepsilon > 50\%$), the 60° honeycomb structure was stiffest; while during the late response ($50\% < \varepsilon$), the 30° honeycomb structure was stiffest.

Comparison between the red and blue dashed lines shows that the stress being transmitted by the internal air pressures σ_{Air} was always higher for the 90° honeycomb than for the 30° honeycomb; during the late response σ_{Air} for the 30° and 60° honeycombs was very similar, while σ_{Air} for the 90° honeycomb was an almost consistent 50 kPa greater.

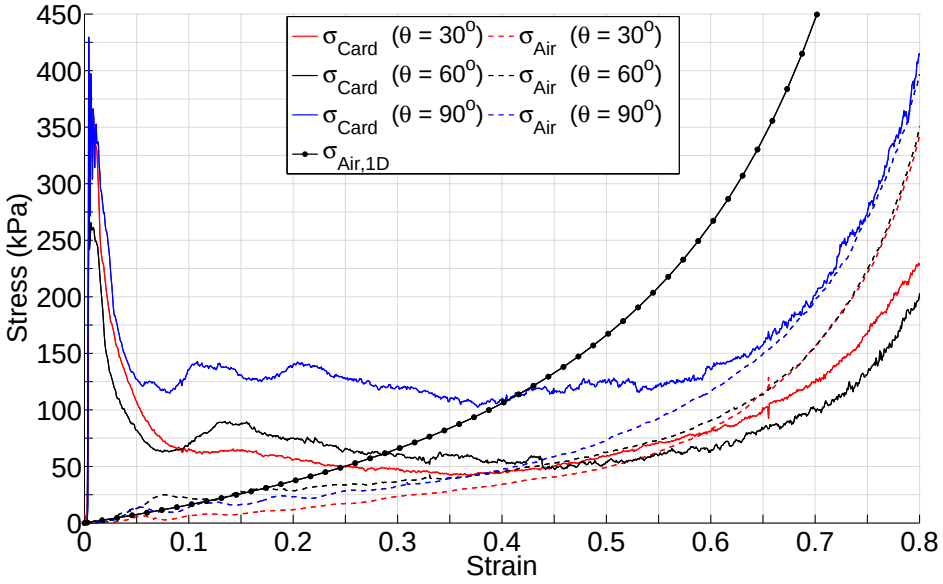

Figure 6.18 Stress transmitted by the cell wall structure σ_{Card} and internal air pressures σ_{Air} vs axial strain ε during the simulations with varied internal expansion angle θ. In addition, $\sigma_{Air,1D}$ (as given by Equation 5.1) has been plotted, illustrating the stress which would be transmitted through the air if it were perfectly constrained and subject to an axial strain of ε.

Figure 6.19 shows how the energies per unit volume, absorbed permanently by the cell walls U_{Card} and temporarily by the air U_{Air}, were affected when the internal expansion angle θ was varied. There was no significant effect on U_{Card} when θ was varied between 30° and 60°; however, increasing θ from 60° to 90° caused an increase of U_{Card}, at 80 % strain, from 64 to 123 kJ/m^3: an increase of 52%. The relative magnitudes of U_{Air} varied with strain; over the full response, the energy stored by the air within the 30° honeycomb was least; during the early response the energy stored by the air within the 60° honeycomb was greatest, at 57% strain this changed and the energy stored within the 90° honeycomb became the greatest.

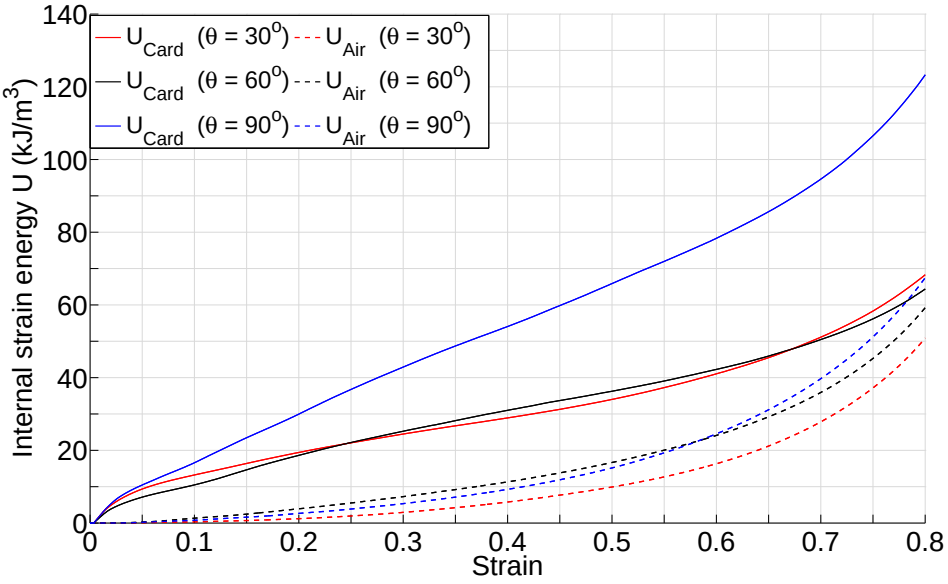

Figure 6.19 Energy per unit volume which was stored permanently as plastic strain energy in the cell walls U_{Card} and temporarily in compression of the internal air U_{Air} vs strain ε during the simulations with varied internal expansion angle θ.

6.6 Effect of macroscopic height (H) on the response

Three analysis were performed to study the effect of variations in sample height on the response. In addition to the default 70 mm tall honeycomb, a 105 and 140 mm tall honeycomb were analysed. These two additional analyses provided an increase of 50 and 100% over the original height H. As the cellular cross section remained unchanged only volume V was affected by variations in H; Table 6.8 shows the three honeycomb heights and their corresponding volumes.

Table 6.8 Secondary geometrical variations which resulted from variations of the macroscopic height H.

H (mm)	V (m^3)
70	8.27×10^{-4}
105	12.41×10^{-4}
140	16.55×10^{-4}

6.6.1 Effect of variations in H on the macroscopic response

Figure 6.20 shows the macroscopic responses for the simulations with varied sample height H. As H was increased, the honeycomb response was softened, however this softening did not occur over the full response; its onset shifted earlier and severity increased with greater values of H, it is illustrated by the separation of the red and blue lines from the black line at 34 and 10 % strain respectively.

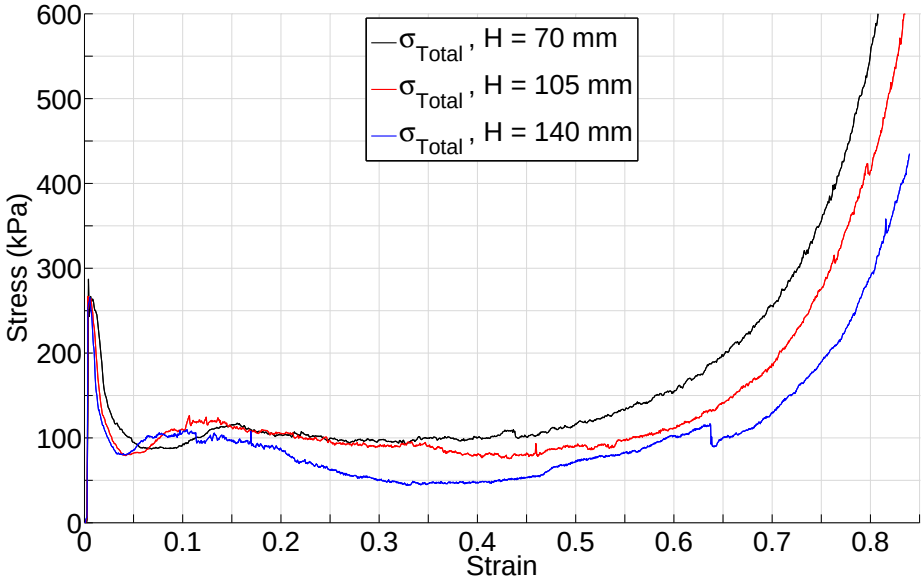

Figure 6.20 Total transmitted stress by the honeycomb σ_{Total} vs axial strain ε during the simulations with varied macroscopic height H.

Figure 6.21 (a) and (b) shows how the peak and plateau transmitted stresses

σ_{Peak}, $\sigma_{Plateau}$ (blue and red lines) and the strain to compaction ε_{Comp} (green line), changed with variations of the honeycomb height H. Variations in the honeycomb height caused no significant effect on the peak transmitted stress; although, there was a modest reduction in σ_{Peak} from 262 to 255 kPa when H was doubled from 70 to 140 mm.

The plateau stress was most greatly affected, dropping by 45% (from 101 to 55 kPa) when the honeycomb height was increased from 70 to 140 mm. Additionally, as the honeycomb height was increased so was the rate of softening; increasing the height from 70 to 105 caused a 12 % reduction in the plateau stress, while increasing the height by the same amount, from 105 to 140 mm, caused a much larger reduction in the plateau stress of 38 %. Softening of the plateau with increased height caused compaction to occur later; ε_{Comp} increased from 70.6 to 78.7 % when H was increased from 70 to 140 mm.

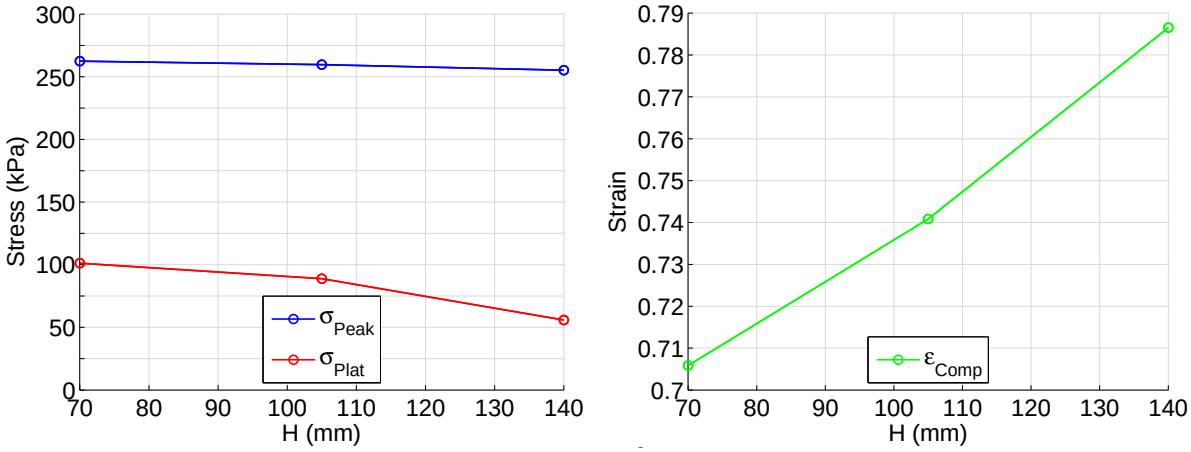

(a) (b)

Figure 6.21 Variations of the macroscopic response parameters (a) σ_{Peak}, $\sigma_{Plateau}$ and (b) ε_{Comp} as a result of variations of the macroscopic height H.

Figure 6.22 shows how the internal strain energy per unit volume U increased with strain ε, as the honeycomb height H was varied. For all values of strain, an increase in the honeycomb height caused a reduction of the energy absorbed per unit volume. This reduction also increased with strain, increasing the honeycomb

height from 70 to 140 mm caused a reduction of U at 20 % strain (black line) of 9.7 % from 22.6 to 20.4 kJ/m^3, while at 80 % strain U reduced by a much larger 38 % from 124 to 76 kJ/m ^{3}.

The black dashed line shows the energy stored per unit volume within the honeycomb at the compaction strain, this also reduced with increased height; increasing H from 70 to 140 mm caused a reduction in energy absorbed at compaction of 18 %, from 88 to 72 kJ/m^3. Note that the negative gradient of the black dashed line was much shallower than the gradient of the green 80 % strain contour, this was due to the 140 mm tall honeycomb being able to deform by an additional 8.1% more than the 70 mm honeycomb.

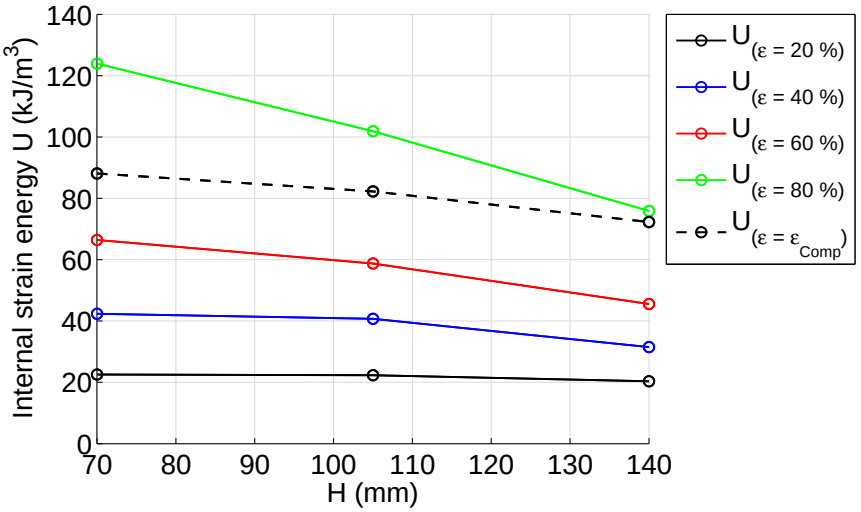

Figure 6.22 Variation of the total strain energy per unit volume $U(\varepsilon)$, at various increments of strain (including ε_{Comp}) as a result of variations in the macroscopic height H.

6.6.2 Effect of variations in H on the mesoscopic load carrying mechanisms

Figure 6.23 shows how the stress carried by the structure σ_{Card} and the stress carried by the internal air pressures σ_{Air} were affected when the honeycomb height H was varied. As the height was increased both the stresses transmitted by the structure

and internal air pressures were reduced. While the magnitude of the early response was mostly unaffected, the softening of the structural response can be observed by the separation of solid blue (140 mm) and red (105 mm) lines from the solid black line (70 mm) at 15 and 50 % strain respectively. Comparison of the dashed lines shows that for any given value of strain, the stress being transmitted by the internal air pressures was inversely proportional to the honeycomb height, with the highest stress being transmitted by the air pressures within the 70 mm tall honeycomb and lowest by the air pressures within the 140 mm tall honeycomb.

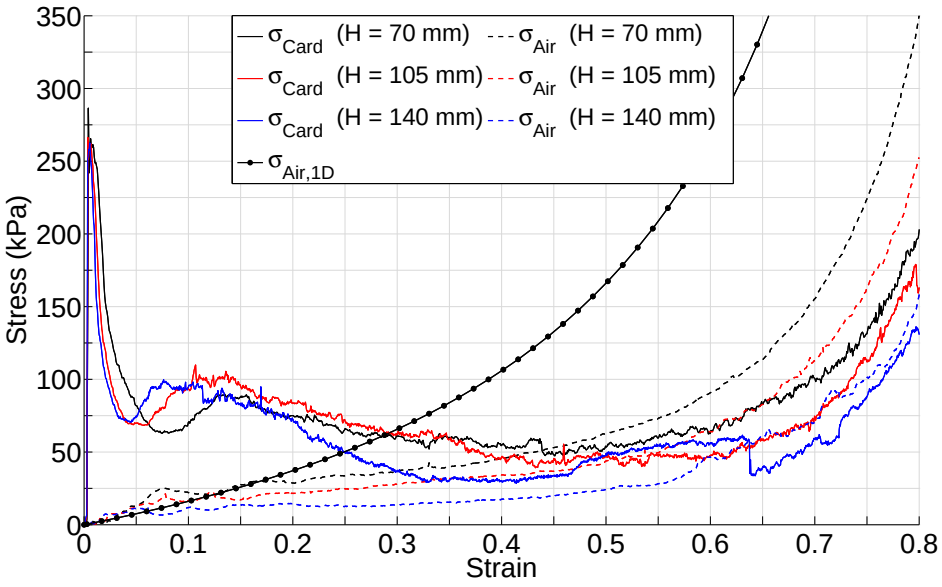

Figure 6.23 Stress transmitted by the cell wall structure σ_{Card} and internal air pressures σ_{Air} vs axial strain ε during the simulations with varied macroscopic height H. In addition, $\sigma_{Air,1D}$ (as given by Equation 5.1) has been plotted, illustrating the stress which would be transmitted through the air if it were perfectly constrained and subject to an axial strain of ε.

Figure 6.19 shows how the energies per unit volume, absorbed permanently by the cell walls U_{Card} and temporarily by the air U_{Air}, were affected when the honeycomb height H was varied.

At 80 % strain, an increase of height caused a reduction in the amount of energy per unit volume absorbed by the cellular structure; however, this was not true for

the full response, at 20 and 55 % strain the energy absorbed by the 140 and 105 mm tall honeycombs diverged, dropping below the upper bound U_{Card} curve for the 70 mm tall honeycomb.

The energy absorbed by the air, was inversely proportional to the height, at 80 % strain 59, 43, and 26 kJ/m^3 stored in the compressed air within the 70, 105 and 140 mm tall honeycombs respectively. Additionally, as the honeycomb height was increased a lower proportion of the total absorbed energy was provided by the internal air pressures; at 80 % strain the ratio of U_{Air} : U_{Card} for the 70 mm tall honeycomb was 1.00 : 1.09, while for the 140 mm tall honeycomb it was 1.00 : 1.88.

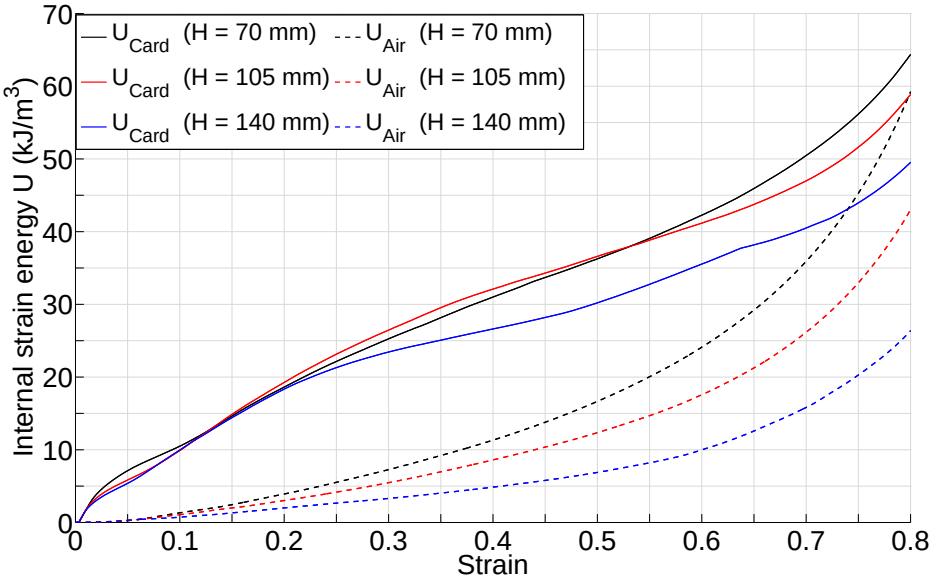

Figure 6.24 Energy per unit volume which was stored permanently as plastic strain energy in the cell walls U_{Card} and temporarily in compression of the internal air U_{Air} vs strain ε during the simulations with varied macroscopic height H.

6.7 Effect of variation in lateral confinement, through variation in the number of complete columns (ncol), on the response

The cellular arrangement was now modified by stripping full columns of cells from the perimeter edges on the X-X plane, thus simulating the effect of taking narrower cuts of honeycomb from the same regular mesh. This is illustrated in Figure 6.25, where the full original geometry is shown between the dashed black lines, the blue and red dashed lines show the two cuts which were made to reduce the number of columns from the original 25 to 17 and then 9. It is worth highlighting that as ncol was reduced, the aspect ratio of the honeycomb ($^{\delta_x}/_{\delta_y}$) also changed from being roughly square on plan to being much more rectangular. Table 6.9 shows the dependent parameters which were affected and how they varied as the cellular structure was modified by removing columns of cells.

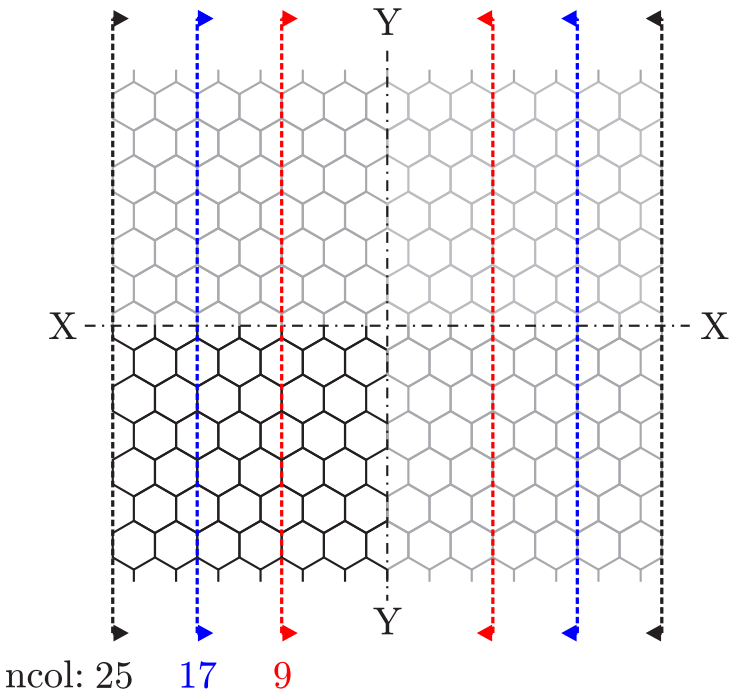

Figure 6.25 Illustration of how the original cellular geometry was modified to study the effect of variations in the number of columns on the response. The blue and red dashed lines show the position of the two cuts which were made to reduce the default 25 column wide honeycomb to one which was 17 and then 9 columns wide.

For both cuts, four columns were removed from each side, resulting in a loss of 13 sealed cells in the modelled quarter segment, reducing the area of sealed air A_{Air}, the width of the cross section in the x-x direction δ_x, and the total footprint area A_{Trib}. Moreover, with each cut, 4 of the original 13, continuous cell walls were removed causing the total length of cell wall material ΣL and area of cell wall material A_{Card} to drop proportionally.

Table 6.9 Secondary geometrical variations which resulted from variations in the number of complete columns ncol.

ncol (full)	ncell	δ_X (mm)	A_{Trib} (mm^2)	ΣL (mm)	A_{Card} (mm^2)	A_{Air} (mm^2)	V (m^3)
12.5 (25)	40.75	112.6	11821	1820	546	10220	8.27×10^{-4}
8.5 (17)	27.75	77.9	8183	1260	378	6960	5.73×10^{-4}
4.5 (9)	14.75	43.3	4547	700	210	3699	3.18×10^{-4}

To add clarity, the value for ncol used during the remainder of this section will refer only to the number of columns within the full honeycomb structure (rather than the number being modelled in the quarter segment). Figure 6.26 shows the macroscopic responses for the three simulations with a varied number of columns ncol.

There was no significant effect on the response below 20 % strain; at 20 % strain, the stress transmitted by the honeycomb with 9 rows began a gradual decline dropping below the unaffected 17 and 25 row responses; at 47 % strain, the 17 row honeycomb softened slightly in comparison to the honeycomb with 25 rows, this magnitude of softening then remained constant until compaction.

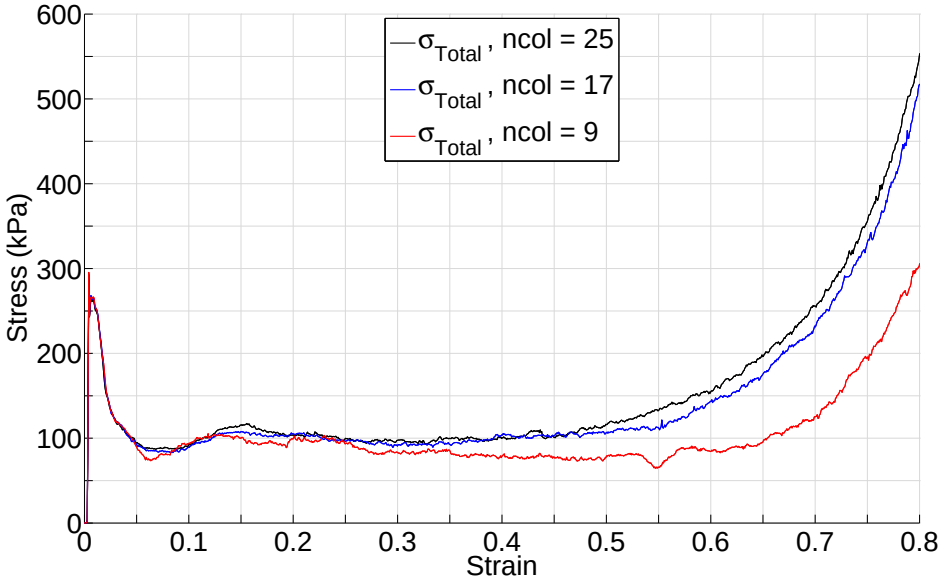

Figure 6.26 Total transmitted stress by the honeycomb σ_{Total} vs axial strain ε during the simulations, where the number of complete columns of cells ncol was varied.

Figures 6.27 (a) and (b) show how the peak and plateau transmitted stresses σ_{Peak}, $\sigma_{Plateau}$ (blue and red lines) and the strain to compaction ε_{Comp} (green line), varied due to changes in the number of columns ncol. As previously observed in Figure 6.26, there was no significant effect on the peak stress while the plateau stress was reduced when the number of columns was changed from 17 to 9. Also, as ncol was reduced the compaction strain occurred later.

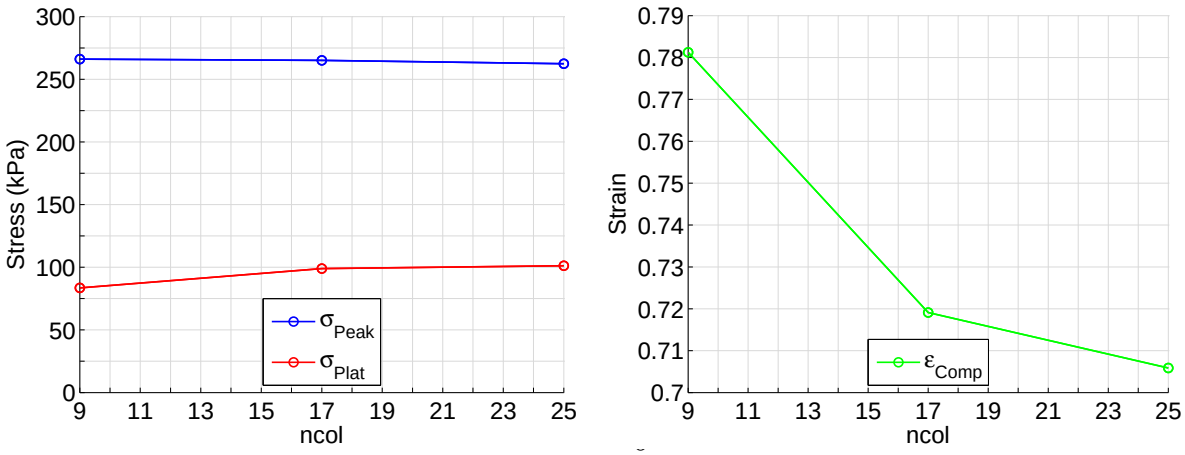

(a) (b)

Figure 6.27 Variations of the macroscopic response parameters (a) σ_{Peak}, $\sigma_{Plateau}$ and (b) ε_{Comp} as a result of variations in the number of complete columns ncol.

Figure 6.28 shows how the internal strain energy per unit volume U increased with strain ε, as the number of columns was varied.

All three honeycombs had absorbed the same amount of energy per unit volume at 20 % strain; however, all subsequent contours show an increase of absorbed energy per unit volume as the number of columns is increased, with the greatest effect being when the number of columns was increased from 9 to 17. The dashed line shows the energy per unit volume which was absorbed by the compaction point, this increased by 7.5% from 80 to 86 kJ/m^3 when the number of columns was increased from 9 to 17 but only 2.3 % when the number of columns was increased from 17 to 25.

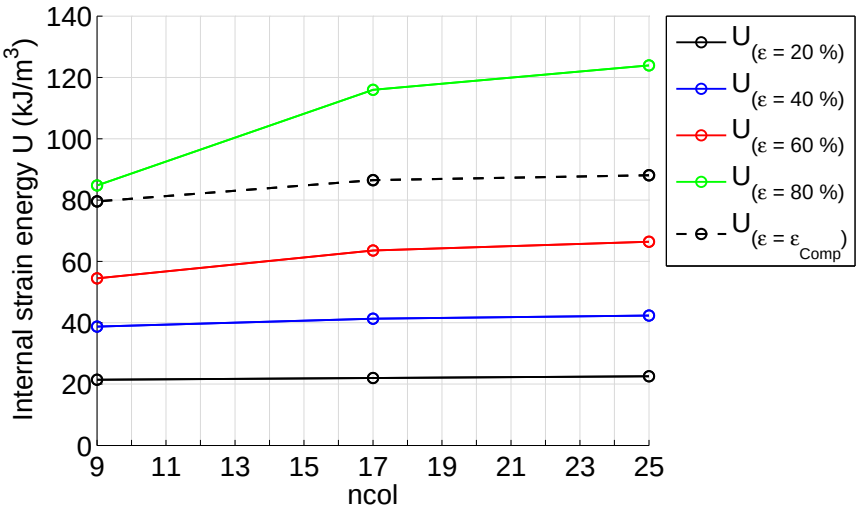

Figure 6.28 Variation of the total strain energy per unit volume $U(\varepsilon)$, at various increments of strain (including ε_{Comp}) as a result of variations in the number of columns ncol.

6.7.1 Effect of variations in the number of columns (ncol) on the mesoscopic load carrying mechanisms

Figure 6.29 shows how the stresses carried by the structures σ_{Card} and the stresses carried by the internal air pressures σ_{Air} were affected when the number of columns ncol was varied.

The stress transmitted by the honeycomb structure was unaffected by variations in the number of columns until 55 % strain. At 55 % strain, the stress being transmitted by the 9 column-wide honeycomb structure (solid red line) dropped below the other two, began fluctuating and then resumed stiffening (at an increased rate) at 68 % strain; by 80 % strain the stress being transmitted through the 9 column honeycomb had almost re-converged with the stress being transmitted by the 17 column honeycomb.

In contrast, the number of columns affected the magnitude of stress being transmitted by the internal air pressures over the full response; for any given value of strain, a honeycomb structure with more columns transmitted more stress via air

pressures. The rate of pressure development was much lower within the 9 column honeycomb than the other two, this can be seen when comparing the relatively flat gradient of the dashed red line (between 0 and 50 % strain) with the steeper incline of the dashed blue and black lines.

Comparison between the solid and red dashed lines in the region between 50 and 80 % (the late response of the 9 column honeycomb) strain shows that the stress being transmitted by the internal air pressures experiences similar turbulence to that which was observed in the structural response. In this turbulent region, oscillatory features which are visible in the structural response are also mirrored in the stress being transmitted by the air pressures, a clear example of this can be seen between 65 and 70 % strain. The turbulent region was not visible in Figure 6.26, and so these oscillations must be an equal and opposite transfer of stress between the structure and the air pressures. It is worth nothing that this turbulent region was preceded by a small trough at 53 % strain in the air pressure transmitted stress.

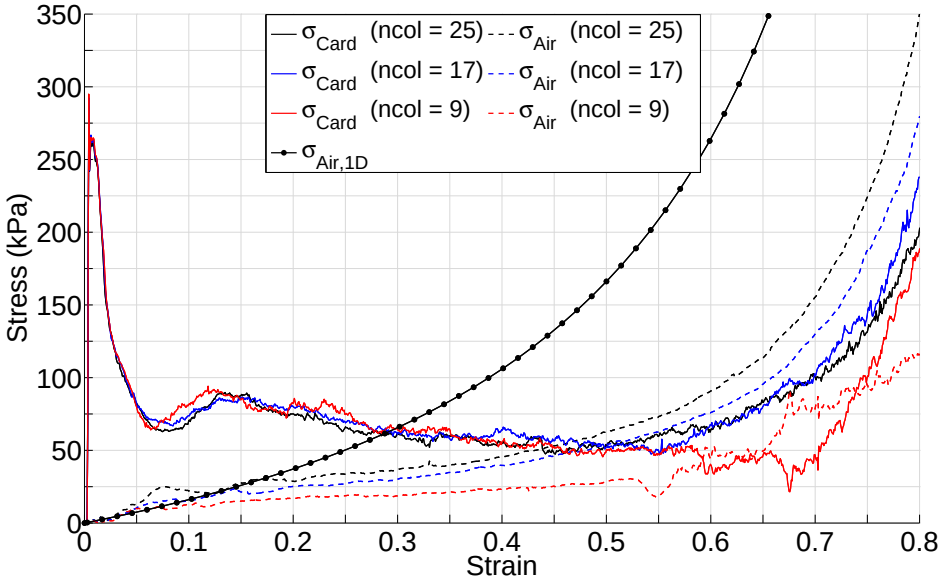

Figure 6.29 Stress transmitted by the cell wall structure σ_{Card} and internal air pressures σ_{Air} vs axial strain ε during the simulations with varied number of columns ncol. In addition, $\sigma_{Air,1D}$ (as given by Equation 5.1) has been plotted, illustrating the stress which would be transmitted through the air if it were perfectly constrained and subject to an axial strain of ε.

Figure 6.30 shows how the energies per unit volume, absorbed permanently by the cell walls U_{Card} and temporarily by the air U_{Air}, were affected when the number of columns ncol was varied.

Variations in the number of columns had no effect on the energy absorbed by the honeycomb structure until 65 % strain; at 65 % strain, the rate of energy absorption for the honeycomb with 9 columns reduced in comparison to the other two. At 80 % strain, the 17 column honeycomb structure had absorbed 67 kJ/m^3, which was 17 % more than the 57 kJ/m^3 absorbed by the honeycomb with 9 columns.

Comparison between the three dashed lines shows that for all values of strain, the energy per unit volume stored within the air and the rate of its increase was proportional to the number of columns. At 80 % strain, the energy per unit volume stored in the air contained within the honeycomb with 25 columns was 59 kJ/m^3, this was 20 % and 118 % more than the 49 kJ/m^3 and 27 kJ/m^3 stored within the

honeycombs with 17 and 9 columns respectively.

The difference in energy conversion rates between the structural and air pressure components resulted in a significant difference in the energy distribution at 80 % strain due to a variation in the number of columns; for the analysis with 25 columns the ratio of energies within the structure and air $U_{Card} : U_{Air}$ was 1.08 : 1.00 (almost equal) while for the honeycomb with 9 columns the ratio was 2.11 : 1.00 (roughly double).

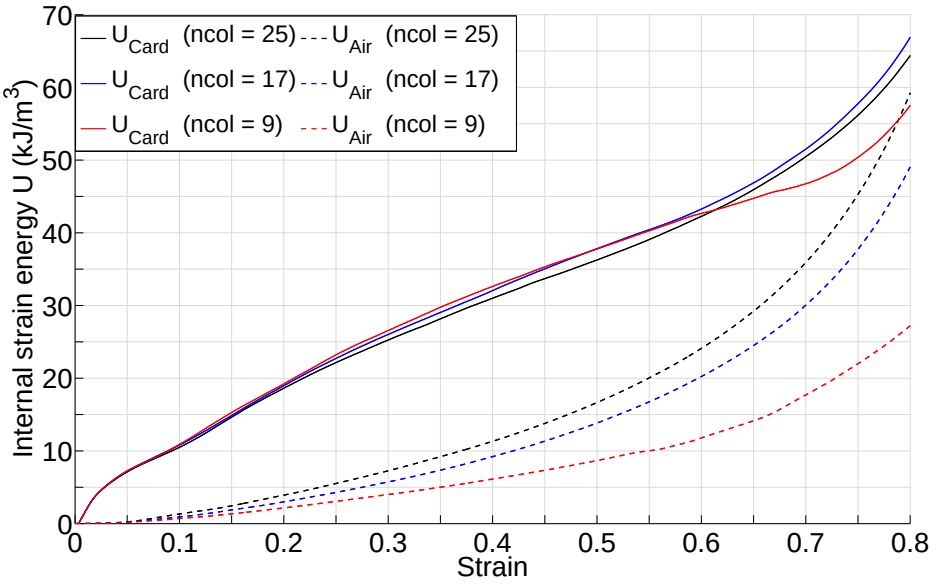

Figure 6.30 Energy per unit volume which was stored permanently as plastic strain energy in the cell walls U_{Card} and temporarily in compression of the internal air U_{Air} vs strain ε during the simulations with varied number of columns ncol.

6.8 Effect of variation in lateral confinement, through variation in the number of complete rows (nrows), on the response

The original geometry was now altered by removing rows of cells parallel to the Y-Y plane. Figure 6.31 shows how four cuts were made, each removing a single row of

cells from the top and bottom edge, to create four honeycomb structures: 13, 11, 9, 7 and 5 rows thick.

Due to anisotropy of the honeycomb geometry, removing rows introduced differing mechanical variations in comparison to the removal of columns; by removing rows, the potential pathway length between each pressurised cell and the perimeter is reduced.

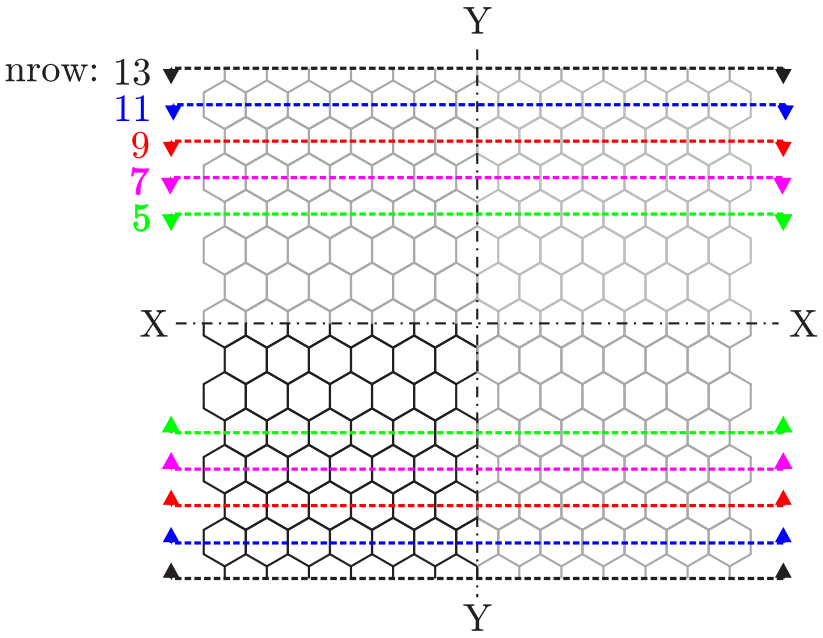

Figure 6.31 Illustration of how the original cellular geometry was modified to study the effect of variations in the number of rows on the response. The coloured dashed lines show the position of the four cuts which were made to reduce the default 13 row deep honeycomb to one which was 11, 9, 7 and then 5 columns deep.

Table 6.10 shows the dependent geometrical parameters and how they were affected as nrow was reduced. The number of cells in each row alternated between 13 and 12, and so removing one row at a time caused slight relative alternating variations in the number of cells ncell and the area of contained air A_{Air}. The proportion of structure removed with each cut was identical, being symmetrical about the cut line, and so the remaining dependent parameters all reduced by a constant value with each removed row.

Table 6.10 Secondary geometrical variations which resulted from variations in the number of complete rows nrow.

nrow (full)	ncell	δ_Y (mm)	A_{Trib} (mm^2)	ΣL (mm)	A_{Card} (mm^2)	A_{Air} (mm^2)	V (m^3)
6.5 (13)	40.75	105.0	11821	1820	546	10220	8.27×10^{-4}
5.5 (11)	34.25	90	10132	1560	468	8590	7.09×10^{-4}
4.5 (9)	28.25	75	8444	1300	390	7085	5.91×10^{-4}
3.5 (7)	21.75	60	6755	1040	312	5455	4.73×10^{-4}
2.5 (5)	15.75	45	5066	780	234	3950	3.55×10^{-4}

To add clarity, the value of nrow used during the remainder of this section, will refer to the number of complete columns in the full honeycomb structure (rather than the number being modelled in the quarter segment). Figure 6.32 shows the macroscopic responses for all 5 simulations with varied number of rows, nrow.

Comparison between the black and blue lines shows that there was no significant effect on the response when one row was removed from each side and nrow was reduced to from 13 to 11; additionally, all simulations transmitted the same stress during the early response.

After 5 % strain, as rows were removed below 11 the response softened. The magnitude of softening, which was introduced by the progressive removal of each row, was not constant. Comparison between the red and pink lines shows that reducing the number of rows from 11 to 7 had by far the greatest softening effect.

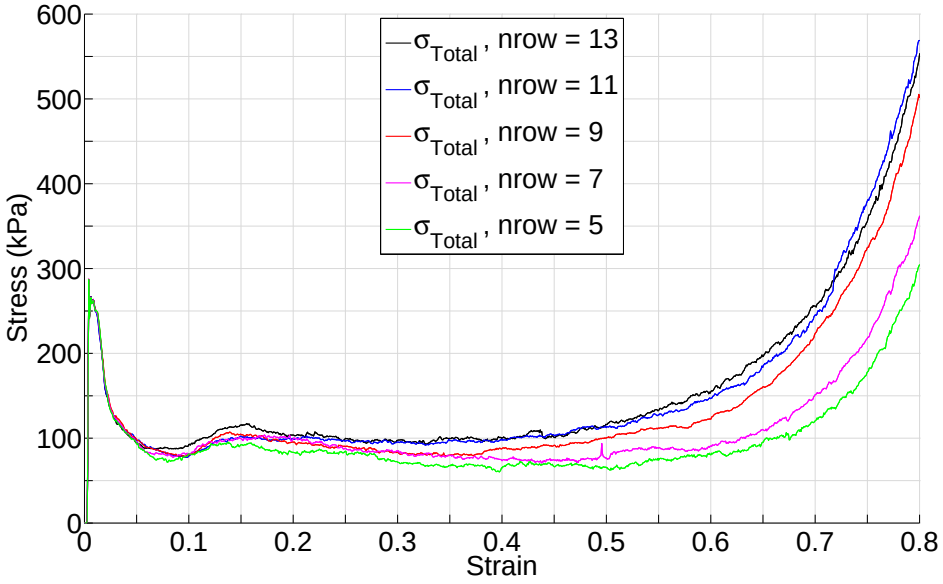

Figure 6.32 Total transmitted stress by the honeycomb σ_{Total} vs axial strain ε during the simulations where the number of complete rows of cells nrow was varied.

Figure 6.33 (a) and (b) shows how the peak and plateau transmitted stresses σ_{Peak}, $\sigma_{Plateau}$ (blue and red lines) and the strain to compaction ε_{Comp} (green line), varied due to changes in the number of rows (nrow). Variations in the number of rows had no significant effect on the early response, and so the peak stress was unchanged. Increasing the number of rows from 5 to 11 caused a linear increase in the plateau stress of 39 %, from 72 to 100 kPa; however, when nrow was increased from 11 to 13 there was no significant effect. An increase in the number of rows caused the honeycomb to compact sooner; the honeycomb with 5 rows of cells compacted at 78.6 % strain, while the honeycomb with 13 rows of cells compacted at 71 % strain.

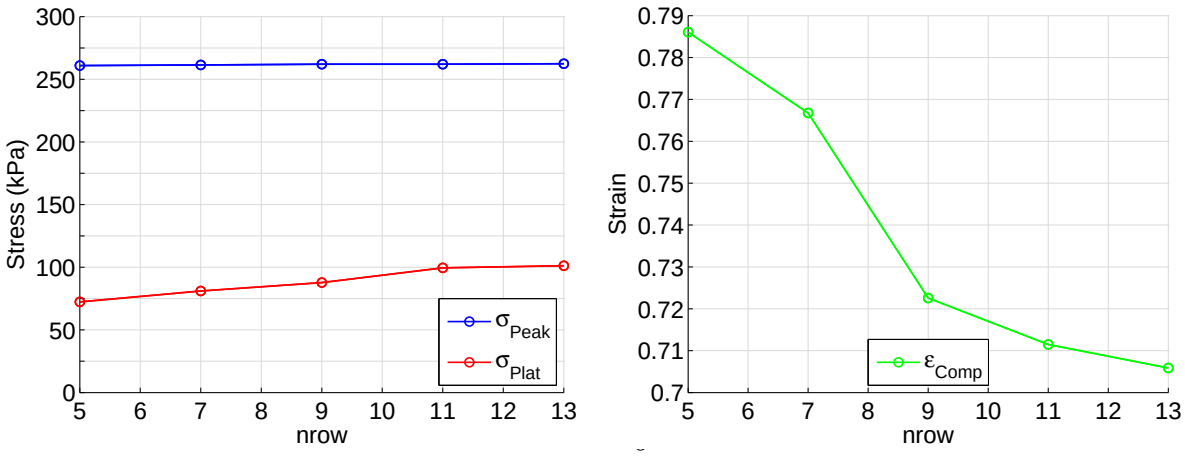

(a) (b)

Figure 6.33 Variations of the macroscopic response parameters (a) σ_{Peak}, $\sigma_{Plateau}$ and (b) ε_{Comp} as a result of variations in the number of complete rows nrow.

Figure 6.34 shows how the internal strain energy per unit volume U increased with strain ε, as the number of rows was varied. At 20 % strain, variations in the number of rows had no obvious effect on the absorbed energy. As strain was increased, an upwards positive trend between the number of rows and the absorbed energy per unit volume began to emerge, its gradient being proportional to the level of strain. For the 20 and 40 % strain contours, the trend was linear; however, at 80 % strain increasing, decreasing the number of rows below 7, or increasing above 11 had less effect on the absorbed energy per unit volume, than for variations between 7 and 11 rows.

The absorbed energy per unit volume at compaction is shown by the dashed black line, the relationship was positive and linear, increasing by 18 % from 74 kJ/m^3 for the honeycomb with 5 rows, to 88 kJ/m^3 for the honeycomb with 13 rows.

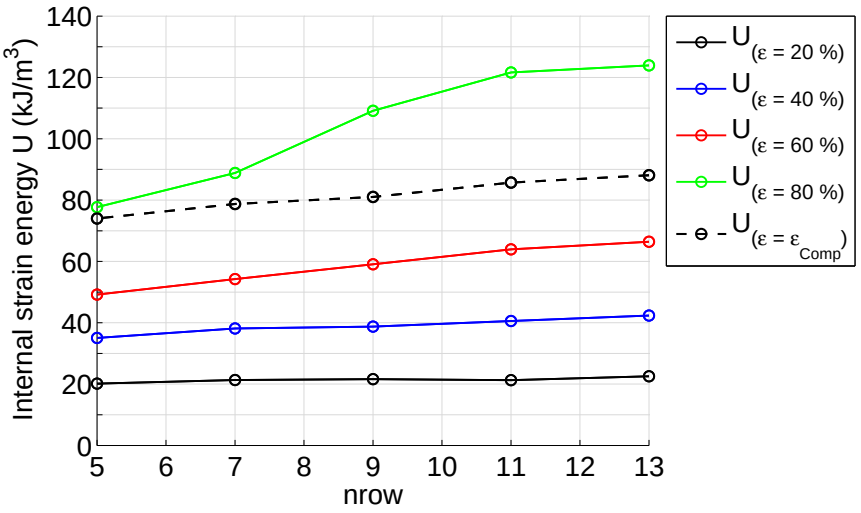

Figure 6.34 Variation of the total strain energy per unit volume $U(\varepsilon)$, at various increments of strain (including ε_{Comp}) as a result of variations in the number of rows nrow.

6.8.1 Effect of variations in the number of rows (nrow) on the mesoscopic load carrying mechanisms

Of the 5 numerical analyses performed to study the effect of variations in the number of rows on the response, three had geometries which were directly comparable to each other, they were the analyses with 13, 9 and 5 rows (see Figure 6.31 for detail). Figure 6.35 shows the stresses carried by the structures σ_{Card} and the stresses carried by the internal air pressures σ_{Air} of the three directly comparable analyses.

The magnitude of stress transmitted by the structure was unaffected until 60 % strain, after which the stress transmitted by the honeycomb with 5 rows (green line) dropped below the stress transmitted by the other two. In contrast, the magnitude of stress transmitted by the internal air pressures was sensitive to the number of rows over the full response; for all values of strain, the stress being transmitted by the internal air pressures and the rate of pressure increase was greater for a honeycomb with more rows. Comparison between the gradients of the dashed lines in the region between 20 and 60 % strain shows that the rate of pressure development within the

honeycomb with 5 rows was significantly less than in the other two.

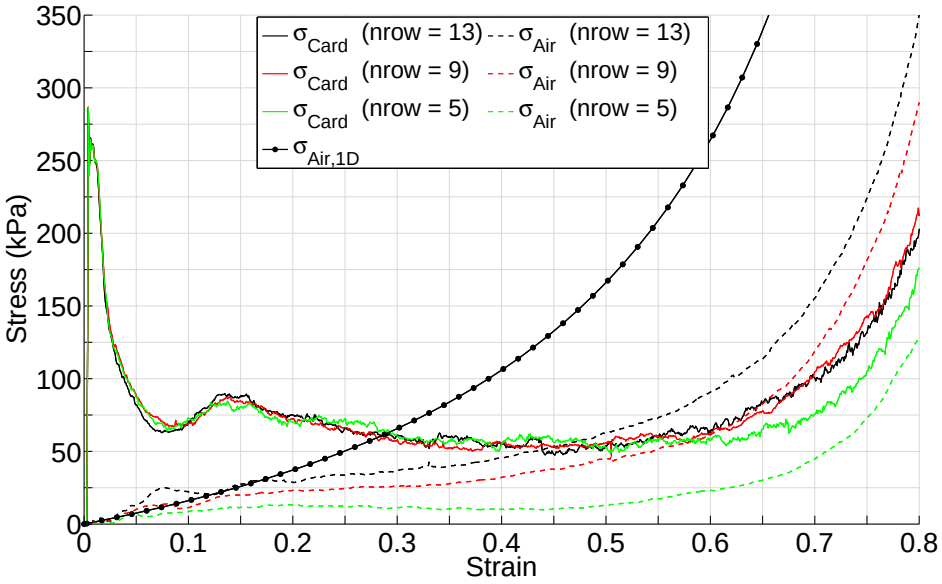

Figure 6.35 Stress transmitted by the cell wall structure σ_{Card} and internal air pressures σ_{Air} vs axial strain ε during the simulations with varied number of rows nrow. In addition, $\sigma_{Air,1D}$ (as given by Equation 5.1) has been plotted, illustrating the stress which would be transmitted through the air if it were perfectly constrained and subject to an axial strain of ε.

Figure 6.36 shows how the energies per unit volume, absorbed permanently by the cell walls U_{Card} and temporarily by the air U_{Air}, were affected when the number of rows nrow was varied. There was no significant effect on the energy per unit volume absorbed due to plastic strain of the cell walls. In contrast, the energy stored in the internal air pressures was significantly affected by variations in the number of rows. At any given value of strain, a honeycomb with more rows of cells had more energy per unit volume stored within the compressed air. At 80 % strain there was 59 kJ/m^3 stored in the air within the honeycomb with 13 rows, this reduced by 25 % and 71 % to 44 kJ/m^3 and 17 kJ/m^3, when the number of rows was reduced to 9 and then 5 respectively.

The variation of the energy per unit volume of air due to a variation in the number of rows, coupled with a relatively constant energy per unit volume of structure,

resulted in a significant shift in the distribution of energy between the two mechanisms. At 80 % strain the ratio of energies within the structure and air $U_{Card} : U_{Air}$ was 1.08 : 1.00 (almost equal) for the honeycomb with 13 rows, when the number of rows was reduced to 5 this ratio increased to 3.41 : 1.00 (severely biased towards U_{Card}).

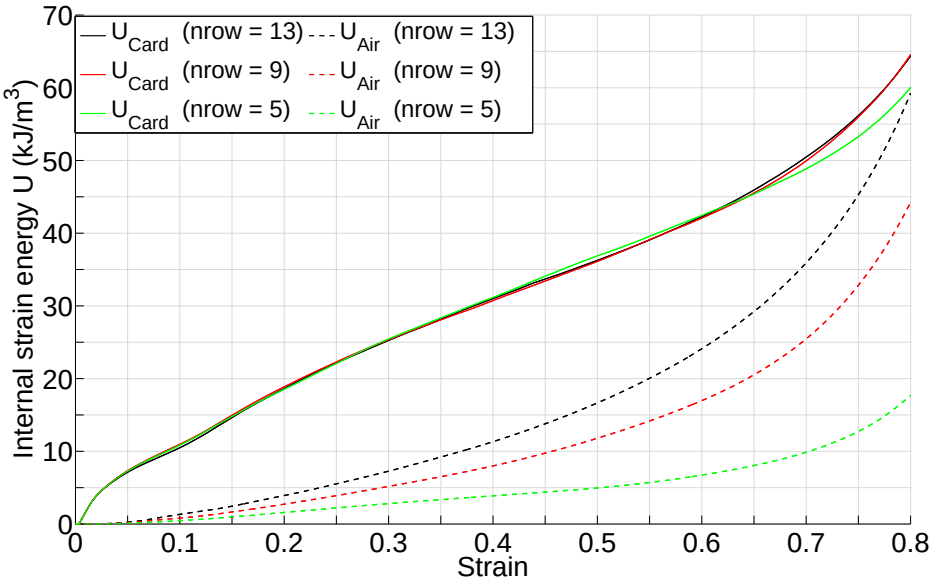

Figure 6.36 Energy per unit volume which was stored permanently as plastic strain energy in the cell walls U_{Card} and temporarily in compression of the internal air U_{Air} vs strain ε during the simulations with varied number of rows nrow.

6.9 Conclusions and end user implications of the geometrical parameter study

The cardboard honeycomb structure is defined using an array of geometrical parameters; many of these parameters are coupled, which poses practical difficulties when attempting to distil their individual effects on the EDM response. Practical constraints, such as the construction and sourcing of specific geometries and the sizing and geometry of testing apparatus would normally impose additional, non-essential variations on honeycomb geometry. By identifying a series of independent and de-

pendent geometrical parameters (see Tables 6.1 and 6.2), and adapting the numerical model to incorporate singular variations on each of the independent parameters, it was possible to study their effects without any influence from non-essential variations.

The cardboard honeycomb macroscopic EDM response is composed of two components: the component carried by the cell wall structure and the component carried by the internal air pressures. The magnitude of the structural component is theoretically unlimited (being a function of the cell wall material properties), while the air pressure component is limited (being a function of the internal volumetric strain). Within the range of potential cardboard honeycomb geometrical and material parameters, it has been observed that either the structural or air pressure component can be dominant. Both the structural and air pressure components were found to be sensitive to variations in all six independent geometrical parameters.

Increasing the cell wall thickness from 0.15 mm to 0.9 mm caused an increase and divergence of the peak and plateau stresses; the peak stress increased linearly from 126 to 847 kPa, and the total energy per unit volume absorbed at compaction increased linearly by a factor of 9.6.

The structural component scaled proportionally with all variations in the cell wall thickness. The air pressure component was unaffected when the cell wall thickness was reduced below 0.3 mm, and may have reached the upper limit for the simulation where the cell wall thickness was 0.9 mm. As a result, the simulation with 0.15 mm thick cell walls was dominated by the air pressure component while (with the air pressures exceeding the structural response at 15 % strain) for the simulation with the 0.9 mm thick cell walls the dominance had shifted towards the structural component (with the air pressures remaining below the structural response during the full analysis).

Increasing the cell wall length from 5 to 30 mm caused a reduction and convergence of the peak and plateau stresses; the rate of reduction was observed to be of the form $f(x) = ax^b + c$, and was stated by the empirical Equations 6.5 and 6.6; the peak stress reduced from 520 to 138 kPa and the plateau stress reduced from 223

to 80 kPa as the cell wall length was increased from 5 to 30 mm. The total energy per unit volume absorbed at compaction reduced by a factor of 9.9.

Like variations of the cell wall thickness, varying the cell wall length shifted the bias from a structurally dominated response when the cell walls were at their shortest (5mm), to an air pressure dominated response when the cell walls were at their longest (30mm). For the simulation with 30 mm long cell walls, the air pressure component exceeded the structural component at 6 % strain, i.e. the honeycomb was effectively acting as a column of air with lateral flow restraint provided by the honeycomb cell walls. An alternative perspective is that: with a short cell wall more energy was absorbed per unit volume, whereas for a long cell wall more energy was absorbed per unit mass.

During the experimental work a strong correlation between the area of cardboard and peak and plateau stresses was observed (see Figure 3.34); furthermore, in Figure 3.33 it was shown that the air pressure component reduces in significance as the amount of cardboard within the cellular cross section is increased. This agrees with the findings from the numerical modelling, discussed above, where variations in both the cell wall length and thickness (which also caused large variations in the area of cardboard), were observed to cause substantial variations in the magnitude of the peak and plateau stresses while shifting the bias of the response between the structural and air pressure component.

Table 6.3 showed that the proportion of cardboard increased from 2.31 % to 13.9 % when the cell wall thickness was increased from 0.15 mm to 0.9 mm and Table 6.9 shows that it reduced from 9.24 % to 1.54 % when the cell wall length was increased from 5 mm to 30 mm. Clearly, the area/proportion of the cross section which is composed of cardboard is a significant variable when determining the magnitude and type (structural or air) of response.

Variations in the height of the honeycomb had no significant effect on the initial peak; however, an increased height was found to significantly reduce the magnitudes of the post peak structural and air pressure components of the macroscopic response. When the air within the honeycomb is compressed, the pressure which develops is

proportional to the axial strain, i.e. if two columns of air with initial heights of 70 mm and 140 mm are subject to a 1 dimensional axial compression, the air will be at the same pressure when the two columns are compressed by 50 % to 35 mm and 70 mm respectively. Therefore, when cardboard honeycomb height is increased, for any given value of axial strain, the same air pressures have a larger height/area of cell wall to act over, meaning that they can more readily form blow out pathways and deform the structure due to lateral drift. The result is a reduction in both the air pressure and structural components of the macroscopic response.

When the honeycomb height was doubled from 70 mm to 140 mm the reduction in both components was substantial, although, because this resulted in a later compaction strain (78.7 % rather than 70.6 %), the total energy per unit volume at compaction reduced by just 18 %. It is thought that if further increases in height were made, the increase in height-to-plan-area aspect ratio may cause such a substantial reduction in the degree of lateral confinement and result in a structure which does not reach compaction, and in this case the reduction in the in the energy absorption capacity would be substantial. The 140 mm tall model required 3 months of computational time to complete, and therefore represented the limit of what was possible with the computational resources available at the time of analysis.

The implication from a design perspective is that if additional energy absorption is required, using multiple thicker cells, rather than one very thick cell, will be more efficient. Where the gains will be inversely proportional to the lateral confinement (resistance against drift and blow out) provided by the structure, i.e. for a theoretical honeycomb structure which provides infinite lateral stiffness, the effect of height variation on the response will be nil.

During the sample manufacturing process for the experimental testing, discussed in Section 3.2.2, it was discovered that variations of the internal expansion angle are extremely likely to occur when the cardboard honeycomb is expanded from its flat pack form. A regular hexagonal geometry has an internal expansion angle of 60°, the two additional simulations represented an under- and over-expanded honeycomb with internal expansion angles of 30° and 90° respectively.

As the honeycomb is expanded, the cross sectional area of cardboard remains constant, while its tributary area changes. The maximum tributary area occurs when the expansion angle is equal to 60°; the peak stress reflected this change in area, being a minimum of 262 kPa when the internal expansion angle was equal to 60°, either side of this the peak stress was increased by 35 % to 324 kPa and 357 kPa for the 30° and 90° analyses respectively. Furthermore, the plateau stress increased with the internal expansion angle causing the peak and plateau stresses to be closer when the expansion angle was 90° than when it was 30°. The energy per unit volume at compaction was unaffected when the honeycomb was under-expanded, but increased by 44 % when the honeycomb was over-expanded (when the expansion angle was increased from 60° to 90°).

The above stated trends suggest that, ideally, the honeycomb should be expanded to 60° and where possible, any manufacturing error, should be due to over- rather than under-expansion. In practice, extreme difficulty was encountered when expanding the finest B mesh; with two people, it was only physically possible to expand B mesh honeycomb to an average of 37.5° (see Table 3.21), the coarser D and F meshes could have been expanded further if required. Therefore, either the difficulty of expansion must be taken into consideration or an alternative expansion method must be investigated when using cardboard honeycomb with a small cell size.

The removal of columns and rows of complete cells from the edges of the honeycomb had no significant effect on the early response; there was no effect on the structural component for all but two of the analyses (9 columns, 5 rows), which showed some softening after 60 % strain. The air pressure components of the response were much more sensitive to variations in the number of rows and columns, where removal of cells from the honeycomb perimeter caused a reduction in lateral confinement and therefore a substantial drop in the magnitude of transmitted stress, and energy stored, by the internal air pressures.

When the number of *columns* was reduced from 25 to 9, and the number of *rows* from 13 to 5, the proportion of structural removal was similar (loss of 26 and 25

cells from the original 40.75 in the quarter symmetry segment), but the energy absorbed (per unit volume) at compaction reduced by 11 % and 18 % respectively i.e. there was a greater reduction in absorption capacity when rows were removed over columns. The response was most sensitive to the removal of rows than columns, because when rows were removed the length of potential blowout pathway was reduced, allowing air to escape much more readily.

The design implication of this is that: for a fixed cellular geometry, the structural response will be mostly unaffected (unless a sample with a very narrow aspect ratio is used) by changes in the number of adjacent cells; however, cardboard honeycombs will generate higher internal pressures and perform more efficiently as an EDM when the number of adjacent cells is increased. An increase in the number of adjacent cells can be made by increasing the plan area of the sample.

Chapter 7

Conclusions and Future Work

Cardboard honeycombs provide a low-cost and lightweight energy dissipating material (EDM) which is easily transported and disposed of once used. They are used extensively in the packaging industry and have historically been used to protect air dropped cargo against damage from shock loading on impact with the ground.

Cellular structures, such as honeycombs, behave as efficient energy dissipating materials due to a geometrically efficient arrangement of their constituent material; their structural form encourages a mesoscopic deformation mode, which for a given macroscopic compaction, will result in a significant amount of internal plastic work (energy dissipation). When cardboard honeycombs are subject to high strain rate deformations, the internal air pressures which develop as a result of the rapid compression of the entrapped air, reach magnitudes which are significant in comparison to the stiffness of the structural response. Consequently, the impact energy dissipation characteristics of cardboard honeycomb are not simply a function of the structural deformation, but of a complex, coupled, non-linear deformation mode which emerges as a result of the interaction between the rapidly deforming cell wall structure and the air trapped within.

The importance of internal air pressures on the cardboard honeycomb's impact response was highlighted by Ripperger and Briggs [8, 31], after which very little was published on the matter (see Section 2.4). Over the years, various series' of impact tests have been used to characterise the cardboard honeycomb's energy dissipating

characteristics, within a given window of design parameters. What has been lacking is understanding of the fundamental mesoscopic mechanisms which occur within the cardboard honeycomb, and how they compose the macroscopic response. It is also worth noting that while the understanding of the impact response of stiffer, metallic honeycombs, has advanced to the stage of well defined mathematical models, the analytical understanding of the complicated, air-structure coupled, cardboard honeycomb response is still in its infancy.

In this study, a detailed series of impact tests was performed to investigate the effect of geometrical variations on the cardboard honeycomb EDM impact response (see Chapter 3); samples from three different mesh sizes (B, D and F) were tested, providing a broad range of cellular geometries. The exact mesoscopic cellular geometry of all tested samples was recorded and digitised, allowing each experimentally induced response to be attributed to an exact, known, cellular geometry. While existing research has tended to identify samples simply by their mesh size, it quickly became apparent that mesh size alone was inadequate to facilitate a detailed investigation of the mechanisms involved in the impact response of the cardboard honeycomb. This was because, even when the construction process was tightly controlled, the inter-sample geometrical variation was high, and these variations were found to have a significant effect on the cardboard honeycomb response.

During each impact test measurements were made of the axial strain, total load transmitted through the sample and the air pressures at four internal locations within each known geometry. This provided novel insight into both the spatial and temporal development of internal air pressures, how the air pressure distribution was affected by variations in the cellular geometry and the significance of the internal air pressures in comparison to the structural response.

To enable the cardboard honeycomb impact response to be studied without the practical, economical and time constraints imposed by experimental methods, a numerical model capable of capturing the high strain rate axial crushing response of an air filled cellular honeycomb structure was constructed (see Chapter 4).

During the cardboard honeycomb impact response, both the structure and the

entrapped air undergo high rate extreme deformations, and while doing so continually redistribute load between one another. The cardboard honeycomb structure also contains a substantial number of glue bonds, and the model must accurately capture the process by which these bonds fail, in order for the correct structural collapse and air venting mechanisms to occur. Numerical techniques capable of capturing each individual component were identified, and verified, before being combined to create a computationally efficient, full-scale, numerical model of the cardboard honeycomb and its entrapped air (Chapter 4).

Precise geometrical records, of the experimentally tested samples, allowed digital replications to be constructed. A simple material parameter calibration, against the measured experimental response of one sample, yielded material parameter values which were characteristic of a cardboard honeycomb cell wall. These material parameter values were then applied to a sample with radically different cellular geometry, and while there were discrepancies between the numerical model and experimental data, considering the minimal variations performed during the calibration, the correlation was surprisingly good.

The numerical modelling techniques were used to produce a further refined, computationally efficient, regular hexagonal honeycomb model as a platform to study the effects of structural parameter variations on the cardboard honeycomb's impact response (see Chapter 5). The refined model was initialised with a set of geometrical and material parameters characteristic of the cardboard honeycomb; while holding the geometry constant, isolated variations of each material parameter allowed a perfectly clean assessment of their effect on the response.

A thorough investigation into the effects of geometrical variations was also performed (see Chapter 6). During previous research into the cardboard honeycomb impact response, a pre-determined macroscopic sample size (plan area and/or height) ensured that any mesoscopic geometrical variations would also result in additional enforced variations of the internal cellular structure. If the macroscopic response could be expressed as simply a summation of many identical local mechanisms, these enforced structural variations would not be a problem: a direct comparison

could be made simply by scaling the response by the amount of cell wall material present; however, during the experimental work it was observed that the magnitude of internal air pressures is non-homogeneous throughout the honeycomb's structure, meaning the cardboard honeycomb impact response must be at least partly determined on the global scale; and therefore, for any analysis aiming to isolate the effects of geometrical variations, a direct comparison can only be made if all other enforced, non-essential geometrical variations are eliminated. The numerical modelling allowed a fundamental geometrical analysis to be performed, singular variations in one of six identified independent geometrical parameters were studied (see Table 6.1), while any dependent geometrical parameters were allowed to vary unhindered (see Table 6.2).

The numerical modelling also revealed the mesoscopic mechanisms and how they evolve within the cardboard honeycomb during its impact response. It was possible to view the structural deformation and internal pressure development with an extremely high, 3 dimensional, spatial resolution. Being able to view and analyse the response in this way, allowed significant advancement towards its understanding and therefore, quantification (see Section 5.2).

7.1 Key findings

a) When subject to a forced axial compression, at the rates characteristic of low velocity impact loading, the cardboard honeycomb structure buckles due to crushing of the cell wall material and not Euler buckling; furthermore, during the early response (low strain), the magnitude of the internal air pressures has not yet developed to be of any significance (see Figure 6.35). Consequently, a good estimation of the peak load can be determined by taking the sum of the cardboard cross sectional area and multiplying by its yield stress.

b) The magnitude of internal air pressures which develop within the cardboard honeycomb EDM, during its high strain rate axial crushing response, is a function

of both the geometrical arrangement and material properties of its cell walls. The internal air pressures increase with strain, and are shown to be significant during the late response; whereas, during the early response, the load transmitted through the cell wall structure is dominant.

Potential geometrical and material characteristics, particular of cardboard honeycombs, happen to place the them in a region where their response can be severely dominated by either the stiffness of the structural response or the internal air pressures, mostly it is a combination of the two. During the experimental testing, a decrease in the cell size was found to increase the magnitude of load transmitted by the internal air pressures but reduce their significance in comparison to the load transmitted by the cellular structure (Figure 3.33).

c) The presence of internal air pressures allows the lateral transfer of load throughout the honeycomb, and therefore modifies the response, from what would otherwise be simply a summation of many localised collapse mechanisms, to a response which is global in nature and dependent on the lateral properties of the cell walls. The cardboard honeycomb's impact response is a complex mechanism which is constantly in flux; a forced axial driving displacement provides a continuous source of additional pressure while the internal air pressures which are driving structural deformations are coupled to themselves via the magnitude of structural deformations which result.

d) The air pressure distribution within the cardboard honeycomb is discretised by the cell walls, and takes the form of many regions of equal pressure matching the geometry of each cell. The cellular air pressures are highest in the centre of the honeycomb and reduce towards the edges, forming a global pressure gradient which increases in steepness with increased axial strain. The magnitude of air pressure within any given cell is a function of the current axial strain and the degree of lateral confinement provided by both the surrounding cellular structure and cellular air pressures.

If sufficient lateral confinement is provided, the cellular air pressure reaches a

theoretical maximum, which is the pressure as predicted by the adiabatic equation of state for a volumetric compaction consisting of the current axial strain and the volume occupied by the folded cellular structure. It is also possible for multiple cells to reach the theoretical maximum air pressure, when this occurs a central equal-pressure plateau develops, the plateau reduces in size as the axial strain, and therefore pressure gradient increases.

e) Two mechanisms result in a reduction of the cellular air pressure below the theoretical maximum. They are: a lateral expansion of the internal volume due to outwards lateral drift of the cell walls, and loss of the entrapped pressurised gas as a result of blowout. Lateral drift has components in two planes, parallel and perpendicular to the glue bonds. The magnitude of lateral drift endured by any region of cell wall is a function of the current pressure gradient across it, and its current lateral structural stiffness. The pressure gradient across the perimeter cell walls tends to be the largest, as the perimeter cell walls are restraining the high cellular over pressure against the surrounding atmospheric pressure (see Figure 5.8); the cell wall material available to restrain this pressure gradient is also at a minimum. The result is an increase in the magnitude of lateral drift towards the perimeter.

Blowout occurs in only one plane, parallel to the glue bonds. For the pressurised air in any given cell to escape, it must have a clear path to the honeycomb perimeter. For a blowout path to form, the pressure gradient between two adjacent cells, which are separated by a pair of double-ply cell walls, must be sufficient to destroy the glue bond and separate the cell walls. Furthermore, double-ply cell walls situated deeper within the honeycomb will have a higher cellular air pressures acting on their back faces; thus, increasing the pressure gradient required to separate them and for a pathway to form, and so the air entrapped in many internal cells may not escape during the course of an impact response while the air in cells close to the perimeter will escape easily.

f) Over the range of material parameter variations studied (see Table 5.6), the cardboard honeycomb's impact response was most sensitive to variations in the glue bond strength, yield stress, and rate of strain hardening (gradient of the post yield constitutive stress-strain curve); an in depth discussion of their effects is given in Section 5.6.

g) The cardboard honeycomb impact response was sensitive to variations in all geometrical parameters shown in Table 6.2. A detailed discussion of the nature and magnitude of each effect is given in Section 6.9.

h) Convergence of the peak and plateau stresses is caused by: an increase of the glue strength, rate of post yield hardening, wall length, and number of adjacent columns and rows of complete cells (plan area); a decrease of yield stress, wall thickness and sample height; and adjustments of the internal expansion angle towards 60° (regular hexagons).

i) An increase of the energy absorption, per unit volume, at compaction (energy absorption capacity) is caused by: an increase of the elastic modulus, yield stress, rate of post yield hardening, cell wall thickness, internal expansion angle (above 60°), and number of adjacent columns and rows of complete cells (plan area); and a decrease of the glue strength, cell wall length and sample height.

j) A shift in dominance of the macroscopic response towards the internal air pressures is caused by: an increase of the glue strength, cell wall length, and number of adjacent columns and rows of complete cells (plan area); and a decrease of the yield stress, rate of post yield hardening, cell wall thickness, internal expansion angle (above 60°) and sample height.

The greatest uncertainty during the work presented in this thesis is a lack of experimental data on the material properties for the cell wall material which com-

posed the experimentally tested samples. To be valid, any material testing of the cell wall material would have had to have been performed at the same, high, strain rates used during the impact test. Apparatus was not readily available to perform such tests, and it was felt that it would require a substantial time investment to develop a testing procedure from scratch. It was also not clear as to how the cell wall material could be tested in a configuration which would be relevant to the compressive loading conditions and deformations mechanism present within the cell walls of a cardboard honeycomb during its impact response.

A common method of numerical model development is where the modeller begins with a experimentally measured material properties and performs iterations on the numerical techniques until the response matches experimental results. As the material properties were unknown, an opposite approach was necessary whereby the accuracy of each numerical technique was first verified before being included the full model, an approach which is arguably more valid but much more tedious.

Fortunately, in this case the model development produced a numerical model which gave good agreement with the experimental data with a after a simple calibration and produced values which are perfectly acceptable for a cardboard honeycomb cell wall, which suggested that the modelling methods were sound. Unfortunately, due to the large number of possible values for material properties, the high computational cost required to check different combinations of values, and problems in the accuracy of the experimentally recorded data, an iron clad experimental validation of the numerical model was not possible. To combat this, an extensive material parameter study was performed with a scope wide enough to cover any uncertainties.

It is also likely that the linear elastic-plastic material model used for the cell walls could be substantially improved upon. Although it is felt that the relative variations in the response and therefore any trends would be observed regardless of the complexity of the material model, and at this stage, a simple material model is perhaps advantageous in allowing the behaviour to be understood without introducing additional, unquantified, complexity.

7.2 Further work

The next logical step would be to use the large bank of numerical results produced throughout this thesis to characterise the cardboard honeycomb, one possible method of characterisation would be to produce a series of characterisation curves. This process is covered thoroughly in a publication by Gibson and Ashby [41] who develop various characterisation curves for the EDM response of foams.

Some characterisation work has previously been performed for cardboard honeycombs, although limited in scope due to oversimplification, experimental data of the impact responses of various honeycomb samples were used to produce cushion curves (maximum deceleration vs static stress) [38], and the quasi-static responses to produce energy absorption diagrams (energy absorption per unit volume vs transmitted stress) [42–44].

The next step would be to produce design guidance based on fundamental research rather than ad hoc series of experimental tests. It is hoped that this will allow more efficient and reliable design of cardboard honeycombs by providing tighter control over their energy dissipating characteristics and making better use of the free energy dissipation provided by compression of the entrapped air.

The development of an experimentally derived constitutive model of the cell wall material would be of great benefit to numerical modellers. To do so, it will be necessary to collect experimental data regarding the cardboards elastic properties, tearing strength, and tensile/compressive strengths at the in-situ strain rates experienced by the cell wall, during the honeycomb's impact response. It will also be necessary to identify the effects of any orthotropy, and if found to be significant, the cell wall material will need to be tested in both the machine and cross directions, and various angles of rotation between the two.

For a truly comprehensive model of the high-strain rate behaviour of the cell wall material to be developed it may necessary to consider the cardboard microstructure and the mechanical interaction between adjacent fibres. Experimental testing to determine the properties of the glue bonds would also be useful. Burst

tests of specially constructed individual cells (such as was performed by Ripperger and Briggs [31]) would provide experimental data, which could be used to validate a small scale accompanying numerical model.

The ultimate goal is a fully comprehensive mathematical model of the collapsing cardboard honeycomb structure and its interaction with the entrapped air. This mathematical model would be able to predict the cardboard honeycomb's EDM characteristics for a known set of material and geometrical parameters. Fundamentally, a mathematical model of the response will need to predict the magnitude of load transmitted by a) the structure and b) the internal air pressures. It may be possible to do this by adapting existing mathematical models, which predict the structural only response, by including the modifications to the structural response mechanism, which result from the internal air pressures.

To predict the load transmitted by the internal air pressures, it will be necessary to consider the strain dependent permeability and lateral stiffness of the honeycomb structure. If the permeability and lateral stiffness of the honeycomb structure are known, predictions could be made of the proportion of retained air, the average internal air pressure, and the average cell walls lateral displacement for the average internal air pressure. The load transmitted by the structure could then be predicted by modifying the mechanics of the perfectly axial buckling response to account for lateral deformations.

Another approach may be to consider the mechanics of a *super element* whereby all of the internal cell wall material is lumped at the honeycomb's perimeter. This super element will have an axial stiffness, permeability and orthotropic lateral stiffness representative of the average internal mesoscopic behaviour.

To develop a truly comprehensive mathematical model of the cardboard honeycomb, there are many areas of research which must be investigated. In the author's opinion, those which should be of high priority are:

- Variations in strain rate. Including an analysis of the transition between the quasi-static and dynamic response modes. It is suggested that for any future experimental impact tests, a complementary quasi-static series be performed.

Thus, allowing the emergence of the dynamic mechanisms to be observed.

- Further geometrical variations and other combinations of parameters, e.g. single to double cell wall length ratio.
- Multiple stacks, and multiple stacks of varied geometries.
- Oblique impacts, i.e. loading with a horizontal component.

With recent advancements in 3 dimensional printing techniques, it is expected that further research will be performed into the design of bespoke, computationally optimised, energy dissipating structures. It has been shown during this thesis that the computational power now exists to perform numerical simulations of a rapidly deforming structure in composite with an entrapped fluid, and that the entrapped fluid can provide a substantial proportion of additional energy absorption capacity.

There is no reason why the structure must be of honeycomb geometry, be made of cardboard or that the entrapped fluid must be air. Clearly, there is now enormous potential for the simulation, design and construction, of a new breed of extremely efficient and bespoke, fluid-structure-composite, energy dissipating materials.

References

[1] Page, W. J. S. *Parachute Rigging in Afghanistan*. 2010.

[2] USAF. *Airdrop of supplied and equipment: rigging airdrop platforms, report ref FM 4-20.102*. Tech. rep. United States Air Force, 2001.

[3] U.S. Army. *Machinery for the expansion of paper honeycomb core into energy dissipation pads (EDPs)*. 2012.

[4] U.S. Army. *Pad, Energy dissipator - Performance specification, report ref MIL-PRF-9884F*. Tech. rep. Natick Research Development and Engineering Center, 1997.

[5] Wang, D.-M. and Wang, Z.-W. *Experimental investigation into the cushioning properties of honeycomb paperboard*. Packaging Technology and Science (published online), 2008.

[6] Dufaylite Group. *[www.dufaylite.com]*.

[7] Lacey, A. *The secret ingredient for a safer bike helmet: paper*. http://www.bbc.co.uk/news/health-25681895. 2014.

[8] Ripperger, E. A. and Briggs, W. R. *Variations in the crushing strength of paper honeycomb, report ref 70-57-AD*. Tech. rep. Austin, Texas: Engineering Mechanics Research Laboratory, The University of Texas, 1969.

[9] Smithson, G. *Energy dissipation characteristics of air-drop materials under impact loading*. Tech. rep. Lowell Technological Institute Research Foundation, 1957.

[10] Tyas, A. *Blastech Ltd report to DSTL Porton Down Physical Protection Group on crush behaviour of expanded honeycomb cardboard, report ref BT-058-01.* Tech. rep. Blastech Ltd, 2008.

[11] Alghamdi, A. *Collapsible impact energy absorbers: an overview.* Thin-Walled Structures 39, 2001, pp. 189–213.

[12] Abramowicz, W. and Jones, N. *Dynamic axial crushing of circular tubes.* International Journal of Impact Engineering 2.3, 1984, pp. 263–281.

[13] Abramowicz, W. and Jones, N. *Dynamic axial crushing of square tubes.* International Journal of Impact Engineering 2.2, 1984, pp. 179–208.

[14] Abramowicz, W. and Jones, N. *Dynamic progressive buckling of circular and square tubes.* International Journal of Impact Engineering 4.4, 1986, pp. 243–270.

[15] Jones, N. *Structural Impact.* 2nd. Cambridge University Press, 1989.

[16] Langseth, M and Hopperstad, O. *Static and dynamic axial crushing of square thin-walled aluminium extrusions.* International Journal of Impact Engineering 18.7-8, 1996, pp. 949–968.

[17] Zhao, H. and Abdennadher, S. *On the strength enhancement under impact loading of square tubes made from rate insensitive metals.* International Journal of Solids and Structures 41.24-25, 2004, pp. 6677–6697.

[18] White, M. and Jones, N. *Experimental quasi-static axial crushing of top-hat and double-hat thin-walled sections.* International Journal of Mechanical Sciences 41, 1999, pp. 179–208.

[19] White, M., Jones, N., and Abramowicz, W. *A theoretical analysis for the quasi-static axial crushing of top-hat and double-hat thin-walled sections.* International Journal of Mechanical Sciences 41, 1999, pp. 209–233.

[20] Reid, S., Reddy, T., and Gray, M. *Static and dynamic axial crushing of foam-filled sheet metal tubes.* International Journal of Mechanical Sciences 28.5, 1986, pp. 295–322.

[21] Abramowicz, W. and Wierzbicki, T. *Axial crushing of foam-filled columns.* International Journal of Mechanical Sciences 30.3-4, 1988, pp. 263–271.

[22] Wierzbicki, T. *Crushing analysis of metal honeycombs.* International Journal of Impact Engineering 1.2, 1983, pp. 157–174.

[23] Wu, E and Jiang, W. *Axial crush of metallic honeycombs.* International Journal of Impact Engineering 19.5-6, 1997, pp. 439–456.

[24] Zhao, H and Gary, G. *Crushing behaviour of aluminium honeycombs under impact loading.* International Journal of Impact Engineering 21.10, 1998, pp. 827–836.

[25] Zhao, H., Elnasri, I., and Abdennadher, S. *An experimental study on the behaviour under impact loading of metallic cellular materials.* International Journal of Mechanical Sciences 47.4-5, 2005, pp. 757–774.

[26] Yamashita, M. and Gotoh, M. *Impact behavior of honeycomb structures with various cell specifications-numerical simulation and experiment.* International Journal of Impact Engineering 32, 2005, pp. 618–630.

[27] Xu, S. et al. *Strength enhancement of aluminium honeycombs caused by entrapped air under dynamic out-of-plane compression.* International Journal of Impact Engineering 47, 2012, pp. 1–13.

[28] McFarland, R. K. *Hexagonal cell structures under post-buckling axial load.* AIAA Journal 1.6, 1963, pp. 1380–1385.

[29] Zhang, J and Ashby, M. F. *The out-of-plane properties of honeycombs.* International Journal of Mechanical Sciences 34.6, 1992, pp. 475–489.

[30] *Airdrop of supplies and equipment: rigging typical supply loads, report ref FM 4-20.112.* Tech. rep. February. United States Army, 2009.

[31] Ripperger, E. A. and Briggs, W. R. *The crushing strength of paper honeycomb, report ref 73-31-AD.* Tech. rep. Austin, Texas: Engineering Mechanics Research Laboratory, The University of Texas, 1973.

[32] Ripperger, E. A. and Briggs. *The crushing strength of paper honeycomb, report ref 73-31-AD*. Tech. rep. Austin, Texas: Engineering Mechanics Research Laboratory, The University of Texas, 1973.

[33] Briggs, W. R. and Ripperger, E. A. *Paper honeycomb cushioning pad*. U.S. pat. 3,982,057, 1976.

[34] Ripperger, E. A. and Hannon, G. J. *The effects of moisture content on the energy dissipation characteristics of paper honeycomb, report ref 69-67-AD*. Tech. rep. 1969. Austin, Texas: Engineering Mechanics Research Laboratory, 1969.

[35] Hopf, J. P. *Equilibrium moisture content of paper honeycomb and its effect on energy absorption*. Tech. rep. Forest Products Laboratory, 1955.

[36] Guo, Y. and Zhang, J. *Shock absorbing characteristics and vibration transmissibility of honeycomb paperboard*. Shock and Vibration 11.5, 2004, pp. 521–531.

[37] ATSM D 1596. *Standard test method for shock absorbing characteristics of package cushioning materials*.

[38] Wang, D. *Impact behavior and energy absorption of paper honeycomb sandwich panels*. International Journal of Impact Engineering 36.1, 2009, pp. 110–114.

[39] Aminanda, Y. et al. *Experimental Analysis and Modeling of the Crushing of Honeycomb Cores*. Applied Composite Materials 12.3-4, 2005, pp. 213–227.

[40] Lu, L.-X., Sun, Y.-P., and Wang, Z.-W. *Critical buckling load of paper honeycomb under out-of-plane pressure*. Packaging Technology and Science 18.3, 2005, pp. 141–150.

[41] Gibson, L. J. and Ashby, M. F. *Cellular Solids: Structure And Properties*. 2nd. Cambridge University Press, 1999.

[42] Wang, D.-M., Wang, Z.-W., and Liao, Q.-h. *Energy absorption diagrams of paper honeycomb sandwich structures*. Packaging Technology and Science 22.2008, 2009, pp. 63–67.

[43] E, Y.-P. and Wang, Z.-W. *Effect of Relative Humidity on Energy Absorption Properties of Honeycomb Paperboards*. Packaging Technology and Science 23, 2010, pp. 471–483.

[44] Wang, Z.-W. and E, Y. P. *Mathematical modelling of energy absorption property for paper honeycomb in various ambient humidities*. Materials & Design 31.9, 2010, pp. 4321–4328.

[45] Mann, R. W., Baum, G. A., and Habeger, C. C. *Determination of all nine orthotropic elastic constants for machine-made paper*. Tech. rep. 84. Appleton, Wisconsin: The Institute of Paper Chemistry, 1979.

[46] Baum, G. A., Habeger, C. C., and Fleischman, E. H. *Measurement of the orthotropic elastic constants of paper*. Tech. rep. 117. Appleton, Wisconsin: The Institute of Paper Chemistry, 1981.

[47] Castro, J and Ostoja-Starzewski, M. *Elasto-plasticity of paper*. International Journal of Plasticity 19.12, 2003, pp. 2083–2098.

[48] Dillon, S, Jones, R, and Buzzi, V. *On the mechanical behaviour of aging and recycled paper structures under cyclic humidity*. Composite structures 47, 1999, pp. 727–736.

[49] Mäkelä, P. and Östlund, S. *Orthotropic elasticplastic material model for paper materials*. International Journal of Solids and Structures 40.21, 2003, pp. 5599–5620.

[50] Allaoui, S., Aboura, Z., and Benzeggagh, M. L. *Phenomena governing uni-axial tensile behaviour of paperboard and corrugated cardboard*. Composite Structures 87, 2009, pp. 80–92.

[51] E, Y.-P. and Wang, Z.-W. *Plateau stress of paper honeycomb as response to various relative humidities*. Packaging Technology and Science 23, 2010, pp. 203–216.

[52] Schulgasser, K. *The in-plane poisson ratio of paper*. Fibre Science and Technology 19.4, 1983, pp. 297–309.

[53] Szewczyk, W. *Determination of poissons ratio in the plane of the paper*. Fibres & Textiles in eastern Europe 16.4, 2008, pp. 117–120.

[54] Hewitt, E. and Hewitt, R. E. *The Gibbs-Wilbraham phenomenon: an episode in Fourier analysis*. Archive for history of Exact Sciences 21, 1979.

[55] Butterworth, S. *On the theory of filter amplifiers*. Experimental and Wireless, 1930, pp. 536–541.

[56] Timoshenko, S and Gere, J. *Theory of Elastic Stability*. 2nd. McGraw-Hill, 1963.

[57] Young, W. C. and Budynas, R. G. *Roark's Formulas for Stress and Strain*. 7th. McGraw-Hill, 2002.

[58] Magee, C. and Thornton, P. *Design considerations in energy absorption by structural collapse*. Tech. rep. Society of Automotive Engineers, 1978.

[59] Belytschko, T., Lin, J. I., and Tsay, C.-S. *Explicit algorithms for the nonlinear dynamics of shells*. Computer methods in applied mechanics and engineering 42, 1984, pp. 225–251.

[60] Hallquist, J. *LS-Dyna Theory Manual*. Tech. rep. Livermore Software Technology Corporation, 2006.

[61] Belytschko, T., Wong, B. L., and Chiang, H.-Y. *Advances in one-point quadrature shell elements*. Computer Methods in Applied Mechanics and Engineering 96.1, 1992, pp. 93–107.

[62] Flanagan, D. and Belytschko, T. *A uniform strain hexahedron and quadrilateral with orthogonal hourglass control*. International Journal for Numerical Methods in Engineering 17.August 1980, 1981, pp. 679–706.

[63] Perry, R. and Maloney, J. *Perry's Chemical Engineers' Handbook*. Ed. by Perry, R., Green, D., and Maloney, J. 7th. McGraw-Hill, 1999.

[64] Magee, J. W. *Molar heat capacity at constant volume for air from 67 to 300 K at pressures to 35 MPa*. International Journal of Thermophysics 15.5, 1994, pp. 849–861.

[65] Serway, R. and Jewett, J. *Physics for Scientists and Engineers*. 9th. Cengage Learning, 2013, p. 1344.